

**UNIVERSITY  
OF OSLO**

Renate Mauland-Hus

**Large-scale structure with massive  
neutrinos and modified gravity**

A simulation-based approach

**Thesis submitted for the degree of Philosophiae Doctor**

Institute of Theoretical Astrophysics  
Faculty of Mathematics and Natural Sciences



**2023**

© **Renate Mauland-Hus, 2023**

*Series of dissertations submitted to the  
Faculty of Mathematics and Natural Sciences, University of Oslo  
No. 2694*

ISSN 1501-7710

All rights reserved. No part of this publication may be reproduced or transmitted, in any form or by any means, without permission.

Cover: UiO.  
Print production: Graphic center, University of Oslo.

*To my past self. You made it.*



# Summaries

## Summary

The large-scale structure of the cosmos holds much information about the components and laws of nature that govern our Universe. As it stands, the  $\Lambda$ -cold-dark matter ( $\Lambda$ CDM) model, where the Universe contains dark energy, dark matter, and ordinary matter, and gravity is described by the theory of general relativity, recreates our cosmological observations with high accuracy when implemented in simulations. Although this indicates that the model fits reality well, the recent increase in observational data has revealed some parameter tensions and has also yet to uncover the mysteries of the dark sector. In light of this, extending our simulations to include more details has become important, to better gauge the agreement between the observed Universe and the simulated one. In addition, exploring models outside of the standard model of the Universe, to offer alternatives to the dark sector, continues to be meaningful, so long as its nature remains elusive. In this thesis work, I have investigated a small, yet connected, portion of both categories.

Neutrino particles were originally thought to be massless, but have since the change of the millennium been known to harbour a small, non-zero, mass. However, neutrinos were relativistic particles early on in the history of the Universe, and became non-relativistic sometime in the matter-dominated era, after recombination. Because of this behaviour, neutrinos contribute to structure formation in a unique way. Below a certain scale, depending on the neutrino masses, the neutrino particles cannot be gravitationally bound and will free-stream out of gravitational potential wells. This results in a suppression of structure growth on non-linear scales. The amount of suppression depends on the neutrino masses, which up to the present time are unknown. Particle physics experiments provide upper and lower mass bounds, but they are not yet determined exactly. Cosmological observations, due to the neutrino impact on structure formation, can be used to put further constraints on the sum of the neutrino masses, however, the bound will always depend on the chosen cosmological model. Neutrinos have often been ignored in cosmological simulations due to their low total mass and therefore small impact. However, as the precision of observations continues to improve, the suppression in the matter power spectrum due to massive neutrinos can be measured directly within expected error estimates. This makes it important to include neutrinos in our numerical simulations, to capture their effect on small-scale structures. A part of this thesis work thus included incorporating massive neutrinos into the well-known **RAMSES** cosmological  $N$ -body simulation, resulting in the code **ANUBIS**. This was compared to other codes including the impact of massive

neutrinos in a *Euclid* Consortium code comparison project, making up the first paper of this thesis and contributing to the goal of adding more details to our  $\Lambda$ CDM simulations.

It is possible that not everything can be understood by increasing our  $\Lambda$ CDM simulation details. Although the  $\Lambda$ CDM model and general relativity seem to explain our Universe well, there is still a possibility that this is not our final Universe model. One popular beyond- $\Lambda$ CDM model category is  $f(R)$ -modified gravity. Here, the framework of general relativity is extended by a function of the Ricci scalar in the gravitational action, which can be constructed to produce an expansion history similar to that of  $\Lambda$ CDM. In these models, the  $f(R)$  extension can take the role of the cosmological constant,  $\Lambda$ , eliminating the need for dark energy through a modification of gravity. Interestingly, this leads to an enhancement of gravity, which increases clustering on scales similar to the ones suppressed by massive neutrinos. This means that the  $f(R)$ -modified gravity theories and massive neutrinos have degenerate observables, and therefore that the sum of the neutrino masses and the parameter determining the strength of the modification to gravity depend on each other. Because of this, it is therefore important to include massive neutrinos in  $f(R)$  simulations when trying to put constraints on the modifications to gravity allowed by observations, and ideally, we should find a way to break this degeneracy. As a part of this thesis work, we have therefore merged the **ANUBIS** code with an already existing modified gravity **RAMSES**-based code, **ISIS**, creating the code **ANUBISIS**, which includes both massive neutrinos and modified gravity.

Investigating cosmologies with massive neutrinos and  $f(R)$ -modified gravity theories, both simultaneously and individually, is important in order to disentangle the effects of the two from each other. One promising avenue for doing so is cosmic voids, which are large underdense regions in the cosmic web, sensitive to both massive neutrinos and modified gravity. During this thesis work, for the second paper, we used simulations from **ANUBISIS** to investigate how well voids can extract cosmological information in the settings of  $f(R)$  gravity, massive neutrinos, and their combination. We did this in order to understand if the current void modelling techniques are accurate enough to separate the various scenarios, which is important if we want to use voids to break the neutrino- $f(R)$  degeneracy. This required some specific information, like halo and void catalogues, which is why it was convenient to work with detailed  $N$ -body simulations where this can be extracted. Sometimes, however, we are primarily interested in some of the main clustering statistics of various cosmologies, like the matter power spectrum. In these cases, it can be inconvenient to perform time and resource-consuming full  $N$ -body simulations, and luckily, emulators already exist for several cosmological models. The emulators themselves, however, are typically created from a large set of detailed simulations and are therefore not easily extended to new cosmologies. For the third paper, also in the light of exploring modified gravity in comparison to  $\Lambda$ CDM, we therefore developed a full pipeline for creating a power spectrum ratio emulator for beyond- $\Lambda$ CDM versus  $\Lambda$ CDM models, functioning entirely without the need for supercomputers. It uses approximate methods to perform a suite of simulations, and machine

---

learning to construct the emulator through neural network training. We named the pipeline *Sesame*, as it opens up the opportunity for anyone to create an emulator without the time and resources required to run full, detailed  $N$ -body simulations.

All in all, this thesis work is an exploration of how extensions to the  $\Lambda$ CDM model affect large-scale structure probes, like the matter power spectrum and the void-galaxy cross-correlation function, and sheds light on why it is important to investigate and disentangle degenerate components for future precision cosmology. Left behind are the  $N$ -body codes **ANUBIS** and **ANUBISIS**, and the emulator pipeline, *Sesame*, allowing further exploration of beyond- $\Lambda$ CDM models in the time to come.

## Sammendrag

Den kosmiske storskalastrukturen inneholder mye informasjon om komponentene og naturlovene som styrer universet.  $\Lambda$ -kald-mørk-materie-modellen ( $\Lambda$ -cold-dark-matter;  $\Lambda$ CDM), hvor universet inneholder mørk energi, mørk materie og vanlig materie, og tyngdekraften er beskrevet av den generelle relativitetsteorien, kan gjenskape observasjonene våre svært nøyaktig når den implementeres i kosmologiske simuleringer. Selv om dette tyder på at modellen beskriver virkeligheten godt, har den nylige økningen i mengden observasjonell data avslørt gnisninger for noen kosmologiske parameterverdier. I tillegg har vi fremdeles ikke løst mysteriet rundt mørk materie og mørk energi. I lys av dette har det blitt viktig å utvide simuleringene våre slik at de inneholder flere detaljer, for å bedre kunne vurdere hvor godt det virkelige og det simulerte universet stemmer overens. Så lenge mørk materie og mørk energi forblir ukjente, er det i tillegg også interessant å undersøke alternative universmodeller, som har andre forklaringer på de mørke komponentene av universet. I denne avhandlingen har jeg undersøkt et lite, men overlappende, område av begge disse kategoriene.

Originalt trodde man at nøytrinopartikler var masseløse. Senere, rundt år 2000, ble det oppdaget at nøytrinoer faktisk har en liten, ikke-neglisjerbar, masse. Nøytrinoer var likevel relativistiske partikler i det tidlige universet, og ble først ikke-relativistiske i den materiedominerte tidsepoken, etter at rekombinasjon hadde funnet sted. På grunn av denne oppførselen, bidrar nøytrinoer til strukturdannelse på en unik måte. Under en viss størrelsesorden, avhengig av de ulike nøytrinomassene, kan ikke nøytrinopartiklene bli gravitasjonelt bundet og vil strømme fritt ut av gravitasjonsbrønner. Dette fører til en undertrykkelse av strukturvekst for ikke-lineære størrelsesordener. Hvor mye veksten blir undertrykt avhenger av nøytrinomassene, som så langt er ukjente. Eksperimenter innen partikkelfysikk har funnet nedre og øvre grenser på nøytrinomassene, men de er fremdeles ikke nøyaktig fastslått. Kosmologiske observasjoner kan også bli brukt til å sette grenser på summen av nøytrinomassene, på grunn av måten nøytrinoene påvirker strukturformasjon på, men vil alltid avhenge av den valgte kosmologiske modellen. Nøytrinoer har ofte blitt ignorert i kosmologiske simuleringer på grunn av partiklenes lave masse, og derav beskjedne påvirkning. Nå som detaljnivået i kosmologiske observasjoner har økt, kan nøytrinoenes påvirkning på de vanligste statistiske observablene måles direkte innenfor forventede feilmarginer. På grunn av dette er det nå viktig å inkludere massive nøytrinoer i numeriske simuleringer, for å få med deres undertrykkelse av strukturformasjon for små størrelsesordener. Som en del av dette Ph.D.-arbeidet har vi derfor inkludert massive nøytrinoer i den kjente  $N$ -legeme-koden **RAMSES**. Dette resulterte i koden **ANUBIS**, som ble sammenlignet med andre lignende koder i et *Euclid*-konsortium-prosjekt. Dette utgjør den første artikkelen i avhandlingen, og bidrar til målet om å inkludere flere detaljer i allerede eksisterende  $\Lambda$ CDM-simuleringer.

Selv om  $\Lambda$ CDM-modellen og generell relativitetsteori ser ut til å beskrive universet godt, er det fremdeles en mulighet for at dette ikke er den endelige måten å beskrive universet vårt på. Dette betyr at inkludering av flere detaljer i  $\Lambda$ CDM-simuleringer ikke nødvendigvis kan hjelpe oss å beskrive alle observasjoner.



---

En populær alternativ universmodell er  $f(R)$ -modifisert tyngdekraft, hvor generell-relativitets-rammeverket blir utvidet med en funksjon av Ricci-skalaren i gravitasjonsvirkningen. Denne funksjonen kan bli laget slik at det oppnås en univershistorie som ligner den i  $\Lambda$ CDM, og  $f(R)$  kan til og med ta rollen til den kosmologiske konstanten,  $\Lambda$ , slik at effekten av mørk energi oppnås gjennom modifisert tyngdekraft. Dette fører til en forsterkning av tyngdekraften, som igjen øker strukturformasjon på størrelsesordener lignende de som blir undertrykt av massive nøytrinoer. Dette betyr at  $f(R)$ -teorier og massive nøytrinopartikler har degenererte observabler, og dermed at summen av nøytrinomassene og parameteren som beskriver styrken av den modifiserte tyngdekraften avhenger av hverandre. På grunn av dette er det derfor viktig å inkludere massive nøytrinoer i  $f(R)$ -simuleringer når vi prøver å estimere den tillatte mengden modifisert tyngdekraft basert på observasjoner. Ideelt sett ønsker vi å finne en måte å bryte denne degenerasjonen på. Som en del av dette Ph.D.-arbeidet har vi derfor slått sammen ANUBIS-koden vår med en allerede eksisterende RAMSES-basert kode, ISIS, som inneholder modifisert tyngdekraft. Dette resulterte i koden ANUBISIS, som da inneholder både massive nøytrinoer og modifisert tyngdekraft.

Det er viktig å undersøke kosmologier med massive nøytrinoer og  $f(R)$ -modifisert tyngdekraft både samtidig og individuelt for å prøve å skille deres påvirkning på strukturdannelse fra hverandre. En lovende måte å gjøre dette på er gjennom å studere kosmiske hulrom. Dette er store områder i den kosmiske nettverkstrukturen som har under gjennomsnittlig tetthet og er sensitive til både massive nøytrinoer og modifisert tyngdekraft. For å studere dette videre brukte vi simuleringer fra ANUBISIS for å undersøke hvor godt den nåværende hulromsmodelleringen kan hente ut kosmologisk informasjon fra ulike setninger med  $f(R)$ -tyngdekraft, massive nøytrinoer og begge deler samtidig. Dette gjorde vi for å finne ut av om den nåværende modelleringen er nøyaktig nok til å skille de ulike scenarioene fra hverandre. Undersøkelsen resulterte i den andre artikkelen som er en del av denne avhandlingen, og er en viktig del av prosessen for å eventuelt kunne bruke kosmiske hulrom til å bryte degenerasjonen mellom modifisert tyngdekraft og massive nøytrinoer. Dette krevde spesifikk informasjon, som for eksempel kataloger av mørk materie haloer og kosmiske hulrom, som gjorde det beleilig å jobbe med detaljerte  $N$ -legeme-simuleringer hvor man kan hente ut denne dataen. I andre situasjoner, derimot, er man ofte bare interessert i noen av hovedobservablene for ulike kosmologier, som for eksempel effektspektrumet. I disse tilfellene er det ikke lengre nyttig å utføre tid- og ressurskrevende simuleringer. Heldigvis finnes det emulatorer for disse observablene for ulike kosmologiske modeller, men disse krever likevel ofte detaljerte simuleringer for å konstrueres og kan ikke lett utvides til nye kosmologiske modeller. På grunn av dette, og for å videre utforske alternative universmodeller, utviklet vi en pipeline for å lage en emulator som estimerer forholdet mellom effektspektrumet for en alternativ universmodell og  $\Lambda$ CDM-modellen, helt uten bruken av superdatamaskiner. Pipelinen bruker tilnæringsmetoder til å utføre en rekke simuleringer, og maskinlæring, i form at et nevralt nettverk, til å lage emulatoren. Dette resulterte i den tredje artikkelen i denne Ph.D.-avhandlingen og selve pipelinen, *Sesame*, navngitt for mulighetene

den åpner opp for andre til å lage sin egen emulator uten tilgang til store beregningsressurser.

Alt i alt er denne avhandlingen en utforskning av utvidelser av  $\Lambda$ CDM-modellen og hvordan disse påvirker vanlige statistiske observabler. I tillegg belyser den temaet om degenererte parametre og hvorfor det er viktig å skille disse fra hverandre for framtidig presisjonskosmologi. Vi etterlater oss  $N$ -legeme-kodene **ANUBIS** og **ANUBISIS**, og emulator-pipelinen, *Sesame*, som alle bidrar til muligheten for videre utforskning av alternative universmodeller i tiden som kommer.

---

## Preface

Describing the world that we live in, from deep beneath the sea to high above the clouds, has long been a calling for humanity. In early times, we studied patterns here on Earth; the movement of animals, the changing of seasons, the ebb and flow of the sea, and the positions of celestial objects. We used the knowledge to get food, navigate, and evolve, but also as a way to understand the world through legends, songs, and beliefs. Now, the pursuit of knowledge lives on, perhaps more than ever, as we try to understand and describe everything from tiny elemental particles to the vast architecture of the Universe. This thesis is a part of the continued quest to study our world and it looks outwards toward the larger structures of our Universe and how they came to be.

It all starts, as it must, with Chapter 1, where I first take you through a brief history of our Universe, from its birth to the present time. I follow up by introducing the framework of our current standard model of cosmology, focusing on the growth of structure - from tiny density perturbations to the giant formations we observe today. By the end of the chapter, I point out some questions that are currently left unanswered, setting the stage for the main topic of my thesis work, the subjects of massive neutrinos and modified gravity. I proceed, in Chapter 2, by introducing said matters individually, first addressing the nature of massive neutrino particles and their impact on cosmology, and then the essence of  $f(R)$ -modified gravity, and its influence. Although they are quite different, on one side particles of the standard model, and on the other an extension of the general relativity framework, they have similar, yet opposite, ways of affecting cosmological structure formation, resulting in several degenerate observables where their individual effects are hard to disentangle. This leads us to Chapter 3, where I introduce the main observables used in my thesis work, to investigate the above-mentioned situation. However, this thesis work has not involved directly observed data from telescopes and satellites, but rather data from cosmological  $N$ -body simulations, where we can better study the direct effects of our chosen cosmological parameters. A general introduction to this topic, along with a more specific description of the codes employed for this work, is therefore found in Chapter 4. Finally, Chapter 5, the last chapter of this thesis, summarises each of the papers going into the thesis and concludes the work as a whole. Following this, the three papers of the thesis can be found in their entirety, in writing order.

This thesis is submitted in partial fulfilment of the requirements for the degree of *Philosophiae Doctor* at the University of Oslo. The research presented here was conducted at the Institute of Theoretical Astrophysics under the supervision of professor Øystein Elgarøy and associate professor Hans A. Winther. This work was supported by the Norwegian Research Council through grant 144838, focusing on Norwegian participation in *Euclid*. Some of the research was performed as a part of the *Euclid* Consortium and this thesis thus contains *Euclid* Consortium material. In addition, some of the computations performed for this thesis work depended on resources provided by UNINETT Sigma2 – the National Infrastructure for High-Performance Computing and Data Storage in Norway.

## Acknowledgements

I would like to thank my supervisors, professor Øystein Elgarøy and associate professor Hans A. Winther, for their guidance, help, and effort throughout this thesis work. I would also like to thank the people I have shared a workspace with, not only in office 502, but the entire fourth and fifth floor. Thank you so much for the scientific discussions, but most of all, thank you for the good times. Good luck to you all on the road - I hope our paths cross again.

Thank you, a million times, to my family and friends for your support throughout this degree. Thank you for the countless phone calls, constant emotional support, and calming walks. Thank you for all the cat pictures, for the books devoured in companionship, and for the therapy sessions disguised as pancake breakfasts, workout sessions, and tea breaks. Thank you for the feedback on my work, for the important conversations, and for the hours of TV series watched. Without all of you, I would not have made it.

And finally, Even. My lovely husband, who has been there for me always. From the very beginning, when we moved to Oslo and I started my bachelor's degree in physics and astronomy, to the very end, when this roller-coaster of a thesis has finally passed through its closing loop. You fed me. You watered me. You made sure I saw the sun and touched the grass. Thank you so much for believing in me, even when I didn't believe in myself. You made all the difference.

✿ **Renate Mauland-Hus**

Oslo, September 2023

# List of papers

## Paper I

**Euclid: Modelling massive neutrinos in cosmology – a code comparison**

*Euclid* Consortium, Julian Adamek, and Others.

*Journal of Cosmology and Astroparticle Physics*, JCAP06(2023)035.

DOI: 10.1088/1475-7516/2023/06/035

arXiv: 2211.12457

## Paper II

**The void-galaxy cross-correlation function with massive neutrinos and modified gravity**

Renate Mauland, Øystein Elgarøy, David F. Mota, and Hans A. Winther.

*Astronomy & Astrophysics*, A&A 674 A185 (2023).

DOI: 10.1051/0004-6361/202346287

arXiv: 2303.05820

## Paper III

**Sesame: A power spectrum emulator pipeline for beyond- $\Lambda$ CDM models**

Renate Mauland, Hans A. Winther, and Cheng-Zong Ruan.

Submitted to *Astronomy & Astrophysics*.

## Additional papers not included in the thesis

**The Ubiquitous Imprint of Radiative Acceleration in the Mean Absorption Spectrum of Quasar Outflows**

Lluís Mas-Ribas and Renate Mauland.

*The Astrophysical Journal*, ApJ 886 151 (2019).

DOI: 10.3847/1538-4357/ab4efd

arXiv: 1902.04085

**Quantized Vortices in Superfluid Dark Matter**

Renate Mauland and Øystein Elgarøy.

*Journal of Cosmology and Astroparticle Physics*, JCAP01(2022)044.

DOI: 10.1088/1475-7516/2022/01/044

arXiv: 2109.01011



# Contents

Summaries	iii
List of papers	xi
Contents	xiii
<b>1 The standard model of cosmology</b>	<b>1</b>
1.1 The history of our Universe . . . . .	1
1.2 General relativity . . . . .	2
1.3 The growth of structure . . . . .	5
1.4 Unanswered questions . . . . .	14
<b>2 Beyond the standard model of cosmology</b>	<b>19</b>
2.1 Massive neutrinos . . . . .	19
2.2 $f(R)$ -modified gravity . . . . .	22
2.3 Degeneracy . . . . .	25
<b>3 Observing the large-scale structure</b>	<b>27</b>
3.1 Cross-correlation function . . . . .	27
3.2 Power spectrum . . . . .	28
3.3 The halo mass function . . . . .	30
3.4 The halo bias . . . . .	30
3.5 Cosmic voids . . . . .	31
<b>4 Cosmological <math>N</math>-body simulations</b>	<b>35</b>
4.1 General . . . . .	35
4.2 ANUBISIS . . . . .	37
4.3 <i>Sesame</i> – A power spectrum ratio emulator pipeline . . . . .	39
<b>5 Summary and outlook</b>	<b>43</b>
5.1 Summaries of papers . . . . .	43
5.2 Conclusions and outlook . . . . .	45
<b>Papers</b>	<b>50</b>
<b>I Euclid: Modelling massive neutrinos in cosmology – a code comparison</b>	<b>51</b>
<b>II The void-galaxy cross-correlation function with massive neutrinos and modified gravity</b>	<b>103</b>

## Contents

---

III Sesame: A power spectrum emulator pipeline for beyond- $\Lambda$ CDM models	129
Bibliography	143



# Chapter 1

## The standard model of cosmology

In this chapter, I will set the stage for modern cosmology and introduce the building blocks needed for the foundation of this thesis work. This review is mainly based on Dodelson and Schmidt, 2020.

### 1.1 The history of our Universe

The  $\Lambda$ -cold-dark-matter ( $\Lambda$ CDM) model is today generally accepted as the standard model of cosmology. It describes the past, present, and future evolution of our Universe, along with its energy content. In this model, the Universe is made out of baryonic matter ( $\sim 5\%$ ), dark matter ( $\sim 25\%$ ), and dark energy ( $\sim 70\%$ ) (Planck Collaboration et al., 2020b), the latter of which today drives an accelerated expansion of the Universe. But how did we get here, and where did it all start? In the  $\Lambda$ CDM model, the history of our Universe goes a little something like this (Baumann, 2022):

- ★ First, approximately 13.8 billion years ago, there was the Big Bang. This marked the beginning of our Universe, and how everything spread out today was once concentrated in a region of vanishing volume.
- ★ Closely following, it is theorised that there was a brief period of inflation. Here, the Universe expanded exponentially and grew about  $10^{26}$  orders of magnitude in just a fraction of a second. Once inflation ended, around  $10^{-32}$  seconds after the Big Bang, the inflation scalar field decayed into the elemental particles of the standard model, with relativistic velocities. Fluctuations in the inflation field were then carried over to the density field, leaving small density perturbations as seeds for future structure formation. At this point in time, the energy density of radiation dominated the Universe and everything existed in one big hot soup.
- ★ The Universe continued to expand, although noticeably slower than during inflation, and the Universe gradually cooled with the expansion. In the first few microseconds after the Big Bang, the first particles (like protons and neutrons) were formed, and in the next couple of minutes, the atomic nuclei of the lightest elements (mostly hydrogen and helium). However, it was still too hot for the electrons to combine with the nuclei to create atoms.
- ★ After some time, approximately 50 000 years, the energy density of radiation became lower than that of matter, and we entered an era of matter domination.
- ★ At one point, some hundred thousand years after the Big Bang, the Universe had expanded and cooled enough for electrons to be captured and neutral

## 1. The standard model of cosmology

---

hydrogen to be formed. This is known as the epoch of recombination. The free electrons had previously scattered light, making the Universe opaque. During recombination, this process became less and less frequent and the photons eventually decoupled around 380 000 years after the Big Bang, making the Universe transparent. This process left behind a stream of photons capturing a freeze-frame of the density fluctuations present in the matter at the given time, known as the cosmic microwave background (CMB). This light is observable today and contains a wealth of information about our Universe that is actively studied in its own research field.

- ★ The Universe kept on expanding at the same time as the small overdensities in the matter field steadily grew. First, dark matter clumped together and then baryonic matter fell into the gravitational wells created by the dark matter. This was a gloomy period in the evolution of our Universe, known as the dark ages - a time before stars existed.
- ★ After around 200 million years, matter had contracted enough to start forming the first stars. The light produced by them started to slowly reionise the Universe, breaking up the atoms in the hydrogen gas surrounding the first stars. At the same time, structures continued to grow and the first galaxies appeared.
- ★ Around 1 billion years after the Big Bang, stars and galaxies had reionised most of the hydrogen gas (Planck Collaboration et al., 2020a). Still, the Universe as a whole remained largely transparent.
- ★ Recently, about 9 billion years after the Big Bang, we entered the era of dark energy domination, resulting in an accelerated expansion of the Universe.
- ★ Today, the growth of structure has led to an intricate large-scale formation, known as the cosmic web, made up of halos, walls, filaments, and voids.

This concludes the broad overview of the evolutionary traits of our Universe. In Fig. 1.1, the history of the Universe is illustrated, highlighting some of the points above. With this information at hand, it is time to delve into some more concrete details of the  $\Lambda$ CDM model.

## 1.2 General relativity

In the  $\Lambda$ CDM model, gravity is described by the theory of general relativity (GR), first proposed by Albert Einstein in November 1915. In this theory, the geometry of space and the energy content of the Universe are related through the Einstein field equations (EFEs);

$$G_{\mu\nu} + \Lambda g_{\mu\nu} = \kappa T_{\mu\nu}. \quad (1.1)$$

Here,  $G_{\mu\nu}$  is the Einstein tensor, given by

$$G_{\mu\nu} = R_{\mu\nu} - \frac{1}{2}g_{\mu\nu}R, \quad (1.2)$$

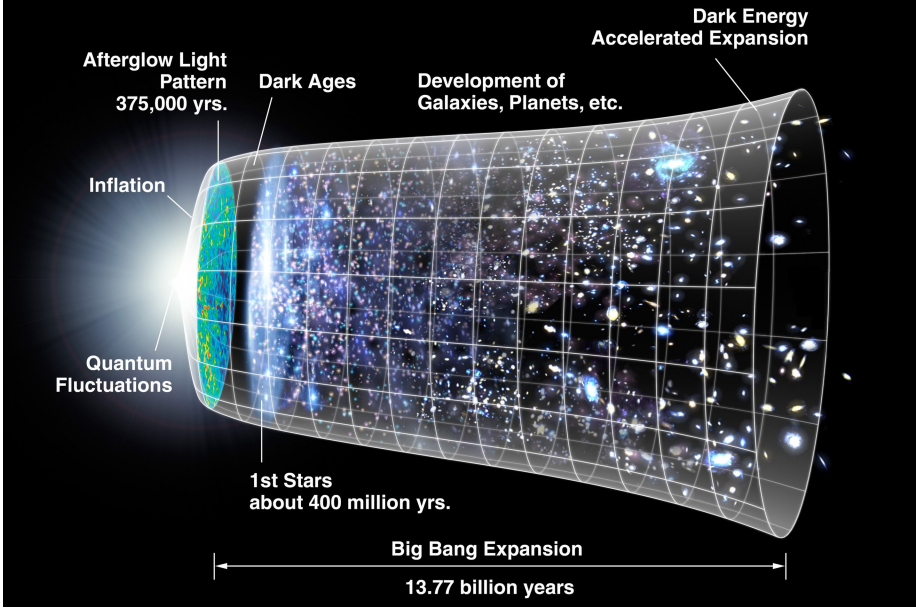


Figure 1.1: Timeline depicting the evolution of the  $\Lambda$ CDM Universe. Credit: NASA/WMAP Science Team - modified by Cherkash.

where  $R_{\mu\nu}$  and  $R = g^{\mu\nu}R_{\mu\nu}$  are the Ricci tensor and scalar respectively, defined by

$$R_{\mu\nu} = \Gamma_{\mu\nu,\alpha}^{\alpha} - \Gamma_{\mu\alpha,\nu}^{\alpha} + \Gamma_{\beta\alpha}^{\alpha}\Gamma_{\mu\nu}^{\beta} - \Gamma_{\beta\nu}^{\alpha}\Gamma_{\mu\alpha}^{\beta}. \quad (1.3)$$

The comma denotes a derivative with respect to  $x$ , so that  $\Gamma_{\mu\nu,\alpha}^{\alpha} = \partial\Gamma_{\mu\nu}^{\alpha}/\partial x^{\alpha}$ , and

$$\Gamma_{\alpha\beta}^{\mu} = \frac{g^{\mu\nu}}{2} \left[ \frac{\partial g_{\alpha\nu}}{\partial x^{\beta}} + \frac{\partial g_{\beta\nu}}{\partial x^{\alpha}} + \frac{\partial g_{\alpha\beta}}{\partial x^{\nu}} \right] \quad (1.4)$$

are known as the Christoffel symbols.  $g_{\mu\nu}$  is the metric tensor, which relates space-time coordinates,  $x^{\mu} = (t, x^i)$ , to the invariant distance between them, known as the line-element,

$$ds^2 = g_{\mu\nu}dx^{\mu}dx^{\nu}. \quad (1.5)$$

The metric describes curved space-time, and by doing so, incorporates gravity into the formalism itself. In the following, we will use the metric signature  $(-1, 1, 1, 1)$ . The only parameter left over on the left-hand side of Eq. (1.1) is now  $\Lambda$ , which is the cosmological constant. This is often viewed as the energy density of vacuum,

## 1. The standard model of cosmology

---

and it is the term responsible for an accelerated expansion of the Universe<sup>1</sup>. On the right-hand side of Eq. (1.1), we find Einstein's gravitational constant, given by  $\kappa = 8\pi G/c^4$ , with  $c$  the speed of light (which is typically set to  $c = 1$ ) and  $G$ , Newton's gravitational constant, together with  $T_{\mu\nu}$ , the energy-momentum tensor. The latter contains information about the content of the Universe in terms of density and flux of energy and momentum. In order for energy and momentum to be conserved in this theory, we therefore need

$$\nabla_\mu T_\nu^\mu \equiv \frac{\partial T_\nu^\mu}{\partial x^\mu} + \Gamma_{\alpha\mu}^\mu T_\nu^\alpha - \Gamma_{\mu\nu}^\alpha T_\alpha^\mu = 0, \quad (1.6)$$

where  $\nabla_\mu$  is called the covariant derivative. This leads to the GR versions of the continuity and Euler equations. In this way, Eq. (1.1) describes the interplay between space-time on the left-hand side and the energy and matter content of the Universe on the right-hand side. But where do these equations come from?

Generally, when we want to study the dynamics of a system, we can look at the action of that system. The action is defined as a mathematical functional that takes the Lagrangian density,  $\mathcal{L}$ , of the system we want to study as an argument, integrated over space and time:

$$\mathcal{S} = \int \mathcal{L} \sqrt{-g} d^4x, \quad (1.7)$$

where  $\mathcal{L}$  is a function of the fields in the system and their derivatives, along with the space-time coordinates, and  $g$  is the determinant of the metric tensor. In GR, we have the Einstein-Hilbert action with a cosmological constant and matter fields (Ishak, 2018), given by

$$\mathcal{S} = \int \left( \frac{R - 2\Lambda}{16\pi G} + \mathcal{L}_m \right) \sqrt{-g} d^4x. \quad (1.8)$$

Here, the parameters are the same as above, in addition to  $\mathcal{L}_m$ ; the matter Lagrangian density. The EFEs can be obtained through the principle of least action, by requiring that  $\delta\mathcal{S} = 0$  when varying the action with respect to the metric,  $g_{\mu\nu}$ .

From Newtonian physics, we know that an object in motion will move in a straight line unless it is disturbed by any external forces. In the curved space-time of GR, we instead say that an object in free-fall moves along a geodesic, the shortest path between two points. The equation of motion of a particle, the geodesic equation, can again be found through the principle of least action, with the action

$$\mathcal{S} = \int ds, \quad (1.9)$$

where  $ds$  is the line-element as defined in Eq. (1.5). This process requires the introduction of a parameter,  $\lambda$ , which monotonically increases along the path of

---

<sup>1</sup>This term can be found on either side of the equation. On the left-hand side, it is seen as a property of space-time resulting in an accelerated expansion, while on the right-hand side it is seen as the energy density of vacuum, which is a constituent of the Universe.

the particle, and results in the geodesic equation

$$\frac{d^2 x^\mu}{d\lambda^2} + \Gamma_{\alpha\beta}^\mu \frac{dx^\alpha}{d\lambda} \frac{dx^\beta}{d\lambda} = 0, \quad (1.10)$$

when demanding  $\delta\mathcal{S} = 0$  when varying the action with respect to  $\lambda$ . Here,  $\Gamma_{\alpha\beta}^\mu$  are the Christoffel symbols and  $\lambda$  is typically taken to be the particle's proper time,  $\tau$ . Equation (1.10) is thus the path taken by a particle in free-fall in curved space-time - the equivalent of the familiar "straight path" motion of objects.

## 1.3 The growth of structure

A part of our current comprehension of the Universe comes from observing the large-scale structure (LSS). Knowledge about how overdensities grew throughout universal history and formed the structures we see today is essential when it comes to our understanding of how the Universe works. In this section, I will take you through a brief explanation of how the tiny overdensities left over after the inflationary epoch grew into large overdensities, capable of hosting or becoming planets, stars, and galaxies.

### 1.3.1 The smooth Universe

Before looking at structure growth, we need a quick overview of how the Universe behaves. A spatially flat, homogeneous, isotropic, and expanding universe can be described through the Friedmann–Lemaître–Robertson–Walker (FLRW) metric, given by

$$g_{\mu\nu} = \begin{pmatrix} -1 & 0 & 0 & 0 \\ 0 & a^2(t) & 0 & 0 \\ 0 & 0 & a^2(t) & 0 \\ 0 & 0 & 0 & a^2(t) \end{pmatrix}, \quad (1.11)$$

or, equivalently,

$$ds^2 = -dt^2 + a^2(t)\delta_{ij}dx^i dx^j, \quad (1.12)$$

where  $a(t)$  is known as the scale factor, incorporating all time dependence of the metric,  $\delta_{ij}$  is the Kronecker delta function, and  $x^i = x_{\text{physical}}^i/a(t)$  are comoving coordinates. In this smooth, isotropic background universe, the energy-momentum tensor takes the simple form

$$T_{\mu\nu} = (\rho + P)u_\mu u_\nu - P g_{\mu\nu}, \quad (1.13)$$

equal to that of a perfect fluid. Here,  $\rho$  is the energy density,  $P$  the pressure, and  $u_\mu$  the four-velocity of the fluid. Pulling this through the full machinery of Eq. (1.1), we obtain the Friedmann equations

$$\left(\frac{\dot{a}}{a}\right)^2 = \frac{8\pi G}{3}\bar{\rho}, \quad (1.14)$$

$$\frac{\ddot{a}}{a} = -\frac{4\pi G}{3}(\bar{\rho} + 3\bar{P}), \quad (1.15)$$

## 1. The standard model of cosmology

---

where the dot denotes the derivative with respect to time and  $\bar{\rho}$  and  $\bar{P}$  are the total energy density and pressure of the background universe. Equation (1.14) is often known as *the* Friedmann equation, although in a slightly different form. In order to get there, we first have to take a look at how the evolution of different components of the Universe depends on the scale factor. This can be done through the  $\nu = 0$  component of Eq. (1.6), which for the energy-momentum tensor of Eq. (1.13) gives

$$\frac{\partial \bar{\rho}}{\partial t} + \frac{\dot{a}}{a}(3\bar{\rho} + 3\bar{P}) = 0. \quad (1.16)$$

Defining the equation of state parameter,  $w$ , as  $w = P/\rho$ , we can use the knowledge that matter (m) has  $w = 0$ , radiation (r) or relativistic particles has  $w = 1/3$ , and a cosmological constant ( $\Lambda$ ) has  $w = -1$  to find<sup>2</sup>

$$\bar{\rho}_m \propto a^{-3}, \quad \bar{\rho}_r \propto a^{-4}, \quad \text{and} \quad \bar{\rho}_\Lambda \propto a^0. \quad (1.17)$$

In the case of massive neutrino particles ( $\nu$ ), which are relativistic at early times and later become non-relativistic, they will switch from  $\bar{\rho}_\nu \propto a^{-4}$  to  $\bar{\rho}_\nu \propto a^{-3}$ .

Moving forward, it is convenient to define the density parameters

$$\Omega_{i0} = \frac{\bar{\rho}_{i0}}{\rho_{\text{cr}0}}, \quad (1.18)$$

where  $i$  denotes the various components ( $i = \text{m}, \text{r}, \Lambda$ ) and “0” indicates the values today. The parameter

$$\rho_{\text{cr}0} = \frac{3H_0^2}{8\pi G} \quad (1.19)$$

is known as the critical density - the total energy density needed for the Universe to be flat. Here,  $H_0$  is the present value of the Hubble parameter,  $H = \dot{a}/a$ . With this definition, we now have  $\sum \Omega_{i0} = 1$ . Applying all this knowledge, and defining  $a(t_0) = 1$ , the Friedmann equation (Eq. 1.14) can be rewritten as

$$H^2 = H_0^2(\Omega_{\text{m}0}a^{-3} + \Omega_{\text{r}0}a^{-4} + \Omega_{\Lambda 0}), \quad (1.20)$$

where  $\Omega_{\text{m}}$  is the total matter, containing both baryons and cold dark matter,  $\Omega_{\text{m}} = \Omega_{\text{b}} + \Omega_{\text{cdm}}$ . At the present day, the massive neutrinos also belong to the total matter density parameter, and their energy budget is taken from the cold dark matter component. This form of the Friedmann equation clearly showcases the evolution of the different components of our Universe and how they dominate in different cosmological eras.

### 1.3.2 Linear growth

The Universe is more complex than the smooth case presented above. After inflation, small fluctuations in the density field were present throughout the

---

<sup>2</sup>Assuming that  $w$  is time-independent.

Universe, slowly evolving over time. This complicates the picture, and we need to extend our framework in order to understand how overdensities grew as time went by.

First of all, the energy-momentum tensor can no longer be described by the simple perfect fluid case. Instead, we can construct it by looking at the particle ensembles of the various species populating our Universe. A particle ensemble can be described by a distribution function,  $f(\mathbf{x}, \mathbf{p}, t)$ , which represents the behaviour of a collection of particles in a statistical sense. In this way, we do not have to keep track of individual particles, and we can focus on their collective properties. If we ignore particle interactions, we know that the number of particles must be conserved, meaning that

$$\frac{df}{dt} = \frac{\partial f}{\partial t} + \frac{\partial f}{\partial x^i} \cdot \frac{dx^i}{dt} + \frac{\partial f}{\partial p} \frac{dp}{dt} + \frac{\partial f}{\partial \hat{p}^i} \cdot \frac{d\hat{p}^i}{dt} = 0, \quad (1.21)$$

where the momentum dependence has been separated into the magnitude and unit vector components,  $p^i = p\hat{p}^i$ . This equation is known as *the Boltzmann equation* of the particle ensemble. Now, if we also include particle interactions, a collision term,  $C[f]$ , must be added to the Boltzmann equation,

$$\frac{df}{dt} = C[f]. \quad (1.22)$$

This takes care of interactions like scattering, pair creation, annihilation, and particle decay. The various particle (and radiation) species populating the Universe will have different Boltzmann equations which need to be calculated individually<sup>3</sup>.

This framework is general. Applying it to the smooth and expanding universe of Sect. 1.3.1 would lead to the energy-momentum tensor seen in Eq. (1.13). But we are not interested in a smooth universe anymore. Now we want to see how perturbations in the density field affect space-time and vice-versa. We also want to know how perturbations in the density field grow over time to form the structures we observe today. Let us introduce some scalar perturbations to our Universe. First, for the properties of the constituents of the Universe, we will look at

$$\rho = \bar{\rho} + \delta\rho \quad \text{and} \quad P = \bar{P} + \delta P, \quad (1.23)$$

where the  $\delta$ 's are deviations from the background values, marked with a bar. Secondly, we also want to introduce scalar perturbations to the metric. In general, the perturbed metric can be given as (Baumann, 2022)

$$ds^2 = -(1 + 2A)dt^2 + 2a(t)B_i dx^i dt + a^2(t)(\delta_{ij} + h_{ij})dx^i dx^j, \quad (1.24)$$

---

<sup>3</sup>This will not be included here (there is a loose understanding that this should be done by everyone at least once, and I have already paid my dues), but can be found in works like Dodelson and Schmidt, 2020.

## 1. The standard model of cosmology

---

where  $A$ ,  $B_i$ , and  $h_{ij}$  are scalar, vector, and tensor perturbations respectively<sup>4</sup>. If we only include scalar perturbations, and use the Newtonian gauge, we get

$$ds^2 = -(1 + 2\Psi)dt + a^2(t)(1 + 2\Phi)\delta_{ij}dx^i dx^j, \quad (1.25)$$

where  $\Psi$  and  $\Phi$  are scalar perturbations that are functions of time and space. Moving forward, we will assume that all perturbations are small ( $\delta\rho, \delta P, \Psi, \Phi \ll 1$ ), and also that the bulk velocity of dark matter is small ( $\mathbf{u} \ll 1$ ), so that we can drop terms that are second-order or higher in these parameters, and thereby obtain a linear approximation. This works well in the early Universe and also on large scales at the present time.

So, everything has now changed. To simplify (and shorten) this section, we will focus on dark matter moving forward, as this is the main ingredient needed to understand the growth of structure. Specific details for baryonic matter, radiation, and neutrinos can be found in Dodelson and Schmidt, 2020. Without going into too much detail, the Boltzmann equation depends on the geodesic equation, which has now changed due to the perturbed metric. Taking all of this into account, the left-hand side of the Boltzmann equation, for massive particles, is now given by<sup>5</sup>

$$\frac{df}{dt} = \frac{\partial f}{\partial t} + \frac{p}{E} \frac{\hat{p}^i}{a} \frac{\partial f}{\partial x^i} - p \frac{\partial f}{\partial p} \left( H + \dot{\Phi} + \frac{E}{ap} \hat{p}^i \frac{\partial \Psi}{\partial x^i} \right), \quad (1.26)$$

with  $E^2 = p^2 + m^2$  and  $m$  the mass of the particle. For radiation, we have the same equation, only for  $E^2 = p^2$ . Luckily for us, as we are focusing on dark matter, the right-hand side of the Boltzmann equation is zero, as dark matter does not interact (or, if so, interacts very weakly) with the other constituents of the Universe. In addition, dark matter is non-relativistic, meaning that we can neglect higher orders of  $p$ . Using this information, we can take the zeroth moment of Eq. (1.26), which will lead us to a generalisation of the continuity equation<sup>6</sup>. If we then only look at the evolution of the perturbations, we get

$$\frac{\partial \delta_{\text{cdm}}}{\partial t} + \frac{1}{a} \frac{\partial u_{\text{cdm}}^i}{\partial x^i} + 3\dot{\Phi} = 0, \quad (1.27)$$

where  $\delta_{\text{cdm}} = \delta\rho_{\text{cdm}}/\bar{\rho}_{\text{cdm}}$  and  $u_{\text{cdm}}^i$  is the bulk velocity of dark matter. We follow up by taking the first moment of Eq. (1.26), which gives a generalised version of the Euler equation. Again, ignoring the background components, we get

$$\frac{\partial u_{\text{cdm}}^i}{\partial t} + H u_{\text{cdm}}^i + \frac{1}{a} \frac{\partial \Psi}{\partial x^i} = 0. \quad (1.28)$$

---

<sup>4</sup>The vector and tensor perturbations can further be rewritten into scalar, vector, and tensor components, resulting in a total 10 degrees of freedom of the metric, divided into four scalar, two vector, and two tensor degrees of freedom.

<sup>5</sup>The right-hand side, which contains the collision terms, will distinguish the different species.

<sup>6</sup>Taking the  $n$ -th moment of Eq. (1.26) means multiplying it by a velocity factor to the  $n$ -th power and integrating over the phase-space volume. This is a way to extract the overall behaviour of the underlying particles described by the distribution function,  $f$ .



It is convenient to move these two equations to Fourier space ( $\delta_k(\mathbf{k}) = \int e^{i\mathbf{k}\cdot\mathbf{x}} \delta(\mathbf{x}) d^3x$ , where  $k$  is the comoving wavenumber of the perturbation) and switch to conformal time,  $d\eta = dt/a$ , so that

$$\delta'_{\text{cdm}} + ik u_{\text{cdm}} + 3\Phi' = 0, \quad (1.29)$$

$$u'_{\text{cdm}} + \frac{a'}{a} u_{\text{cdm}} + ik\Psi = 0. \quad (1.30)$$

Here, the apostrophe denotes the derivative with respect to conformal time. In this form, we see that the Fourier modes are independent of each other.

Equations (1.29) and (1.30) govern the evolution of dark matter perturbations and their velocity. However, to fully understand them, we must also learn about  $\Phi$  and  $\Psi$ . For this, we need to have a look at the Einstein equations, again to linear order in perturbations. For the left-hand side, since we have a new metric, the Christoffel symbols, Ricci tensor, and Ricci scalar needs to be recalculated to include  $\Phi$  and  $\Psi$ . For the right-hand side, the energy-momentum tensor must be constructed from the relevant particle ensembles. Looking at the temporal part of the EFEs, only including first-order terms, we get

$$k^2\Phi + 3\frac{a'}{a}\left(\Phi' - \Psi\frac{a'}{a}\right) = 4\pi G a^2 \bar{\rho}_{\text{cdm}} \delta_{\text{cdm}} \quad (1.31)$$

for conformal time and in Fourier space. This equation is our version of the regular Poisson equation,  $\nabla^2\phi = 4\pi G\rho$ , where  $\phi$  is the gravitational potential. Looking at the spatial part of the EFEs instead gives

$$\Phi = -\Psi, \quad (1.32)$$

if we neglect anisotropic stress<sup>7</sup>. And with that, we have the two needed constraint equations for  $\Phi$  and  $\Psi$ .

Now, how a perturbation behaves depends on its mode and in which era of the Universe it is developing. In addition, baryonic and dark matter perturbations grow differently during some time periods. This is easier to get a grasp of if we look at the Newtonian approximation of what we did above, meaning no perturbations to space-time, for total matter. In that case, the linear continuity, Euler, and Poisson equations may be derived and combined to form

$$\ddot{\delta}_{\text{m}} + 2H\dot{\delta}_{\text{m}} = \delta_{\text{m}}(4\pi G\bar{\rho}_{\text{m}} - k^2c_s^2), \quad (1.33)$$

in Fourier space, where the derivative is with respect to time,  $t$ . The term including  $c_s$ , the speed of sound, originates from pressure perturbations as  $\delta P_{\text{m}} = c_s^2\delta\rho_{\text{m}} = c_s^2\bar{\rho}_{\text{m}}\delta_{\text{m}}$ . Solving for  $\delta_{\text{m}}$  in equation Eq. (1.33) will give us information about how overdensities in the matter field grow. However, one

<sup>7</sup>This is a contribution to the energy-momentum tensor from the quadrupole of the temperature perturbations to the distribution functions for relativistic species. It is mainly neutrinos that contribute to this component.

## 1. The standard model of cosmology

---

of the conditions that can be derived from it<sup>8</sup> actually tells us that not all overdensities do, in fact, grow. Only perturbations larger than

$$\lambda > c_s \sqrt{\frac{\pi}{G\bar{\rho}_m}}, \quad (1.34)$$

where  $\lambda = 2\pi/k$ , will grow. This threshold is known as the Jeans length ( $\lambda_J$ ), and perturbations shorter than this value will only oscillate around  $\bar{\rho}_m$ . With this knowledge in mind, we will, for the final part of this section, focus on perturbations much larger than the Jeans length. Still, also in this case, the growth of the perturbations depends on their modes. The *particle horizon* tells us the furthest distance over which there can be causal contact at some time  $t$ , which increases with time. Now, how a perturbation grows depends on if it is inside or outside the horizon, and also if we are in the radiation, matter, or dark energy-dominated era. In the radiation-dominated era, the behaviour of  $\delta_m$  outside the horizon is determined by the metric perturbations, which are governed by Eqs. (1.31) and (1.32). Had we included radiation in our short review, there would have been a term on the right-hand side of Eq. (1.31) proportional to  $\bar{\rho}_r$ , which would dominate in this era. Requiring that the metric perturbations remain constant for perturbations outside of the horizon then results in  $\delta_m \propto a^2$  for modes outside the horizon in the radiation-dominated era. As the particle horizon grows with time, perturbations will start entering the horizon as time goes by. Inside the horizon, Eq. (1.33) determines the evolution of  $\delta_m$ . Combining it with the Friedmann equation (Eq. 1.20) to find that  $a \propto t^{1/2}$  during radiation domination and assuming  $\bar{\rho}_r \gg \bar{\rho}_m$ , we find that  $\delta_m \propto \log a$  inside the horizon. This means that the Universe is expanding faster than the perturbations can grow during this period. If we then move on to the matter-dominated era, and follow the same procedure for the behaviour of  $\delta_m$  inside the horizon, we find that  $a \propto t^{2/3}$  from the Friedmann equation by assuming that  $\Omega_m = 1$ . Keeping this assumption, Eq. (1.33) gives  $\delta_m \propto a$  for a perturbation inside the horizon during matter domination. From this, it is clear that the perturbations that enter the horizon during radiation domination are suppressed compared to the ones entering during matter domination. This “stalling” of growth is known as the Meszaros effect (Meszaros, 1974)<sup>9</sup>.

What we have not taken into account so far is that baryons and cold dark matter are different. Before recombination, baryons and photons are coupled together in a baryon-photon relativistic fluid, where the radiation pressure hinders the baryonic perturbations from growing. Dark matter, on the other hand, is not affected by this radiation pressure, and can freely grow as described above. Recombination happens at  $z \sim 1100$ , while matter-radiation equality happens at  $z \sim 3400$ . This means that had we only had baryons, they would

---

<sup>8</sup>By looking at the static case,  $\dot{a} = 0$ .

<sup>9</sup>The relation between  $\delta$  and  $a$  depends on the choice of coordinates/gauge during the calculation. In this simple description using words, I have glazed over the use of a gauge-invariant density perturbation formulation. Details of this can be found in e.g. Baumann, 2022.

first start growing during matter domination, as  $\delta_b \propto a$ . If they then started from fluctuations of the order of the anisotropies observed in the CMB (Planck Collaboration et al., 2020a,b),  $\delta_b \sim 10^{-5}$ , and grew from  $a = \frac{1}{1+z} \sim 10^{-3}$  until today at  $a = 1$ , that is only a growth of a factor 1000, leaving them at  $\delta_b \sim 10^{-2}$ . This does not coincide with the non-linear structures we observe today, in the form of stars and galaxies. This means that, for us to be here and observe the structures we see today, the growth of dark matter perturbations before recombination and the creation of gravitational wells for the baryonic matter to fall into, is absolutely essential.

That dramatic note carries us over to yet another dramatic note. Recently ( $z \sim 0.4$ ), the Universe has no longer been dominated by matter. We have now entered an era of dark energy domination, leading to an accelerated expansion of the Universe, which naturally has consequences for the growth of perturbations. Coming back to the Friedmann equation again (Eq. 1.20), we now have  $a \propto e^{H_0 \sqrt{\Omega_\Lambda} t}$  which when inserted into Eq. (1.33) gives  $\delta_m \sim \text{constant}$  under the assumption that matter still dominates the contribution to the gravitational potential.

### 1.3.3 Non-linear growth

So far, everything we have gone through has been in regard to linear perturbations, ignoring any higher-order contributions. This works up to a certain point ( $\delta \sim 1$ ), but as I mentioned, we are today surrounded by non-linear structures. This is a bit more complicated to describe mathematically, but it can be approximated to a certain degree. One approach is to extend the framework of the previous section by treating the matter density and velocity non-linearly. Another well-known description of non-linear collapse is the spherical top-hat model (Dodelson and Schmidt, 2020; Gunn and Gott, 1972; Peebles, 1980). However, if we want to capture the full effects, numerical simulations are the way to go. As the latter has been vital for this thesis work, it gets its own stage number in Chapter 4. For now, let us simply set the stage by having a quick look at the two other approaches.

The first approach is a way of following our linear density perturbations into the non-linear regime through the Boltzmann equation (Eq. 1.26) and Eq. (1.31). Treating all components non-linearly would be very complex. Luckily, perturbations to the FLRW metric remain small also in the late Universe, meaning that we can continue to treat them linearly. In addition, if we keep to scales large enough for baryonic physics to remain unimportant, while at the same time small enough to enter the non-linear regime, we can treat cold dark matter and baryons together as one cold, collisionless matter component. We can then write Eq. (1.31) as

$$-k^2 \Psi = 4\pi G a^2 \bar{\rho}_m \delta_m, \quad (1.35)$$

where only the first term on the left-hand side has been kept, as it is the dominant one at the relevant scales. This shows that  $\Psi(\mathbf{k}) \propto \delta(\mathbf{k})/k^2$ , meaning that  $\Psi$

## 1. The standard model of cosmology

---

remains small even as  $\delta_m$  becomes large at small scales (large  $k$ ). Because of this, it is sufficient to use the Newtonian limit to describe the gravitational potential, i.e. the regular Poisson equation. Previously, we found equations describing the evolution of our overdensity, in the linear case, by taking the zeroth and first moments of Eq. (1.26). Now we need a version of this Boltzmann equation that does not assume small matter perturbations, but it can remain non-relativistic. We can also continue to assume small metric perturbations. With these assumptions we get

$$\frac{df_m}{dt} = \frac{\partial f_m}{\partial t} + \frac{\partial f_m}{\partial x^i} \frac{p^i}{ma} - \frac{\partial f_m}{\partial p^i} \left( Hp^i + \frac{m}{a} \frac{\partial \Psi}{\partial x^i} \right) = 0, \quad (1.36)$$

known as the Vlasov equation. This set of equations (Eqs. 1.35 and 1.36) is known as the Vlasov-Poisson system and is valid when matter perturbations start evolving non-linearly. It can be expanded further using perturbation theory or be solved numerically. The latter is often incorporated into  $N$ -body simulations (see Ch. 4), which allow us to study the formation of structure in the Universe.

The second approach mentioned above, the spherical top-hat model, or just the spherical collapse model, instead estimates which overdensities will collapse and form dark matter halos. These are important tracers of the LSS of our Universe, but can only be directly identified in simulations. Observationally, we can use tracers, such as galaxy clusters, or gravitational lensing to estimate the mass of dark matter halos. Still, modelling how overdensities collapse and virialise into halos gives us insight into the non-linear growth of structure. The simplest way to do so is by considering the collapse of a spherical region with uniform density. The mass contained within this sphere is then given by  $M = 4\pi\bar{\rho}_m(1 + \delta_m)R^3/3$ , where  $\bar{\rho}_m$  is the background matter density of the Universe at the given time and  $R$  is the physical radius of the sphere. Assuming a flat FLRW universe containing only matter<sup>10</sup>, the spherical region in question should obey Eq. (1.15), which under our assumptions then becomes

$$\ddot{R} = -\frac{GM}{R^2} \quad (1.37)$$

in physical coordinates. If we integrate this equation we get

$$\frac{1}{2}\dot{R}^2 - \frac{GM}{R} = E, \quad (1.38)$$

where the integration constant,  $E$ , corresponds to the energy of a spherical shell of radius  $R$ . In order for the overdensity to be gravitationally bound and decouple from the background expansion, we need  $E < 0$ . The solution is then given by

$$R = \frac{R_{\text{ta}}}{2}(1 - \cos \theta), \quad (1.39)$$

---

<sup>10</sup>Also known as an Einstein-de Sitter universe, which is quite accurate in the thick of the matter-dominated era.

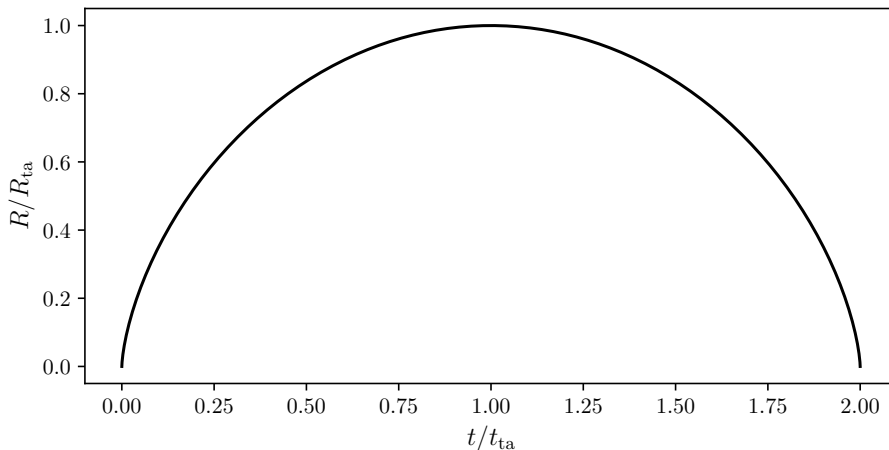


Figure 1.2: Spherical collapse solution. Expansion followed by the turn-around and collapse of an overdense region.

$$t = \frac{t_{ta}}{\pi} (\theta - \sin \theta). \quad (1.40)$$

Here,  $R_{ta}$  is the radius at the turn-around time,  $t_{ta}$ , and  $\theta \in [0, 2\pi]$ . The two first parameters are related through  $\pi^2 R_{ta}^3 / (8t_{ta}^2) = GM$ . The solution is illustrated in Fig. 1.2. In words instead of symbols, we have an overdense region which at first expands with the Universe until it reaches some maximum size, where it turns around (at  $\theta = \pi$ ) and starts collapsing. At  $\theta = 2\pi$  it has completely collapsed, and  $R = 0$ . Using this solution and comparing the density within the spherical region with the background, we find that the overdensity behaves as

$$\delta_m = \frac{9}{2} \frac{(\theta - \sin \theta)^2}{(1 - \cos \theta)^3} - 1 \quad (1.41)$$

in the spherical collapse model. Before looking at this further, let us have a quick look at linear theory again. During matter domination, we found in the previous section that  $\delta_m \propto a \propto t^{2/3}$ . If we Taylor expand Eq. (1.41) to first order, we get  $\delta_m = (3/20)(6\pi)^{2/3}(t/t_{ta})^{2/3}$ , which recovers the linear proportionality. Inserting the time of total collapse we get a value  $\delta_m^{\text{lin}} \approx 1.686$ . This means that, in linear theory, overdensities with  $\delta_m > \delta_m^{\text{lin}}$  can be considered collapsed objects. In our non-linear spherical collapse theory, on the other hand, the time of total collapse gives  $R = 0$  and  $\delta_m \rightarrow \infty$ , which would mean the formation of a black hole. However, in reality, the collapse of overdense regions is not perfectly spherical, and also pressure becomes important, meaning that there will be more complicated dynamics at play. This results in an equilibrium state being reached at some finite radius, the process of which is known as virialisation. The virial

## 1. The standard model of cosmology

---

theorem says that for a virialised system, we have

$$K = -\frac{1}{2}U, \quad (1.42)$$

where  $K$  is the kinetic energy and  $U$  is the gravitational energy. From the conservation of energy, it can be shown that this happens at  $R = R_{\text{ta}}/2$ , where the overdensity has a value  $\delta_{\text{m}}^{\text{vir}} \approx 178$ . This means that in our non-linear spherical collapse model, an overdensity  $\delta_{\text{m}} > \delta_{\text{m}}^{\text{vir}}$  can be considered as a collapsed system. This specific threshold, rounded up to  $\delta_{\text{m}} = 200$ , is often used as a criterion in numerical simulations to identify dark matter halos.

With that, I conclude this review on the growth of structure, all the way from tiny perturbations to virialised halos. These were the building blocks with which the very foundation of my thesis work was built. From now on, the content of this thesis will be more directly related to the work done in Papers I, II, and III, but let us first round off this chapter with a few open questions.

### 1.4 Unanswered questions

The  $\Lambda$ CDM model overall describes our Universe exceptionally well. There are, however, some big questions still left unanswered. Whether or not some of the explanations will lie outside the  $\Lambda$ CDM model is yet unknown, but the scientific community eagerly works towards the common goal of obtaining answers. In this section, I will briefly address some questions that are key components of the work performed for this thesis.

#### What is dark matter?

It was earlier stated that in the  $\Lambda$ CDM model, the Universe is made up of baryonic matter, dark matter, and dark energy. Baryonic matter is the regular matter that we are familiar with. In astronomy, it is defined as matter made out of protons, neutrons, and electrons<sup>11</sup>. In other words, it is the matter that makes up planets, stars, and galaxies. Dark matter, on the other hand, is believed to be made up of something other than protons, neutrons, and electrons - i.e. it is non-baryonic. Even though the  $\Lambda$ CDM model tells us that  $\sim 25\%$  of the energy content of the Universe comes from dark matter, we do not know what it is. From observations such as galactic rotation curves, cluster dynamics, gravitational lensing, and the LSS (e.g. Massey, Kitching, and Richard, 2010; Rubin, Ford, and Thonnard, 1980; Zwicky, 2009) we know that there is much more mass than what we can see - thus the name *dark* matter. Several suggestions for what dark matter might be, like massive compact halo objects (MACHOs), weakly interacting massive particles (WIMPs), and axions (e.g. Brandt, 2016; Duffy and Van Bibber, 2009; Schumann, 2019), already exist in the scientific community, but as of now, the true nature of dark matter remains elusive.

---

<sup>11</sup>In terms of the standard model of particle physics, this is not strictly correct. Only protons and neutrons belong to the baryon category, while electrons are leptons. This plays nicely into astronomers' apparent fondness for approximations.

## What is dark energy?

The driving mechanism behind the current accelerated expansion of our Universe has been given the name *dark energy*. Yet again, it is *dark* because we cannot see it - we can only infer its impact as some sort of energy with negative pressure. As of now, we do not know the nature of dark energy, we only know that we measure an accelerated expansion of the Universe (Riess et al., 1998) and that we need something to drive this acceleration.

Thinking in terms of GR, the behaviour of the Universe is governed by its content and the nature of space-time. In the  $\Lambda$ CDM model, dark energy can be seen as a part of the energy content of the Universe and is given by a cosmological constant,  $\Lambda$ , which can be interpreted as the energy density of the vacuum state. On the cosmological side, this explanation matches observations well, but when the energy of vacuum is calculated using quantum field theory, the resulting value is about 54 orders of magnitude larger than what is gained from observations (Martin, 2012). This is known as the cosmological constant problem.

Another approach is to look at the behaviour of space-time, as opposed to the content of the Universe. A big motivation for the research field of modified gravity (modified compared to GR) is to find a theory of gravity that explains observations well, without the need for dark energy (Joyce, Lombriser, and Schmidt, 2016)<sup>12</sup>.

## What are the neutrino masses?

Neutrinos are small elementary particles that make up a tiny fraction of the energy content of our Universe (see Sect. 2.1). Particle physics experiments put an upper and lower bound on the sum of the neutrino masses, but the absolute mass scale is yet unknown. Even though they are small, the neutrinos affect structure formation (Lesgourgues and Pastor, 2006). Their relativistic nature in the early Universe leads to a suppression of the growth of structure at small scales, depending on their mass. On one side, this means that we can use observations of the LSS to estimate the sum of the neutrino masses, based on how much structure is suppressed compared to a massless neutrino case. On the other side, the result depends on a choice of cosmological model and is also degenerate with models of modified gravity (e.g. Baldi et al., 2014). Knowing the absolute neutrino mass is therefore essential when it comes to accurately determining cosmological parameters at a time when observations have become exceptionally detailed. One of the scientific goals of the newly launched *Euclid* satellite is to measure the sum of the neutrino masses to high accuracy, and possibly determine the neutrino mass hierarchy (Laureijs et al., 2011).

---

<sup>12</sup>And even in some cases, (partially) without the need for dark matter (e.g. Bekenstein, 2004).

### And more?

The three questions above already provide a large challenge for astronomers and physicists alike, and yet there are still a plethora of other questions in need of answers<sup>13</sup>. As not all of them are relevant to this thesis work, most will not be included, and some will have to make do with an honourable mention:

- ★ **The Hubble tension:** In short, different measurements of  $H_0$ , the current value of the Hubble parameter, give different answers. At the core of this, we have the Planck measurements (early time), which give  $H_0 = 67.4 \pm 0.5 \text{ km s}^{-1}\text{Mpc}^{-1}$  (Planck Collaboration et al., 2020b), and the Cepheid and type Ia supernovae measurements (late time), which give  $H_0 = 73.03 \pm 1.04 \text{ km s}^{-1}\text{Mpc}^{-1}$  (Riess et al., 2022). This is a  $5\sigma$  tension, meaning that the chance of the discrepancy being due to random effects is less than one in 3.5 million. The community is working hard to alleviate this issue in different ways, and whether it is systematics, distance measurements, a new cosmological model, or a combination, is yet unsettled.
- ★ **Inflation:** For matter perturbations to grow and create structures as explained earlier in this chapter, we need it to start out with a nearly homogenous density field with small overdensities, as we see in the CMB. But where did the small perturbations come from, and why do we end up with a homogenous, isotropic, and (at least close to) flat universe? The brief period of inflation after the Big Bang, where the Universe expands by a factor of around  $10^{26}$  in a tiny fraction of a second, provides explanations for this. In addition, it solves the horizon problem, explaining how parts of the CMB that should not have been in causal contact can have the same temperature. However, to this day, no direct observation of inflation exists. Experiments are currently looking for primordial B-modes, which are predicted by inflation models through the creation of inflationary gravitational waves (Kamionkowski and Kovetz, 2016; LiteBIRD Collaboration et al., 2023).
- ★ **Baryon asymmetry:** In the first fractions of a second of the Universe's existence, pairs of matter and antimatter particles were continuously created and annihilated. Somehow, we ended up with an imbalance, resulting in more matter than antimatter, leaving the Universe today to be filled with gas, galaxies, stars, and planets. Currently, there is no explanation for why this is the case, or which mechanism kicked in at the very beginning to make it so (Sakharov, 1991).
- ★ **The core-cusp problem:** The inferred dark matter halo profiles of dwarf and low surface brightness galaxies do not coincide with the density profiles found in dark matter  $\Lambda$ CDM  $N$ -body simulations (De Blok, 2010). The inferred profiles show a flat core, while the simulations predict a steeper cusp (e.g. Navarro, Frenk, and White, 1996; Oh et al., 2015). This issue can be alleviated by incorporating baryonic physics into the simulations (e.g.

---

<sup>13</sup>Luckily for us, of course, who would be out of a job had this not been the case.



Del Popolo and Pace, 2016), but whether or not this is the full solution is yet unclear. Another explanation could come (partly) from the nature of dark matter, which would then have to deviate from the standard CDM scenario (e.g. Nguyen et al., 2021).

- ★ **The  $S_8$  tension:** The density fluctuations observed from the CMB can be evolved forward in time using simulations. The resulting clustering, parametrised by  $S_8 = \sigma_8 (\Omega_m/0.3)^{0.5}$  (where  $\sigma_8$  is the root-mean-square of the amplitude of clustering at  $8 h^{-1} \text{Mpc}$ ), as predicted by the  $\Lambda$ CDM model, does not coincide with observations from low-redshift probes like weak gravitational lensing and galaxy clustering. The measurements give a weaker clustering in a  $2 - 3\sigma$  tension with expectations from the CMB. Suggestions have been made to resolve this tension (e.g. Alexander, Bernardo, and Toomey, 2022; Poulin et al., 2023; Tanimura et al., 2023), but it remains an open question.



## Chapter 2

# Beyond the standard model of cosmology

The multiple unanswered questions within our field (see Sect. 1.4) lead many to venture outside of the standard model of cosmology to find answers. In this chapter, I provide a short introduction to massive neutrinos and  $f(R)$ -modified gravity. The latter is a clear step away from the  $\Lambda$ CDM model, where GR is modified in order to avoid the need for dark energy. Massive neutrinos, on the other hand, are already a part of the  $\Lambda$ CDM model. However, they were for a long time thought to be massless, and many theoretical models and simulations still omit them due to their small contribution. Massive neutrinos are now being integrated into existing frameworks, and have become more important than ever as our observational data reach precision beyond the massive neutrino influence. Because of this, the massive neutrinos find themselves in this “beyond the standard model of cosmology” chapter.

### 2.1 Massive neutrinos

The standard model of particle physics divides the building blocks of our Universe into two parts; the elementary particles and the forces acting between them. In the lepton category of the elementary particles, we find the electron, muon, and tau particles ( $e, \mu, \tau$ ) and the associated electron, muon, and tau neutrinos ( $\nu_e, \nu_\mu, \nu_\tau$ ). The latter three were for a long time assumed to be massless particles, until neutrino oscillations were confirmed around the change of the millennium (Fukuda et al., 1998; KamLAND Collaboration et al., 2005; SNO Collaboration et al., 2002), showing that one type of neutrino particle can evolve into another as it propagates through time. The different neutrino particles are all a superposition of neutrino mass states (Thomson, 2013),

$$\begin{pmatrix} \nu_e \\ \nu_\mu \\ \nu_\tau \end{pmatrix} = \begin{pmatrix} U_{e1} & U_{e2} & U_{e3} \\ U_{\mu1} & U_{\mu2} & U_{\mu3} \\ U_{\tau1} & U_{\tau2} & U_{\tau3} \end{pmatrix} \begin{pmatrix} \nu_1 \\ \nu_2 \\ \nu_3 \end{pmatrix}, \quad (2.1)$$

where  $\nu_i$  with  $i = 1, 2, 3$  are the mass states (often shortened to  $m_i$ ) and  $U_{si}$  are components of a unitary matrix,  $U$ , for the various neutrino flavours,  $s = e, \mu, \tau$ . In other words, a neutrino propagates through space as a linear superposition of the three mass states and collapses into a specific flavour once it interacts. If the masses of the different  $\nu_i$  states are not the same, phase differences between the terms in the linear superposition will arise as the neutrino propagates through space. This indicates that, for example, what was originally an electron neutrino

## 2. Beyond the standard model of cosmology

---

could become a muon neutrino. The detection of neutrino oscillations, therefore, means that at least two of the three neutrino mass states are non-zero.

Currently, neutrino oscillation experiments are able to put constraints on the difference between neutrino mass states (Particle Data Group, Workman, et al., 2022),

$$\begin{aligned}\Delta m_{21}^2 &= (7.53 \pm 0.18) \times 10^{-5} \text{ eV}^2, \\ \Delta m_{32}^2 &= (-2.519 \pm 0.033) \times 10^{-3} \text{ eV}^2 \text{ (IH)}, \\ \Delta m_{32}^2 &= (2.437 \pm 0.033) \times 10^{-3} \text{ eV}^2 \text{ (NH)}.\end{aligned}\tag{2.2}$$

The experiments cannot, however, always know the sign of the difference, which results in two possible mass orderings of the three neutrino mass states. We have the normal hierarchy (NH), where  $m_1 < m_2 \ll m_3$ , or the inverted hierarchy (IH), where  $m_3 \ll m_1 < m_2$ . Combining the measurements we get a lower bound on the sum of the neutrino masses given by  $\sum m_\nu \gtrsim 0.1 \text{ eV}$  and  $\sum m_\nu \gtrsim 0.06 \text{ eV}$  for the inverted and normal hierarchies respectively. An upper bound on the sum of the neutrino masses,  $\sum m_\nu \lesssim 2.4 \text{ eV}$ , is given by the KATRIN (KARlsruhe TRItium Neutrino) experiment, which studies the single  $\beta$ -decay of molecular tritium (KATRIN Collaboration et al., 2022).

Besides the neutrino mass being of interest in the field of particle physics, it also affects cosmology. In the early Universe, neutrinos were relativistic and made up a fraction of the radiation content of the Universe. After some time, depending on their mass, they became non-relativistic and instead now make up a part of the matter content of the Universe. This is often taken out of the dark matter budget and, in general, means that neutrinos play a special role in the growth of structure. The neutrino density fraction depends on the sum of the neutrino masses and is given by (Lesgourgues and Pastor, 2006)

$$\Omega_\nu = \frac{\sum m_\nu}{93.14 \text{ eV} h^2}.\tag{2.3}$$

Based on the lower mass constraints from particle physics experiments, this means that the neutrinos make up at least 0.14% of the total energy content of the Universe, or at least 0.4% of the matter content. This does not seem like a lot, and it is understandable why, up until recently, neutrinos have often been ignored in cosmological simulations. However, newer satellites, such as *Euclid*, have a high enough resolution to detect the effects of the neutrinos on structure formation directly in the matter power spectrum (see Sect. 3.2; Laureijs et al., 2011). We, therefore, need to take them into account in order to match our observations with our theory and simulations. Paper I is a *Euclid* collaboration paper where different implementations of massive neutrinos in various cosmological simulations are compared to each other, to prepare for the comparison with new high-precision data. It includes the ANUBIS code, which was developed as a part of this thesis.

So, we need to include massive neutrinos in our simulations because they affect structure formation. But how do they affect structure formation? Let us

paint a picture by trailing the neutrinos through the history of the Universe, in broad strokes (following the works of Lesgourgues and Pastor, 2006). At early times, the neutrinos were a part of the primeval soup together with everything else, and they were ultra-relativistic. As the Universe expanded and cooled, the neutrinos decoupled from the rest of the plasma. This happened when the Universe had a temperature of roughly 1 MeV, about 1 second after the Big Bang, and the neutrinos remained ultra-relativistic. So long as this was the case, the neutrinos contributed to the radiation content of the Universe. The Universe continued to expand and cool, and once we reached a state where the neutrino temperature fell below its mass, the neutrinos became non-relativistic<sup>1</sup>. At this point, they no longer contributed to the radiation content of the Universe (scaling like  $a^{-4}$ ), but to the matter content instead (scaling as  $a^{-3}$ ). The time of the transition depends on the neutrino mass, and based on current limits, it happened during matter domination, after the time of recombination. But even though at least two of the three neutrino mass states are non-relativistic today, they have a large velocity distribution. This means that they contribute to the dark matter content as hot dark matter (HDM) and not as cold dark matter (CDM). Because of this, the neutrinos free-stream at some characteristic length, depending on their mass,  $m$ ,

$$\lambda_{\text{FS}}(t) = 7.7 \frac{1+z}{\sqrt{\Omega_{\Lambda} + \Omega_{\text{m}}(1+z)^3}} \left( \frac{1 \text{ eV}}{m} \right) h^{-1} \text{Mpc}, \quad (2.4)$$

during the time of matter and  $\Lambda$  domination (Lesgourgues and Pastor, 2006). This results in a damping of neutrino density fluctuations on small scales, as the neutrinos cannot be confined to regions smaller than  $\lambda_{\text{FS}}$ . When the neutrinos were still relativistic, the free-streaming length was equal to the Hubble radius, roughly the size of the observable Universe, confirming that the neutrinos did not cluster while relativistic during matter domination. Now, once the neutrinos have become non-relativistic, they behave like ordinary non-relativistic matter, meaning that the neutrino overdensities (inside the horizon) start moving towards a  $\delta_{\nu} \propto a$  behaviour on scales larger than the free-streaming length. Still, due to the effects of free-streaming,  $\delta_{\nu}$  is much smaller than  $\delta_{\text{cdm}}$ <sup>2</sup>.

The presence of neutrinos has various effects on the CMB and the LSS. We are most interested in how massive neutrinos impact the growth of matter perturbations during the era of matter domination, as this is the dominant observable effect. On scales smaller than the free-streaming length, the neutrinos do not cluster and do not need to be included in the Poisson equation. However, the neutrinos still contribute to the Friedmann equation and thus the background expansion rate. If we assume that the neutrino density is dominated by non-

<sup>1</sup>This transition was individual for each of the neutrino flavours, depending on their mass.

<sup>2</sup>The neutrino overdensities that were outside the horizon during the non-relativistic transition are not affected by the free-streaming in the same way, and quickly move towards  $\delta_{\nu} \approx \delta_{\text{cdm}}$  once they enter the horizon.

## 2. Beyond the standard model of cosmology

---

relativistic neutrinos in this regime ( $\propto a^{-3}$ ), we can define

$$f_\nu = \frac{\rho_\nu}{\rho_{\text{cdm}} + \rho_{\text{b}} + \rho_\nu} = \frac{\Omega_\nu}{\Omega_{\text{m}}}, \quad (2.5)$$

which will then stay constant. Including the massive neutrinos in our equations for the evolution of matter overdensities, through the expansion rate, will then lead to approximately  $\delta_{\text{m}} \propto a^{1-(3/5)f_\nu}$ , assuming  $f_\nu \ll 1$ . This shows that the growth of matter perturbations is damped on scales smaller than the neutrino free-streaming length due to the fact that the neutrinos do not cluster, but still contribute to the expansion rate. Overall, the nature of the massive neutrinos results in a damping of the linear matter power spectrum given by

$$\frac{P(k)^{f_\nu}}{P(k)^{f_\nu=0}} \approx -8f_\nu \quad (2.6)$$

on small scales and for small  $f_\nu$  at redshift zero. This has been shown to be even larger on non-linear scales, in the lines of  $-10f_\nu$ , with a turn-around at  $k \sim 1 h \text{Mpc}^{-1}$  due to the virialisation of halos at small scales, resulting in a spoon-like feature (Hannestad, Upadhye, and Wong, 2020). A lot more details than what is presented here goes into this overall result, and can be found in e.g. Lesgourgues and Pastor, 2006 for anyone interested. In addition to the behaviour of the perturbations, massive neutrinos also affect the time of matter-radiation equality and delay it by a fraction  $(1 - f_\nu)^{-1}$  compared to a massless case. This also suppresses the matter perturbations and shows up both in the CMB temperature anisotropy spectrum and the matter power spectrum.

Given the information above, it is clear that determining the absolute mass scale of neutrinos is important for cosmology. If found from particle physics experiments, it would help put constraints on our cosmological models, as we would know exactly how much suppression of structure to expect, in addition to the neutrino impact on the CMB. Naturally, we can do this the other way around as well. We can use cosmological observations to put constraints on the neutrino mass. Current bounds, based on CMB, lensing, Supernovae Ia, and BAO observations, give  $\sum m_\nu < 0.09 \text{eV}$  at 95% confidence by Di Valentino, Gariazzo, and Mena, 2021, putting pressure on the IH mass ordering. This, although providing a tighter upper bound than particle physics experiments, depends on the choice of cosmological model ( $\Lambda\text{CDM}$ ), and can therefore never be completely independent. The neutrino mass is also known to have degeneracies with modified gravity models (e.g. Baldi et al., 2014), which can further relax the mass constraints.

### 2.2 $f(R)$ -modified gravity

The concordance  $\Lambda\text{CDM}$  model incorporates GR as the theory of gravity, as detailed in Sect. 1.2. Even though both  $\Lambda\text{CDM}$  and GR by themselves are thoroughly tested and widely accepted theories (e.g. Ishak, 2018; Planck Collaboration et al., 2020a; Will, 2014), there are still some questions that are

left unanswered. Some of these are addressed in Sect. 1.4 and motivate, amongst others, the research field of modified gravity theories.

One well-known branch of the modified gravity field contains the  $f(R)$ -modified gravity theories (Sotiriou and Faraoni, 2010). Here, the Einstein-Hilbert action, as introduced in Sect. 1.2, is extended by a function of the Ricci scalar,  $f(R)$ ,

$$S = \int \left( \frac{R + f(R)}{16\pi G} + \mathcal{L}_m \right) \sqrt{-g} d^4x. \quad (2.7)$$

With the exception of this new function, all the other parameters are as before. An alternative description of this is an addition of a fifth force on top of gravity, which also works attractively<sup>3</sup>. In  $f(R)$ -modified gravity, this fifth force is carried by the scalaron, which is a scalar degree of freedom of the theory, described by  $f_R = df/dR$ .

If we again follow the principle of least action, as in Sect. 1.2, and require  $\delta S = 0$  when varying the action with respect to the metric, we get the new field equations (Sotiriou and Faraoni, 2010)

$$G_{\mu\nu} + f_R R_{\mu\nu} - \left( \frac{f_R}{2} - \square f_R \right) g_{\mu\nu} - \nabla_\mu \nabla_\nu f_R = 8\pi G T_{\mu\nu}. \quad (2.8)$$

Here,  $\square = \nabla^\mu \nabla_\mu$ ,  $c = 1$ , and the rest of the parameters are as before. In the Newtonian (quasi-static and weak field) limit, this can be reduced to two equations,

$$\nabla^2 \Phi = \frac{16\pi G}{3} \delta\rho - \frac{1}{6} \delta R, \quad (2.9)$$

$$\nabla^2 f_R = \frac{1}{3} (\delta R - 8\pi G \delta\rho), \quad (2.10)$$

a modified version of the Poisson equation and the equation of motion of  $f_R$ , respectively. Here,  $\delta R$  and  $\delta\rho$  are the perturbations to the Ricci scalar and density field. If we then look at regions with low curvature ( $\delta R \approx 0$ ), we see that the Poisson equation is enhanced by a factor  $4/3$  compared to what we found for  $\Lambda$ CDM in Eq. (1.35). The range of this additional ‘‘gravitational force’’ is determined by the Compton wavelength of the scalaron, which again depends on the specific  $f(R)$ -modified gravity theory.

In order to coincide with observations, modified gravity theories need to behave like regular GR in regions where deviations from GR are well-tested and confirmed to be insignificantly small (Will, 2014). In other words, we must have  $f_R \rightarrow 0$  in high-density regions, reverting back to the regular Poisson equation. This is achieved through a chameleon screening mechanism, which scales with density in such a way that the gravity theory reverts back to GR in regions with deep Newtonian potentials (Brax et al., 2008; Khoury and Weltman, 2004). This mechanism, although allowing for the  $f(R)$ -modified gravity theories to coincide

---

<sup>3</sup>This can be seen by rewriting this into a scalar-tensor theory.

## 2. Beyond the standard model of cosmology

---

with observations, makes it harder to study their effects. Because of this, cosmic voids are good environments to do exactly this, as they are underdense regions where the enhanced gravity of  $f(R)$  theories are less affected by screening. In Paper II, we investigated the current framework of void modelling and how it performs in the presence of massive neutrinos and  $f(R)$ -modified gravity.

### 2.2.1 Hu-Sawicki

In this thesis work, I have focused on Hu-Sawicki  $f(R)$ -modified gravity (Hu and Sawicki, 2007). In this specific case, the function added to the Einstein-Hilbert action is given by

$$f(R) = -m^2 \frac{c_1(R/m^2)^n}{c_2(R/m^2)^n + 1}. \quad (2.11)$$

Here,  $m^2 = H_0^2 \Omega_m$  and  $n$ ,  $c_1$ , and  $c_2$  are parameters of the model which are constant, non-negative, and dimensionless. With this form of the  $f(R)$  function, the limit  $c_2(R/m^2)^n \gg 1$  gives

$$f(R) = -m^2 \frac{c_1}{c_2} + \mathcal{O}\left(\left(\frac{m^2}{R}\right)^n\right), \quad (2.12)$$

meaning that equating  $-m^2 c_1/c_2$  with  $-2\Lambda$  gives an expansion history similar to that of  $\Lambda$ CDM. This corresponds to the relation  $c_1/c_2 = 6\Omega_\Lambda/\Omega_{\text{cdm}}$  between the parameters  $c_1$  and  $c_2$ . We can now calculate the scalar degree of freedom as

$$f_R = \frac{df(R)}{dR} = -n \frac{c_1 \left(\frac{R}{m^2}\right)^{n-1}}{\left(c_2 \left(\frac{R}{m^2}\right)^n + 1\right)^2} \approx -n \frac{c_1}{c_2^2} \left(\frac{m^2}{R}\right)^{n+1}, \quad (2.13)$$

where a value  $n = 1$  is typically adopted, determining how the  $f(R)$  theory scales with  $R$ . It is possible to completely specify the model using only  $n$  and  $f_{R0}$ , where  $f_{R0}$  is the present-day background value of the scalar degree of freedom, given by (Llinares, Mota, and Winther, 2014)

$$f_{R0} = -n \frac{c_1}{c_2^2} \left(\frac{\Omega_m}{3(\Omega_m + 4\Omega_\Lambda)}\right)^{n+1}. \quad (2.14)$$

As we have made our choice for  $n$ , the value of  $f_{R0}$  is the only free parameter we work with. It determines when the chameleon screening kicks in and moves the modified gravity theory towards GR. In addition, it tells us the current range of the fifth force through the Compton wavelength of the scalaron as (Llinares, Mota, and Winther, 2014)

$$\lambda_C^0 = 3 \sqrt{\frac{n+1}{\Omega_m + 4\Omega_\Lambda}} \sqrt{\frac{|f_{R0}|}{10^{-6}}} h^{-1} \text{Mpc}. \quad (2.15)$$



From the information above it is clear that  $f(R)$ -modified gravity theory enhances gravity, further leading to an enhancement of structure growth on scales smaller than the Compton wavelength of the scalaron. This will show up in cosmological observational probes, like the matter power spectrum and the halo mass function (HMF; see Secs. 3.2 and 3.3). A recent combination of datasets, mainly based on galaxy clusters, gave  $\log_{10}|f_{R0}| < -4.79$  for  $n = 1$  at 95.4% confidence level (Cataneo et al., 2015). Stronger bounds from different astrophysical probes exist, driving the value of  $|f_{R0}|$  even lower (Koyama, 2016), where the effects of the modification to gravity become unobservable on cosmological scales. Still,  $f(R)$  theory is well studied and provides a good testing ground for GR as an effective modified gravity model. The exploration of beyond- $\Lambda$ CDM models is not always solely about the model investigated, but also about understanding and pushing the limits of what we can do with cosmology. Can we detect the effects of modified gravity with cosmological probes alone? Can we constrain the model, rule it out, or confirm it, or must we also include astrophysical probes? Can we disentangle degeneracies with cosmological probes alone, and which probes must we combine to do so? This is what we want to know, and why we keep investigating, even when astrophysical probes might have already put tight constraints in place.

## 2.3 Degeneracy

From Secs. 2.1 and 2.2 it is evident that massive neutrinos and  $f(R)$ -modified gravity have the opposite effect on structure formation. While the massive neutrinos suppress structure growth below the free-streaming length,  $f(R)$ -modified gravity enhances structure growth on scales smaller than the Compton wavelength of the scalaron. This leads to degenerate observables, like the matter power spectrum, the HMF, the halo bias, and the void-galaxy cross-correlation function (Baldi et al., 2014; Giocoli, Baldi, and Moscardini, 2018; Hagstotz et al., 2019; Mauland et al., 2023), where different combinations of  $\sum m_\nu$  and  $f_{R0}$  even can give results consistent with a massless neutrino  $\Lambda$ CDM scenario. Figure 2.1 shows the effect of massive neutrinos,  $f(R)$ -modified gravity, and their combination on the CDM+baryon matter power spectrum (see Sect. 3.2 for details on the power spectrum) compared to a massless neutrino  $\Lambda$ CDM scenario.

The cases of massive neutrinos and  $f(R)$ -modified gravity do not stand on completely even ground though. As neutrino oscillations have been detected, we know that massive neutrinos have a place in our cosmological model. This is not the case for modified gravity. What we do know then, is that the uncertainty in the neutrino mass leaves some extra wiggle room when putting constraints on  $f_{R0}$ . If, however, a modified gravity model turns out to be a better description of our Universe than  $\Lambda$ CDM, the opposite could also be true, where the parameters constraining the modified gravity theory could affect the cosmological constraints on the neutrino mass. Still, this is only the case if the degeneracy remains. If it can be broken, through for example the combination of various observables,

## 2. Beyond the standard model of cosmology

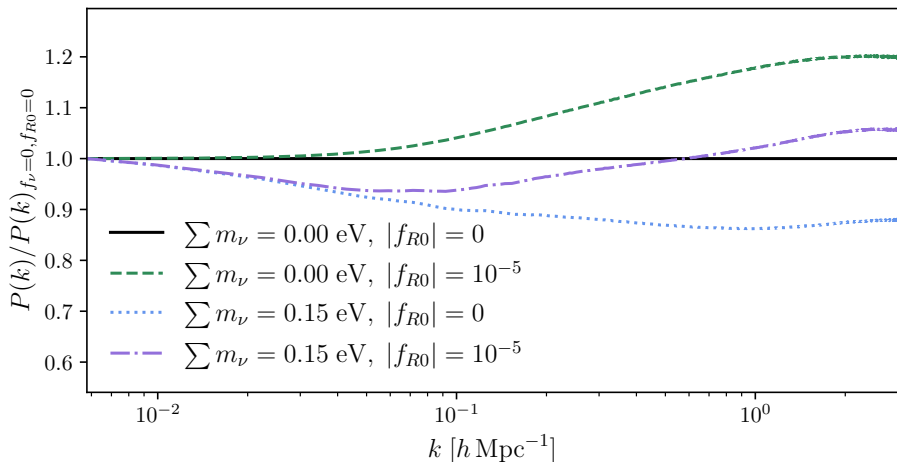


Figure 2.1: CDM+baryon matter power spectrum for simulations run with massive neutrinos and  $f(R)$  gravity compared to a massless neutrino  $\Lambda$ CDM case. The modifications to gravity enhance structure formation on small scales (large  $k$ ), while the massive neutrinos suppress it on similar scales. Their combined effect, therefore, lies closer to the massless  $\Lambda$ CDM scenario. The simulations are taken from Paper II.

the constraints can become tighter. Observing at higher redshifts is a possible way of breaking the degeneracy, as  $f(R)$ -modified gravity becomes almost fully screened for  $z \gtrsim 3$  for  $|f_{R0}| < 10^{-5}$  (Zhao, Li, and Koyama, 2011) when looking at the matter power spectrum, and effectively screened for cluster abundances at  $z > 0.5$  (Hagstotz et al., 2019). Some specific suggested observables for breaking the degeneracy are the void size function at high redshifts for large voids (Contarini et al., 2021), redshift space distortions (Wright et al., 2019), and weak lensing (e.g. Giocoli, Baldi, and Moscardini, 2018). Ideally, however, would be the achievement of tight constraints on the neutrino mass from particle physics experiments, independent of a cosmological model.

## Chapter 3

# Observing the large-scale structure

A well-established way of observing the LSS of the Universe is through galaxy surveys. Here, a patch of sky is observed and data are gathered so that galaxies may be catalogued together with properties such as their inferred distance. The placement of galaxies in a large volume helps us ascertain information about the structure of the cosmic web, along with information about the distribution of dark matter. Cosmological  $N$ -body simulations (see Ch. 4) help us further understand the theory behind the distribution of matter, especially dark matter, for which galaxies are biased tracers (Benson et al., 2000; Desjacques, Jeong, and Schmidt, 2018). With data from surveys and simulations, various properties can be calculated to make sure that theory and observations coincide. In this chapter, I will briefly introduce some statistical properties that are key components in the papers that make up this thesis. There are other observational probes of the LSS, like gravitational lensing and the CMB, but these were not a part of this thesis work and will therefore not be included in the following short review.

### 3.1 Cross-correlation function

The spatial two-point cross-correlation function (CCF) describes the excess probability over random of finding two objects (typically galaxies) separated by a distance  $\mathbf{r}$  (Carroll and Ostlie, 2014). If galaxies were distributed evenly, the probability of finding a galaxy in a small volume,  $dV_1$ , and another in a small volume,  $dV_2$ , separated by a distance,  $\mathbf{r}$ , would be  $dP = n^2 dV_1 dV_2$ , with  $n$  the average number density of galaxies. We know that galaxies are not distributed evenly, and the probability is therefore instead given by

$$dP = n(1 + \xi(\mathbf{r}))dV_1 dV_2, \quad (3.1)$$

where  $\xi(\mathbf{r})$  is the two-point correlation function,

$$\xi(\mathbf{r}) = \langle \delta(\mathbf{x})\delta(\mathbf{x} + \mathbf{r}) \rangle, \quad (3.2)$$

with  $\delta(\mathbf{x}) = (\rho(\mathbf{x}) - \bar{\rho})/\bar{\rho}$  the overdensity at position  $\mathbf{x}$ . Commonly, isotropy is assumed, reducing  $\xi(\mathbf{r})$  to  $\xi(r)$ . The galaxy correlation function gives us information about clustering and has been studied for a long time. Observations find that it approximately follows a power law on separation scales  $r < 10 h^{-1}\text{Mpc}$ , given by  $\xi(r) \propto r^{-\gamma}$ , with  $\gamma \sim 1.8$  (Peebles, 1980; Totsuji and Kihara, 1969; Watson, Berlind, and Zentner, 2011). However, it is not only the correlation function of galaxy positions that holds important information. In Paper II, we

### 3. Observing the large-scale structure

---

studied the cross-correlation function between voids and dark matter halos<sup>1</sup> in different cosmologies. Cosmic voids have recently become an active research field, with the void-galaxy CCF at its centre. More details about this can be found below, in Sect. 3.5.

If the density field were Gaussian, the two-point correlation function would hold all possible information. Due to non-linear evolution, this is not the case, and higher-order statistics are needed in order to capture all the information. The two-point correlation function can be generalised to an  $n$ -point correlation function, with the three-point correlation function the most commonly encountered case:

$$\zeta(r_{12}, r_{23}, \theta) = \langle \delta(\mathbf{x})\delta(\mathbf{x} + \mathbf{r}_{12})\delta(\mathbf{x} + \mathbf{r}_{23}) \rangle. \quad (3.3)$$

This describes the excess over random of finding a specific configuration of three galaxies, with  $\mathbf{r}_{12}$  the separation between galaxy 1 and 2,  $\mathbf{r}_{23}$  the separation between galaxy 2 and 3, and  $\theta$  the angle between them. For the three-point correlation function to be nonzero, the configuration must form a closed triangle.

### 3.2 Power spectrum

Another important statistic for studying the LSS and clustering of mass is the matter power spectrum (Dodelson and Schmidt, 2020). This is the Fourier transform of the two-point correlation function (Sect. 3.1), defined as

$$P(k) = \int \xi(r) e^{-i\mathbf{k}\cdot\mathbf{r}} d^3r, \quad (3.4)$$

where  $k$  is the wavenumber. Alternatively, we can look at it as Fourier transforming the overdensity field,

$$\delta(k) = \int \delta(r) e^{-i\mathbf{k}\cdot\mathbf{r}} d^3r, \quad (3.5)$$

giving

$$P(k_1)(2\pi)^3 \delta_{\text{D}}(\mathbf{k}_{12}) = \langle \delta(\mathbf{k}_1)\delta(\mathbf{k}_2) \rangle, \quad (3.6)$$

where  $\delta_{\text{D}}$  is the Dirac-delta function. Analysing the matter distribution in Fourier space, as opposed to the CCF in physical space, has its advantages. On large scales, where  $\delta \ll 1$ , linear theory applies and each Fourier mode evolves independently as seen in Sect. 1.3.2. This direct link between the large scales of the matter power spectrum and linear theory makes it a convenient observable for comparison between data and models. In addition, performing computations in Fourier space usually requires less time and computational power. Figure 3.1 shows a comparison between data and theory for the linear matter power spectrum.

---

<sup>1</sup>Of course, we cannot observe dark matter halos directly. This research was performed on simulation data. If we had used observational data, we would have studied the void-galaxy cross-correlation function instead.

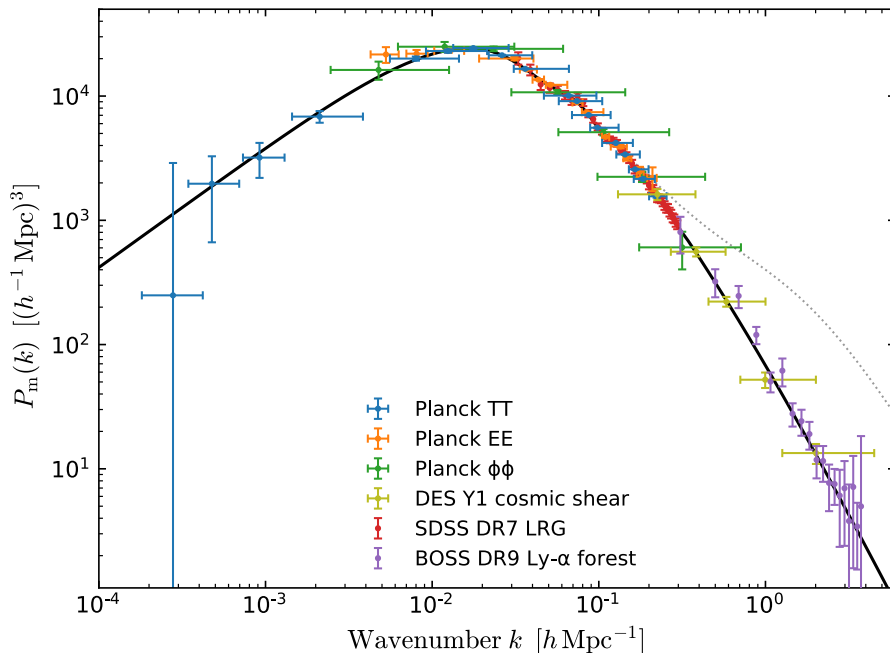


Figure 3.1: Data from various cosmological probes compared to the theoretical prediction of the linear matter power spectrum (black line) at redshift zero. The turn-around value,  $k_{\text{ta}}$ , represents the scale where modes started entering the horizon during matter domination instead of radiation domination. The results of the Meszaros effect can thus be seen for  $k > k_{\text{ta}}$ . The dotted line shows the predicted behaviour of the non-linear power spectrum. Credit: ESA and the Planck Collaboration (Planck Collaboration et al., 2020a)

Again, due to the non-linear evolution of matter fluctuations, some information about the matter field leaks over to higher-order statistics. Repeating the above process for the three-point correlation function we get the bispectrum,

$$B(k_1, k_2, k_3)(2\pi)^3 \delta_{\text{D}}(\mathbf{k}_{123}) = \langle \delta(\mathbf{k}_1) \delta(\mathbf{k}_2) \delta(\mathbf{k}_3) \rangle. \quad (3.7)$$

Studying the bispectrum is interesting in itself to better understand non-Gaussianities in the matter field, but can also provide additional information, for example when massive neutrinos are present in the cosmological model, as their effects are larger on the non-linear level. Both the power spectrum and the bispectrum were studied for various neutrino masses in Paper I.

In addition to studying the observed power and bispectrum, investigating the ratio of power and bispectra for various simulated cosmologies are of interest. Especially the power spectrum ratio of alternative cosmologies to that of  $\Lambda$ CDM, known as the boost, has gained interest as a probe of the difference in clustering statistics between the models. In Paper III, we made a pipeline for the creation

### 3. Observing the large-scale structure

---

of a boost emulator for beyond- $\Lambda$ CDM models. As an example, we created a boost emulator for  $f(R)$ -modified gravity in the presence of massive neutrinos, incorporating their degenerate effect.

#### 3.3 The halo mass function

The halo mass function (HMF) describes the abundance of dark matter halos as a function of their mass. Typically, it is measured by

$$\text{HMF} = \frac{dn}{d \ln M}, \quad (3.8)$$

the number density,  $n$ , of halos within a narrow logarithmic halo mass band,  $d \ln M$ . As mentioned in Sect. 1.3.3, halos are virialised objects that have detached from the background expansion (Peacock and Heavens, 1990; Press et al., 1974). They form hierarchically, meaning that small halos form first and merge with each other to create more massive halos. The largest, and most recently formed, halo structures are today the hosts of galaxy clusters. Because of this, the HMF is sensitive to the expansion history of the Universe and the nature of gravity and can be used to estimate cosmological parameters (Despali et al., 2016; Dodelson and Schmidt, 2020).

Constraints are generally obtained by comparing theoretical predictions and simulations with observations. The setback here is, yet again, that dark matter halos are not directly observable. Luckily, dark matter halos are hosts to galaxies, which are biased tracers of the underlying dark matter field (e.g. Desjacques, Jeong, and Schmidt, 2018). By applying models for how galaxies populate their hosts, galaxy surveys, and especially the abundance of galaxy clusters, may be used to infer the distribution of dark matter halos (Castro, Marra, and Quartin, 2016). This can again be cross-checked with predictions from detailed simulations, where multiple tools already exist for creating halo catalogues out of dark matter density fields (e.g. Behroozi, Wechsler, and Wu, 2012; Despali et al., 2016). In Paper I, the impact of massive neutrinos on the HMF was studied for various  $N$ -body simulations and emulators. The HMF was also included in Paper II, to investigate the difference between cosmologies with massive neutrinos and  $f(R)$  gravity.

#### 3.4 The halo bias

Both galaxies and halos are biased tracers of the underlying matter field. The halo bias can be defined as (e.g. Castorina et al., 2014)

$$b(k) = \frac{P_{\text{h,cb}}(k)}{P_{\text{cb}}(k)}, \quad (3.9)$$

where  $P_{\text{h,cb}}(k)$  is the cross-power spectrum between halos and CDM+baryons and  $P_{\text{cb}}(k)$  is the auto power spectrum of CDM+baryons. The halo bias tells us

something about how the distribution of halos follows that of the underlying dark matter, and it will depend on the nature of gravity and the expansion history of the Universe. For example, for a  $\Lambda$ CDM scenario with massless neutrinos, the halo bias is scale-independent on linear scales, while the introduction of massive neutrinos introduces a scale dependence (e.g. Chiang, Loverde, and Villaescusa-Navarro, 2019). Because of its alterations to gravity, and thereby structure growth, a modification to gravity will also induce a change in the observed bias (e.g. Arnold et al., 2019).

The halo bias is most easily studied in simulations, where we have access to the underlying dark matter field, and can create halo catalogues as mentioned in Sect 3.3. Because of this, the halo bias is included in Papers I and II, as a way of studying the impact of massive neutrinos and  $f(R)$ -modified gravity.

### 3.5 Cosmic voids

The CCF, matter power spectrum, HMF, and halo bias (Sect. 3.1-3.4) are statistical observables based on the distribution of matter. However, much can also be learned by studying the opposite - the absence of matter. Cosmic voids have recently emerged as important independent probes of cosmological parameters and gravity. They are vast regions in space that have not undergone virialisation and can therefore be described well by linear perturbation theory. In addition to this, their empty nature makes them the areas in the Universe with the highest neutrino-to-other-matter ratio, and their sizes are of similar scales to the neutrino free-streaming length. This makes them excellent candidates for studying the effects of massive neutrinos. Being underdense, voids are also promising regions for studying modified gravity theories, which include screening mechanisms to adhere to already established observational knowledge of our local Universe. Seeing as these mechanisms kick in for high-density regions, cosmic voids will experience modified gravity in a less screened manner.

To extract cosmological information from voids, we can study the redshift space distortions (RSDs) in the quadrupole of the void-galaxy CCF. Firstly, redshift space is the space, or the coordinate system, in which objects are placed based on their redshift. In our Universe, the redshift of an object, like a galaxy, depends on its distance from us, due to the expansion of space. The further away an object is, the faster it moves away from us, as known from Hubble's law,  $v = H_0 r$ , where  $v$  is the velocity of the object,  $H_0$  is the Hubble constant, and  $r$  is the distance to the object. Because of this, the light that is emitted from the galaxy is redshifted before it reaches us, courtesy of the Doppler effect. In addition to the recessional velocity due to the expansion of space, objects will also have an additional redshift or blueshift due to their individual peculiar velocities. These velocities result in distortions in the redshift space. Secondly, the CCF in itself tells us something about how galaxies are distributed around voids and can be divided up into multipoles (e.g. Nadathur et al., 2019),

$$\xi_\ell(s) = \frac{2\ell + 1}{2} \int_{-1}^1 L_\ell(\mu) \xi(s, \mu) d\mu, \quad (3.10)$$

### 3. Observing the large-scale structure

where  $\ell$  denotes the multipole,  $s$  is the distance between the void centre and galaxy in redshift space,  $L_\ell$  is the Legendre polynomial of order  $\ell$ , and  $\mu = \cos \theta$  where  $\theta$  is the angle between the line-of-sight (LOS) and void-galaxy separation vector. The RSDs in the quadrupole ( $\ell = 2$ ) relay information about how the galaxies in and around a void move along the LOS.

Now, in order to gain information from the multipoles of the void-galaxy CCF in redshift space, we need a model. Let us denote the void-galaxy separation vector by  $\mathbf{r}$  in real space and  $\mathbf{s}$  in redshift space. Then, the CCF in redshift space,  $\xi^s(\mathbf{s})$ , can be related to the CCF in real space,  $\xi^r(\mathbf{r})$ , by the streaming model (Fisher, 1995; Paillas et al., 2021; Peebles, 1980),

$$1 + \xi^s(\mathbf{s}) = \int (1 + \xi^r(\mathbf{r}))P(v_{\parallel}, \mathbf{r})dv_{\parallel}. \quad (3.11)$$

Here,  $P(v_{\parallel}, \mathbf{r})$  is the probability distribution function (PDF) of the galaxies' peculiar velocities parallel to the LOS,  $v_{\parallel}$ . By dividing this velocity into two components, one which comes from stochastic motion,  $\tilde{v}_{\parallel}$ , and another which comes from a coherent, spherically symmetric outflow from the void centre,  $v_r(r)$ , Eq. (3.11) can be rewritten as (Woodfinden et al., 2022)

$$1 + \xi^s(\mathbf{s}) = \int (1 + \xi^r(\mathbf{r}))P(\tilde{v}_{\parallel}, \mathbf{r})J_{\mathbf{r}\mathbf{s}}d\tilde{v}_{\parallel}. \quad (3.12)$$

Now,  $P(\tilde{v}_{\parallel}, \mathbf{r})$  is the PDF for the stochastic velocity component, which is centred around zero, and  $J_{\mathbf{r}\mathbf{s}}$  is the Jacobian of the coordinate shift from real to redshift space, given by

$$J_{\mathbf{r}\mathbf{s}} = \left[ 1 + \frac{v_r}{raH} + \frac{(v_r' - v_r/r)}{aH} \mu_r^2 \right]^{-1}. \quad (3.13)$$

Here,  $v_r$  is the coherent outflow velocity from earlier,  $\mu_r$  is the cosine of the angle between the LOS and  $\mathbf{r}$ ,  $H$  is the Hubble parameter, and the prime denotes the derivative with respect to  $r$ .

The void velocity profile,  $v_r(r)$ , is not readily observable and is therefore typically modelled or obtained from simulations. One common model is the linear velocity profile, given by (Peebles, 1980, 1993)

$$v_r^{\text{Lin}} = -\frac{1}{3}faH\Delta(r)r, \quad (3.14)$$

where  $f = d \ln D / d \ln a$  is the linear growth rate, with  $a$  the scale factor and  $D$  the linear growth factor<sup>2</sup>, and  $\Delta(r) = \frac{3}{r^3} \int_0^r \delta(x)x^2 dx$ , with  $\delta(r)$  the overdensity profile of dark matter around the void. Figure 3.2 shows the quadrupole of the void-galaxy CCF for a massless neutrino  $\Lambda$ CDM simulation compared to the model presented above, using the linear velocity profile as model input.

<sup>2</sup>The growth factor,  $D(a)$ , quantifies the growth of matter perturbations as  $\delta(k, a) = \delta(k, a_{\text{ini}})D(a)$ , where  $a_{\text{ini}}$  is some initial value. During matter domination, inside the horizon, we have  $D(a) = a$ .



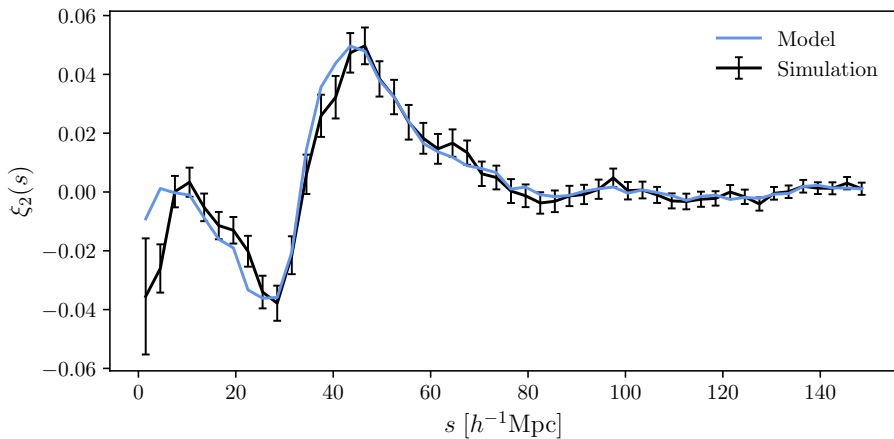


Figure 3.2: Quadrupole of the void-galaxy CCF for a massless neutrino  $\Lambda$ CDM simulation compared to the void-galaxy CCF model of Eq. (3.12). The velocity input to the model is given by Eq. (3.14) and the simulation is taken from Paper II. The shape of the quadrupole illustrates how galaxies inside the void move towards a slight overdensity at the void edge, while galaxies outside the void move towards the same overdensity from the other side.

When deriving Eq. (3.14), the growth rate is assumed to be scale-independent. This assumption does not hold for cosmologies with modified gravity or massive neutrinos (e.g. Hernández, 2017; Mirzatuny and Pierpaoli, 2019), which was one of the points of interest in Paper II, where we investigated how the void-galaxy CCF modelling performs compared to simulations with massive neutrinos and  $f(R)$ -modified gravity.

Now, if we can accurately model the RSDs in the quadrupole of the void-galaxy CCF resulting from the peculiar velocities of the galaxies, voids can also be used to test our cosmological model through the Alcock-Paczyński (AP) effect (Alcock and Paczyński, 1979). Here, the ratio of the observed angular size and redshift size of an object of known shape is used to study a fiducial cosmology. Any deviations from the expected shape will show up in the CCF in addition to contributions from peculiar velocities. Voids are excellent candidates for testing this effect, as the average shape of many voids stacked together should be spherical. Any deviations from this indicate that the chosen fiducial cosmology is not the true cosmology and can thus be used to help estimate cosmological parameters.

This was a short recap of the main observables appearing in the three papers included in this thesis. For more details, see the papers themselves and sources therein, or e.g. Carroll and Ostlie, 2014 and Dodelson and Schmidt, 2020. With that, let us now move away from theory and have a quick look at  $N$ -body simulations.



## Chapter 4

# Cosmological $N$ -body simulations

A good way to test the current models of our Universe, or to investigate the effects of new ones, is to perform cosmological simulations. Simply put, a volume of space is filled up with matter corresponding to the expected distribution at some early cosmic time. We then press “play” and allow the matter distribution to evolve with time according to the laws of physics implemented in the simulation. For a large simulated volume of space, these types of simulations are typically focused on dark matter, as it constitutes most of the matter content and can be described by less complicated physics than baryonic matter. For this thesis work, I have performed a series of dark matter simulations including both massive neutrinos and  $f(R)$ -modified gravity. In this chapter, I will provide a brief overview of the simulation codes I have used and how they work.

### 4.1 General

Before addressing the individual simulations, a general overview of cosmological  $N$ -body simulations, focusing on dark matter, is quite useful. Although complicated to construct numerically, the premise behind the framework is rather simple: Starting from Gaussian initial conditions, in the form of density fluctuations, we want to evolve collisionless matter through time and space under the effect of gravity. How this endeavor is undertaken varies from code to code (see e.g. codes like **GADGET**, **gevolution**, **CONCEPT**, and **RAMSES**: Adamek et al., 2016; Dakin, Hannestad, and Tram, 2022; Springel et al., 2021; Teyssier, 2002), but the main idea behind  $N$ -body codes is the division of the matter content into “particles”. Now, remembering back to the Vlasov-Poisson system of Sect. 1.3.3, what we are interested in is the behaviour of the distribution function,  $f$ , of cold dark matter. To follow this numerically, we can take advantage of the fact that the matter occupies a thin sheet in phase-space, and discretise the sheet. The small elements each have a position and momentum, and as the movement of the dark matter in each small phase-space region is described by the geodesic equation, so is the movement of the small phase-space element itself. Instead of solving the Vlasov-Poisson system directly, we can then follow the evolution of the particles under the influence of gravity, using the geodesic equation. For cold dark matter, we can look at the non-relativistic limit, leading to a system of equations given by

$$\begin{aligned} \mathbf{x}' &= \frac{\mathbf{p}}{ma}, \\ \mathbf{p}' &= -ma\nabla\Psi, \\ \nabla^2\Psi &= 4\pi Ga^2\rho, \end{aligned} \tag{4.1}$$

## 4. Cosmological $N$ -body simulations

---

where  $\mathbf{p}$  is the canonical momentum,  $\Psi$  is the gravitational potential, the derivatives are taken with respect to conformal time, and  $\mathbf{x}$  is given in comoving coordinates, thereby including the Hubble expansion. It is the small discretised elements of phase space that we call particles in this setting. This means that the particle mass,  $m$ , depends on the amount of matter we have in the simulation volume, and the amount of particles we want to include.

Once initial conditions in the form of particle positions and velocities are in place<sup>1</sup>, an important part of the numerical setup is computing the gravitational potential experienced by each particle. This could be obtained by directly summing up the gravitational force exerted on each particle from all the other particles, but this is not computationally effective and quickly becomes quite expensive ( $\mathcal{O}(N^2)$ ) for a large number of particles,  $N$ . Two well-known methods of improving this process are the particle mesh (PM) based approach and the tree algorithm (see e.g. Bagla, 2005, for a review). In the first method, the masses of the particles are conveyed to a grid, or mesh, creating a 3D density field. Once this is obtained, the Poisson equation can easily be solved in Fourier space, thereby acquiring the gravitational potential. How well this process works depends on the spatial resolution of the mesh. Equal, and high, resolution of the density field throughout the full simulation volume can still quickly get computationally expensive ( $\mathcal{O}(N_m \log N_m)$ , where  $N_m$  is the number of mesh points). Because of this, some codes use adaptive mesh refinement (AMR), where the mesh has a higher resolution in regions of high density while keeping a lower resolution in regions of low density. For the other approach, the tree algorithm, the simulation domain is divided into sub-domains, or tree nodes, which make up levels of a hierarchical tree structure. The idea is to divide the simulation box into fractions of eight, so that level 1 is 1/8th of the simulation volume, level 2 is 1/64th, and so on. This division goes on until each cell contains, at most, one particle. The advantage of this approach is that, when calculating the sum of gravitational forces on one particle, distant particles in the vicinity of each other may be grouped into one tree node. The collective contribution to the gravitational potential from the group of distant particles may be approximated by a multipole expansion, keeping only the lower modes. This reduces the force calculation to  $\mathcal{O}(N \log N)$ . This approach does not have the spatial resolution issue of the previous one, but will instead struggle with nearly homogenous density fields. To get the best of both worlds, some codes combine the two approaches explained below into a tree-PM method (Xu, 1995). We then look at the Poisson equation in Fourier space and split the gravitational potential into a short and a long-range contribution. For the long-range contribution, the Poisson equation is solved in Fourier space, using the PM method, and for the short-range contribution, we revert back to real space and find the gravitational

---

<sup>1</sup>I will not cover this part here, but in short words, it is typically acquired by rescaling the linear matter power spectrum of today to some desired starting redshift, followed by drawing random phases for each perturbation mode from a Gaussian distribution depending on the initial power spectrum, creating a density field. This is then converted into particle positions and velocities using e.g. the Zel'dovich approximation (Efstathiou et al., 1985; Zel'dovich, 1970). For more details, see e.g. Sirko, 2005.

potential using the tree algorithm. This combination leads to an algorithm that does not have the same spatial restrictions as the PM method, and at the same time computes the contribution from long-range forces accurately also for nearly homogenous density fields. Of course, once the gravitational potential is obtained, there still remains the time integration portion of the particle evolution. Many different numerical algorithms exist for this part of the calculation, where the leapfrog method (Quinn et al., 1997) is a well-known example.

The implementation of the above-mentioned methods is complicated and has, to my advantage, been performed in different variations by many skilled astronomers and programmers before me. As a part of my Ph.D. work, I have utilised the already existing  $N$ -body codes **RAMSES** (Teyssier, 2002), **ISIS** (Llinares, Mota, and Winther, 2014), and **COLASolver**<sup>2</sup>. The two former were expanded and merged to create **ANUBISIS** (Papers I and II), and the latter was used to create a power spectrum ratio emulator pipeline, *Sesame* (Paper III). Let us have a look at the codes and their purpose in more detail.

## 4.2 ANUBISIS

**ANUBISIS** is a **RAMSES**-based<sup>3</sup> (Teyssier, 2002) cosmological  $N$ -body simulation including massive neutrinos and modified gravity. It is a merging of the **ISIS** (Llinares, Mota, and Winther, 2014) and **ANUBIS**<sup>4</sup> codes, which separately incorporate modified gravity and massive neutrinos respectively. The latter was developed as a part of this thesis work and was rigorously tested in Paper I. Below follows a short recap of the codes used to build **ANUBISIS**.

### 4.2.1 RAMSES

**RAMSES** is a hydrodynamical Newtonian  $N$ -body code with multiple areas of applicability. On smaller scales, it can be used to simulate galaxies, and is built to handle the hydrodynamics of baryonic matter. On larger scales, it can carry out cosmological dark matter simulations, providing us with time-stamped positions and velocities of the particles in the simulation box. **RAMSES** is a PM code, but utilises a tree algorithm to incorporate AMR, enabling it to locally change the refinement of the simulation mesh in areas of high density. This provides the opportunity of highly resolved regions where there is a lot of clustering, without having to refine large empty areas to the same degree.

### 4.2.2 ANUBIS

**ANUBIS** is an extension of the **RAMSES** code which incorporates massive neutrino particles. It was developed as a part of this thesis work, with the ultimate goal of combining it with the **ISIS** code (see Sect. 4.2.3), to create **ANUBISIS**. On its

---

<sup>2</sup><https://github.com/HAWinther/FML/tree/master/FML/COLASolver>

<sup>3</sup><https://bitbucket.org/rteyssie/ramses/src/master/>

<sup>4</sup><https://github.com/renmau/anubis>

## 4. Cosmological $N$ -body simulations

---

own, it was a part of the *Euclid* Consortium massive neutrino code comparison project in Paper I.

Originally, **RAMSES** is a Newtonian  $N$ -body code, meaning that the equations of motion (EOMs) of the simulated particles are given by Eq. (4.1). While this is a good approach for cold dark matter particles, which move slowly compared to the speed of light, it is not valid for massive neutrino particles. The neutrinos are relativistic at early times, and in order for the EOMs to handle arbitrarily high momenta, they must be rewritten in a relativistic form. By proceeding as before, but not taking the non-relativistic limit, the geodesic equation gives

$$\mathbf{x}' = \frac{\mathbf{p}}{\sqrt{\mathbf{p}^2 + m^2 a^2}}, \quad (4.2)$$

$$\mathbf{p}' = -\frac{2\mathbf{p}^2 + m^2 a^2}{\sqrt{\mathbf{p}^2 + m^2 a^2}} \nabla \Psi, \quad (4.3)$$

where the parameters are as before and  $c = 1$ . To include massive neutrinos in **RAMSES**, we thus created a separate particle ensemble for the neutrinos and changed the EOMs to the form given here. This is implemented in such a way that the total matter density,  $\Omega_m$ , stays fixed, meaning that an increase in  $\Omega_\nu$  gives a corresponding decrease in  $\Omega_{\text{cdm}}$ , and vice-versa. We also included radiation in the background expansion, through the Hubble function, and allowed for the option of reading this from file instead of calculating it within the code. In Fig. 4.1, the dark matter density field of an **ANUBIS** simulation is shown, clearly displaying the cosmic web structure of our Universe.

The performance of **ANUBIS** compared to other  $N$ -body codes incorporating massive neutrinos was tested in Paper I for various simulation setups and neutrino masses. The comparison was performed with less than optimal resolution (Schneider et al., 2016)<sup>5</sup>, but **ANUBIS** overall still gave results consistent with the other codes, both in the massless and massive neutrino cases for the various observables. However, the performance at small scales was noticeably better for redshift zero and for the simulations with a higher particle density compared to the standard particle density chosen for the comparison.

### 4.2.3 ISIS

**ISIS** (Llinares, Mota, and Winther, 2014) is an extension of the **RAMSES** code incorporating modified gravity, with screening mechanisms, in the form of scalar-tensor gravitational theories. Thus, it is a PM  $N$ -body code with AMR, where additional fifth forces are included in the gravitational potential calculations. It includes a non-linear implicit solver for a general scalar field, thereby handling different modified gravity theories. Among them is Hu-Sawicki  $f(R)$  gravity

---

<sup>5</sup>This was due to limited time and computing resources on our end. **ANUBIS** was developed alongside the comparison project and was not optimised in terms of time stepping. This, combined with the high memory requirements of **RAMSES** for increasing the base grid resolution, led to us settling for a lower resolution option.

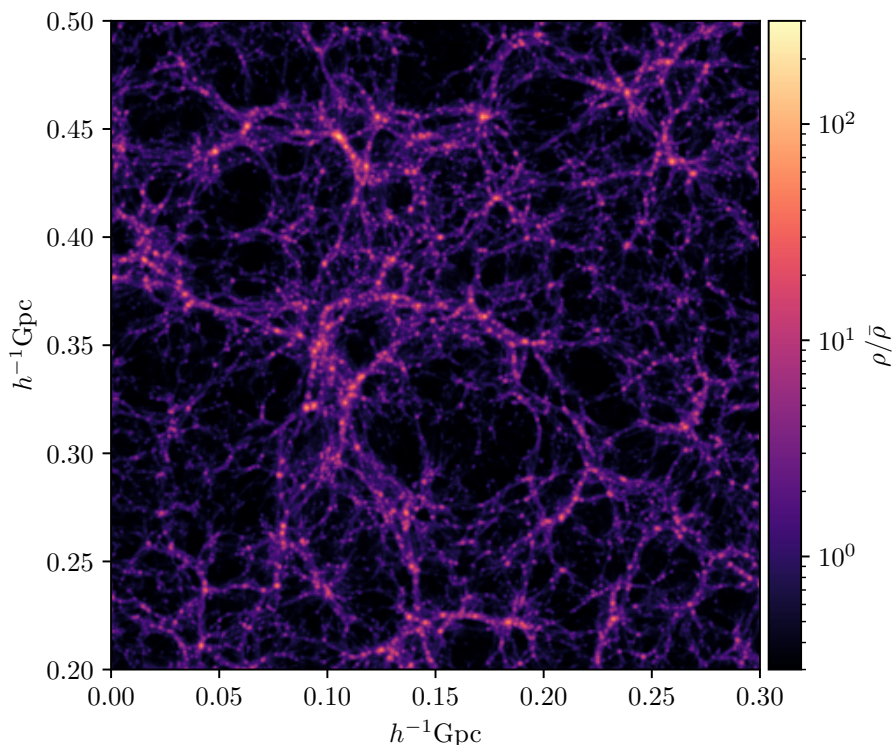


Figure 4.1: Dark matter density field for the high-resolution massless neutrino simulation performed by ANUBIS for Paper I. The original box has dimensions of  $512 h^{-1}\text{Mpc}$ , and the plot shows a  $300 \times 300 \times 25 h^{-3}\text{Mpc}^3$  slice projected onto two dimensions for redshift zero.

(Sect. 2.2.1), incorporated through its scalar-tensor formulation, which has been the main interest of this thesis work.

The resulting combination of ANUBIS and ISIS, ANUBISIS, was used in Paper II to perform simulations including both massive neutrinos and  $f(R)$ -modified gravity. These were further analysed using cosmic voids, clearly showcasing the degenerate nature of massive neutrinos and  $f(R)$  gravity.

### 4.3 Sesame – A power spectrum ratio emulator pipeline

In the final project of this Ph.D. thesis (Paper III), I moved away from the ANUBIS and ANUBISIS simulations, and instead looked at an approximate  $N$ -body simulation, the COLASolver in the FML library<sup>6</sup>. Taking advantage of the low computing resource requirements of the code, we used it as a baseline for

<sup>6</sup><https://github.com/HAWinther/FML/tree/master/FML/COLASolver>

## 4. Cosmological $N$ -body simulations

---

creating a full emulator pipeline for the power spectrum boost of beyond- $\Lambda$ CDM cosmologies,  $B(k, z) = P_{\text{beyond-}\Lambda\text{CDM}}(k, z)/P_{\Lambda\text{CDM}}(k, z)$ . This was achieved by running a large set of simulations for varying cosmological parameter values with the `COLASolver`, and then using the output as training data for a neural network. As an example, we created an emulator for  $f(R)$ -modified gravity, including massive neutrinos. The full pipeline was named *Sesame* - from simulations to emulators using approximate methods<sup>7</sup>. Below follows a brief overview of the `COLASolver` and the machine learning techniques applied when creating the emulator.

### 4.3.1 The `COLASolver`

Sometimes, for statistical analysis, we do not necessarily need incredibly accurate simulations, but rather a high quantity of simulations. For this, the above approach with `ANUBISIS` is too time- and memory-consuming. What we can do instead, is use approximate methods, which do not fully solve the particle trajectories as explained in Sect. 4.1, but rather employ some shortcuts. One such method is the comoving Lagrangian acceleration (COLA) method (Tassev, Zaldarriaga, and Eisenstein, 2013), which takes advantage of the fact that structure formation can be described accurately on large scales by Lagrangian perturbation theory (LPT). To reduce the simulation time substantially, a simulation can therefore use LPT at large scales, while still using, in this case, a full PM  $N$ -body solution at small scales. This is obtained by, instead of solving for the full trajectory of the particle, solving for the displacement ( $\delta\mathbf{x}$ ) between the LPT trajectory ( $\mathbf{x}_{\text{LPT}}$ ) and the full trajectory ( $\mathbf{x}$ ). So, instead of solving something along the lines of (ignoring factors of  $m$  and  $a$ )

$$\mathbf{x}'' = -\nabla\Psi, \quad (4.4)$$

we instead solve, using  $\mathbf{x} = \delta\mathbf{x} + \mathbf{x}_{\text{LPT}}$ ,

$$\delta\mathbf{x}'' = -\nabla\Psi - \mathbf{x}_{\text{LPT}}''. \quad (4.5)$$

This stays accurate on large scales even with few time steps, reducing the computation time substantially. In practice, we are trading accuracy on small scales for speed. However, increasing the amount of time steps makes the method converge towards a regular PM  $N$ -body simulation, meaning that you can control the trade-off.

This method is implemented in the `COLASolver` in the `FML` library, which is the version following the `MG-PICOLA` code (Winther et al., 2017)<sup>8</sup>, which uses the COLA method in the setting of  $f(R)$ -modified gravity. The `COLASolver` version also includes massive neutrinos, as explained by Wright, Winther, and Koyama, 2017. The implementation of massive neutrinos is different in the `COLASolver` compared to `ANUBISIS`. As we saw earlier, `ANUBISIS` implements the neutrinos

---

<sup>7</sup>[https://github.com/renmau/Sesame\\_pipeline](https://github.com/renmau/Sesame_pipeline)

<sup>8</sup><https://github.com/HAWinther/MG-PICOLA-PUBLIC>



as particles. The neutrinos in the `COLASolver` are instead described through a mesh-based approach, where the distribution function of neutrinos, based on linear theory, is represented on a spatial mesh (Brandbyge and Hannestad, 2009). This does not allow us to follow the neutrinos into the non-linear regime, but as they cluster weakly, this is still a good approximation.

### 4.3.2 Machine learning

The efficiency of the `COLASolver` makes it possible to perform a large number of simulations with varying cosmological parameters over a short timespan. Doing this for both a beyond- $\Lambda$ CDM and a  $\Lambda$ CDM model allows us to extract the matter power spectrum boost. Using machine learning, we can then use this data to train a neural network, which in turn can provide us with an emulator capable of predicting the matter power spectrum boost at any desired redshift and cosmological parameter values within some allowed intervals.

In order to obtain the emulator, we use the `PyTorch-Lightning`<sup>9</sup> package in `Python`, which is a wrapper for the `PyTorch`<sup>10</sup> module. This provides a simple interface for accessing a machine learning framework, focusing on deep learning through training neural networks with multiple layers. The architecture of the neural network is engineered by the user, allowing adaptation based on need in terms of performance. Figure 4.2 illustrates an example structure of a neural network with multiple layers, each consisting of a number of neurons. In this specific case, we have the input layer in green, to the left, which takes all our data and presents it to the rest of the network. For simplicity, the figure only contains three neurons in the input layer, but these will represent the amount of features you have in your data. If you have a function that depends on 20 variables,  $x_i$  with  $i = 1, \dots, 20$ , then you need 20 neurons in your input layer. Each neuron in the input layer then takes one data feature,  $x_i$ , and passes it on to all the neurons in the first hidden layer, through a connection (the arrows in the figure). This is where the magic starts to happen. Each connection has an associated weight,  $w$ , so that the values that arrive at the neurons in the hidden layers are weighted. The inputs to each neuron are then summed up so that we have  $Y = \sum x_i w_i$ . Next, a bias value,  $b$ , is added to allow the sum to be adjusted, providing more flexibility. An activation function,  $g$ , is then applied to the sum, which is where the possibilities of non-linearities are introduced. From each neuron in the first hidden layer,  $g(Y + b)$  is then sent to each neuron in the next hidden layer, and the process with weights, bias, and activation function repeats itself. Finally, the last hidden layer passes data to the output layer, repeating the aforementioned process one last time. The output neurons then produce the final results. In our illustration, there is only one output neuron, representing, for example, the value of a function that we want to estimate given some feature values. How much the output data differs from the input data can now be estimated, and is often known as the loss. The goal is then for the

<sup>9</sup><https://www.pytorchlightning.ai/index.html>

<sup>10</sup><https://pytorch.org/>

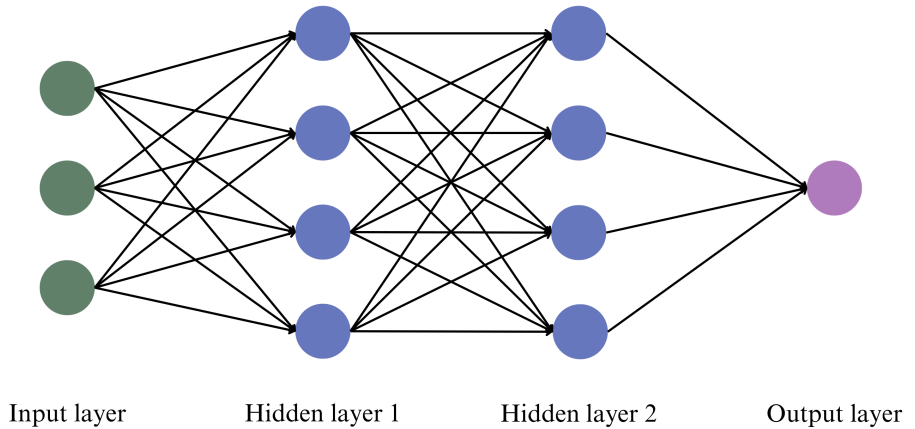


Figure 4.2: Neural network with two hidden layers.

weights to be updated so that the error between the input data and output data is reduced, which is done through several iterations of the process above, using the gradient of the loss to estimate how the weights should be changed. This is the training algorithm of the neural network. Interestingly, if the function we were trying to estimate was linear in nature, we would not need any hidden layers and could go directly from the input layer to the output layer. The process would then be similar to linear regression. For more information about machine learning and neural networks, see e.g. Hastie, Tibshirani, and Friedman, 2009; Marsland, 2014.

In the manner explained above, neural networks were trained on power spectrum boost data in Paper III, creating emulators for the example case of  $f(R)$  gravity with massive neutrinos, as a means to demonstrate the *Sesame* pipeline.

## Chapter 5

# Summary and outlook

After four chapters introducing and reviewing the area of interest of this thesis, it is finally time to summarise and conclude the work. Below follows first a short recap of each individual paper in writing order, and then a conclusion and outlook for the time to come.

### 5.1 Summaries of papers

#### Paper I

*This paper is a collaboration project performed within the Euclid Consortium, led by Julian Adamek, SNSF Eccellenza professor at the University of Zurich.*

The *Euclid* mission has many scientific goals revolving around the study of the dark components of our Universe. Therein lies the aim of measuring the sum of the neutrino masses to a precision better than 0.03 eV (Laureijs et al., 2011). This measurement will be obtained through a joint analysis of galaxy clustering and weak gravitational lensing and therefore requires extensive knowledge of how neutrinos affect structure formation. With our current model of the Universe, this can be studied in detail with  $N$ -body simulations. In this paper, 17 simulations incorporating neutrinos were compared through the power spectrum, bispectrum, halo mass function, and halo bias for  $\sum m_\nu = 0.0 \text{ eV}$ , 0.15 eV, 0.3 eV, and 0.6 eV. The codes varied in structure, ranging from full  $N$ -body implementations to emulators. All in all, they showed good agreement, especially when studying the ratio between the massive and massless neutrino scenarios for the various observables, as this cancels out some of the internal code systematics.

This is the paper where **ANUBIS** made its debut (see Sect. 4.2.2). Overall, **ANUBIS** agreed well with the other codes in the comparison project, but suffered slightly from restricted resolution due to the neutrino implementation and limited computer resources. Because of the memory requirements of **RAMSES**, **ANUBIS** was run with a base-grid of 512. As mentioned in Paper II, no changes were made to the time-stepping algorithm in **RAMSES** when neutrinos were introduced, resulting in time-consuming calculations, but also a more detailed time-evolution of the dark matter particles in the simulations where neutrinos were included. This showed up as a slight excess in the power spectrum ratio between the massive and massless neutrino runs at large scales, and again at small scales where the AMR-scheme of **RAMSES** led to less refinement where neutrinos suppress structure formation. Still, convergence tests show that the issue of different refinement at small scales due to the neutrinos can be solved by a higher particle density.

In conclusion, this paper confirms that different implementations of massive neutrinos in the cosmological simulations included in the comparison perform similarly. It is left up to the reader to choose the code that best suits them when

modelling the impact of massive neutrinos on structure formation, depending on resources and desired output. In addition, this project served as an excellent testing ground for the **ANUBIS** code.

### Paper II

In this paper, the effects of massive neutrinos and  $f(R)$ -modified gravity were studied through void statistics (see Sect. 3.5). Cosmic voids are promising grounds for investigating both massive neutrinos and modified gravity due to their underdense nature. This means that the ratio of neutrinos to other species is high in these regions, and also that the screening mechanisms in play for modified gravities are not invoked, which should make it easier to study both of their signatures. We used simulations performed with **ANUBISIS** (see Sect. 4.2) to obtain void catalogues in the cases of a reference  $\Lambda$ CDM run with massless neutrinos, two massive neutrino runs ( $\sum m_\nu = 0.15 \text{ eV}$  and  $0.6 \text{ eV}$ ), one  $f(R)$ -modified gravity run ( $|f_{R0}| = 10^{-5}$ ), and two combined simulations with massive neutrinos and modified gravity. In each case, we calculated the void velocity profile and the void-halo cross-correlation function from the simulation data and compared them to theory. First, we did this by using the real space halo data available to us from the simulations. However, galaxy surveys can only observe in redshift space, and we therefore also carried out these calculations on the redshift data after applying a reconstruction method (Nadathur, Carter, and Percival, 2019) to put the redshift space information back into real space.

The purpose of this paper was to test the current void modelling framework in the presence of massive neutrinos and  $f(R)$ -modified gravity, which breaks the assumption of a scale-invariant growth rate going into the CCF and reconstruction models. In theory, this means that we expected the models to perform better in the  $\Lambda$ CDM scenario. Although we found higher velocities and velocity dispersions for the galaxies surrounding voids in the  $f(R)$  gravity case, and the opposite for massive neutrinos, the uncertainties connected to the velocity models and the fact that we had a sparse sample of tracers outweighed any possible differences in the model performance. In addition, the reconstruction process did not perform noticeably different for the various cosmologies. If anything, it performed slightly better in the massive neutrino scenario, possibly due to lower velocities adhering to the assumptions of linearity. We also performed Markov chain Monte Carlo (MCMC) fits for the cosmological parameter  $f\sigma_8$  and the Alcock-Paczyński parameter  $\epsilon$ , to see if the obtained values better matched the fiducial cosmology for the massless neutrino  $\Lambda$ CDM case. All in all, we did not find a better match between the models and the simulations for the massless neutrino  $\Lambda$ CDM case compared to massive neutrinos and  $f(R)$  gravity, even though voids are sensitive to their effects. This led us to conclude that more accurate modelling and simulations are needed in order to use the void-galaxy CCF to distinguish between the cosmological models. In addition, we also found that the void-galaxy CCF is yet another degenerate observable for massive neutrinos and  $f(R)$ -modified gravity at redshift zero.

### Paper III

In the final paper of this thesis work, we created a full pipeline, *Sesame*, for constructing a matter power spectrum boost emulator for beyond- $\Lambda$ CDM models, without the need for supercomputers. Emulators are great tools when we are interested in specific global clustering statistics, like the matter power spectrum, and are much faster and less resource-demanding than performing full cosmological simulations. However, to create the emulator, a large suite of simulations for various parameter choices is typically required in order to interpolate and achieve estimates for intermediate parameter values. Because of this, once an emulator is constructed for a chosen cosmological model, it is not straightforward to create a new emulator for a different model. To forego this issue, we created an emulator pipeline using the fast and approximate COLA method (Sect. 4.3.1) for the  $N$ -body simulation step. In this way, if we are interested in, for example, the matter power spectrum boost between a  $\Lambda$ CDM and beyond- $\Lambda$ CDM model, we can perform both the  $\Lambda$ CDM and beyond- $\Lambda$ CDM simulations efficiently. Focusing on the boost, as opposed to the full matter power spectrum, is convenient as some effects from the internal code structure cancel out (see e.g. Euclid Consortium et al., 2023), allowing us to reach precision at higher  $k$ -values. To extract the beyond- $\Lambda$ CDM matter power spectrum afterwards, we can utilise already existing highly-accurate  $\Lambda$ CDM emulators. In addition, the shape of the boost curve is easier to estimate using machine learning, compared to the full matter power spectrum. The next step in our emulator pipeline is thus to use the `PyTorch-Lightning` package (see Sect. 4.3.2) to give the boost value for various values of cosmological parameters, redshifts, and scales to a neural network. Here, the data is used to train the network, resulting in an emulator for the boost.

As an example demonstration of *Sesame*, we created emulators for the linear and non-linear boost of  $f(R)$ -modified gravity, including massive neutrinos. For our setup, we achieved below 1% accuracy between the simulated and emulated boost in the fully linear case, and around 2% agreement for the non-linear boost, using approximately 3000 CPU hours for the creation of each emulator. We provide the emulators and the full pipeline, *Sesame*, for the reader, opening up the opportunity for the user to create their own emulator by implementing their desired cosmology to the `COLASolver` and applying the pipeline.

## 5.2 Conclusions and outlook

It has been said by many, in different variations, that endings are often no more than beginnings in disguise. We have now arrived here, at what will be the final paragraphs of this thesis work - so where better to start the ending, than at the beginning?

I opened this thesis with an introduction to the standard model of cosmology and how perturbations in the early Universe grew into the intricate structures we observe today. This laid the groundwork for everything following, from how we can observe large-scale structure at the present time, to how we can simulate it

## 5. Summary and outlook

---

throughout time. In addition, a standard model of cosmology also opens up the possibility of a non-standard model of cosmology. This is a broad research field, and in this thesis, I cover only a small corner of it. My topics of interest have been massive neutrino particles and  $f(R)$ -modified gravity, and their impact on large-scale structure probes. Neutrinos, on one side, are a part of the  $\Lambda$ CDM model, and make up a small fraction of the dark matter content of the Universe. Their unique nature, changing from relativistic to non-relativistic, results in a suppression of structure formation on small scales.  $f(R)$ -modified gravity, on the other side, is what I above called a non-standard model of cosmology, where the GR framework is extended in such a way that the accelerated expansion of the Universe can be explained without dark energy. This results in an enhancement of structure growth, also on small scales, yielding several degenerate observables for massive neutrinos and  $f(R)$  gravity. Understanding and breaking this degeneracy has been the topic of several research papers in recent times (e.g. Baldi et al., 2014; Contarini et al., 2021; Giocoli, Baldi, and Moscardini, 2018; Wright et al., 2019), and some interesting avenues, like the void size function at high redshifts, weak lensing, and RSDs, have been found.

For this thesis work, I approached the above topic numerically. This resulted in the  $N$ -body code **ANUBISIS**, which includes both modified gravity and massive neutrinos, and the emulator pipeline, *Sesame*, which creates emulators for the matter power spectrum boost for beyond- $\Lambda$ CDM models compared to  $\Lambda$ CDM. These are both tools that can be used for further exploration of the degenerate effect of massive neutrinos and modified gravity on structure formation. The code **ANUBIS**, including the effect of massive neutrinos, was also part of a *Euclid* project, confirming that current simulations incorporate neutrinos accurately enough to model their impact at the sub-percent level. *Sesame*, the emulator pipeline, is perhaps the most general output to result from this thesis work, as it can be used by others to create emulators for global clustering statistics for a cosmological model of their choice. In addition to the creation and testing of these codes, which is covered in Papers I and III, I also spent a large portion of my time using **ANUBISIS** simulations to test the void modelling framework in the presence of massive neutrinos and  $f(R)$ -modified gravity, resulting in Paper II. Here, we found that we need a more accurate velocity modelling for the void velocity profile, along with a more precise reconstruction method and high-resolution simulations or observational data in order for the cosmological parameters extracted by void statistics to be accurate enough to pick up the effects of massive neutrinos and modified gravity. In addition, we found that the void-halo cross-correlation function is yet another degenerate observable, at least for redshift zero. A new investigation with simulations of increased resolution, and at higher redshifts, would therefore be of interest. This knowledge, along with **ANUBIS**, **ANUBISIS**, and *Sesame*, are the main takeaways from this thesis work.

Exciting times are now coming for cosmologists worldwide. With the recent launch of the *Euclid* satellite on the 1st of July this year, we are patiently awaiting new constraints on gravity and the dark sector of our Universe. Two of the main science goals of *Euclid* particularly concern this thesis work. First, we

have the goal of measuring the sum of the neutrino masses to a  $1\sigma$  precision better than  $0.03\text{ eV}$ , and secondly, we have the goal of measuring the rate of structure growth accurately enough to distinguish general relativity from several modified gravity theories (Laureijs et al., 2011). A reasonable question is then, with their known degeneracy, can we reach both of these goals to the desired accuracy? A recent paper by Euclid Collaboration et al., 2023 investigates the expected constraining power of the  $f_{R0}$  parameter in Hu-Sawicki  $f(R)$  gravity. They find that by combining probes, in an optimistic setting, *Euclid* should be able to constrain  $\log f_{R0}$  at the 1% level when using a fiducial value of  $|f_{R0}| = 5 \times 10^{-6}$  in the analysis. They also find that *Euclid* should be able to distinguish between models with  $|f_{R0}| = 5 \times 10^{-5}$ ,  $5 \times 10^{-6}$ , and  $5 \times 10^{-7}$  and  $\Lambda\text{CDM}$  at more than  $3\sigma$  in this optimistic scenario. The analysis includes a neutrino mass of  $\sum m_\nu = 0.06\text{ eV}$ , but does not allow it to vary, and thereby does not include the degeneracy between modified gravity and massive neutrinos. As mentioned in the paper, this might result in constraints that are tighter than they would be if  $\sum m_\nu$  was allowed to vary. How much tighter is not yet determined. Still, the Euclid observational data, with its gravitational lensing, galaxy clustering, high redshift observations, and complementary data like redshift space distortions, is very promising in regards to breaking the degeneracy between modified gravity and massive neutrinos. Accomplishing this would help us further constrain the total neutrino mass and modified gravity individually, but also allow us to better understand their interplay on cosmological probes throughout time and scale. This leaves us here, at the precipice, waiting for data that might further solidify the standard model of cosmology - or better yet, might not.





# Papers



Paper I

# **Euclid: Modelling massive neutrinos in cosmology – a code comparison**

***Euclid* Consortium, Julian Adamek, and Others**

Published in the Journal of Cosmology and Astroparticle Physics, JCAP06(2023)035.

DOI: 10.1088/1475-7516/2023/06/035.



PAPER • OPEN ACCESS

## *Euclid*: modelling massive neutrinos in cosmology — a code comparison

To cite this article: On behalf of Euclid consortium JCAP06(2023)035

View the [article online](#) for updates and enhancements.
















































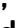
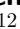
























You may also like

- [The AGORA High-resolution Galaxy Simulations Comparison Project. III. Cosmological Zoom-in Simulation of a Milky Way-mass Halo](#)  
Santi Roca-Fàbrega, Ji-hoon Kim, Loic Hausammann et al.
- [EBWeyl: a code to invariantly characterize numerical spacetimes](#)  
Robyn L. Munoz and Marco Bruni
- [Reconstructing the cosmological density and velocity fields from redshifted galaxy distributions using V-net](#)  
Fei Qin, David Parkinson, Sungwook E. Hong et al.

# *Euclid*: modelling massive neutrinos in cosmology — a code comparison



On behalf of Euclid consortium

J. Adamek <sup>1</sup>, R.E. Angulo <sup>2,3</sup>, C. Arnold,<sup>4</sup> M. Baldi <sup>5,6,7</sup>,  
M. Biagetti <sup>8,9,10,11</sup>, B. Bose <sup>12,13,1</sup>, C. Carbone,<sup>14</sup>  
T. Castro <sup>9,10,8</sup>, J. Dakin <sup>1,15</sup>, K. Dolag,<sup>16,17</sup> W. Elbers <sup>4</sup>,  
C. Fidler,<sup>18</sup> C. Giocoli <sup>6,19</sup>, S. Hannestad,<sup>15</sup> F. Hassani <sup>20</sup>,  
C. Hernández-Aguayo <sup>17</sup>, K. Koyama <sup>21</sup>, B. Li <sup>4</sup>,  
R. Mauland <sup>20</sup>, P. Monaco <sup>22,9,10,8</sup>, C. Moretti <sup>12,9</sup>,  
D.F. Mota,<sup>20</sup> C. Partmann,<sup>17</sup> G. Parimbelli <sup>23,9,11,8</sup>, D. Potter <sup>1</sup>,  
A. Schneider <sup>1</sup>, S. Schulz <sup>1</sup>, R.E. Smith <sup>24</sup>, V. Springel <sup>17</sup>,  
J. Stadel <sup>1</sup>, T. Tram <sup>15</sup>, M. Viel <sup>11,8,9,10</sup>,  
F. Villaescusa-Navarro <sup>25,26</sup>, H.A. Winther <sup>20</sup>, B.S. Wright <sup>27</sup>,  
M. Zennaro <sup>2</sup>, N. Aghanim,<sup>28</sup> L. Amendola,<sup>29</sup> N. Auricchio <sup>6</sup>,  
D. Bonino,<sup>30</sup> E. Branchini <sup>31,32</sup>, M. Brescia <sup>33,34</sup>,  
S. Camera <sup>35,36,30</sup>, V. Capobianco <sup>30</sup>, V.F. Cardone,<sup>37,38</sup>  
J. Carretero <sup>39,40</sup>, F.J. Castander,<sup>41,42</sup> M. Castellano <sup>37</sup>,  
S. Cavuoti <sup>34,43</sup>, A. Cimatti,<sup>44,45</sup> R. Cledassou <sup>46,47</sup>,  
G. Congedo <sup>12</sup>, L. Conversi <sup>48,49</sup>, Y. Copin <sup>50</sup>,  
A. Da Silva <sup>51,52</sup>, H. Degaudenzi <sup>53</sup>, M. Douspis,<sup>28</sup>  
F. Dubath <sup>53</sup>, C.A.J. Duncan,<sup>54,55</sup> X. Dupac,<sup>48</sup> S. Dusini <sup>56</sup>,  
S. Farrens <sup>57</sup>, S. Ferriol,<sup>50</sup> P. Fosalba <sup>42,41</sup>, M. Frailis <sup>9</sup>,  
E. Franceschi <sup>6</sup>, S. Galeotta <sup>9</sup>, B. Garilli <sup>14</sup>, W. Gillard <sup>58</sup>,  
B. Gillis <sup>12</sup>, A. Grazian <sup>59</sup>, S.V. Haugan <sup>20</sup>, W. Holmes,<sup>60</sup>  
A. Hornstrup <sup>61,62</sup>, K. Jahnke <sup>63</sup>, S. Kermiche <sup>58</sup>,  
A. Kiessling <sup>60</sup>, M. Kilbinger <sup>57</sup>, T. Kitching <sup>64</sup>, M. Kunz <sup>13</sup>,  
H. Kurki-Suonio <sup>65,66</sup>, P.B. Lilje <sup>20</sup>, I. Lloro,<sup>67</sup> O. Mansutti <sup>9</sup>,  
O. Marggraf <sup>68</sup>, F. Marulli,<sup>5,6,7</sup> R. Massey <sup>4</sup>, E. Medinaceli <sup>6</sup>,  
M. Meneghetti <sup>6,7</sup>, G. Meylan,<sup>69</sup> M. Moresco <sup>5,6</sup>,  
L. Moscardini <sup>5,6,7</sup>, E. Munari <sup>9</sup>, S.-M. Niemi,<sup>70</sup> C. Padilla <sup>39</sup>

JCAP06(2023)035

S. Paltani,<sup>53</sup> F. Pasian,<sup>9</sup> K. Pedersen,<sup>15</sup> W.J. Percival<sup>71,72,73</sup>  
 V. Pettorino,<sup>57</sup> G. Polenta<sup>74</sup>, M. Poncet,<sup>46</sup> L.A. Popa,<sup>75</sup>  
 F. Raison<sup>76</sup>, R. Rebolo,<sup>77,78</sup> A. Renzi<sup>79,56</sup>, J. Rhodes,<sup>60</sup>  
 G. Riccio,<sup>34</sup> E. Romelli<sup>9</sup>, M. Roncarelli,<sup>6</sup> R. Saglia<sup>16,76</sup>,  
 D. Sapone<sup>80</sup>, B. Sartoris,<sup>16,9</sup> P. Schneider<sup>68</sup>,  
 T. Schrabback<sup>68,81</sup>, A. Secroun<sup>58</sup>, G. Seidel<sup>63</sup>,  
 C. Sirignano<sup>79,56</sup>, G. Sirri<sup>7</sup>, L. Stanco<sup>56</sup>, J.-L. Starck,<sup>82</sup>  
 P. Tallada-Crespí,<sup>83,40</sup> A.N. Taylor,<sup>12</sup> I. Tereno,<sup>51,84</sup>  
 R. Toledo-Moreo<sup>85</sup>, F. Torradeflot<sup>83,40</sup>, I. Tutusaus<sup>86,13</sup>,  
 L. Valenziano<sup>6,7</sup>, T. Vassallo<sup>9</sup>, Y. Wang<sup>87</sup>, J. Weller<sup>16,76</sup>,  
 A. Zacchei<sup>9,8</sup>, G. Zamorani<sup>6</sup>, J. Zoubian,<sup>58</sup> G. Fabbian<sup>25,88</sup>  
 and V. Scottez<sup>89,90</sup>

<sup>1</sup>Institute for Computational Science, Universität Zürich,  
 Winterthurerstrasse 190, 8057 Zürich, Switzerland

<sup>2</sup>Donostia International Physics Center (DIPC),

Paseo Manuel de Lardizabal 4, 20018 Donostia-San Sebastián, Guipuzkoa, Spain

<sup>3</sup>IKERBASQUE, Basque Foundation for Science, 48013 Bilbao, Spain

<sup>4</sup>Department of Physics, Institute for Computational Cosmology, Durham University,  
 South Road, Durham DH1 3LE, U.K.

<sup>5</sup>Dipartimento di Fisica e Astronomia “Augusto Righi” — Alma Mater Studiorum Università  
 di Bologna, via Piero Gobetti 93/2, 40129 Bologna, Italy

<sup>6</sup>INAF-Osservatorio di Astrofisica e Scienza dello Spazio di Bologna,  
 Via Piero Gobetti 93/3, 40129 Bologna, Italy

<sup>7</sup>INFN-Sezione di Bologna, Viale Berti Pichat 6/2, 40127 Bologna, Italy

<sup>8</sup>IFPU, Institute for Fundamental Physics of the Universe, via Beirut 2, 34151 Trieste, Italy

<sup>9</sup>INAF-Osservatorio Astronomico di Trieste, Via G. B. Tiepolo 11, 34143 Trieste, Italy

<sup>10</sup>INFN, Sezione di Trieste, Via Valerio 2, 34127 Trieste, Italy

<sup>11</sup>SISSA, International School for Advanced Studies, Via Bonomea 265, 34136 Trieste, Italy

<sup>12</sup>Institute for Astronomy, University of Edinburgh, Royal Observatory,  
 Blackford Hill, Edinburgh EH9 3HJ, U.K.

<sup>13</sup>Université de Genève, Département de Physique Théorique  
 and Centre for Astroparticle Physics, 24 quai Ernest-Ansermet, 1211 Genève 4, Switzerland

<sup>14</sup>INAF-IASF Milano, Via Alfonso Corti 12, 20133 Milano, Italy

<sup>15</sup>Department of Physics and Astronomy, University of Aarhus,  
 Ny Munkegade 120, 8000 Aarhus C, Denmark

<sup>16</sup>Universitäts-Sternwarte München, Fakultät für Physik,  
 Ludwig-Maximilians-Universität München, Scheinerstrasse 1, 81679 München, Germany

<sup>17</sup>Max-Planck-Institut für Astrophysik, Karl-Schwarzschild Str. 1, 85741 Garching, Germany

<sup>18</sup>Institute for Theoretical Particle Physics and Cosmology (TTK), RWTH Aachen University,  
 52056 Aachen, Germany

<sup>19</sup>Istituto Nazionale di Fisica Nucleare, Sezione di Bologna,  
 Via Irnerio 46, 40126 Bologna, Italy

- <sup>20</sup>Institute of Theoretical Astrophysics, University of Oslo,  
P.O. Box 1029 Blindern, 0315 Oslo, Norway
- <sup>21</sup>Institute of Cosmology and Gravitation, University of Portsmouth,  
Portsmouth PO1 3FX, U.K.
- <sup>22</sup>Dipartimento di Fisica — Sezione di Astronomia, Università di Trieste,  
Via Tiepolo 11, 34131 Trieste, Italy
- <sup>23</sup>Dipartimento di Fisica, Università degli studi di Genova, and INFN-Sezione di Genova,  
via Dodecaneso 33, 16146 Genova, Italy
- <sup>24</sup>Department of Physics & Astronomy, University of Sussex, Brighton BN1 9QH, U.K.
- <sup>25</sup>Center for Computational Astrophysics, Flatiron Institute,  
162 5th Avenue, New York, NY 10010, U.S.A.
- <sup>26</sup>Department of Astrophysical Sciences, Peyton Hall, Princeton University,  
Princeton, NJ 08544, U.S.A.
- <sup>27</sup>School of Physics and Astronomy, Queen Mary University of London,  
Mile End Road, London E1 4NS, U.K.
- <sup>28</sup>Université Paris-Saclay, CNRS, Institut d’astrophysique spatiale, 91405 Orsay, France
- <sup>29</sup>Institut für Theoretische Physik, University of Heidelberg,  
Philosophenweg 16, 69120 Heidelberg, Germany
- <sup>30</sup>INAF-Osservatorio Astrofisico di Torino, Via Osservatorio 20, 10025 Pino Torinese, Italy
- <sup>31</sup>Dipartimento di Fisica, Università di Genova, Via Dodecaneso 33, 16146 Genova, Italy
- <sup>32</sup>INFN-Sezione di Roma Tre, Via della Vasca Navale 84, 00146 Roma, Italy
- <sup>33</sup>Department of Physics “E. Pancini”, University Federico II,  
Via Cinthia 6, 80126 Napoli, Italy
- <sup>34</sup>INAF-Osservatorio Astronomico di Capodimonte, Via Moiariello 16, 80131 Napoli, Italy
- <sup>35</sup>Dipartimento di Fisica, Università degli Studi di Torino,  
Via P. Giuria 1, 10125 Torino, Italy
- <sup>36</sup>INFN-Sezione di Torino, Via P. Giuria 1, 10125 Torino, Italy
- <sup>37</sup>INAF-Osservatorio Astronomico di Roma,  
Via Frascati 33, 00078 Monteporzio Catone, Italy
- <sup>38</sup>INFN-Sezione di Roma, Piazzale Aldo Moro, 2 — c/o Dipartimento di Fisica,  
Edificio G. Marconi, 00185 Roma, Italy
- <sup>39</sup>Institut de Física d’Altes Energies (IFAE), The Barcelona Institute of Science  
and Technology, Campus UAB, 08193 Bellaterra (Barcelona), Spain
- <sup>40</sup>Port d’Informació Científica, Campus UAB,  
C. Albareda s/n, 08193 Bellaterra (Barcelona), Spain
- <sup>41</sup>Institut d’Estudis Espacials de Catalunya (IEEC),  
Carrer Gran Capitá 2-4, 08034 Barcelona, Spain
- <sup>42</sup>Institute of Space Sciences (ICE, CSIC), Campus UAB, Carrer de Can Magrans, s/n, 08193  
Barcelona, Spain
- <sup>43</sup>INFN section of Naples, Via Cinthia 6, 80126 Napoli, Italy
- <sup>44</sup>Dipartimento di Fisica e Astronomia “Augusto Righi” — Alma Mater Studiorum Università  
di Bologna, Viale Berti Pichat 6/2, 40127 Bologna, Italy
- <sup>45</sup>INAF-Osservatorio Astrofisico di Arcetri, Largo E. Fermi 5, 50125 Firenze, Italy
- <sup>46</sup>Centre National d’Etudes Spatiales, Toulouse, France



- <sup>47</sup>Institut national de physique nucléaire et de physique des particules,  
3 rue Michel-Ange, 75794 Paris CEDEX 16, France
- <sup>48</sup>ESAC/ESA, Camino Bajo del Castillo, s/n., Urb. Villafranca del Castillo,  
28692 Villanueva de la Cañada, Madrid, Spain
- <sup>49</sup>European Space Agency/ESRIN, Largo Galileo Galilei 1, 00044 Frascati, Roma, Italy
- <sup>50</sup>Université Lyon, Université Claude Bernard Lyon 1, CNRS/IN2P3, IP2I Lyon,  
UMR 5822, 69622 Villeurbanne, France
- <sup>51</sup>Departamento de Física, Faculdade de Ciências, Universidade de Lisboa,  
Edifício C8, Campo Grande, 1749-016 Lisboa, Portugal
- <sup>52</sup>Instituto de Astrofísica e Ciências do Espaço, Faculdade de Ciências,  
Universidade de Lisboa, Campo Grande, 1749-016 Lisboa, Portugal
- <sup>53</sup>Department of Astronomy, University of Geneva, ch. d'Ecogia 16, 1290 Versoix, Switzerland
- <sup>54</sup>Department of Physics, Oxford University, Keble Road, Oxford OX1 3RH, U.K.
- <sup>55</sup>Jodrell Bank Centre for Astrophysics, Department of Physics and Astronomy,  
University of Manchester, Oxford Road, Manchester M13 9PL, U.K.
- <sup>56</sup>INFN-Padova, Via Marzolo 8, 35131 Padova, Italy
- <sup>57</sup>Université Paris-Saclay, Université Paris Cité, CEA, CNRS, Astrophysique,  
Instrumentation et Modélisation Paris-Saclay, 91191 Gif-sur-Yvette, France
- <sup>58</sup>Aix-Marseille Université, CNRS/IN2P3, CPPM, Marseille, France
- <sup>59</sup>INAF-Osservatorio Astronomico di Padova, Via dell'Osservatorio 5, 35122 Padova, Italy
- <sup>60</sup>Jet Propulsion Laboratory, California Institute of Technology,  
4800 Oak Grove Drive, Pasadena, CA 91109, U.S.A.
- <sup>61</sup>Technical University of Denmark, Elektrovej 327, 2800 Kgs. Lyngby, Denmark
- <sup>62</sup>Cosmic Dawn Center (DAWN), Denmark
- <sup>63</sup>Max-Planck-Institut für Astronomie, Königstuhl 17, 69117 Heidelberg, Germany
- <sup>64</sup>Mullard Space Science Laboratory, University College London,  
Holmbury St Mary, Dorking, Surrey RH5 6NT, U.K.
- <sup>65</sup>Department of Physics, P.O. Box 64, 00014 University of Helsinki, Finland
- <sup>66</sup>Helsinki Institute of Physics, Gustaf Hällströmin katu 2, University of Helsinki,  
Helsinki, Finland
- <sup>67</sup>NOVA optical infrared instrumentation group at ASTRON,  
Oude Hoogeveensedijk 4, 7991PD, Dwingeloo, The Netherlands
- <sup>68</sup>Argelander-Institut für Astronomie, Universität Bonn,  
Auf dem Hügel 71, 53121 Bonn, Germany
- <sup>69</sup>Institute of Physics, Laboratory of Astrophysics, Ecole Polytechnique Fédérale de Lausanne  
(EPFL), Observatoire de Sauverny, 1290 Versoix, Switzerland
- <sup>70</sup>European Space Agency/ESTEC, Keplerlaan 1, 2201 AZ Noordwijk, The Netherlands
- <sup>71</sup>Centre for Astrophysics, University of Waterloo, Waterloo, Ontario N2L 3G1, Canada
- <sup>72</sup>Department of Physics and Astronomy, University of Waterloo,  
Waterloo, Ontario N2L 3G1, Canada
- <sup>73</sup>Perimeter Institute for Theoretical Physics, Waterloo, Ontario N2L 2Y5, Canada
- <sup>74</sup>Space Science Data Center, Italian Space Agency,  
via del Politecnico snc, 00133 Roma, Italy
- <sup>75</sup>Institute of Space Science, Bucharest 077125, Romania

- <sup>76</sup>Max Planck Institute for Extraterrestrial Physics,  
Giessenbachstr. 1, 85748 Garching, Germany
- <sup>77</sup>Instituto de Astrofísica de Canarias,  
Calle Vía Láctea s/n, 38204 San Cristóbal de La Laguna, Tenerife, Spain
- <sup>78</sup>Departamento de Astrofísica, Universidad de La Laguna, 38206 La Laguna, Tenerife, Spain
- <sup>79</sup>Dipartimento di Fisica e Astronomia “G. Galilei”, Università di Padova,  
Via Marzolo 8, 35131 Padova, Italy
- <sup>80</sup>Departamento de Física, FCFM, Universidad de Chile,  
Blanco Encalada 2008, Santiago, Chile
- <sup>81</sup>Institut für Astro- und Teilchenphysik, Universität Innsbruck,  
Technikerstr. 25/8, 6020 Innsbruck, Austria
- <sup>82</sup>AIM, CEA, CNRS, Université Paris-Saclay, Université de Paris,  
91191 Gif-sur-Yvette, France
- <sup>83</sup>Centro de Investigaciones Energéticas, Medioambientales y Tecnológicas (CIEMAT),  
Avenida Complutense 40, 28040 Madrid, Spain
- <sup>84</sup>Instituto de Astrofísica e Ciências do Espaço, Faculdade de Ciências,  
Universidade de Lisboa, Tapada da Ajuda, 1349-018 Lisboa, Portugal
- <sup>85</sup>Universidad Politécnica de Cartagena, Departamento de Electrónica y Tecnología  
de Computadoras, 30202 Cartagena, Spain
- <sup>86</sup>Institut de Recherche en Astrophysique et Planétologie (IRAP), Université de Toulouse,  
CNRS, UPS, CNES, 14 Av. Edouard Belin, 31400 Toulouse, France
- <sup>87</sup>Infrared Processing and Analysis Center, California Institute of Technology,  
Pasadena, CA 91125, U.S.A.
- <sup>88</sup>School of Physics and Astronomy, Cardiff University, The Parade, Cardiff CF24 3AA, U.K.
- <sup>89</sup>Institut d’Astrophysique de Paris, 98bis Boulevard Arago, 75014 Paris, France
- <sup>90</sup>Junia, EPA department, 59000 Lille, France

E-mail: [julian.adamek@uzh.ch](mailto:julian.adamek@uzh.ch)

Received November 23, 2022

Accepted April 27, 2023

Published June 16, 2023

**Abstract.** The measurement of the absolute neutrino mass scale from cosmological large-scale clustering data is one of the key science goals of the *Euclid* mission. Such a measurement relies on precise modelling of the impact of neutrinos on structure formation, which can be studied with  $N$ -body simulations. Here we present the results from a major code comparison effort to establish the maturity and reliability of numerical methods for treating massive neutrinos. The comparison includes eleven full  $N$ -body implementations (not all of them independent), two  $N$ -body schemes with approximate time integration, and four additional codes that directly predict or emulate the matter power spectrum. Using a common set of initial data we quantify the relative agreement on the nonlinear power spectrum of cold dark matter and baryons and, for the  $N$ -body codes, also the relative agreement on the bispectrum, halo mass function, and halo bias. We find that the different numerical implementations produce fully consistent results. We can therefore be confident that we can model the impact of massive neutrinos at the sub-percent level in the most common summary statistics. We also provide a code validation pipeline for future reference.

**Keywords:** cosmological neutrinos, cosmological simulations, neutrino masses from cosmology, power spectrum

**ArXiv ePrint:** [2211.12457](https://arxiv.org/abs/2211.12457)

---

## Contents

<b>1</b>	<b>Introduction</b>	<b>1</b>
<b>2</b>	<b>Neutrino physics</b>	<b>3</b>
<b>3</b>	<b>Numerical methods</b>	<b>4</b>
3.1	Particle-based methods	4
3.2	Mesh-based methods	6
3.3	Approximations and other methods	7
3.3.1	COLA	8
3.3.2	PINOCCHIO	8
3.3.3	Newtonian motion gauge	10
3.4	Halo-model reaction	10
3.5	Power-spectrum emulation	12
<b>4</b>	<b>Simulations</b>	<b>13</b>
4.1	Initial conditions	14
4.2	Post-processing pipeline	15
4.2.1	Power spectra	15
4.2.2	Bispectra	16
4.2.3	Halo catalogues	16
<b>5</b>	<b>Results</b>	<b>17</b>
5.1	Power spectra	17
5.1.1	CDM and baryons	17
5.1.2	Convergence tests	21
5.1.3	Contributions from neutrinos	22
5.1.4	Total matter	23
5.2	Bispectra	23
5.3	Halo mass function	29
5.4	Halo bias	31
<b>6</b>	<b>Discussion</b>	<b>34</b>

---

## 1 Introduction

The upcoming *Euclid* mission [1] will provide very detailed observations of the large-scale structure of our Universe, making it possible to probe physics related to dark energy and neutrinos at an unprecedented level of precision. The analysis and interpretation of these data require a very accurate modelling of the process of structure formation. This is of particular relevance since a precise modelling of the mass-dependent effect neutrinos have on various summary statistics will allow a cosmological measurement of the absolute neutrino mass scale, which is one of the key science objectives of *Euclid*.

Here we focus on the treatment of massive neutrinos in cosmological  $N$ -body simulations and investigate the convergence of a number of different codes over a variety of different scales

and redshifts. Oscillation experiments have established a firm lower bound on the sum of neutrino masses of around 0.06 eV. Using the well-known relation between neutrino mass and cosmological energy density,  $\sum m_\nu \approx \Omega_\nu h^2 \times 94 \text{ eV}$ , this lower bound on the sum of neutrino masses corresponds to a lower bound of  $\Omega_\nu h^2 > 6 \times 10^{-4}$ , or approximately 0.5% of the total matter density. As usual, the cosmological density of any component X can be given in terms of  $\Omega_X$ , which is its present-day energy density in units of the critical density, and physical density parameters are then denoted as  $\omega_X = \Omega_X h^2$ , where  $h$  is the reduced Hubble parameter.

The sum of the neutrino masses is already constrained using information from the cosmic microwave background (CMB) combined with observations of large-scale structure like baryon acoustic oscillations [2], redshift-space distortions [3], and the Lyman- $\alpha$  forest [4]. While currently providing only upper bounds, these constraints are expected to improve significantly with upcoming surveys like *Euclid* which will be able to measure the neutrino mass fraction even if it is close to the lower bound. The matter power spectrum is still affected at the level of 4% in this scenario, which is well within the sensitivity of the *Euclid* main probes.

For instance, the weak-lensing signal probed by *Euclid* is sensitive to the matter power spectrum up to  $k \approx 7 h \text{ Mpc}^{-1}$  [5]. A linear model would be completely inadequate at such short scales and we therefore need robust nonlinear models. The forecast for galaxy clustering in *Euclid* typically assumes that the matter power spectrum and the galaxy bias is well understood at least up to  $k \approx 0.3 h \text{ Mpc}^{-1}$  which also requires some nonlinear prescription [6]. Many codes considered here are used in *Euclid* preparation papers and reference simulations. For instance, PKDGRAV3 ran *Euclid*'s flagship simulations and the simulations used by Knabenhans et al. [7, 8] to train the *EuclidEmulator2*; openGADGET3 was used to calibrate the halo mass function for the *Euclid* cluster abundance analysis by Castro et al. [9], and PINOCCHIO was used to create the synthetic catalogues for the validation of the covariance matrix of cluster abundance and the clustering of clusters by Fumagalli et al. [10, 11]. Our objective is therefore to establish a reliable calibration baseline for the measurement of the neutrino mass scale within the cosmological analysis of *Euclid* data. We expect that our results are also relevant in the context of other so-called “stage IV surveys” like the *Vera C. Rubin Observatory* or the *Nancy Grace Roman Space Telescope*.

Over the past decade, a variety of different methods have been employed to incorporate massive neutrinos in  $N$ -body simulations [12]. As discussed in more detail later, they broadly fall into two categories which we may refer to as “particle based” and “mesh based,” respectively. They follow different philosophies of keeping track of the evolving neutrino phase-space distribution function. Particle-based methods sample the six-dimensional phase-space directly, see e.g. refs. [13–22]. Mesh-based methods, on the other hand, work under the approximation that neutrino perturbations remain small and can be treated with perturbation theory [23–26]. In the simplest case that is sufficient for low neutrino masses one works with a linear realisation of the neutrino density field on a grid [23]. The linear theory for neutrinos may also be solved using the full nonlinear gravitational potential calculated in the simulation [24–26]. A different approach is to treat the massive neutrinos as a fluid and then solve the corresponding fluid equations, employing some approximation scheme to close the set of equations [27]. One can also attempt to integrate the Vlasov-Poisson equations on a six-dimensional phase-space grid [28].

Generally speaking, the mesh-based schemes work best for relatively small neutrino masses where neutrino perturbations remain linear or quasi-linear at all times. There are also hybrid schemes that use elements from both approaches. For instance, one may use a linear mesh-based representation at early times which is then converted to a particle representation

at late time [29, 30]. The so-called “ $\delta f$  method” introduced in Elbers et al. [31] is another hybrid approach that uses a particle ensemble to estimate perturbations  $\delta f$  to the smooth background phase-space distribution function  $f$ . Finally, a coordinate (gauge) transformation can be used to include linear neutrino perturbations without modifications to the  $N$ -body simulation code [32]. Cosmology-rescaling algorithms that are applied in post-processing have been shown to provide accurate results as well [33]. In this work, we aim to compare these different numerical approaches by employing them to run cosmological  $N$ -body simulations starting from the same initial conditions, and comparing the properties of the resulting matter and halo distributions using a controlled post-processing pipeline.

This paper is structured as follows. We begin with a brief review of neutrino physics and its impact on cosmology in section 2. In section 3, we describe the numerical methods that can be used to account for the cosmological effects of neutrinos. Our simulations are described in section 4 and in section 5 we present our numerical results. We conclude with a discussion in section 6.

## 2 Neutrino physics

From oscillation experiments it is firmly established that at least two of the standard-model neutrino mass states have non-zero mass, but the absolute mass scale is unknown and two mass orderings remain possible: normal and inverted. The current best-fit values for the mass-square differences measured in oscillation experiments are given by [34]

$$\Delta m_{21}^2 = 7.42_{-0.20}^{+0.21} \times 10^{-5} \text{ eV}^2, \quad (2.1)$$

$$\Delta m_{31}^2 = 2.517_{-0.028}^{+0.026} \times 10^{-3} \text{ eV}^2 \quad (\text{NO}), \quad (2.2)$$

$$\Delta m_{32}^2 = -2.498_{-0.028}^{+0.028} \times 10^{-3} \text{ eV}^2 \quad (\text{IO}), \quad (2.3)$$

where “NO” denotes the normal mass ordering and “IO” the inverted one. This leads to lower bounds on the sum of neutrino masses of  $\sum m_\nu \gtrsim 0.06 \text{ eV}$  (NO) and  $\sum m_\nu \gtrsim 0.1 \text{ eV}$  (IO), respectively. The best current experimental upper bound on the neutrino masses comes from the *KATRIN* experiment, which measures an incoherent sum of mass states using beta decay of tritium [35, 36]. This bound approximately translates to  $\sum m_\nu \lesssim 2.4 \text{ eV}$ .

However, cosmology already provides much more stringent bounds, typically around  $\sum m_\nu \lesssim 0.1 - 0.2 \text{ eV}$ . Assuming a minimal  $\Lambda$ CDM cosmology with massive neutrinos, a joint analysis of cosmological probes currently obtains  $\sum m_\nu < 0.09 \text{ eV}$  at 95% confidence, already putting pressure on the inverted mass ordering scenario [37]. These constraints are based on several physical effects affecting the CMB and large-scale structure in different ways, see Archidiacono et al. [38] for a review. Some of the effects are simply related to the change in the expansion history, others to the explicit coupling of neutrinos to cosmological perturbations. More specifically, massive neutrinos modify the shape of the matter power spectrum both in the linear and the nonlinear regimes. First, as neutrinos behave like radiation in the early Universe, they move the radiation-matter equality to slightly later times, therefore shifting the peak of the power spectrum towards smaller wavenumbers. Second, after the non-relativistic transition, they slow down the linear growth of perturbations at scales smaller than the free-streaming length, leading to a scale-dependent growth rate. The small-scale suppression in the linear power spectra of cold dark matter (CDM) and baryons,  $P_{\text{cb}}$ , or total matter (which includes massive neutrinos),  $P_{\text{m}}$ , with respect to a model with massless

neutrinos, can be quantified as [18, 39, 40]

$$\frac{\Delta P_{\text{cb}}}{P_{\text{cb}}} \approx 6 f_\nu, \quad \frac{\Delta P_{\text{m}}}{P_{\text{m}}} \approx 8 f_\nu, \quad (2.4)$$

respectively, where  $f_\nu = \Omega_\nu/\Omega_{\text{m}}$  is the neutrino mass fraction. In the nonlinear regime, this suppression is even more prominent and exhibits a dip at  $k \approx 1 \text{ h Mpc}^{-1}$  for low redshift, giving rise to the well-known “spoon-like” feature [41]. In the context of the halo model, this feature appears at the transition region of the two-halo and the one-halo terms. In particular, the dip is caused by the small-scale suppression of two-halo clustering that is induced by free-streaming, while the subsequent rise reflects the fact that the number of the most massive halos is rather independent of the neutrino masses. All these effects can be accurately predicted by modelling the neutrino component in cosmological  $N$ -body simulations. Assessing the relative accuracy and convergence of such modelling over a range of different numerical methods and simulation codes is the main goal of this paper.

### 3 Numerical methods

In this section, we give an overview of the various methods that have been developed for the treatment of massive neutrinos in  $N$ -body simulations and other numerical models. The most accurate results are expected when the local density of neutrinos in configuration space is accounted for within a simulation itself. This is technically challenging because of the large phase-space volume that is populated by neutrino particles. The methods to deal with this broadly fall into two categories that shall be discussed in turn: particle-based and mesh-based. Hybrid methods that use concepts from both categories have also been developed. Apart from full  $N$ -body simulations that may try to incorporate (as much as possible) the neutrino physics, there also exist approximate methods to generate realisations of large-scale structure. These can be augmented with recipes to account for the effect of massive neutrinos. Finally, if one is only interested in summary statistics like the power spectrum, emulators are a powerful tool that can be calibrated to include the sum of the neutrino masses as a free parameter. An overview of the various numerical codes employed in this work is given in table 1.

#### 3.1 Particle-based methods

Conceptually, the most straightforward method of accounting for cosmic neutrinos in a simulation is to represent them by a separate  $N$ -body ensemble. However, this method faces several challenges that need to be addressed carefully.

The first challenge is posed by the aforementioned phase-space volume that needs to be sampled. The phase-space distribution of neutrino particles typically has a very large velocity dispersion that is orders of magnitude larger than the bulk velocity. Therefore, representing the neutrinos with a small number of  $N$ -body particles that simply track the bulk velocities, which is essentially the method of choice for CDM or baryons, would completely miss the fact that most neutrinos are unbound and easily free stream out of gravity wells. Thus, the common practice is to sample the  $N$ -body particles from the true phase-space distribution, effectively performing a Monte-Carlo integration of the evolution equations. The main drawback of this method is that a poor sampling usually introduces significant shot noise, while high sampling rates quickly become very expensive as both the memory requirement and computations become completely dominated by the neutrino particle load. This is undesirable since neutrinos are just a tiny fraction of the matter after all.

Code	type	neutrino method(s)	reference(s)
GADGET-3	$N$ -body (Tree-PM)	particle	[42, 43]
L-GADGET3	$N$ -body (Tree-PM)	mesh	[43–45]
openGADGET3	$N$ -body (Tree-PM)	particle	[46, 47]
GADGET-4	$N$ -body (Tree-PM)	particle	[48]
NM-GADGET4	$N$ -body (Tree-PM)	Newtonian motion gauge	[32, 49]
AREPO	$N$ -body (Tree-PM)	particle	[50, 51]
CONCEPT	$N$ -body (P <sup>3</sup> M)	mesh	[27, 52]
PKDGRAV3	$N$ -body (Tree + FMM)	mesh	[53]
SWIFT	$N$ -body (PM + FMM)	particle / $\delta f$	[31, 54, 55]
ANUBIS	$N$ -body (PM + AMR)	particle	[56, 57]
gevolution	$N$ -body (uniform PM)	particle / mesh	[20, 58, 59]
COLA	$N$ -body surrogate	mesh	[60, 61]
PINOCCHIO	$N$ -body surrogate	linear growth factor	[62, 63]
ReACT	$P(k)$ prediction	halo-model reaction	[64, 65]
BACCOemulator	$P(k)$ prediction	emulation	[45]
EuclidEmulator2	$P(k)$ prediction	emulation	[8]
Cosmic Emu	$P(k)$ prediction	emulation	[66, 67]

**Table 1.** Overview of the numerical codes employed in this code comparison.  $N$ -body codes typically use a particle-mesh (PM) method coupled to some scheme to increase the force resolution in high-density regions. Methods featured here include Tree-PM, adaptive mesh refinement (AMR), fast multipole method (FMM), particle-particle/particle-mesh (P<sup>3</sup>M), and moving mesh. No adaptive force computation is used in *gevolution*, COLA, and PINOCCHIO, which all work with a uniform mesh.

Shot noise affects all moments of the distribution function, and in particular the density. This means that shot noise will also propagate into the gravitational field computed from the neutrino perturbations. While this could in principle severely degrade the accuracy of the gravitational evolution as a whole, the impact is actually mitigated by the fact that neutrinos only account for a very small fraction of the total matter, and the gravitational fields are therefore dominated by cold species. Nevertheless, some shot noise does propagate into the other matter species, particularly on large scales where the contribution of neutrino perturbations is largest. Various strategies have been developed to reduce the impact of shot noise, e.g. by filtering small-scale fluctuations. One effective strategy is to implement a statistical weighting of the neutrino particles, as is done in the  $\delta f$  method [31]. This method works by decomposing the distribution function  $f$  into an analytical background component  $\bar{f}$  and a perturbation  $\delta f$  computed from the particle ensemble. The weights are given at each time step by requiring phase-space density conservation. These weights are typically negligible, except for particles that are significantly perturbed, such as those captured by halos. Shot noise is thereby minimised as particles only contribute to the gravitational potential when needed. The  $\delta f$  method has been implemented in a number of codes, but is only used by SWIFT in this comparison (see table 1). Other strategies aimed at reducing shot noise while still using particles include alternate sampling of neutrino momenta [21] and various hybrid methods [29, 30, 68].



The second challenge pertains to the kinematics of neutrino  $N$ -body particles. If one were to apply a similar time-stepping criterion as for cold matter species, the high velocities would typically result in extremely small integration time steps, making the simulations considerably more expensive. This is often solved by relaxing the time-stepping criterion and allowing the neutrino particles to travel a larger distance in each integration step than what would be considered “safe” for cold species. High-velocity neutrino particles then respond poorly to small-scale fluctuations in the gravitational forces. Given that the neutrino distribution at small scales is plagued by the shot-noise problem anyway, this additional problem is often considered to be of little concern.

Still regarding kinematics, further issues arise due to the relativistic nature of neutrinos. In the weak-field limit, the propagation of a collisionless massive particle is governed by the Hamiltonian equations of motion [69]

$$\mathbf{v} = \frac{\mathbf{p}c}{\sqrt{\mathbf{p}^2 + m^2c^2a^2}}, \quad (3.1)$$

$$\mathbf{p}' = -\frac{2\mathbf{p}^2 + m^2c^2a^2}{c\sqrt{\mathbf{p}^2 + m^2c^2a^2}}\nabla\Psi, \quad (3.2)$$

where  $\mathbf{v}$  is the peculiar velocity,  $\mathbf{p}$  is the canonical momentum,  $m$  is the particle’s rest-mass,  $a$  is the scale factor, and  $\Psi$  is the gravitational potential, assuming as usual that gravitational slip can be neglected, i.e. that non-relativistic and ultra-relativistic particles essentially see the same potential. Here, a prime denotes the derivative with respect to conformal time and  $c$  denotes the speed of light. The canonical momentum is conserved in the absence of a gravitational force. For non-relativistic particles one usually considers the limit  $\mathbf{p}^2 \ll m^2c^2a^2$  in which the equations simplify to

$$\mathbf{v} = \frac{\mathbf{p}}{ma}, \quad (3.3)$$

$$\mathbf{p}' = -ma\nabla\Psi. \quad (3.4)$$

This simpler set of equations has the advantage that it is easy to find integration methods that are symplectic, i.e. that preserve the phase-space volume exactly as demanded by Hamiltonian time evolution. Note also that, in the absence of a gravitational force, the peculiar velocity scales exactly as  $\propto a^{-1}$  in this case.

Even though the evolution of high-momentum particles suffers from severe errors, including the breakdown of causality for  $\mathbf{p}^2 > m^2c^2a^2$ , some implementations might still use the simplified equations. The propagation of these errors into the clustering amplitude of matter is limited by the fact that high-momentum particles barely contribute to clustering in the first place. However, using the more accurate eqs. (3.1) and (3.2) is a more common choice. The issue of symplectic time integration in this case is discussed e.g. in appendix A of Adamek et al. [20] and appendix D of Elbers et al. [31].

### 3.2 Mesh-based methods

The main alternative to particle-based methods is to represent the distribution function on a spatial mesh. Yoshikawa et al. [28] discretise the distribution function on a six-dimensional mesh in phase-space, however, a brute-force approach like this is rather expensive and cannot easily be applied to very large simulations where memory requirements are a particular concern. A possible way out is to take moments of the distribution function (density, bulk velocity, and so on) where the momentum coordinates are integrated out so that a discretisation in the three spatial dimensions is sufficient.

Experience from solving the hierarchy of moments (the so-called Boltzmann hierarchy) in linear perturbation theory shows that a considerable number of moments must be taken into account in order to reach good accuracy for the evolution of the lowest moments. This concerns in particular the density that also affects the clustering of other matter components through gravitational coupling. On the other hand, the numerical solutions are readily available in the linear regime where they can be expressed in terms of linear transfer functions. Throughout this paper, we follow the convention from standard linear cosmological perturbation theory where the transfer function  $T_X$  of any perturbation variable  $X$  in Fourier space is defined through the relation

$$X(\mathbf{k}, z) = T_X(k, z)\zeta(\mathbf{k}), \quad (3.5)$$

where  $\zeta(\mathbf{k})$  is the comoving curvature perturbation of the mode  $\mathbf{k}$  before it enters the horizon. Those transfer functions provide a deterministic factor by which any given initial random perturbation mode needs to be multiplied in order to obtain, for instance, the density perturbation at any given time. Using these transfer functions that can be calculated at the outset, a simulation code can therefore construct the linear density field of neutrinos at any point in time for any given realisation of the random initial conditions. This is precisely what basic mesh-based methods do: they use the density field of neutrinos extrapolated from linear perturbation theory, which is often a reasonable approximation because neutrinos do not cluster strongly. The method is free of shot noise and is by construction exact in the limit of linear perturbations. However, it obviously lacks any response to nonlinear gravitational potentials that develop in a simulation.

While the linear method produces results that are sufficiently accurate for many purposes, some more advanced approaches have been developed in attempts to address the shortcomings. Ali-Haïmoud & Bird [24] solve for the transfer function of the neutrino perturbations using the nonlinear matter power spectrum of the simulation to construct an effective source term, assuming that the phase correlation between neutrino and matter perturbations remain largely intact even at nonlinear scales. Dakin et al. [27] employ the coupled evolution equations for the lowest moments in their nonlinear form. Then, to avoid having to calculate a large Boltzmann hierarchy for every wavevector represented in the simulation, the hierarchy is truncated by assuming that a “scaling” holds approximately for ratios of higher moments, where the scaling coefficients are taken from linear theory. This approximation is then used to close the system of equations using only a small number of nonlinear moments. By construction this method agrees with the simpler method in the limit of linear perturbations. While the resulting nonlinear neutrino density is somewhat more realistic, the distribution function still has some residual errors that cannot easily be reduced without including further moments in the nonlinear computation.

### 3.3 Approximations and other methods

For some purposes, such as the computation of covariance matrices for different cosmological probes, it is useful to have methods for making cosmological predictions that are faster, although less accurate, than the traditional  $N$ -body methods discussed so far. Here we present two such methods that can be used as surrogates for  $N$ -body simulations: the COmoving Lagrangian Acceleration (COLA) approach and the PINpointing Orbit-Crossing Collapsed Hierarchical Objects (PINOCCHIO) approach. In both cases, a speed-up is achieved by drastically simplifying the time integration in the particle evolution. Finally, we also present a method

that avoids the need to include any neutrino physics in the actual  $N$ -body simulation altogether, apart from in the background solution. This method employs the so-called *Newtonian motion gauge* and can be used with virtually any numerical scheme that solves the Newtonian gravity problem.

### 3.3.1 COLA

The COLA approach by Tassev et al. [70] produces fast, approximate simulations of cosmological structure formation. Essentially, instead of solving for a full particle trajectory  $\mathbf{x}(t)$ , in this approach we solve for the deviations of the full trajectory about the trajectory predicted by second-order Lagrangian perturbation theory (2LPT)  $\delta\mathbf{x}(t) = \mathbf{x}(t) - \mathbf{x}_{2\text{LPT}}(t)$ . Since the evolution of the particles on large scales will be very close to that predicted by 2LPT, we can decrease the number of time steps of the simulation to trade accuracy at small scales for overall simulation speed while maintaining good accuracy at large scales. For a large number of time steps, the method effectively converges to a standard PM  $N$ -body method.

Adding massive neutrinos to the COLA method was described by Wright et al. [61], which also included an implementation in the MG-PICOLA simulation code<sup>1</sup> by Winther et al. [60]. This implementation was carried over to the COLA solver within FML<sup>2</sup> which succeeded MG-PICOLA. It is this implementation of the COLA solver within FML that we use in this paper. These implementations rely on the linear mesh-based method described above, i.e. we use the density field of neutrinos extrapolated from linear perturbation theory on a mesh for the PM part. For the 2LPT part of the COLA code, we make a further approximation to the 2LPT equation and use the  $\Lambda$ CDM kernel to speed up the computation.

To demonstrate the key advantage of COLA over traditional  $N$ -body codes, we use only 50 time steps linearly distributed in scale factor for the COLA simulations in this paper. However, the COLA method does not work well for simulations starting from high initial redshifts when using a relatively small number of time steps; for a discussion on how to optimise initial redshift and number of time steps in COLA simulations see sections 4.1 and 4.3 of Izard et al. [71]. Therefore, we use a slightly modified<sup>3</sup> version of FML's built-in generator of initial conditions to generate initial particle data at  $z = 19$  instead of  $z = 127$  as is described in section 4.1 and used for the other methods in this paper. In addition, we use the CAMB Boltzmann solver by Lewis et al. [72, 73] to generate the density transfer function for massive neutrinos. Finally, we note that for all COLA simulations in this paper we use a force grid that is a factor of three finer than the mean inter-particle distance; for a thorough investigation of the impact of varying this factor in COLA simulations see section 4.4 of Izard et al. [71].

### 3.3.2 PINOCCHIO

The PINOCCHIO code<sup>4</sup> [62, 74, 75] is an approximate method to generate halo catalogues in a very small fraction (of the order of 1/1000) of the time taken by an equivalent  $N$ -body simulation. Starting from a linear density field generated in Lagrangian space over a regular grid, its main goal is to construct halo catalogues by predicting which particles will end up in dark matter halos. To achieve this goal the algorithm first smoothes the linear density on a grid of

<sup>1</sup><https://github.com/HAWinther/MG-PICOLA-PUBLIC>.

<sup>2</sup><https://github.com/HAWinther/FML/tree/master/FML/COLASolver>.

<sup>3</sup>The modifications are to the order in which (pseudo-)random numbers are drawn for the phases and amplitudes, such that we now do the same as the version of N-GenIC used for the other methods in this paper, see section 4.1.

<sup>4</sup><https://github.com/pigimonaco/Pinocchio>.

smoothing radii, then uses ellipsoidal collapse to compute the collapse time of each particle. In the second step, it proceeds to group the collapsed particles into halos, using an algorithm that mimics their hierarchical clustering and distinguishes between halos and filaments.

As opposed to the other  $N$ -body methods employed in this work, PINOCCHIO does not integrate particle orbits but places halos at their final position using a single 2LPT or 3LPT displacement. Indeed, once the displacement fields are averaged over the multi-stream region that corresponds to a dark matter halo, LPT is very effective in predicting halo positions [76]. Another difference is that PINOCCHIO does not start from a set of displaced particles but generates the linear density field internally. Having implemented the same sequence for populating modes in  $k$ -space as the N-GenIC code that is used for the purpose of generating initial data in this work (see section 4.1), it can reproduce the same large-scale structure if the same seed for random numbers is provided.

The extension of PINOCCHIO to massive neutrinos is presented by Rizzo et al. [63] and is based on the result of Castorina et al. [18, 77] that the nonlinear clustering of massive neutrinos is negligible. We use CAMB to compute linear power spectra in massive neutrino cosmologies, and compute the scale-dependent growth rate of matter by taking ratios of power spectra of CDM and baryons (i.e. without neutrinos) at different times. We also adapt the code to incorporate a scale-dependent growth rate. With respect to the original implementation of Rizzo et al. [63], which was limited to 2LPT, we extend here the computation to third order: as shown by Munari et al. [75] this results in a significant improvement at mildly nonlinear scales.

Although the code has been conceived to predict the properties of dark matter halos, it can produce a full nonlinear density field as follows: particles that do not belong to halos are moved to their final position using 3LPT, halo particles are distributed around their halo center of mass following a Navarro-Frenk-White (NFW) profile [78] with Maxwellian velocity distributions. This allows us to construct snapshots like an  $N$ -body simulation, representing density fields that are far more accurate than a straight LPT implementation. Because we have only one type of particle, to compute the power spectrum of CDM and baryons needed below (section 5) we subtract the linear neutrino contribution from the total matter power spectrum obtained from the snapshot. To this end we also assume that the neutrino-matter cross-power spectrum,  $P_{\nu,m}(k)$ , can be approximated by  $P_{\nu,m}(k) = \sqrt{P_{\nu}^L(k)P_m(k)}$ , where the superscript “L” denotes a power spectrum from linear theory. This approximation is strictly only true in the linear regime but we apply it at all scales.

We do not expect PINOCCHIO to be competitive with  $N$ -body codes in predicting the matter power spectrum: taking it as a sophisticated implementation of 3LPT, we expect it to lose power on scales smaller than  $k = 0.3 h \text{ Mpc}^{-1}$  for the halo power spectrum and  $k = 0.2 h \text{ Mpc}^{-1}$  for the matter power spectrum. It will not be competitive with COLA as well which, being a PM code, can converge to the solution (on scales larger than the mesh) if a sufficient number of time steps is used. This better accuracy comes at a higher cost in computing time, by approximately a factor of eight in the configuration used in this paper (see also Blot et al. [79] for a similar benchmark), as well as in memory since our COLA runs use a grid three times finer than the mean particle separation. The PINOCCHIO code is widely used especially to characterise the covariance of galaxy clustering measurements, thanks to its low computational cost and its ability to generate halo catalogues.

### 3.3.3 Newtonian motion gauge

The Newtonian motion gauge approach for massive neutrinos was developed by Partmann et al. [32] and Heuschling et al. [49]. It allows for a simulation of nonlinear CDM in an ordinary Newtonian  $N$ -body simulation while accounting for the impact of linear neutrinos via a modification of the dark matter initial conditions and by employing a dynamically evolving coordinate system. The method is agnostic towards the implementation of the  $N$ -body simulation and for this paper we choose to employ GADGET-4 [48]. However, any method solving Newtonian nonlinear gravity is compatible, even methods other than  $N$ -body simulations. We would like to stress that our method is exact in the weak-field limit of general relativity (see Fidler et al. [80]) and therefore captures the full effect of linear neutrino perturbations on the nonlinear matter clustering.

The Newtonian motion approach allows for a very simple inclusion of massive neutrinos, requiring only three additional steps applied to a simulation without any neutrinos. First, we start from a set of “back-scaled” initial conditions based on the present-day power spectrum of CDM and baryons in the Newtonian motion coordinates, excluding neutrino perturbations. In contrast to other neutrino methods presented in this paper, these initial conditions do not assume a scale-dependent growth, i.e. the rescaling of the power spectrum is done using the scale-independent growth factor  $D_+$ . The residual effect of decaying modes due to neutrinos is included in the construction of the present-day matter power spectrum in the Newtonian motion coordinate system. This also has the added benefit that ordinary generators of initial conditions can be used without modifications, provided that the correctly back-scaled Newtonian motion gauge power spectrum is used. We then evolve the initial data with the Newtonian solver, taking into account the impact of the massive neutrinos on the background evolution via the Hubble rate. Finally, we obtain the output in the Newtonian motion gauge. To make it comparable to the output of other methods, we need to transform the result to the gauge employed therein (usually the “ $N$ -boisson” gauge [80]). This step is realised by a displacement field acting on the particle positions that is implemented in a similar way to how the initial conditions are set. The transformation accounts for the residual impact of neutrinos and other relativistic effects on the evolution of the CDM and baryon particles. However, by construction, the transformation vanishes exactly at  $z = 0$  (or another chosen target redshift) while it is in general very small at late times, for small neutrino masses and on small scales. Therefore, it can often be neglected as it will only lead to small corrections in which case the output of the simulation can be used as-is.

For this work, we include only the first two steps, while omitting the final particle displacement. This leads to a small mismatch in the results shown for  $z = 1$  at large scales for the cases of the highest neutrino masses. By leaving this correction out, we demonstrate that for most neutrino masses, box sizes, and redshifts the method is already sufficiently accurate in its simplest form. For more details on the transformation we refer the reader to the original work by Partmann et al. [32].

### 3.4 Halo-model reaction

The halo-model reaction approach provides the nonlinear corrections caused by massive neutrinos to a  $\Lambda$ CDM power spectrum through a ratio of halo-model predictions. Following Cataneo et al. [81], the nonlinear power spectrum is then given by

$$P^{\text{NL}}(k, z) = \mathcal{R}(k, z) P_{\text{pseudo}}^{\text{NL}}(k, z), \quad (3.6)$$

where  $\mathcal{R}(k, z)$  is the halo-model reaction and  $P_{\text{pseudo}}^{\text{NL}}(k, z)$  is the nonlinear pseudo power spectrum.

The pseudo spectrum is a nonlinear  $\Lambda$ CDM power spectrum but with the initial conditions tuned such that its linear clustering exactly matches the linear clustering in the non-standard cosmology at the target redshift. For example, if the non-standard physics introduces a simple rescaling of the linear clustering amplitude, one could just rescale the amplitude of any  $\Lambda$ CDM power spectrum to produce the pseudo spectrum. In the case of scale-dependent modifications, this becomes a bit trickier in practice. We approximate this quantity as in previous works by Cataneo et al. [64, 81] and pass the modified linear spectrum as produced by CAMB to HMcode developed by Mead et al. [82], with  $\Lambda$ CDM presets, i.e. no baryonic feedback nor massive neutrinos. The benefit of using the pseudo rather than  $\Lambda$ CDM cosmology is that it guarantees the mass functions in target and pseudo cosmologies are similar as they have the same linear clustering. This produces a smoother transition between the two-halo and one-halo terms. This transition was one of the previous issues in calculating this nonlinear response using the halo model [83–85].

Following Cataneo et al. [64], the halo-model reaction for massive neutrinos is given by

$$\mathcal{R}(k) = \frac{(1 - f_\nu)^2 P_{\text{cb}}^{\text{HM}}(k) + 2f_\nu(1 - f_\nu) P_{\nu,\text{cb}}^{\text{HM}}(k) + f_\nu^2 P_\nu^{\text{L}}(k)}{P_{\text{m}}^{\text{L}}(k) + P_{\text{pseudo}}^{\text{1h}}(k)}, \quad (3.7)$$

with “cb” denoting the CDM and baryon component and “ $\nu$ ” denoting massive neutrinos. We include the effects of massive neutrinos at the linear level in the numerator via the weighted sum of the nonlinear halo-model (cb) spectrum and the massive neutrino linear spectrum [15]. The components of the reaction are

$$P_{\nu,\text{cb}}^{\text{HM}}(k) \approx \sqrt{P_{\text{cb}}^{\text{HM}}(k) P_\nu^{\text{L}}(k)}, \quad (3.8)$$

$$P_{\text{cb}}^{\text{HM}}(k) = P_{\text{cb}}^{\text{L}}(k) + P_{\text{cb}}^{\text{1h}}(k). \quad (3.9)$$

Explicitly, the one-halo terms are given as integrals over the Fourier space halo density profile  $u(k, M)$  and the halo mass function  $n(M)$ ,

$$P_{\text{cb}}^{\text{1h}}(k) = \int d \ln M n_{\text{cb}}(M) \left( \frac{M}{\bar{\rho}_{\text{cb}}} \right)^2 |u_{\text{cb}}(k, M)|^2, \quad (3.10)$$

$$P_{\text{pseudo}}^{\text{1h}}(k) = \int d \ln M n_{\text{pseudo}}(M) \left( \frac{M}{\bar{\rho}_{\text{m}}} \right)^2 |u_{\text{pseudo}}(k, M)|^2, \quad (3.11)$$

where  $\bar{\rho}$  is the background density for the specified matter species. The halo mass functions are given as

$$n_{\text{cb}}(M) = \frac{\bar{\rho}_{\text{cb}}}{M} [\nu' f(\nu')] \frac{d \ln \nu'}{d \ln M}, \quad (3.12)$$

$$n_{\text{pseudo}}(M) = \frac{\bar{\rho}_{\text{m}}}{M} [\nu'' f(\nu'')] \frac{d \ln \nu''}{d \ln M}. \quad (3.13)$$

The peak heights are defined as  $\nu' = \delta_{\text{sc,cb}}(M)/\sigma_{\text{cb}}[R_{\text{cb}}(M)]$  and  $\nu'' = \delta_{\text{sc,m}}/\sigma_{\text{m}}[R_{\text{m}}(M)]$ , where the subscript “sc” indicates this quantity is calculated by solving the standard  $\Lambda$ CDM spherical-collapse equations but with the indicated matter density. The mass fluctuation

variances are given by

$$[\sigma_{\text{cb}}(R)]^2 = \int \frac{d^3k}{(2\pi)^3} |\tilde{W}(kR)|^2 P_{\text{cb}}^{\text{L}}(k), \quad (3.14)$$

$$[\sigma_{\text{m}}(R)]^2 = \int \frac{d^3k}{(2\pi)^3} |\tilde{W}(kR)|^2 P_{\text{m}}^{\text{L}}(k). \quad (3.15)$$

In all predictions from halo-model reaction, we employ a Sheth-Tormen halo mass function [86, 87], a power-law concentration-mass relation (see for example the work by Bullock et al. [88]), and an NFW halo density profile [78]. The predictions are computed numerically using the public code `ReACT`<sup>5</sup> by Bose et al. [65, 89].

### 3.5 Power-spectrum emulation

Fast predictors of the matter power spectrum are an essential ingredient for many inference pipelines in cosmology. Since numerical simulations are too costly to be directly applied in this context, different approaches based on approximate methods or elaborate fitting techniques have been used in the past. Apart from the halo-model reaction discussed in the previous section, well-known examples are the *halofit* predictor developed by Smith et al. [90] and later improved by Takahashi et al. [91], and the `HMcode` predictor by Mead et al. [82], the latter being based on the halo model. In terms of the power-suppression signal of neutrinos, fitting routines by Bird et al. [16] have been used in the past.

More recently, the emulation technique has become a popular alternative to obtain fast predictions of the matter power spectrum within the cosmological parameter space. Broadly speaking, emulators are interpolation routines based on a suite of numerical simulations that sample the cosmological parameter space and act as a training set. There are different surrogate techniques currently used for cosmological emulators, such as Gaussian process regression [66, 92–94], polynomial chaos expansion [7, 8], or neural network approaches [95].

In addition to the predictions from *halofit* and `HMcode` mentioned above, we focus in this paper on the `Cosmic Emu` [66], the `EuclidEmulator2` [8], and the `BACCOemulator` [45]. These emulators provide predictions of the matter power spectrum and include a free parameter for the sum of the neutrino masses. We will now summarise the particularities of these three emulators, specifically focusing on the neutrino implementation.

- The `Cosmic Emu-2022` is built upon the *Mira-Titan* simulations [67, 96], a suite of 111 simulations run with the `HACC` code [97]. The simulations are distributed over an eight-dimensional cosmological parameter space comprising  $(\omega_{\text{m}}, \omega_{\text{b}}, \omega_{\nu}, \sigma_8, h, n_{\text{s}}, w_0, w_a)$ , where  $\sigma_8$  is the present-day amplitude of linear matter density fluctuations at the scale of  $8 h^{-1} \text{Mpc}$ ,  $n_{\text{s}}$  is the scalar spectral index, and  $w_0, w_a$  parameterise the effective equation of state of dark energy in terms of the first two coefficients of the Taylor series expansion around  $a = 1$ . The emulator achieves an absolute precision of about four percent for modes of  $k < 5 h \text{Mpc}^{-1}$  within the redshift range  $z \in [0, 2]$ . Neutrinos are not incorporated in the simulations and are effectively treated as a smooth background component. The power spectra are then corrected on large scales for enhanced growth beyond the neutrino free-streaming scale using the scale-dependent linear growth factor.
- The `EuclidEmulator2` is trained on 200 paired and fixed simulations that were run with `PKDGRAV3`. It emulates the nonlinear boost factor that is then multiplied by the results

<sup>5</sup><https://github.com/nebbu/ReACT>.

of a linear Boltzmann solver. The emulator covers eight cosmological parameters ( $\Omega_m$ ,  $\Omega_b$ ,  $\sum m_\nu$ ,  $A_s$ ,  $h$ ,  $n_s$ ,  $w_0$ ,  $w_a$ ), where  $A_s$  is the amplitude of primordial perturbations at the scale  $k_p = 0.05 \text{ Mpc}^{-1}$ , and includes redshifts of  $z \in [0, 3]$  and modes up to  $k = 10 h \text{ Mpc}^{-1}$ . It claims an error of below one percent which is better than the other emulators discussed here. Note, however, that the `EuclidEmulator2` covers a somewhat narrower parameter space motivated by the results of the *Planck* mission [98]. Within the training set the neutrinos are modelled using the mesh-based method implemented in PKDGRAV3.

- The `BACCOemulator` is trained on a very large suite of simulations based on the cosmology-rescaling technique [99]. More specifically, four high-resolution simulations with judiciously chosen cosmologies are rescaled to more than 800 cosmologies at different redshifts. Whenever the target cosmologies included massive neutrinos, their effect is added following the extension of the cosmology-rescaling technique presented by Zennaro et al. [33]. This emulator varies eight cosmological parameters ( $\Omega_{cb}$ ,  $\Omega_b$ ,  $\sum m_\nu$ ,  $\sigma_8$ ,  $h$ ,  $n_s$ ,  $w_0$ ,  $w_a$ ) and covers a redshift range of  $z \in [0, 1.5]$  for modes up to  $k = 5 h \text{ Mpc}^{-1}$ . The claimed precision is better than three percent.

We refer to the original references for more information about the emulators.

## 4 Simulations

To compare different numerical methods, we carry out a large suite of  $N$ -body simulations where we employ different codes to run the same set of ten simulations summarised in table 2. These ten simulations cover different choices of total neutrino mass  $\sum m_\nu$  (including the massless case), different box sizes  $L_{\text{box}}$ , and different mass resolutions to check for numerical convergence with respect to finite-volume and discretisation effects.  $N_{\text{part}}$  denotes the number of particles used for CDM and baryons, as well as the number of particles for neutrinos if a particle-based method is employed. For simplicity, we assume degenerate neutrino mass eigenstates because cosmology is mainly sensitive to the total neutrino mass scale [100]. We keep the total matter density (at redshift zero) fixed at  $\Omega_m = 0.319$  by adjusting the CDM density parameter together with the neutrino mass. The baryon density is fixed at  $\Omega_b = 0.049$ , and the remaining cosmological parameters are  $A_s = 2.215 \times 10^{-9}$  at the pivot scale  $k_p = 0.05 \text{ Mpc}^{-1}$ ,  $n_s = 0.9619$ , and  $h = 0.67$ , which are based on the *Euclid Flagship 2* simulation. Dark energy is modelled as a cosmological constant that provides a spatially flat background solution, and the CMB temperature is set to 2.7255 K and the effect of radiation is taken into account in the simulations at the linear level, either by using carefully tailored initial conditions as detailed below or by including the radiation component on the mesh if a mesh-based method is used.

Using identical initial data (see section 4.1 below for details) in each case, the ten simulations are run with each of the thirteen  $N$ -body methods listed in table 1 to produce particle snapshots at redshifts  $z = 1$  and  $z = 0$ . For `AREPO`, due to resource constraints, only the four simulations with  $N_{\text{part}} = 512^3$  are run, precluding the possibility of conducting numerical convergence tests in this case. Therefore, a total of 248 individual snapshots are analysed in this code comparison. In addition, nonlinear power spectra are predicted for each distinct choice of neutrino masses using the remaining methods in table 1, as well as using the `HMcode` and *halofit* fitting methods.



Simulation	$L_{\text{box}}$	$N_{\text{part}}$	mass resolution	$\sum m_\nu$
0.0eV	512 $h^{-1}$ Mpc	512 <sup>3</sup>	$8.85 \times 10^{10} h^{-1} M_\odot$	0.0 eV
0.15eV	512 $h^{-1}$ Mpc	512 <sup>3</sup>	$8.75 \times 10^{10} h^{-1} M_\odot$	0.15 eV
0.3eV	512 $h^{-1}$ Mpc	512 <sup>3</sup>	$8.65 \times 10^{10} h^{-1} M_\odot$	0.3 eV
0.6eV	512 $h^{-1}$ Mpc	512 <sup>3</sup>	$8.45 \times 10^{10} h^{-1} M_\odot$	0.6 eV
0.0eV_HR	512 $h^{-1}$ Mpc	1024 <sup>3</sup>	$1.11 \times 10^{10} h^{-1} M_\odot$	0.0 eV
0.15eV_HR	512 $h^{-1}$ Mpc	1024 <sup>3</sup>	$1.09 \times 10^{10} h^{-1} M_\odot$	0.15 eV
0.0eV_1024Mpc	1024 $h^{-1}$ Mpc	1024 <sup>3</sup>	$8.85 \times 10^{10} h^{-1} M_\odot$	0.0 eV
0.15eV_1024Mpc	1024 $h^{-1}$ Mpc	1024 <sup>3</sup>	$8.75 \times 10^{10} h^{-1} M_\odot$	0.15 eV
0.3eV_1024Mpc	1024 $h^{-1}$ Mpc	1024 <sup>3</sup>	$8.65 \times 10^{10} h^{-1} M_\odot$	0.3 eV
0.6eV_1024Mpc	1024 $h^{-1}$ Mpc	1024 <sup>3</sup>	$8.45 \times 10^{10} h^{-1} M_\odot$	0.6 eV

**Table 2.** Overview of the basic parameters used in our simulation suite. The cases with  $\sum m_\nu = 0$  eV and  $\sum m_\nu = 0.15$  eV are the two main baselines for our comparison, but we include some cases with larger masses, up to  $\sum m_\nu = 0.6$  eV, to probe more “extreme” regions of parameter space.

#### 4.1 Initial conditions

The initial conditions of all simulations are generated at redshift  $z = 127$ .<sup>6</sup> The linear matter power spectra and transfer functions are obtained by running either **CAMB** or the **CLASS** Boltzmann code by Blas et al. [101]. These files are then used by the **REPS**<sup>7</sup> code to compute the *rescaled* power spectra and transfer functions at  $z = 127$  by solving the multi-fluid linear equations as outlined by Zennaro et al. [102]. This procedure, known as *rescaling*, guarantees that the power spectrum of the output of the simulation on linear scales at low redshift will match the correct linear power spectra. A realisation of initial data is then generated by drawing random phases for all perturbation modes and fixing their amplitudes according to the initial transfer functions. This approach of “fixing” the amplitudes effectively removes cosmic variance at linear scales and has been shown to generally produce less noisy summary statistics [103]. It introduces a specific type of non-Gaussianity that is not expected to affect any of our results. Given the density field of CDM and baryons, the initial positions and velocities of the  $N$ -body particles are computed from the Zeldovich approximation [104]. We employ a modified version of the **N-GenIC** code<sup>8</sup> that accounts for the scale-dependence present in both the growth rate and growth factor in cosmologies with massive neutrinos.

For neutrinos, the different implementations make use of distinct methods. For particle-based implementations, the positions and velocities of the massive neutrino particles are generated in a similar fashion as CDM. This means we effectively make use of the Zeldovich approximation to set the first two moments of the phase-space distribution function which correspond to the density perturbation and bulk velocity, respectively. The initial velocities of neutrino particles are then offset by a random thermal component drawn from their Fermi-Dirac distribution [105, 106]. We assume the standard Big Bang scenario where this distribution is set in equilibrium before the weak interaction freezes out — when the Universe was about 1 second old — and after freeze-out simply redshifts as the Universe expands. Note that this means that the typical thermal velocities are much larger than those of a dis-

<sup>6</sup>COLA exceptionally uses  $z = 19$  as initial redshift (see section 3.3.1).

<sup>7</sup><https://github.com/matteozennaro/reps>.

<sup>8</sup>[https://github.com/franciscovillaescusa/N-GenIC\\_growth](https://github.com/franciscovillaescusa/N-GenIC_growth).

tribution that is in thermal equilibrium at low redshift. For SWIFT, neutrino particles are instead set up with the `FastDF` code,<sup>9</sup> using geodesic integration from high redshift [20, 69], to reproduce the full distribution function and to prevent the initial perturbations from being erased by thermal motions [55]. For mesh-based implementations, on the other hand, the density field of each neutrino species is directly computed using the phases from the random field realisation of the linear initial conditions.

## 4.2 Post-processing pipeline

In order to quantify differences in our numerical schemes as precisely as possible, we analyse the snapshots of all our  $N$ -body simulations in a common pipeline. We compute the power spectra and bispectra of the CDM and baryon component, and produce halo catalogues from which we measure the halo mass functions and halo bias. In cases where the simulations provide a neutrino distribution, we also compute the cross-power spectra of neutrinos with the CDM and baryon component, as well as the neutrino auto-power spectra.

### 4.2.1 Power spectra

The power spectra of the different snapshots have been estimated using `Pylians3`.<sup>10</sup> The routine first deposits particle masses into a regular 3D grid with  $N^3$  voxels using the cloud-in-cell mass-assignment scheme. In this work, we always use a mesh with  $N^3 = N_{\text{part}}$  such that the Nyquist scales match between particles and mesh. Although using larger grids may improve measurements on smaller scales, we recommend caution due to potential systematics and advise against relying on results near or beyond the Nyquist scale set by the mean particle separation. The constructed field is then Fourier transformed and the effects of the mass-assignment scheme are corrected. Next, for each mode the square of its amplitude is computed,  $|\delta(\mathbf{k})|^2$ . The modes are then binned in intervals of width equal to the fundamental frequency  $k_F = 2\pi L_{\text{box}}^{-1}$  and the power spectrum is finally estimated as

$$P(k_i) = \frac{1}{N_i} \sum_{\mathbf{k} \in B_i} |\delta(\mathbf{k})|^2, \quad (4.1)$$

where  $N_i$  is the number of independent modes in the considered bin  $B_i = \{\mathbf{k} \mid i k_F \leq |\mathbf{k}| < (i+1)k_F\}$  and  $k_i$  is computed as

$$k_i = \frac{1}{N_i} \sum_{\mathbf{k} \in B_i} |\mathbf{k}|. \quad (4.2)$$

To compute the cross-power spectrum of two fields instead, the estimator is generalised in the most straightforward way,

$$P_{X,Y}(k_i) = \frac{1}{2N_i} \sum_{\mathbf{k} \in B_i} [\delta_X(\mathbf{k})\delta_Y^*(\mathbf{k}) + \delta_X^*(\mathbf{k})\delta_Y(\mathbf{k})], \quad (4.3)$$

where the subscripts ‘‘X’’ and ‘‘Y’’ denote the two different fields. When presenting the results, we combine the measurements into larger bins logarithmically spaced in  $k$ . This reduces the noise at large  $k$  and makes our plots more readable.

Some codes do not produce snapshots at exactly the desired redshift, but at redshifts that deviate by less than  $\pm 0.01$  from the target redshift. These differences can be visible when

<sup>9</sup><https://github.com/wulm/fastdf>.

<sup>10</sup><https://pylians3.readthedocs.io>.

comparing power spectra on a sub-percent level. For those cases, we rescale the power spectra by the square of the ratio of the linear growth factors at the respective redshift values. Such a rescaling is applied to ANUBIS for all snapshots and to L-GADGET3 and PKDGRAV3 at  $z = 1$ .

#### 4.2.2 Bispectra

We measure the bispectrum of CDM and baryons (ccc) using the estimator

$$\hat{B}_{\text{ccc}}(k_l, k_m, k_n) \equiv \frac{k_F^3}{N_{\text{tr}}(k_l, k_m, k_n)} \sum_{\mathbf{q}_1 \in B_l} \sum_{\mathbf{q}_2 \in B_m} \sum_{\mathbf{q}_3 \in B_n} \delta_{\text{K}}(\mathbf{q}_1 + \mathbf{q}_2 + \mathbf{q}_3) \delta(\mathbf{q}_1) \delta(\mathbf{q}_2) \delta(\mathbf{q}_3), \quad (4.4)$$

where  $N_{\text{tr}}$  is the number of “fundamental triangles”,

$$N_{\text{tr}}(k_l, k_m, k_n) \equiv \sum_{\mathbf{q}_1 \in B_l} \sum_{\mathbf{q}_2 \in B_m} \sum_{\mathbf{q}_3 \in B_n} \delta_{\text{K}}(\mathbf{q}_1 + \mathbf{q}_2 + \mathbf{q}_3), \quad (4.5)$$

formed by the vectors  $\mathbf{q}_i$  satisfying the triangle condition  $\mathbf{q}_1 + \mathbf{q}_2 + \mathbf{q}_3 = 0$  that are included within the “triangle bin” defined by the triplet of centers  $(k_l, k_m, k_n)$  and corresponding bins  $B_l, B_m, B_n$ .

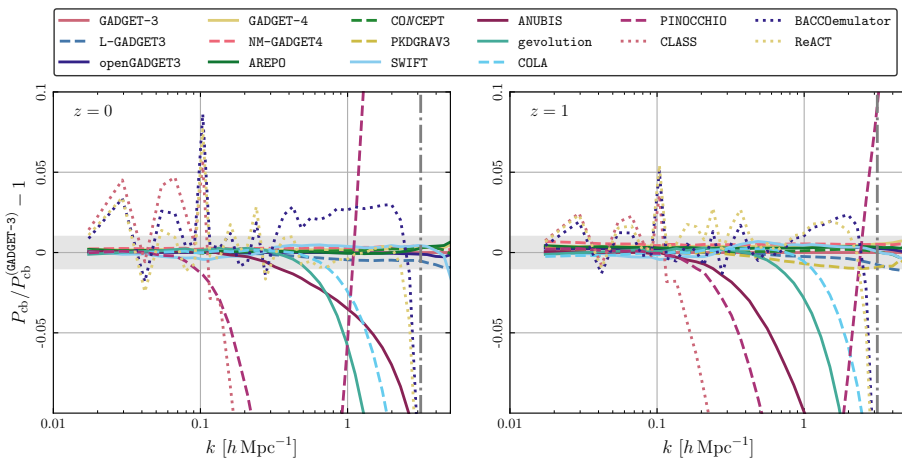
We use a Python code implementing the fourth-order density interpolation and the interlacing scheme described by Sefusatti et al. [107]. In order to compare the large-volume simulations ( $L_{\text{box}} = 1024 h^{-1}$  Mpc) more easily with the small-volume ones, we use the same  $k$ -space binning in both cases, fixing the bin width to  $k_F$  of the small box. Just like for the power spectra, to account for inaccuracies in the redshift of some snapshots, we rescale some of the resulting bispectra by the cube of the ratio of the linear growth factors at the respective redshift values. Such a rescaling is applied to ANUBIS for all snapshots and to L-GADGET3 and PKDGRAV3 at  $z = 1$ .

#### 4.2.3 Halo catalogues

For the considered snapshots of the various simulations, we identify halos with the code `Denhf` [108–111] which uses a “spherical overdensity” criterion. The algorithm does not rely on any pre-identification method. Only CDM and baryon particles are considered in the characterisation of halos; neutrino particles (if present at all in the simulation) are considered as a background component [17, 77].

`Denhf` estimates the local density at the position of each  $N$ -body particle by calculating the distance to its 10<sup>th</sup>-nearest neighbour  $d_{10}$ , and assigning to each particle a density that is proportional to  $d_{10}^{-3}$ . Centered on the particle with the highest density value, the algorithm grows a sphere and stops when the mean density within the sphere falls below a desired overdensity threshold, set to 200 times the background density of CDM and baryons for the purpose of this work. All particles assigned to this spherical overdensity halo are then removed from the global list of particles, and the algorithm proceeds recursively until none of the remaining particles has a local density large enough to be the center of a 10-particle halo. Particles not assigned to halos will be part of the field.

Only in the case of PINOCCHIO we use the halo catalogues as produced by the code itself instead of `Denhf`. Because PINOCCHIO is calibrated on the friends-of-friends halo mass function, we translate its masses to spherical overdensity ones by applying the rescaling of halo masses that translates the halo mass function of Watson et al. [112], that has been used to calibrate the code, to the one of Tinker et al. [113]. Such a rescaling has been used, e.g., by Fumagalli et al. [10] to force the halo mass function averaged over 1000 realisations to



**Figure 1.** Power spectrum of CDM and baryons as measured from different codes, relative to GADGET-3 at  $z = 0$  and  $z = 1$  for a neutrino mass of  $\sum m_\nu = 0.15\text{eV}$  in the simulation with  $L_{\text{box}} = 512 h^{-1}\text{Mpc}$  and  $N_{\text{part}} = 512^3$  CDM and baryon particles. The corresponding particle Nyquist wavenumber is indicated by the grey dash-dotted line. The grey bands highlight the interval of  $\pm 0.01$ .

follow a target one. We compute the rescaling only once, in the case of massless neutrinos, and use it for all neutrino masses.

For the codes that do not produce snapshots at the exact values of the desired redshifts, we apply no further corrections here. The error in the redshift is less than  $\pm 0.01$  while our halo properties typically display disagreements larger than 1% between different codes. We therefore assume that the error due to mismatching redshift values is subdominant.

## 5 Results

### 5.1 Power spectra

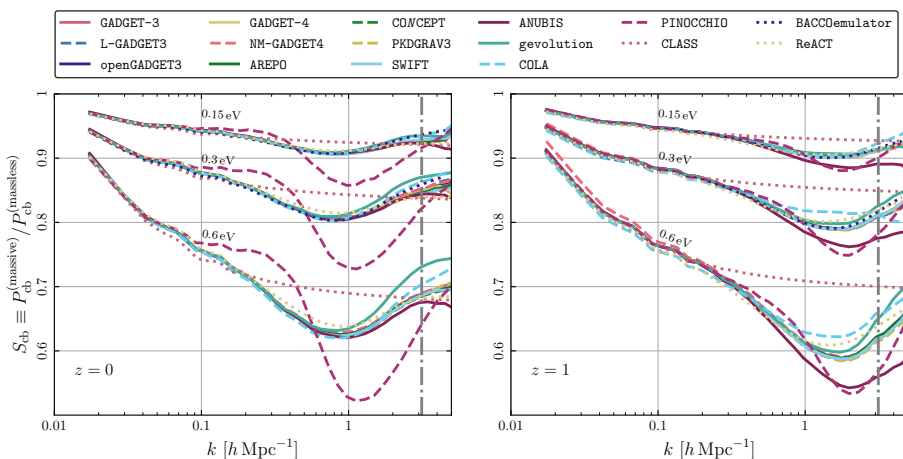
A key prediction from neutrino simulations is a suppression of the matter power spectrum that exceeds the maximum linear theory prediction of  $\Delta P_m/P_m \approx 8f_\nu$ . The matter power spectrum can be decomposed as follows

$$P_m(k) = (1 - f_\nu)^2 P_{\text{cb}}(k) + 2f_\nu(1 - f_\nu)P_{\nu,\text{cb}}(k) + f_\nu^2 P_\nu(k), \quad (5.1)$$

where  $P_{\text{cb}}$  is the power spectrum of CDM and baryons,  $P_{\nu,\text{cb}}$  the cross-power spectrum of neutrinos with CDM and baryons, and  $P_\nu$  the neutrino power spectrum. Various methods treat these components differently or make predictions for only some of them, so we discuss each component in turn. Finally, we will also compare the total  $P_m(k)$  with various power spectrum emulators, including *EuclidEmulator2* which only predicts this quantity.

#### 5.1.1 CDM and baryons

The leading contribution to  $P_m(k)$  is  $P_{\text{cb}}(k)$ , which is suppressed in massive neutrino models. Figure 1 shows the ratio of  $P_{\text{cb}}(k)$  for models with a neutrino mass of  $\sum m_\nu = 0.15\text{eV}$  relative



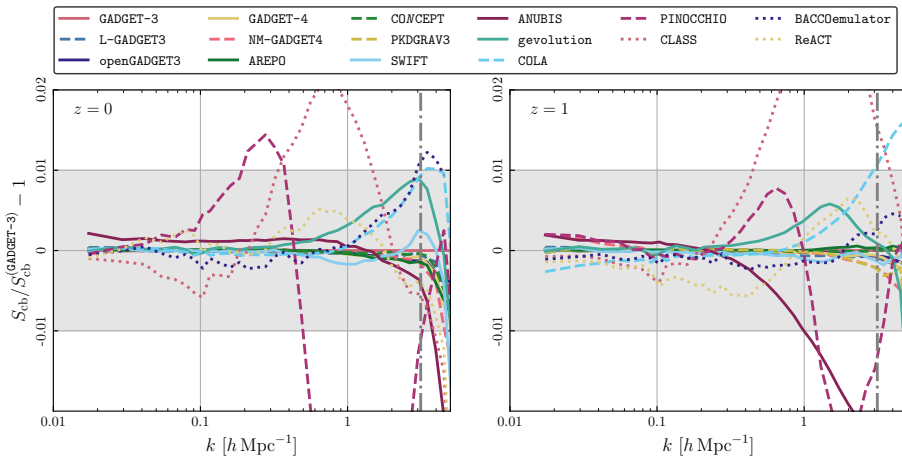
**Figure 2.** Suppression of the power spectrum of CDM and baryons at  $z = 0$  and  $z = 1$  for three different neutrino masses,  $\sum m_\nu \in \{0.15, 0.3, 0.6\}$  eV, when compared to the massless case. Results are from the simulations with  $L_{\text{box}} = 512 h^{-1} \text{Mpc}$  and  $N_{\text{part}} = 512^3$ . The corresponding particle Nyquist wavenumber is indicated by the grey dash-dotted line.

to the `GADGET-3` simulation which we arbitrarily pick as the reference. In all our figures, results from codes where massive neutrinos are represented through an  $N$ -body ensemble are plotted using solid lines, while other  $N$ -body methods, including surrogates, use dashed lines. Any additional predictions use dotted lines. In figure 1, the linear prediction, computed with `CLASS`, is shown by the rose dotted line that drops off sharply at  $k \approx 0.1 h \text{Mpc}^{-1}$  beyond which the error quickly exceeds 10%. At  $z = 0$ , on the largest scales, all codes deviate less than 1% — the fluctuations seen in the dotted lines are largely due to the lack of cosmic variance in the codes that predict  $P_{\text{cb}}(k)$  directly. On smaller scales, some of the codes start to deviate from the `GADGET-3` reference. `PINOCCHIO` is in agreement within 1% up to  $k \approx 0.1 h \text{Mpc}^{-1}$ , `ANUBIS` up to  $k \approx 0.3 h \text{Mpc}^{-1}$ , `gevolution` up to  $k \approx 0.5 h \text{Mpc}^{-1}$ , and `COLA` up to  $k \approx 0.7 h \text{Mpc}^{-1}$ . The other codes stay within a 1% deviation from `GADGET-3` for all scales down to the particle Nyquist scale of  $k_{\text{Nyq}} = \pi N_{\text{part}}^{1/3} L_{\text{box}}^{-1} \approx 3 h \text{Mpc}^{-1}$ . This scale is indicated by a vertical dash-dotted line. The `ReACT` and `BACCOemulator` codes stay accurate within 1% to 5% on all scales down to the Nyquist scale. At  $z = 1$  the qualitative behaviour is similar, but most notably the codes disagree more on large scales while still staying within a 1% agreement. Here, `PINOCCHIO` is accurate up to  $k \approx 0.2 h \text{Mpc}^{-1}$ .

Figure 2 shows the ratio of  $P_{\text{cb}}(k)$  for models with massive neutrinos relative to the massless case for  $\sum m_\nu \in \{0.15, 0.3, 0.6\}$  eV. For later convenience, we denote this suppression ratio by  $S_{\text{cb}}(k)$ , or in general

$$S_X(k) = \frac{P_X^{(\text{massive})}(k)}{P_X^{(\text{massless})}(k)}, \quad (5.2)$$

where the subscript “X” denotes any component in question, here  $X \rightarrow \text{cb}$ . Linear calculations (taken from `CLASS`) predict that, on the largest scales, the growth of structure is mostly

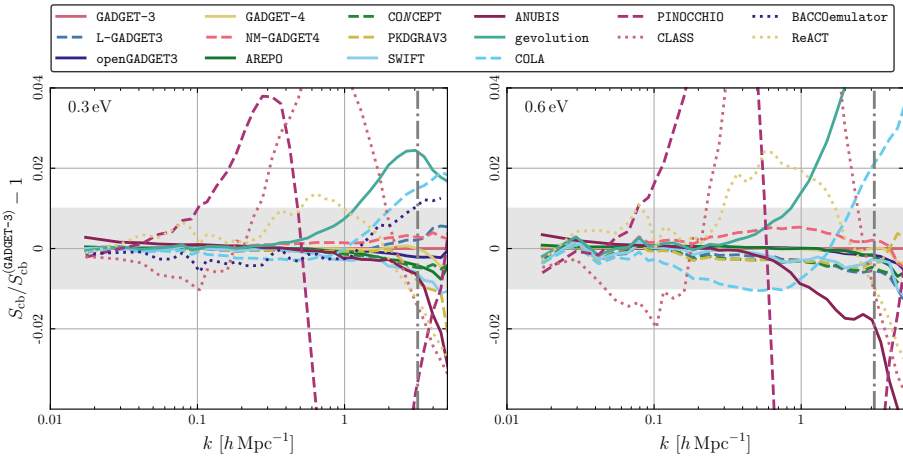


**Figure 3.** The suppression of the power spectrum of CDM and baryons relative to the one measured in the GADGET-3 reference runs at  $z = 0$  and  $z = 1$  for  $\sum m_\nu = 0.15 \text{ eV}$  for the simulations with  $L_{\text{box}} = 512 h^{-1} \text{ Mpc}$  and  $N_{\text{part}} = 512^3$ . The corresponding particle Nyquist wavenumber is indicated by the grey dash-dotted line. The grey bands highlight the interval of  $\pm 0.01$ .

unaffected so that  $S_{\text{cb}}(k)$  approaches unity, while on small scales  $S_{\text{cb}}(k)$  reaches a plateau. Compared to this linear expectation, all codes in the comparison predict slightly less suppression around  $k = 0.1 h \text{ Mpc}^{-1}$  and a much greater suppression for  $k > 0.3 h \text{ Mpc}^{-1}$ , followed by an upturn on nonlinear scales. This upturn has been repeatedly demonstrated and results from the reduced sensitivity of the one-halo contribution [41, 114]. At  $z = 0$ , we obtain excellent agreement between all simulations and most approximate methods up to the scale of maximum suppression at  $k_{\text{max}} \approx 1 h \text{ Mpc}^{-1}$ , where the suppression is 20% greater than the linear prediction. At  $z = 1$ , the scale of maximum suppression shifts to  $k_{\text{max}} \approx 2 h \text{ Mpc}^{-1}$  and the differences are greater, both with the linear prediction and between the codes, with the exception of PINOCCHIO<sup>11</sup> which fares significantly better compared to  $z = 0$ .

To study these relative differences in greater detail, we show  $S_{\text{cb}}(k)$  for the smallest neutrino mass,  $\sum m_\nu = 0.15 \text{ eV}$ , relative to the GADGET-3 prediction for this quantity in figure 3. With the exception of PINOCCHIO and CLASS, all codes agree to better than 1% at  $z = 0$  up to the particle Nyquist scale. Near  $k_{\text{Nyq}}$ , the approximate COLA method and the BACCOfemulator differ by more than 1% from the bulk of the simulations, while *gevolution* differs by slightly less than 1%. Beyond this scale, the predictions diverge and should be compared to higher-resolution runs since our estimator of the power spectrum is computed on a mesh with a matching Nyquist scale. The measured power spectra therefore cannot be used beyond  $k_{\text{Nyq}}$  where they become strongly biased. This particularly affects the comparison between simulations — where the power spectrum estimator is employed — and other methods to predict  $P_{\text{cb}}(k)$ . At  $z = 1$ , nonlinearities are smaller and the agreement between the simulations is better. Here the snapshot produced by PINOCCHIO achieves percent accuracy to  $k \approx 0.3 h \text{ Mpc}^{-1}$ . Some of the approximate methods fare slightly worse at this earlier time

<sup>11</sup>The reason for this disagreement is due to the fact that the accuracy of LPT-based PINOCCHIO depends on the level of nonlinearity that varies with neutrino mass.



**Figure 4.** The suppression of the power spectrum of CDM and baryons relative to the one measured in the GADGET-3 reference runs at  $z = 0$  for  $\sum m_\nu \in \{0.3, 0.6\}$  eV for the simulations with  $L_{\text{box}} = 512 h^{-1} \text{Mpc}$  and  $N_{\text{part}} = 512^3$ . The corresponding particle Nyquist wavenumber is indicated by the grey dash-dotted line. The grey bands highlight the interval of  $\pm 0.01$ .

compared to  $z = 0$ , with the difference between CLASS and the simulations increasing by 50% and COLA diverging beyond  $k = 2 h \text{Mpc}^{-1}$ . The NM-GADGET4 method requires an additional post-processing coordinate transformation at any redshift except  $z = 0$ . Because this additional step is omitted in this work for simplicity, a small error at low wavenumbers remains in the  $z = 1$  data. This explains why the error is larger at that redshift than at the final time.

ANUBIS notably drops off for  $k > 1 h \text{Mpc}^{-1}$  at  $z = 1$  and also shows a small excess on linear scales both at  $z = 0$  and  $z = 1$ . This excess originates from the massless case and is a result of ANUBIS being run with a coarser base grid than the other codes ( $512^3$  for all simulations) due to limited resources. A finer base grid requires more memory but the lack of it can be somewhat compensated by using a smaller time step. For the ANUBIS massive neutrino runs, this is done automatically but for the massless case the time step has been set to half of that originally calculated by the code. Tests indicate that further reducing the time step or ideally using a finer base grid should lessen the excess at large scales, but finding the optimal choice of code settings is not the aim of this work. The drop-off observed for ANUBIS at  $z = 1$  for  $k > 1 h \text{Mpc}^{-1}$  is due to differences in resolution between the various simulations. As ANUBIS is an AMR-code, a modified version of the RAMSES code originally written by Teyssier [56], the inclusion of massive neutrinos, which suppresses clustering on small scales, also reduces the number of refinements reached in the simulation compared to the massless case. This effect increases with the neutrino mass and is more noticeable for higher redshifts where there is also less refinement due to less clustering. This can be solved by a higher particle density which automatically leads to more refinement. Generally this is also necessary to find a better agreement between ANUBIS and GADGET-3 for smaller scales, as can be observed from the high-resolution runs and also in a previous comparison conducted by Schneider et al. [115] between RAMSES, GADGET-3, and PKDGRAV3.

The observed differences are greater when the neutrino mass is increased, especially for the approximate methods. Figure 4 shows  $S_{\text{cb}}(k)$  relative to the GADGET-3 prediction for

models with  $\sum m_\nu = 0.3 \text{ eV}$  (left panel) and  $\sum m_\nu = 0.6 \text{ eV}$  (right panel) at  $z = 0$ . While the `BACCOemulator` agrees to better than 1% with `GADGET-3` up to  $k_{\text{Nyq}}$  for 0.3 eV, it makes no prediction for 0.6 eV because that value lies far outside the range covered by the training set of the emulator. We deliberately include a case of such a large neutrino mass to exacerbate the differences between the various numerical implementations. The reaction method differs by slightly more than 1% and 2% at  $k = 0.7 h \text{ Mpc}^{-1}$  for total neutrino masses of 0.3 eV and 0.6 eV, respectively. The differences with the linear prediction (`CLASS`) and with `PINOCCHIO` are large, as noted above for 0.15 eV.

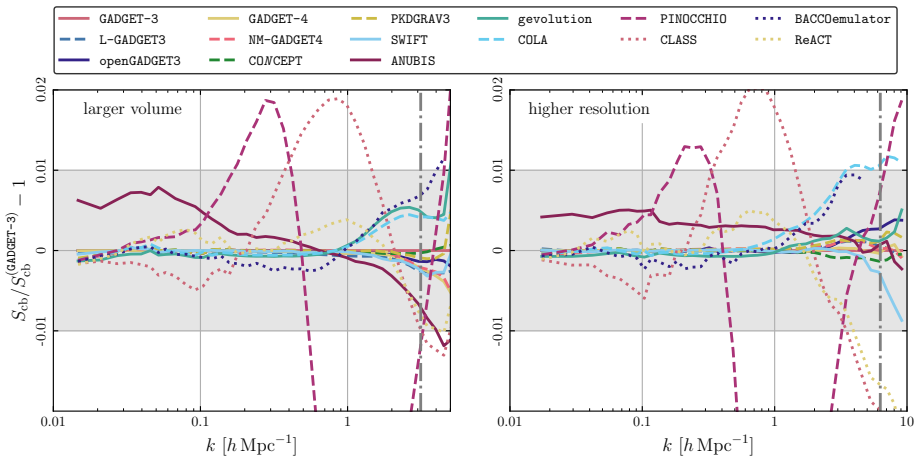
The agreement is excellent for the other codes, but some subtle differences can be discerned. On large scales, we observe that `SWIFT`, `CONCEPT`, `COLA`, `gevolution`, `PKDGRAV3`, `NM-GADGET4`, and `L-GADGET3` show the same coherent scatter relative to `GADGET-3`, especially for a neutrino mass of 0.6 eV. This is due to the contamination from shot noise in the neutrino particle implementation used by the `GADGET-3` run. The other mentioned codes have implementations that do not suffer from shot noise or take measures to limit the contamination. For instance, in `gevolution` the neutrino  $N$ -body ensemble is evolved throughout the simulation, but it is only used as source of gravitational fields from redshift  $z = 7$  and below. At higher redshifts, the code uses the linear grid-based density instead. The reasoning behind this strategy is that shot noise is constant over time and hence more problematic at high redshift where cosmological perturbations are smaller in comparison. On the other hand, the linear prediction for neutrinos is expected to be very accurate at high redshift. One can therefore reduce the total error by judiciously choosing the time at which the code switches from linear to fully nonlinear neutrino treatment. It is nonetheless reassuring that even without mitigating against shot noise the scatter remains far below 1%.

On small scales the differences are also larger. The lines for `COLA` and `gevolution` track each other closely, but differ by more than 1% from the other codes for  $k > 1 h \text{ Mpc}^{-1}$ . `SWIFT`, `PKDGRAV3`, and `CONCEPT` are low compared to `GADGET-3` for  $k > 1 h \text{ Mpc}^{-1}$ , unlike what was seen in figure 3. `ANUBIS` diverges from `GADGET-3` by more than 1% for  $k > 1 h \text{ Mpc}^{-1}$  for the 0.6 eV neutrino mass case. As mentioned earlier, this is due to the fact that the AMR scheme has a lower effective resolution as the neutrino mass increases, simply because refinement is triggered by clustering. Finally, `NM-GADGET4` is slightly higher than `GADGET-3`. However, these differences remain below 1% well beyond  $k_{\text{Nyq}}$ .

### 5.1.2 Convergence tests

To study the numerical convergence of our results, we consider the effects of finite box size and resolution. Figure 5 shows the relative suppression for the runs with larger volume (left panel) and higher resolution (right panel). When  $L_{\text{box}}$  is doubled at fixed resolution, the agreement remains excellent on linear scales and is sometimes even slightly better around  $k_{\text{Nyq}}$ , providing an important consistency check for most codes. Increasing instead the mass resolution by doubling  $k_{\text{Nyq}}$ , the agreement between the simulations improves significantly on nonlinear scales. Including more scales in either direction, most codes remain within 1% of the reference runs done with `GADGET-3`. The excess on large scales for the case of `ANUBIS` persists as a result of the coarse base grid. For the runs with  $N_{\text{part}} = 1024^3$ , this base grid is even less suited and the time-steppings for the massless cases are set to 0.1 and 0.15 times the original time step for the larger-box and high-resolution runs, respectively.

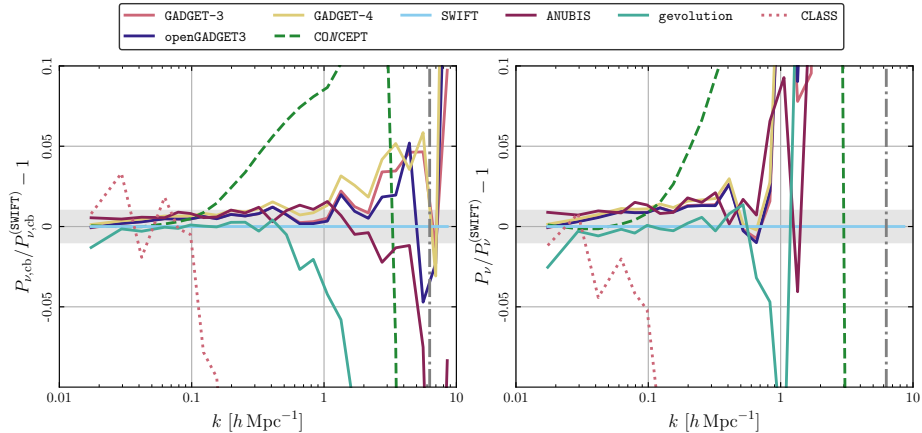




**Figure 5.** The suppression of the power spectrum of CDM and baryons relative to the one measured in the GADGET-3 reference runs at  $z = 0$  for  $\sum m_\nu = 0.15$  eV for the simulations with a larger volume,  $L_{\text{box}} = 1024 h^{-1}$  Mpc and  $N_{\text{part}} = 1024^3$  (left panel), and at a higher resolution in the small volume,  $L_{\text{box}} = 512 h^{-1}$  Mpc and  $N_{\text{part}} = 1024^3$  (right panel). The respective particle Nyquist wavenumbers are indicated by the grey dash-dotted lines. The grey bands highlight the interval of  $\pm 0.01$ .

### 5.1.3 Contributions from neutrinos

The subdominant contributions to  $P_m(k)$  are the cross-power spectrum  $P_{\nu,\text{cb}}(k)$  between neutrinos and the CDM and baryon component, and the auto-power spectrum  $P_\nu(k)$  of neutrinos. As can be seen from eq. (5.1), these are suppressed by the small factors  $f_\nu$  and  $f_\nu^2$ , respectively, and they are themselves additionally strongly suppressed with respect to  $P_{\text{cb}}(k)$  on scales smaller than the neutrino free-streaming scale. While both of these contributions will be exceedingly hard to constrain individually from observations, it is nonetheless interesting to study them in the context of our code comparison in order to highlight some more subtle differences in the numerical schemes. Figure 6 (left panel) shows  $P_{\nu,\text{cb}}(k)$  for various codes relative to the result from the SWIFT code, for the smallest neutrino mass,  $\sum m_\nu = 0.15$  eV, computed from the high-resolution simulations. We use SWIFT as the reference here because it has a very low level of shot noise in the neutrino component, yet is able to track the non-linear evolution of neutrinos very accurately. As is the case with CDM and baryons, linear theory cannot describe neutrino clustering on nonlinear scales and therefore CLASS significantly underestimates the cross-power spectrum for  $k > 0.1 h \text{ Mpc}^{-1}$ . Most other codes use a particle implementation of neutrinos and scatter about the SWIFT prediction partially due to shot noise. The results from CONCEPT have no shot noise, but depart from the other codes for  $k > 0.2 h \text{ Mpc}^{-1}$ . The relative difference to SWIFT is 8% at  $k = 1 h \text{ Mpc}^{-1}$ . Much the same applies to the neutrino auto-power spectrum,  $P_\nu(k)$ , shown relative to the neutrino auto-power spectrum of SWIFT in the right panel of figure 6. Here, for the codes with a neutrino particle ensemble, the dominant contribution to the shot noise is removed. Except for SWIFT this is done by subtracting the inverse of the average neutrino particle density,  $\bar{n}^{-1}$ , from the measured power spectrum, where  $\bar{n}^{-1} = 0.125 h^{-3} \text{ Mpc}^3$  in our high-resolution simulations. For SWIFT the subtracted values are derived from the  $\delta f$  method. The difference



**Figure 6.** Relative cross-power spectrum of neutrinos with CDM and baryons (left) and neutrino auto-power spectrum (right) with respect to `SWIFT` at  $z = 0$  for  $\sum m_\nu = 0.15 \text{ eV}$  for the higher-resolution simulation with  $L_{\text{box}} = 512 h^{-1} \text{ Mpc}$  and  $N_{\text{part}} = 1024^3$ . The Nyquist wavenumber is indicated by the grey dash-dotted line. The grey bands highlight the interval of  $\pm 0.01$ .

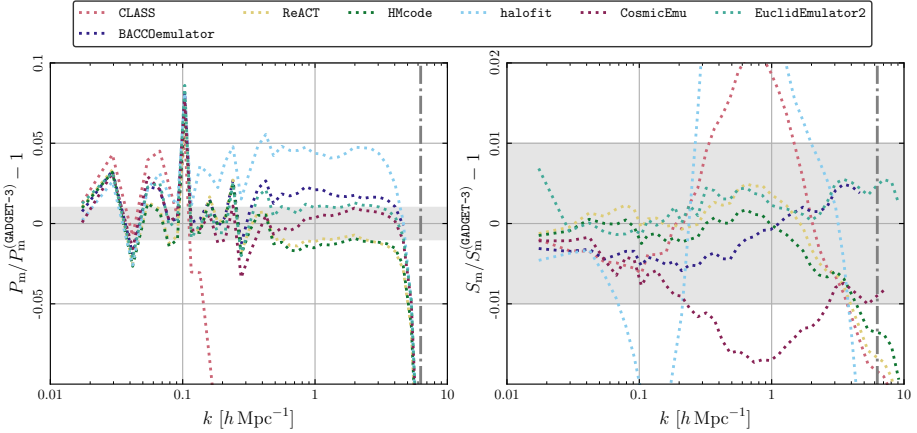
between `SWIFT` and `CONCEPT` is 19% (off the chart) at  $k = 1 h \text{ Mpc}^{-1}$  and the effects of shot noise are even more evident in the other codes. The agreement between `gevolution` and `SWIFT` is quite remarkable, and on the largest scales these results are also more consistent with `CONCEPT` than with the other  $N$ -body codes.

#### 5.1.4 Total matter

Some of the codes, in particular the `EuclidEmulator2`, only provide predictions for the power spectrum of total matter,  $P_m(k)$ . In figure 7, we show the relative agreement of different emulators and other codes predicting  $P_m(k)$  to our high-resolution reference run with `GADGET-3`. The left panel shows the result for the matter power spectrum itself,  $P_m(k)$ , at  $\sum m_\nu = 0.15 \text{ eV}$ . The correlated fluctuations on large scales are due to sample variance which is only present in the reference simulation and not in the predicted spectra. We note that emulators, `HMcode`, and the halo-model reaction method perform slightly better than the fitting recipe of `halofit`. The results of the `EuclidEmulator2` are marginally consistent with the claimed accuracy of 1%, but the neutrino mass lies close to the boundary of parameter space the emulator was trained for. The right panel of figure 7 shows corresponding results for the power suppression factor,  $S_m(k)$ , with respect to the massless scenario. `CosmicEmu` shows a disagreement larger than 1% around  $k \approx 1 h \text{ Mpc}^{-1}$  where the power suppression is largest. Also `halofit` performs poorly, worse even than linear theory (`CLASS`). The other codes remain within 1% of the `GADGET-3` result up to the particle Nyquist scale. Overall our results are in fair agreement with the detailed comparison carried out by Parimbelli et al. [116].

#### 5.2 Bispectra

The nonlinear evolution of matter fluctuations generates a non-vanishing bispectrum, the three-point correlation function of matter in Fourier space, even if non-Gaussianity is negli-



**Figure 7.** Total matter power spectrum  $P_m(k)$  at  $z = 0$  for  $\sum m_\nu = 0.15$  eV from emulators and fitting methods (left panel), and the respective suppression  $S_m(k)$  with respect to the massless case (right panel), compared to the higher-resolution reference **GADGET-3** simulation with  $L_{\text{box}} = 512 h^{-1}$  Mpc and  $N_{\text{part}} = 1024^3$ . The corresponding particle Nyquist wavenumber of the **GADGET-3** run is indicated by the grey dash-dotted line and marks the limit beyond which the estimator of the power spectrum becomes unreliable. Disagreements near and beyond this line are therefore not indicative of errors in the emulators. The grey bands highlight the interval of  $\pm 0.01$ .

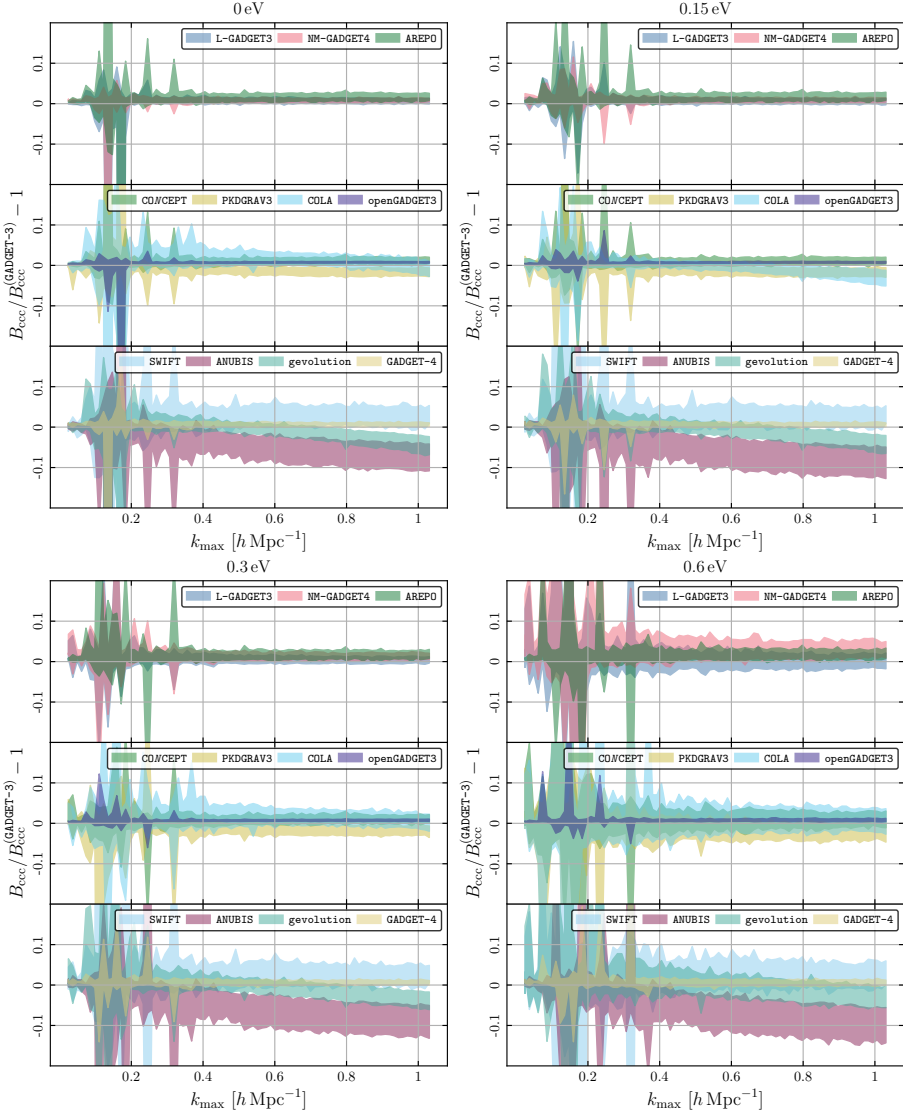
gibly small in the initial conditions. This represents an opportunity for the measurement of neutrino masses, as we expect that the suppression predicted by linear theory is enhanced at the nonlinear level [117–120]. The total matter bispectrum in the presence of massive neutrinos can be schematically defined as

$$\begin{aligned}
 B_{\text{mmm}}(k_1, k_2, k_3) &= (1 - f_\nu)^3 B_{\text{ccc}}(k_1, k_2, k_3) + f_\nu (1 - f_\nu)^2 B_{\text{c}\nu\nu}^{(\text{sym})}(k_1, k_2, k_3) \\
 &\quad + f_\nu^2 (1 - f_\nu) B_{\text{c}\nu\nu}^{(\text{sym})}(k_1, k_2, k_3) + f_\nu^3 B_{\nu\nu\nu}(k_1, k_2, k_3), \quad (5.3)
 \end{aligned}$$

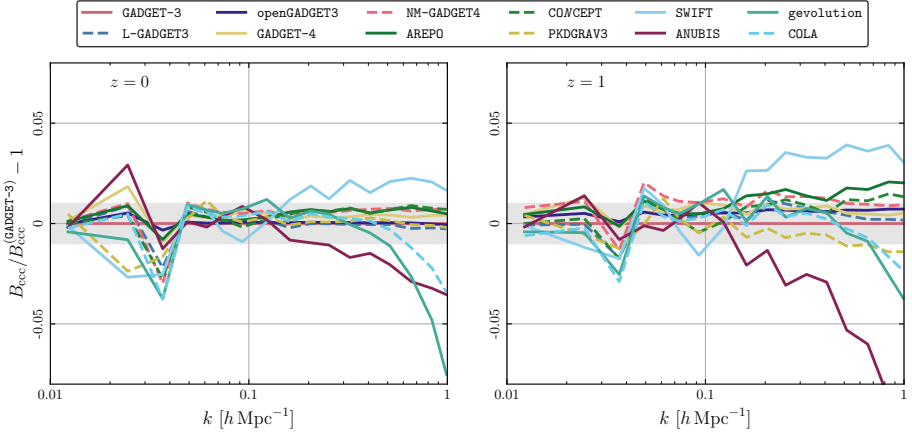
where “ccc” denotes the CDM and baryon bispectrum (we do not write “cbcbcb” to avoid clutter) and we note the presence of cross cold-cold-neutrino “ccν” and cold-neutrino-neutrino “cνν” terms that are symmetrised, as indicated by the superscript “(sym)”. In this work, we focus on the bispectrum of CDM and baryons only, but cross terms have also been investigated in the literature, e.g. by Ruggeri et al. [121]. As for the power spectrum case, the leading term is the one of CDM and baryons.

Figure 8 shows a comparison of the bispectrum  $B_{\text{ccc}}$  as measured at redshift  $z = 1$  by all simulation codes<sup>12</sup> for all triangle configurations and all neutrino masses considered, for the set of runs with  $N_{\text{part}} = 512^3$ . Triangles are plotted as a function of  $k_{\text{max}} = \max(k_1, k_2, k_3)$ . The comparison shows the maximum percentage difference with respect to **GADGET-3** of all triangle configurations at each value of  $k_{\text{max}}$ . For **L-GADGET3**, **openGADGET3**, **GADGET-4**, **PKDGRAV3**, **CONCEPT**, and **NM-GADGET4**, discrepancies are mostly within 5% for  $\sum m_\nu = 0.0$  eV, while steadily growing up to around 10% for massive neutrino cosmologies. Other simulation

<sup>12</sup>**PINOCCHIO** is not used in this test that is mostly focused on nonlinear scales beyond its range of validity.



**Figure 8.** The coloured bands show the scatter of  $B_{\text{ccc}}$  for all triangle configurations with respect to the measurement from GADGET-3 at redshift  $z = 1$ . The horizontal axis indicates the maximum wavenumber in each triangle configuration,  $k_{\text{max}} = \max(k_1, k_2, k_3)$ , in order to present the results in a simple plot. The four panels show different neutrino masses. Each plot uses three subpanels to make the results of the many different codes more visible.



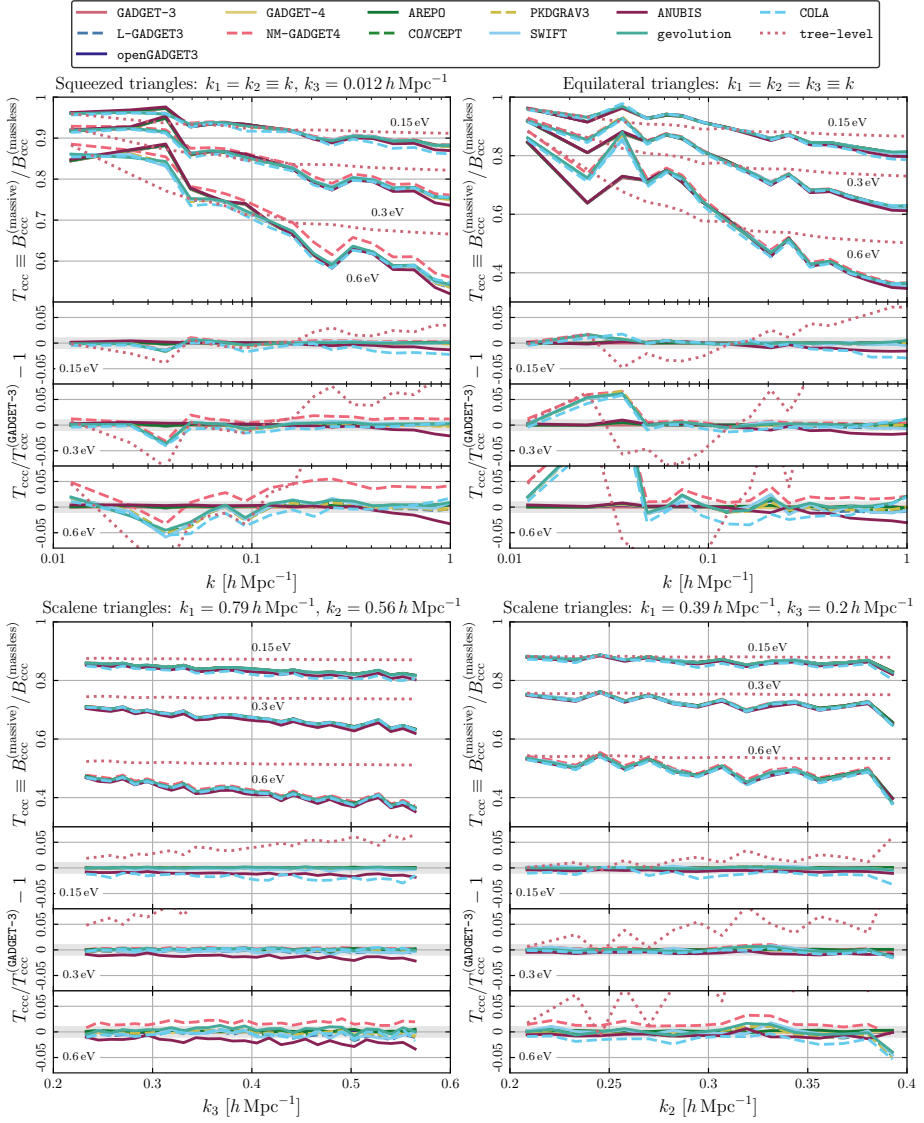
**Figure 9.** Squeezed bispectrum of CDM and baryons as measured from different codes, relative to GADGET-3 at  $z = 0$  and  $z = 1$  for a neutrino mass of  $\sum m_\nu = 0.15\text{eV}$  in the simulation with  $L_{\text{box}} = 512 h^{-1} \text{Mpc}$  and  $N_{\text{part}} = 512^3$  CDM and baryon particles. Results shown are for the squeezed configuration where  $k_1 = k_2 \equiv k$ ,  $k_3 = 0.012 h \text{Mpc}^{-1}$ . The grey bands highlight the interval of  $\pm 0.01$ .

codes are within 10% already at  $\sum m_\nu = 0.0\text{eV}$ . ANUBIS and `gevolution` show some of the strongest deviations at large  $k_{\text{max}}$ , but this is mainly a result of finite resolution as we find much better agreement in the higher-resolution runs. At low  $k_{\text{max}}$ , strong fluctuations can be observed where measurements can cross zero because of sampling variance, which in turn leads to numerical issues when taking ratios.

In figure 9, we consider specifically a squeezed configuration for which  $k_1 = k_2$  and  $k_3 = 0.012 h \text{Mpc}^{-1}$  and show the agreement between different codes for a total neutrino mass of  $\sum m_\nu = 0.15\text{eV}$  at redshift  $z = 0$  (left panel) and  $z = 1$  (right panel). We use measurements from our simulations with  $L_{\text{box}} = 512 h^{-1} \text{Mpc}$  and  $N_{\text{part}} = 512^3$ . The relative agreement is better at low redshift, partially due to the fact that the signal amplitude is larger there.

Figure 10 is a comparison of simulation codes for different triangle configurations, for all choices of neutrino masses at redshift  $z = 1$ . We consider four triangle configurations: squeezed, equilateral and two different scalene configurations. Squeezed configurations refer to triangles where one of the side is much shorter than the other two (in Fourier space) which corresponds to looking at the correlation of a distant point with two points close to each other. Equilateral configurations, instead, refer to the correlation of three points at equal distance. Scalene triangles do not have any specific symmetry. In detail, we consider

- **squeezed configurations**, for which  $k_1 = k_2$  and  $k_3 = 0.012 h \text{Mpc}^{-1}$ , plotted as a function of  $k_1$  as in figure 9;
- **equilateral configurations**, for which  $k_1 = k_2 = k_3$ , plotted as a function of  $k_1$ ;
- **scalene configurations A**, for which  $k_1 = 0.79 h \text{Mpc}^{-1}$ ,  $k_2 = 0.56 h \text{Mpc}^{-1}$ , plotted as a function of  $k_3$ ;



**Figure 10.** The four panels show bispectrum measurements at redshift  $z = 1$  in the simulations with  $L_{\text{box}} = 512 h^{-1} \text{ Mpc}$  and  $N_{\text{part}} = 512^3$  for different triangle configurations: squeezed (top left panel), equilateral (top right panel), and scalene configurations A and B (bottom panels). In each panel, the top subpanel shows the suppression ratio of the bispectrum of CDM and baryons for three different neutrino masses  $\sum m_\nu \in \{0.15, 0.3, 0.6\} \text{ eV}$  with respect to the massless case, and the three bottom subpanels show the respective relative differences of the various codes when compared to GADGET-3.

- **scalene configurations B**, for which  $k_1 = 0.39 h \text{ Mpc}^{-1}$ ,  $k_3 = 0.2 h \text{ Mpc}^{-1}$ , plotted as a function of  $k_2$ .

In each of the four panels of figure 10, the top subpanel shows the ratio between the CDM and baryon bispectrum for massive neutrino cosmologies over massless ones, which we define in analogy to the case of the power spectrum as

$$T_{\text{ccc}}(k_1, k_2, k_3) = \frac{B_{\text{ccc}}^{(\text{massive})}(k_1, k_2, k_3)}{B_{\text{ccc}}^{(\text{massless})}(k_1, k_2, k_3)}. \quad (5.4)$$

The three bottom subpanels show the relative differences of the measurements of the suppression ratio in the various codes with respect to **GADGET-3** at each of the three neutrino masses, i.e.  $\sum m_\nu \in \{0.15, 0.3, 0.6\} \text{ eV}$  (from top to bottom). For all configurations considered, discrepancies fall broadly within the 5% range. As expected, massive neutrinos suppress the bispectrum of CDM and baryons at all scales, with a stronger effect at smaller scales. For comparison, we also show the tree-level prediction from perturbation theory, using

$$B_{\text{ccc}}^{(\text{tree-level})}(k_1, k_2, k_3) = 2F_2(\mathbf{k}_1, \mathbf{k}_2)P_{\text{cb}}^L(k_1)P_{\text{cb}}^L(k_2) + 2 \text{ permutations}, \quad (5.5)$$

where

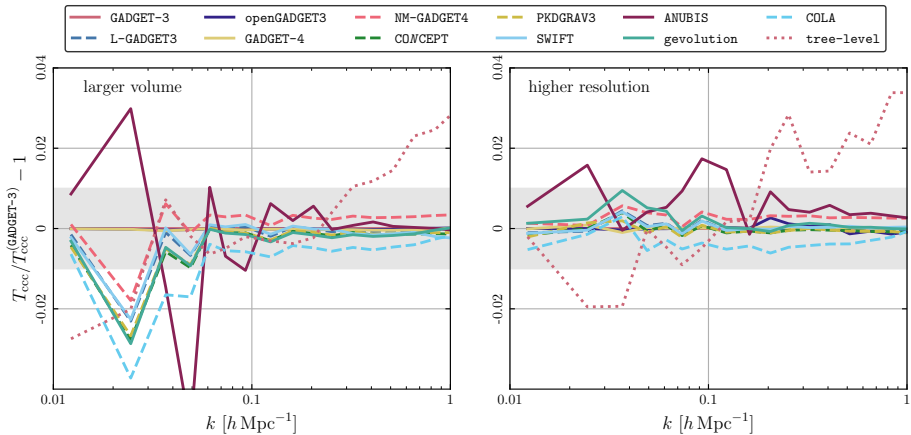
$$F_2(\mathbf{k}_1, \mathbf{k}_2) = \frac{5}{7} + \frac{1}{2} \frac{\mathbf{k}_1 \cdot \mathbf{k}_2}{k_1 k_2} \left( \frac{k_1}{k_2} + \frac{k_2}{k_1} \right) + \frac{2}{7} \frac{(\mathbf{k}_1 \cdot \mathbf{k}_2)^2}{k_1^2 k_2^2}, \quad (5.6)$$

and  $P_{\text{cb}}^L$  is the linear power spectrum of CDM and baryons generated by **CLASS**. We can see in figure 10 that the suppression ratio is in good agreement with this prediction when all the three scales  $k_1, k_2, k_3$  have a small wavenumber, and that the measured suppression is generally stronger if some of the wavenumbers are large. This is in line with the results seen in the power spectrum, where strong nonlinearities lead to additional suppression.

At the largest scales, i.e. when  $k_1, k_2, k_3 \lesssim 0.1 h \text{ Mpc}^{-1}$ , a distinct feature can be discerned which is particularly prominent in the equilateral configuration and for larger neutrino masses: the measurements from the various codes separate into two groups, **GADGET-3**, **openGADGET3**, **GADGET-4**, **AREPO**, and **ANUBIS** on the one side, and **L-GADGET3**, **NM-GADGET4**, **CONCEPT**, **PKDGRAV3**, **SWIFT**, **gevolution**, and **COLA** on the other side. The latter group includes all the codes that employ a mesh-based method, and all of them have means to mitigate against shot noise. We therefore suspect that this dichotomy originates from shot noise in the particle method. This could be tested, e.g. by increasing the number of neutrino particles until convergence is achieved.

As with the case of the power spectrum, we conducted various checks concerning numerical convergence with respect to finite-volume and resolution effects. These show a consistent picture that is in line with what we discussed in section 5.1.2. As an example, figure 11 presents the results for the case of the squeezed configuration in simulations with  $N_{\text{part}} = 1024^3$ , with a larger volume (left panel) or a higher resolution (right panel) than our simulations with  $N_{\text{part}} = 512^3$ . In both cases, the agreement on smaller scales is improved: for the larger volume this happens because more independent triangles contribute to each measurement, while for the higher resolution this is due to the better numerical convergence of the density field on small scales.

Overall we may conclude that the  $N$ -body methods which produce highly consistent two-point statistics also tend to agree very well on the three-point statistics presented here. **NM-GADGET4** appears to be an outlier, showing considerable deviations for squeezed configurations when the sum of the neutrino masses is large. This is however not unexpected since the



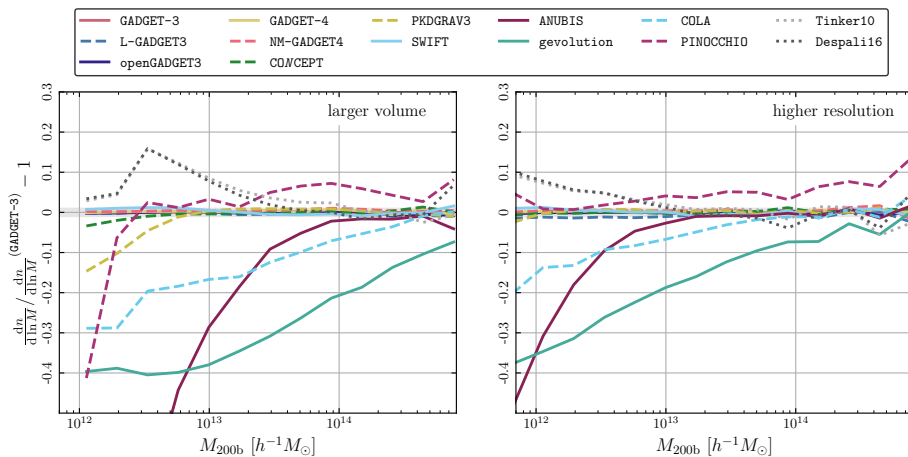
**Figure 11.** The suppression of the squeezed bispectrum of CDM and baryons relative to the one measured in the `GADGET-3` reference runs at  $z = 1$  for  $\sum m_\nu = 0.15$  eV for the simulations with a larger volume,  $L_{\text{box}} = 1024 h^{-1}$  Mpc and  $N_{\text{part}} = 1024^3$  (left panel), and at a higher resolution in the small volume,  $L_{\text{box}} = 512 h^{-1}$  Mpc and  $N_{\text{part}} = 1024^3$  (right panel). Results shown are for the squeezed configuration where  $k_1 = k_2 \equiv k$ ,  $k_3 = 0.012 h \text{ Mpc}^{-1}$ . The grey bands highlight the interval of  $\pm 0.01$ .

final gauge transformation from Newtonian motion gauge has been neglected here. This transformation mainly acts at large scales and would therefore affect the squeezed configurations. At low neutrino mass, where the method works best, this effect is almost negligible though. It also becomes minimal at redshift  $z = 0$  which was set as the target redshift for this method.

### 5.3 Halo mass function

From the halo catalogues produced by `Denhf`, we estimate the halo mass functions (considering only the contribution from CDM and baryons) and compare them to the predictions by Tinker et al. [113], hereafter Tinker10, as well as Despali et al. [111], hereafter Despali16. For these predictions, we use the linear power spectra of CDM and baryons calculated by `CLASS` for the respective neutrino cosmologies in the modelling of the theoretical halo mass functions. It has been shown by Costanzi et al. [122] that this approach reproduces the halo mass function well for neutrino cosmologies. Figure 12 shows the ratio of the halo mass functions relative to the halo mass function of `GADGET-3` at a neutrino mass of  $\sum m_\nu = 0.15$  eV for the runs with  $N_{\text{part}} = 1024^3$ , in the large volume where  $L_{\text{box}} = 1024 h^{-1}$  Mpc (left panel), as well as for the higher-resolution setup with  $L_{\text{box}} = 512 h^{-1}$  Mpc (right panel). At the high-mass end, the agreement between different codes is generally very good, and fluctuations are smaller in the larger volume due to better statistics. At low masses  $M_{200b} < 10^{13} h^{-1} M_\odot$ , the number density of halos is underestimated by `COLA`, `gevolution`, and `ANUBIS` by up to 50% for the lower resolution. At higher resolution the agreement improves. The relatively poor performance of `gevolution` in predicting the halo mass function can be understood from the fact that the code uses a uniform mesh. This leads to a smoothing of small-scale structures and generally to a mass estimate of halos that is poorly converged at the low-mass end. `COLA` suffers from the same limitation, but the simulations used a mesh with significantly higher





**Figure 12.** Halo mass functions relative to the one of GADGET-3, for  $N_{\text{part}} = 1024^3$  at  $z = 0$  and neutrino mass  $\sum m_\nu = 0.15 \text{ eV}$ . The result for the larger-volume runs with  $L_{\text{box}} = 1024 h^{-1} \text{ Mpc}$  is shown in the left panel while the right panel shows the result for the higher-resolution runs with  $L_{\text{box}} = 512 h^{-1} \text{ Mpc}$ .

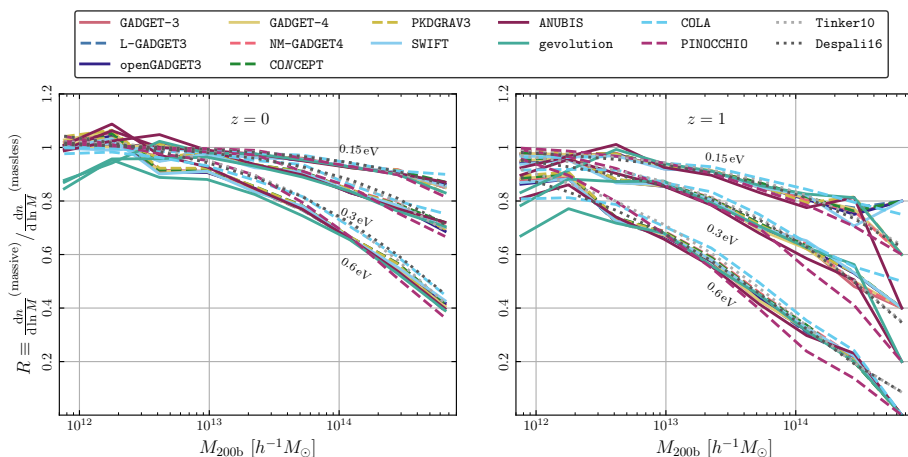
resolution in this case. Specifically, in the runs with  $N_{\text{part}} = 1024^3$ , COLA used a mesh of  $3072^3$  grid points, while `evolution` used a mesh of  $2048^3$  grid points.<sup>13</sup>

Figure 13 shows the suppression of the halo mass function due to neutrinos with masses  $\sum m_\nu \in \{0.15, 0.3, 0.6\} \text{ eV}$  at redshift  $z = 0$  (left panel) and  $z = 1$  (right panel). At low halo masses, there is little suppression, while going to higher masses the number density of halos is more and more suppressed. The higher the neutrino masses, and the higher the redshift, the stronger the suppression: at  $z = 0$  and  $\sum m_\nu = 0.15 \text{ eV}$  the suppression goes down to a factor of 0.9 at halo masses of  $10^{14} h^{-1} M_\odot$ , while at  $z = 1$  and  $\sum m_\nu = 0.6 \text{ eV}$  the suppression goes down to 0.4 at the same halo mass. In analogy to the case of the power spectrum, we define the suppression ratio with respect to the massless case as

$$R = \frac{\frac{dn^{(\text{massive})}}{d \ln M}}{\frac{dn^{(\text{massless})}}{d \ln M}}. \quad (5.7)$$

Figure 14 shows this suppression ratio relative to the one measured from GADGET-3 for a sum of neutrino masses of  $\sum m_\nu = 0.15 \text{ eV}$ . The different codes generally agree within 3% on the suppression ratio, even in cases where the halo mass function was poorly converged in figure 12. Our data show a trend that the suppression is about 1% stronger than predicted by the models of Tinker10 and Despali16. The COLA results are a slight outlier, agreeing more with these models than with the other simulations.

<sup>13</sup>Running `evolution` on such a fine mesh, i.e. with less than one particle per cell on average, was not supported in the public release of the code. In such a situation, the evolution would become unstable due to the low order of the finite-difference gradients used in the particle update. A second-order gradient computation was therefore implemented for this work, a feature that is made available in a recent patch of the code.



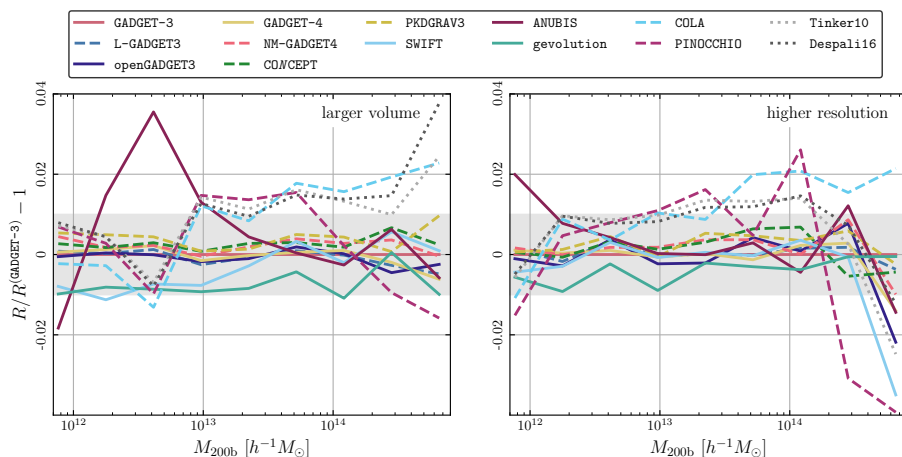
**Figure 13.** The halo mass function for different neutrino masses, relative to the case with massless neutrinos for each code, respectively. We show the results for the simulations with  $L_{\text{box}} = 512 h^{-1} \text{Mpc}$  and  $N_{\text{part}} = 512^3$  at  $z = 0$  (left panel) and at  $z = 1$  (right panel).

#### 5.4 Halo bias

Finally, we study the halo bias for a fixed selection of halos defined by a mass threshold of  $M_{200b} > 10^{13} h^{-1} M_{\odot}$ . However, since the halo mass function shows considerable differences between the different simulations, sometimes due to the fact that the mass estimate is not well converged at the low-mass end (certainly for `gevolution`, `COLA`, and `ANUBIS`), we apply the halo selection as follows. First, we select the halos above the mass threshold in the reference runs done with `GADGET-3`. We may call the size of the selected population  $N_h$ . Then, for each other code, we generate the sample by selecting the  $N_h$  most massive halos. The reasoning for this approach is that, while the estimated masses of individual halos may differ significantly between different codes, we still expect there to be a tight correlation that largely preserves the mass ordering. Another way to think about this is to consider a simple abundance matching of  $N_h$  sources, assigned to the centers of the most massive halos. We compare the bias measurements to the prediction by Tinker et al. [113] (Tinker10). Here the large-scale bias is estimated from the mass-dependent peak height of halos in the linear density field. Given the `GADGET-3` halo masses, we model the peak heights using the linear power spectrum of CDM and baryons calculated by `CLASS` for the respective neutrino cosmology. We then take the average of all biases obtained for each halo mass to get the final prediction. Note that the prediction of Tinker10 is only expected to work in the linear regime.

Figure 15 shows the bias measurements from the simulations with larger volume,  $L_{\text{box}} = 1024 h^{-1} \text{Mpc}$ . We define the scale-dependent halo bias  $b(k)$  as the ratio of the cross-power spectrum of halos with CDM and baryons and the auto-power spectrum of CDM and baryons, i.e.

$$b(k) = \frac{P_{\text{h,cb}}(k)}{P_{\text{cb}}(k)}. \quad (5.8)$$



**Figure 14.** Suppression of the halo mass functions relative to the one measured in `GADGET-3` at redshift  $z = 0$  and for a total neutrino mass of  $\sum m_\nu = 0.15$  eV. We show the results for the simulations with  $L_{\text{box}} = 1024 h^{-1} \text{Mpc}$  and  $N_{\text{part}} = 1024^3$  in the left panel, and  $L_{\text{box}} = 512 h^{-1} \text{Mpc}$  and  $N_{\text{part}} = 1024^3$  in the right panel. The grey bands highlight the interval of  $\pm 0.01$ .

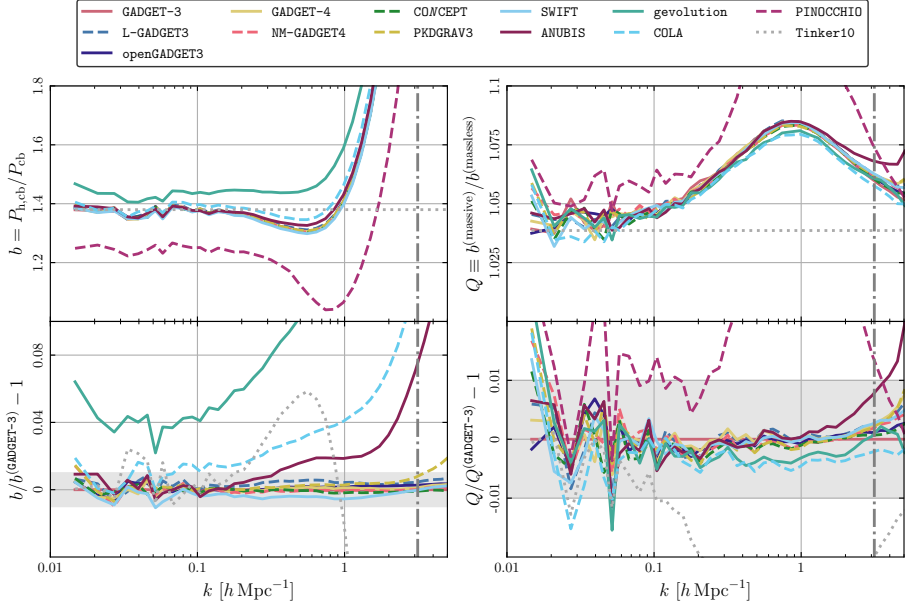
It has been shown by Castorina et al. [77] that defining the bias factor with respect to cold species gives closer-to-universal and less scale-dependent results than using the same definition with respect to total matter. As can be seen in the left panel of figure 15, the bias measurements agree reasonably well on large scales except for `gevolution` where the bias is measured to be about 4% larger, and for `PINOCCHIO` where the bias is measured to be about 10% smaller. In analogy to the case of the power spectrum, we again define a bias ratio with respect to the massless case, which in this situation will quantify the increase (rather than suppression) of the bias in the presence of massive neutrinos,

$$Q(k) = \frac{b^{(\text{massive})}(k)}{b^{(\text{massless})}(k)}. \quad (5.9)$$

Results for this bias ratio are shown in the right panel of figure 15. Here the agreement between different codes is excellent, well within 1% over almost the entire range of scales probed. For `PINOCCHIO` the bias ratio is about 1% accurate up to  $k \simeq 0.3 h \text{Mpc}^{-1}$ .

To study the robustness of our results with respect to the mass resolution of the simulations we repeat the bias measurements in the runs with higher resolution, i.e. with  $L_{\text{box}} = 512 h^{-1} \text{Mpc}$  and  $N_{\text{part}} = 1024^3$ . The smaller simulation volume leads to a higher level of shot noise in the halo counts, which incurs somewhat larger fluctuations when compared to the larger volume. As can be seen in figure 16, the agreement between the different codes is improved significantly, in particular for codes that have difficulties in predicting the halo mass function accurately (`gevolution`, `COLA`, and `ANUBIS`). The results for `PINOCCHIO` do not improve significantly, as the discrepancy is mainly due to the approximate nature of the method rather than lack of resolution.

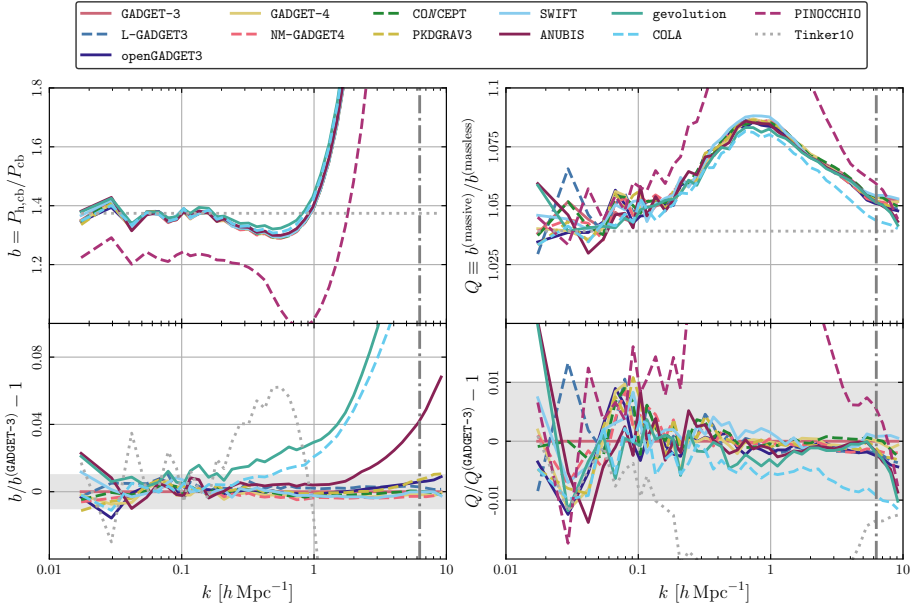
It is worth pointing out that the bias ratio  $Q$  has a shape similar to the inverted power spectrum ratio  $S_{\text{cb}}$ . This is actually expected, and was recently discussed by Hassani et



**Figure 15.** Halo bias with respect to CDM and baryons at  $z = 0$  and neutrino mass  $\sum m_\nu = 0.15 \text{ eV}$  for the simulations with  $L_{\text{box}} = 1024 h^{-1} \text{ Mpc}$  and  $N_{\text{part}} = 1024^3$ . In the GADGET-3 reference simulations, all halos with  $M_{200b} > 10^{13} h^{-1} M_\odot$  are selected, providing a sample of size  $N_h$ . For the other simulations, we then select the most massive  $N_h$  halos. The grey bands in the lower panels highlight the interval of  $\pm 0.01$ .

al. [123]. It means that the power spectrum of halos, when selected at fixed mass threshold, is much less sensitive to the neutrino mass than the power spectrum of CDM and baryons. On the other hand, synthetic catalogues are often created in such a way that the observed abundance of a certain type of object is reproduced (abundance matching). In such a situation, it may be more appropriate to study the dependence of the bias on the neutrino mass at fixed number count. We therefore repeat our measurements, but keeping the size of all samples fixed at  $N_h^{(\text{massless})}$ , which is the number of halos with  $M_{200b} > 10^{13} h^{-1} M_\odot$  in the GADGET-3 reference simulation at zero neutrino mass. In other words, when selecting the halo sample for non-zero neutrino mass, we still select the  $N_h^{(\text{massless})}$  most massive halos in all simulations. This effectively reduces the mass threshold of the selection for the massive neutrino case when compared to the previous procedure.

Figure 17 shows the results of the bias measurement obtained through this procedure, using the higher-resolution simulations. We observe that the bias still increases with neutrino mass, but not quite as much as in figure 16 where a fixed halo mass threshold was used. The large-scale bias indicated by the dotted line (Tinker10) is about 0.01, or one percentage point, lower so that the corresponding bias ratio  $Q$  drops by 0.7%. The largest effect in  $Q$  appears around  $k \approx 1 h \text{ Mpc}^{-1}$  where the change can be as much as 2% due to the different halo selection. The interplay between bias enhancement and the suppression of the matter power

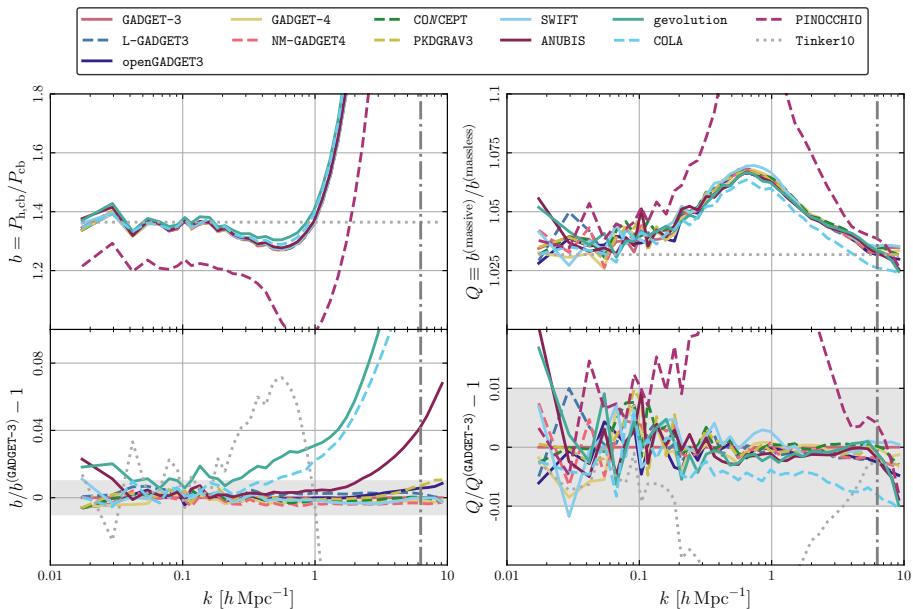


**Figure 16.** Halo bias with respect to CDM and baryons at  $z = 0$  and neutrino mass  $\sum m_\nu = 0.15 \text{ eV}$  for the higher-resolution simulations with  $L_{\text{box}} = 512 h^{-1} \text{ Mpc}$  and  $N_{\text{part}} = 1024^3$ . In the **GADGET-3** reference simulations, all halos with  $M_{200b} > 10^{13} h^{-1} M_\odot$  are selected, providing a sample of size  $N_h$ . For the other simulations, we then select the most massive  $N_h$  halos. The grey bands in the lower panels highlight the interval of  $\pm 0.01$ .

spectrum has another layer of complexity due to the way in which the sample is selected. This needs to be studied carefully in the context of the specific numerical recipes that are employed in the production of synthetic catalogues.

## 6 Discussion

Accurate and reliable modelling of the signatures that the neutrino mass imprints on the observables used to test the cosmological model is an essential ingredient for the data analysis of all upcoming galaxy surveys, and in particular for *Euclid*. Such modelling necessarily requires a self-consistent description of the linear and possibly nonlinear clustering of neutrinos along with the nonlinear evolution of dark matter and baryonic structures. By comparing results across different implementations, including eleven full  $N$ -body implementations, two  $N$ -body schemes with fast time integration based on Lagrangian perturbation theory, and a further four codes that predict the nonlinear matter power spectra directly, we establish that current numerical techniques are in sub-percent agreement with regards to modelling the impact of massive neutrinos on the most common summary statistics of cosmological large-scale structure. We identify several specific situations where larger modelling errors can occur, but such shortfalls are generally well understood in terms of approximations or other compromises that were made in these situations. Our results can therefore be used as



**Figure 17.** Halo bias with respect to CDM and baryons at  $z = 0$  and neutrino mass  $\sum m_\nu = 0.15$  eV for the higher-resolution simulations with  $L_{\text{box}} = 512 h^{-1} \text{Mpc}$  and  $N_{\text{part}} = 1024^3$ . In the **GADGET-3** reference simulation for  $\sum m_\nu = 0$  eV, all halos with  $M_{200b} > 10^{13} h^{-1} M_\odot$  are selected, providing a sample of size  $N_h^{(\text{massless})}$ . We then select the most massive  $N_h^{(\text{massless})}$  halos in all the other simulations, even for those with non-zero neutrino mass. The grey bands in the lower panels highlight the interval of  $\pm 0.01$ .

a detailed guide for choosing the preferred modelling techniques for any application given its requirements in terms of resources, accuracy, and quantities that need to be modelled. The validation presented here is the crucial first step for building up confidence in the numerical tools employed in the data analysis pipeline of *Euclid*. It is particularly vital when considering the actual measurement of the neutrino mass scale from the data, which is one of the key science goals of the mission.

The fastest method of predicting simple summary statistics like the nonlinear matter power spectrum are emulators, and they will therefore play a crucial role in the cosmological likelihood analysis of *Euclid* and other large-scale structure surveys. They are of course many orders of magnitude faster than simulations but tend to outperform even semi-analytic models which often have some bottlenecks in their numerical evaluation. However, emulators can only be as accurate as the simulations they are trained on, and it is therefore important to understand the modelling errors of simulations too. We find that the current state of the art for emulators yield an absolute precision on the power spectrum of total matter better than 2% and can predict the relative change due to the neutrino mass to better than 1% on all scales considered in this work. Interestingly, the best semi-analytic fitting methods available, in particular **ReACT** and **HMcode**, can achieve similar performance.

Overall our results demonstrate that we are in a fairly comfortable position, with several independent numerical techniques at our disposal that produce consistent results at the sub-percent level if we employ them diligently. The community has also implemented such techniques in a large number of different  $N$ -body codes, such that there is no shortage in choice of which code one wants to use. Moreover, our detailed comparison of particle-based and mesh-based techniques shows that the assumption of linear neutrinos is clearly sufficient to reach percent accuracy, even up to scales of the order of  $k \approx 7 h \text{Mpc}^{-1}$  relevant for predicting the weak-lensing signal in *Euclid*. We note that some codes have inherent difficulties reaching such levels of absolute accuracy due to effects of finite resolution. This is obvious in the cases where a uniform mesh is employed in the computation of gravitational interactions (*gevolution* and *COLA*), but AMR does not solve the issue entirely as the example of *ANUBIS* illustrates. The relative impact of massive neutrinos can nonetheless be predicted very accurately with those codes. Here we do of course not attempt to address the additional challenge of modelling baryonic effects, i.e. astrophysical processes, down to such scales as this can be treated separately, see e.g. Martinelli et al. [124] for a discussion. On mildly nonlinear scales and in particular at redshifts  $z \gtrsim 1$  relevant for *Euclid*, a “sophisticated 3LPT” realisation like the one produced with *PINOCCHIO*, based on a scale-dependent linear growth rate computed from *CAMB* and propagated to second- and third-order LPT with standard techniques, can be useful to produce a large number of halo catalogues in a limited amount of computing time, see e.g. Fumagalli et al. [10].

The summary statistics considered in our analysis include auto- and cross-power spectra of the CDM and baryon component and neutrinos, bispectra of the CDM and baryon component, halo mass functions, and halo bias. We present results for redshifts  $z = 0$  and  $z = 1$ , relevant for galaxy surveys like *Euclid*. We do not consider redshift-space distortions or other effects that occur due to taking observations on our past light cone, and leave a detailed investigation of these effects to future work. However, we expect that no big surprises would appear given our level of confidence in the modelling of the summary statistics presented here.

In order to aid future code development, we make our reference simulations and analysis pipelines available via a public repository (see data availability statement below). This provides a reliable baseline against which further numerical methods can be validated, and it showcases the current state-of-the-art in modelling massive neutrinos in cosmology.

## Acknowledgments

JA acknowledges financial support from the Swiss National Science Foundation. BB was supported by a U.K. Research and Innovation Stephen Hawking Fellowship (EP/W005654/1). MBa acknowledges support by the project “Combining Cosmic Microwave Background and Large Scale Structure data: an Integrated Approach for Addressing Fundamental Questions in Cosmology”, funded by the MIUR Progetti di Ricerca di Rilevante Interesse Nazionale (PRIN) Bando 2017 — grant 2017YJYZAH. CH-A acknowledges support from the Excellence Cluster ORIGINS which is funded by the Deutsche Forschungsgemeinschaft (DFG, German Research Foundation) under Germany’s Excellence Strategy — EXC-2094 — 390783311. BSW is supported by a Royal Society Enhancement Award (grant no. RGF\EA\181023). RM, DFM, HAW, FH thank the Research Council of Norway for their support and our computations were performed on resources provided by UNINETT Sigma2 — the National Infrastructure for High Performance Computing and Data Storage in Norway. CM acknowledges support from a U.K. Research and Innovation Future Leaders Fellowship [grant

MR/S016066/1]. The PINOCCHIO simulations were performed on Queen Mary’s Apocrita HPC facility, supported by QMUL Research-IT. CG acknowledges the support from the grant PRIN-MIUR 2017 WSCC32 ZOOMING and from the Italian National Institute of Astrophysics under the grant “Bando PRIN 2019,” PI: Viola Allevato. TC is supported by the INFN INDARK PD51 grant and the FARE MIUR grant ‘ClustersXEuclid’ R165SBKTMA. KD acknowledges support by the Deutsche Forschungsgemeinschaft (DFG, German Research Foundation) under Germany’s Excellence Strategy — EXC-2094 — 390783311 and the COMPLEX project from the European Research Council (ERC) under the European Union’s Horizon 2020 research and innovation program grant agreement ERC-2019-AdG 882679. The openGADGET3 simulations were carried out at the Leibniz Supercomputer Center (LRZ) under the project pr86re. CA and BL are supported by an European Research Council Starting Grant (ERC-StG-716532), and BL also acknowledges support by the U.K. Science and Technology Facilities Council Consolidated Grants No. ST/I00162X/1 and ST/P000541/1. KK is supported by the U.K. Science and Technology Facilities Council (grant numbers ST/S000550/1 and ST/W001225/1). MV and GP are supported by the INFN INDARK PD 51 grant and by the ASI-INAF n. 2017-14-H.0 agreement. REA and MZ acknowledge the support of the ERC-STG number 716151 (BACCO). This work used the DiRAC@Durham facility managed by the Institute for Computational Cosmology on behalf of the STFC DiRAC HPC Facility (<https://dirac.ac.uk/>). The equipment was funded by BEIS via STFC capital grants ST/K00042X/1, ST/P002293/1, ST/R002371/1 and ST/S002502/1, Durham University and STFC operation grant ST/R000832/1. DiRAC is part of the U.K. National e-Infrastructure.

The Euclid Consortium acknowledges the European Space Agency and a number of agencies and institutes that have supported the development of *Euclid*, in particular the Academy of Finland, the Agenzia Spaziale Italiana, the Belgian Science Policy, the Canadian Euclid Consortium, the French Centre National d’Etudes Spatiales, the Deutsches Zentrum für Luft- und Raumfahrt, the Danish Space Research Institute, the Fundação para a Ciência e a Tecnologia, the Ministerio de Ciencia e Innovación, the National Aeronautics and Space Administration, the National Astronomical Observatory of Japan, the Netherlandse Onderzoekschool Voor Astronomie, the Norwegian Space Agency, the Romanian Space Agency, the State Secretariat for Education, Research and Innovation (SERI) at the Swiss Space Office (SSO), and the United Kingdom Space Agency. A complete and detailed list is available on the *Euclid* web site (<http://www.euclid-ec.org>).

For the purpose of open access, the authors have applied a Creative Commons Attribution (CC BY) licence to any Author Accepted Manuscript version arising from this work and upload the accepted version to arXiv with CC BY licence.

**Data availability.** Raw data from our reference runs (GADGET-3), and all reduced data (summary statistics) presented in this work are available at <https://doi.org/10.5281/zenodo.7868793>. We also provide initial data, parameter specifications for CLASS, and a documented analysis pipeline to facilitate further validations against our results.

## References

- [1] R. Laureijs et al., *Euclid definition study report*, [arXiv:1110.3193](https://arxiv.org/abs/1110.3193) [INSPIRE].
- [2] E. Di Valentino, A. Melchiorri and J. Silk, *Cosmological constraints in extended parameter space from the Planck 2018 legacy release*, *JCAP* **01** (2020) 013 [[arXiv:1908.01391](https://arxiv.org/abs/1908.01391)] [INSPIRE].



- [3] eBOSS collaboration, *Completed SDSS-IV extended Baryon Oscillation Spectroscopic Survey: cosmological implications from two decades of spectroscopic surveys at the Apache Point Observatory*, *Phys. Rev. D* **103** (2021) 083533 [[arXiv:2007.08991](#)] [[INSPIRE](#)].
- [4] N. Palanque-Delabrouille et al., *Hints, neutrino bounds and WDM constraints from SDSS DR14 Lyman- $\alpha$  and Planck full-survey data*, *JCAP* **04** (2020) 038 [[arXiv:1911.09073](#)] [[INSPIRE](#)].
- [5] P.L. Taylor, T.D. Kitching and J.D. McEwen, *Preparing for the cosmic shear data flood: optimal data extraction and simulation requirements for stage IV dark energy experiments*, *Phys. Rev. D* **98** (2018) 043532 [[arXiv:1804.03667](#)] [[INSPIRE](#)].
- [6] EUCLID collaboration: A. Blanchard et al., *Euclid preparation: VII. Forecast validation for Euclid cosmological probes*, *Astron. Astrophys.* **642** (2020) A191 [[arXiv:1910.09273](#)] [[INSPIRE](#)].
- [7] EUCLID collaboration: M. Knabenhans et al., *Euclid preparation: II. The EuclidEmulator — a tool to compute the cosmology dependence of the nonlinear matter power spectrum*, *Mon. Not. Roy. Astron. Soc.* **484** (2019) 5509 [[arXiv:1809.04695](#)] [[INSPIRE](#)].
- [8] EUCLID collaboration: M. Knabenhans et al., *Euclid preparation: IX. EuclidEmulator2 — power spectrum emulation with massive neutrinos and self-consistent dark energy perturbations*, *Mon. Not. Roy. Astron. Soc.* **505** (2021) 2840 [[arXiv:2010.11288](#)] [[INSPIRE](#)].
- [9] EUCLID collaboration: T. Castro et al., *Euclid preparation: XXIV. Calibration of the halo mass function in  $\Lambda(\nu)$ CDM cosmologies*, *Astron. Astrophys.* **671** (2023) A100 [[arXiv:2208.02174](#)] [[INSPIRE](#)].
- [10] A. Fumagalli et al., *Euclid: effects of sample covariance on the number counts of galaxy clusters*, *Astron. Astrophys.* **652** (2021) A21 [[arXiv:2102.08914](#)] [[INSPIRE](#)].
- [11] EUCLID collaboration: A. Fumagalli et al., *Euclid preparation. XXVII. Covariance model validation for the 2-point correlation function of galaxy clusters*, [arXiv:2211.12965](#) [[INSPIRE](#)].
- [12] R.E. Angulo and O. Hahn, *Large-scale dark matter simulations*, [arXiv:2112.05165](#) [[DOI:10.1007/s41115-021-00013-z](#)] [[INSPIRE](#)].
- [13] J. Brandbyge, S. Hannestad, T. Haugbølle and B. Thomsen, *The effect of thermal neutrino motion on the non-linear cosmological matter power spectrum*, *JCAP* **08** (2008) 020 [[arXiv:0802.3700](#)] [[INSPIRE](#)].
- [14] M. Viel, M.G. Haehnelt and V. Springel, *The effect of neutrinos on the matter distribution as probed by the intergalactic medium*, *JCAP* **06** (2010) 015 [[arXiv:1003.2422](#)] [[INSPIRE](#)].
- [15] S. Agarwal and H.A. Feldman, *The effect of massive neutrinos on the matter power spectrum*, *Mon. Not. Roy. Astron. Soc.* **410** (2011) 1647 [[arXiv:1006.0689](#)] [[INSPIRE](#)].
- [16] S. Bird, M. Viel and M.G. Haehnelt, *Massive neutrinos and the non-linear matter power spectrum*, *Mon. Not. Roy. Astron. Soc.* **420** (2012) 2551 [[arXiv:1109.4416](#)] [[INSPIRE](#)].
- [17] F. Villaescusa-Navarro et al., *Cosmology with massive neutrinos I: towards a realistic modeling of the relation between matter, haloes and galaxies*, *JCAP* **03** (2014) 011 [[arXiv:1311.0866](#)] [[INSPIRE](#)].
- [18] E. Castorina et al., *DEMNUi: the clustering of large-scale structures in the presence of massive neutrinos*, *JCAP* **07** (2015) 043 [[arXiv:1505.07148](#)] [[INSPIRE](#)].
- [19] J.D. Emberson et al., *Cosmological neutrino simulations at extreme scale*, *Res. Astron. Astrophys.* **17** (2017) 085 [[arXiv:1611.01545](#)] [[INSPIRE](#)].
- [20] J. Adamek, R. Durrer and M. Kunz, *Relativistic N-body simulations with massive neutrinos*, *JCAP* **11** (2017) 004 [[arXiv:1707.06938](#)] [[INSPIRE](#)].
- [21] A. Banerjee, D. Powell, T. Abel and F. Villaescusa-Navarro, *Reducing noise in cosmological N-body simulations with neutrinos*, *JCAP* **09** (2018) 028 [[arXiv:1801.03906](#)] [[INSPIRE](#)].
- [22] J. Brandbyge, S. Hannestad and T. Tram, *Momentum space sampling of neutrinos in N-body simulations*, *JCAP* **03** (2019) 047 [[arXiv:1806.05874](#)] [[INSPIRE](#)].

- [23] J. Brandbyge and S. Hannestad, *Grid based linear neutrino perturbations in cosmological  $N$ -body simulations*, *JCAP* **05** (2009) 002 [[arXiv:0812.3149](#)] [[INSPIRE](#)].
- [24] Y. Ali-Haïmoud and S. Bird, *An efficient implementation of massive neutrinos in non-linear structure formation simulations*, *Mon. Not. Roy. Astron. Soc.* **428** (2012) 3375 [[arXiv:1209.0461](#)] [[INSPIRE](#)].
- [25] J. Liu et al., *MassiveNuS: cosmological massive neutrino simulations*, *JCAP* **03** (2018) 049 [[arXiv:1711.10524](#)] [[INSPIRE](#)].
- [26] J.Z. Chen, A. Upadhye and Y.Y.Y. Wong, *One line to run them all: SuperEasy massive neutrino linear response in  $N$ -body simulations*, *JCAP* **04** (2021) 078 [[arXiv:2011.12504](#)] [[INSPIRE](#)].
- [27] J. Dakin et al.,  *$\nu$ CONCEPT: cosmological neutrino simulations from the non-linear Boltzmann hierarchy*, *JCAP* **02** (2019) 052 [[arXiv:1712.03944](#)] [[INSPIRE](#)].
- [28] K. Yoshikawa, S. Tanaka, N. Yoshida and S. Saito, *Cosmological Vlasov-Poisson simulations of structure formation with relic neutrinos: nonlinear clustering and the neutrino mass*, *Astrophys. J.* **904** (2020) 159 [[arXiv:2010.00248](#)] [[INSPIRE](#)].
- [29] J. Brandbyge and S. Hannestad, *Resolving cosmic neutrino structure: a hybrid neutrino  $N$ -body scheme*, *JCAP* **01** (2010) 021 [[arXiv:0908.1969](#)] [[INSPIRE](#)].
- [30] S. Bird, Y. Ali-Haïmoud, Y. Feng and J. Liu, *An efficient and accurate hybrid method for simulating non-linear neutrino structure*, *Mon. Not. Roy. Astron. Soc.* **481** (2018) 1486 [[arXiv:1803.09854](#)] [[INSPIRE](#)].
- [31] W. Elbers et al., *An optimal non-linear method for simulating relic neutrinos*, *Mon. Not. Roy. Astron. Soc.* **507** (2021) 2614 [[arXiv:2010.07321](#)] [[INSPIRE](#)].
- [32] C. Partmann, C. Fidler, C. Rampf and O. Hahn, *Fast simulations of cosmic large-scale structure with massive neutrinos*, *JCAP* **09** (2020) 018 [[arXiv:2003.07387](#)] [[INSPIRE](#)].
- [33] M. Zennaro et al., *How to add massive neutrinos to your  $\Lambda$ CDM simulation — extending cosmology rescaling algorithms*, *Mon. Not. Roy. Astron. Soc.* **489** (2019) 5938 [[arXiv:1905.08696](#)] [[INSPIRE](#)].
- [34] I. Esteban et al., *The fate of hints: updated global analysis of three-flavor neutrino oscillations*, *JHEP* **09** (2020) 178 [[arXiv:2007.14792](#)] [[INSPIRE](#)].
- [35] KATRIN collaboration, *Improved upper limit on the neutrino mass from a direct kinematic method by KATRIN*, *Phys. Rev. Lett.* **123** (2019) 221802 [[arXiv:1909.06048](#)] [[INSPIRE](#)].
- [36] KATRIN collaboration, *Direct neutrino-mass measurement with sub-electronvolt sensitivity*, *Nature Phys.* **18** (2022) 160 [[arXiv:2105.08533](#)] [[INSPIRE](#)].
- [37] E. Di Valentino, S. Gariazzo and O. Mena, *Most constraining cosmological neutrino mass bounds*, *Phys. Rev. D* **104** (2021) 083504 [[arXiv:2106.15267](#)] [[INSPIRE](#)].
- [38] M. Archidiacono, T. Brinckmann, J. Lesgourgues and V. Poulin, *Physical effects involved in the measurements of neutrino masses with future cosmological data*, *JCAP* **02** (2017) 052 [[arXiv:1610.09852](#)] [[INSPIRE](#)].
- [39] J.R. Bond, G. Efstathiou and J. Silk, *Massive neutrinos and the large scale structure of the universe*, *Phys. Rev. Lett.* **45** (1980) 1980 [[INSPIRE](#)].
- [40] W. Hu, D.J. Eisenstein and M. Tegmark, *Weighing neutrinos with galaxy surveys*, *Phys. Rev. Lett.* **80** (1998) 5255 [[astro-ph/9712057](#)] [[INSPIRE](#)].
- [41] S. Hannestad, A. Upadhye and Y.Y.Y. Wong, *Spoon or slide? The non-linear matter power spectrum in the presence of massive neutrinos*, *JCAP* **11** (2020) 062 [[arXiv:2006.04995](#)] [[INSPIRE](#)].
- [42] V. Springel, *The cosmological simulation code GADGET-2*, *Mon. Not. Roy. Astron. Soc.* **364** (2005) 1105 [[astro-ph/0505010](#)] [[INSPIRE](#)].

- [43] V. Springel et al., *The Aquarius project: the subhalos of galactic halos*, *Mon. Not. Roy. Astron. Soc.* **391** (2008) 1685 [arXiv:0809.0898] [INSPIRE].
- [44] R.E. Angulo et al., *Scaling relations for galaxy clusters in the Millennium-XXL simulation*, *Mon. Not. Roy. Astron. Soc.* **426** (2012) 2046 [arXiv:1203.3216] [INSPIRE].
- [45] R.E. Angulo et al., *The BACCO simulation project: exploiting the full power of large-scale structure for cosmology*, *Mon. Not. Roy. Astron. Soc.* **507** (2021) 5869 [arXiv:2004.06245] [INSPIRE].
- [46] A.M. Beck et al., *An improved SPH scheme for cosmological simulations*, *Mon. Not. Roy. Astron. Soc.* **455** (2016) 2110 [arXiv:1502.07358] [INSPIRE].
- [47] T. Marin-Gilabert, M. Valentini, U.P. Steinwandel and K. Dolag, *The role of physical and numerical viscosity in hydrodynamical instabilities*, *Mon. Not. Roy. Astron. Soc.* **517** (2022) 5971 [arXiv:2205.09135] [INSPIRE].
- [48] V. Springel, R. Pakmor, O. Zier and M. Reinecke, *Simulating cosmic structure formation with the gadget-4 code*, *Mon. Not. Roy. Astron. Soc.* **506** (2021) 2871 [arXiv:2010.03567] [INSPIRE].
- [49] P. Heuschling, C. Partmann and C. Fidler, *A minimal model for massive neutrinos in Newtonian N-body simulations*, *JCAP* **09** (2022) 068 [arXiv:2201.13186] [INSPIRE].
- [50] V. Springel, *E pur si muove: Galilean-invariant cosmological hydrodynamical simulations on a moving mesh*, *Mon. Not. Roy. Astron. Soc.* **401** (2010) 791 [arXiv:0901.4107] [INSPIRE].
- [51] R. Weinberger, V. Springel and R. Pakmor, *The Arepo public code release*, *Astrophys. J. Suppl.* **248** (2020) 32 [arXiv:1909.04667] [INSPIRE].
- [52] J. Dakin, S. Hannestad and T. Tram, *The cosmological simulation code CONCEPT 1.0*, *Mon. Not. Roy. Astron. Soc.* **513** (2022) 991 [arXiv:2112.01508] [INSPIRE].
- [53] D. Potter, J. Stadel and R. Teyssier, *PKDGRAV3: beyond trillion particle cosmological simulations for the next era of galaxy surveys*, arXiv:1609.08621 [INSPIRE].
- [54] M. Schaller et al., *SWIFT: SPH with inter-dependent fine-grained tasking*, Astrophysics source code library <https://ascl.net/1805.020>, May 2018.
- [55] W. Elbers, *Geodesic motion and phase-space evolution of massive neutrinos*, *JCAP* **11** (2022) 058 [arXiv:2207.14256] [INSPIRE].
- [56] R. Teyssier, *Cosmological hydrodynamics with adaptive mesh refinement: a new high resolution code called Ramses*, *Astron. Astrophys.* **385** (2002) 337 [astro-ph/0111367] [INSPIRE].
- [57] R. Mauland, O. Elgarøy, D.F. Mota and H.A. Winther, *The void-galaxy cross-correlation function with massive neutrinos and modified gravity*, arXiv:2303.05820 [INSPIRE].
- [58] J. Adamek, D. Daverio, R. Durrer and M. Kunz, *General relativity and cosmic structure formation*, *Nature Phys.* **12** (2016) 346 [arXiv:1509.01699] [INSPIRE].
- [59] J. Adamek, D. Daverio, R. Durrer and M. Kunz, *Evolution: a cosmological N-body code based on general relativity*, *JCAP* **07** (2016) 053 [arXiv:1604.06065] [INSPIRE].
- [60] H.A. Winther et al., *COLA with scale-dependent growth: applications to screened modified gravity models*, *JCAP* **08** (2017) 006 [arXiv:1703.00879] [INSPIRE].
- [61] B.S. Wright, H.A. Winther and K. Koyama, *COLA with massive neutrinos*, *JCAP* **10** (2017) 054 [arXiv:1705.08165] [INSPIRE].
- [62] P. Monaco et al., *An accurate tool for the fast generation of dark matter halo catalogs*, *Mon. Not. Roy. Astron. Soc.* **433** (2013) 2389 [arXiv:1305.1505] [INSPIRE].
- [63] L.A. Rizzo et al., *Simulating cosmologies beyond  $\Lambda$ CDM with PINOCCHIO*, *JCAP* **01** (2017) 008 [arXiv:1610.07624] [INSPIRE].
- [64] M. Cataneo et al., *On the road to per cent accuracy — III. Non-linear reaction of the matter power spectrum to massive neutrinos*, *Mon. Not. Roy. Astron. Soc.* **491** (2020) 3101 [arXiv:1909.02561] [INSPIRE].

- [65] B. Bose et al., *On the road to per cent accuracy — V. The non-linear power spectrum beyond  $\Lambda$ CDM with massive neutrinos and baryonic feedback*, *Mon. Not. Roy. Astron. Soc.* **508** (2021) 2479 [[arXiv:2105.12114](#)] [[INSPIRE](#)].
- [66] E. Lawrence et al., *The Mira-Titan universe II: matter power spectrum emulation*, *Astrophys. J.* **847** (2017) 50 [[arXiv:1705.03388](#)] [[INSPIRE](#)].
- [67] K.R. Moran et al., *The Mira-Titan universe — IV. High-precision power spectrum emulation*, *Mon. Not. Roy. Astron. Soc.* **520** (2023) 3443 [[arXiv:2207.12345](#)] [[INSPIRE](#)].
- [68] A. Banerjee and N. Dalal, *Simulating nonlinear cosmological structure formation with massive neutrinos*, *JCAP* **11** (2016) 015 [[arXiv:1606.06167](#)] [[INSPIRE](#)].
- [69] C.-P. Ma and E. Bertschinger, *A calculation of the full neutrino phase space in cold + hot dark matter models*, *Astrophys. J.* **429** (1994) 22 [[astro-ph/9308006](#)] [[INSPIRE](#)].
- [70] S. Tassev, M. Zaldarriaga and D. Eisenstein, *Solving large scale structure in ten easy steps with COLA*, *JCAP* **06** (2013) 036 [[arXiv:1301.0322](#)] [[INSPIRE](#)].
- [71] A. Izard, M. Crocce and P. Fosalba, *ICE-COLA: towards fast and accurate synthetic galaxy catalogues optimizing a quasi  $N$ -body method*, *Mon. Not. Roy. Astron. Soc.* **459** (2016) 2327 [[arXiv:1509.04685](#)] [[INSPIRE](#)].
- [72] A. Lewis, A. Challinor and A. Lasenby, *Efficient computation of CMB anisotropies in closed FRW models*, *Astrophys. J.* **538** (2000) 473 [[astro-ph/9911177](#)] [[INSPIRE](#)].
- [73] A. Lewis and S. Bridle, *Cosmological parameters from CMB and other data: a Monte Carlo approach*, *Phys. Rev. D* **66** (2002) 103511 [[astro-ph/0205436](#)] [[INSPIRE](#)].
- [74] P. Monaco, T. Theuns and G. Taffoni, *Pinocchio: pinpointing orbit-crossing collapsed hierarchical objects in a linear density field*, *Mon. Not. Roy. Astron. Soc.* **331** (2002) 587 [[astro-ph/0109323](#)] [[INSPIRE](#)].
- [75] E. Munari et al., *Improving fast generation of halo catalogues with higher order Lagrangian perturbation theory*, *Mon. Not. Roy. Astron. Soc.* **465** (2017) 4658 [[arXiv:1605.04788](#)] [[INSPIRE](#)].
- [76] E. Munari et al., *Testing approximate predictions of displacements of cosmological dark matter halos*, *JCAP* **07** (2017) 050 [[arXiv:1704.00920](#)] [[INSPIRE](#)].
- [77] E. Castorina et al., *Cosmology with massive neutrinos II: on the universality of the halo mass function and bias*, *JCAP* **02** (2014) 049 [[arXiv:1311.1212](#)] [[INSPIRE](#)].
- [78] J.F. Navarro, C.S. Frenk and S.D.M. White, *A universal density profile from hierarchical clustering*, *Astrophys. J.* **490** (1997) 493 [[astro-ph/9611107](#)] [[INSPIRE](#)].
- [79] L. Blot et al., *Comparing approximate methods for mock catalogues and covariance matrices II: power spectrum multipoles*, *Mon. Not. Roy. Astron. Soc.* **485** (2019) 2806 [[arXiv:1806.09497](#)] [[INSPIRE](#)].
- [80] C. Fidler et al., *A new approach to cosmological structure formation with massive neutrinos*, *JCAP* **01** (2019) 025 [[arXiv:1807.03701](#)] [[INSPIRE](#)].
- [81] M. Cataneo et al., *On the road to percent accuracy: non-linear reaction of the matter power spectrum to dark energy and modified gravity*, *Mon. Not. Roy. Astron. Soc.* **488** (2019) 2121 [[arXiv:1812.05594](#)] [[INSPIRE](#)].
- [82] A. Mead, S. Brieden, T. Tröster and C. Heymans, *HMcode-2020: improved modelling of non-linear cosmological power spectra with baryonic feedback*, [arXiv:2009.01858](#) [[DOI:10.1093/mras/stab082](#)] [[INSPIRE](#)].
- [83] A. Cooray and R.K. Sheth, *Halo models of large scale structure*, *Phys. Rept.* **372** (2002) 1 [[astro-ph/0206508](#)] [[INSPIRE](#)].
- [84] M. Cacciato et al., *Galaxy clustering & galaxy-galaxy lensing: a promising union to constrain cosmological parameters*, *Mon. Not. Roy. Astron. Soc.* **394** (2009) 929 [[arXiv:0807.4932](#)] [[INSPIRE](#)].

- [85] C. Giocoli, M. Bartelmann, R.K. Sheth and M. Cacciato, *Halo model description of the non-linear dark matter power spectrum at  $k \gg 1 \text{ Mpc}^{-1}$* , *Mon. Not. Roy. Astron. Soc.* **408** (2010) 300 [[arXiv:1003.4740](#)] [[INSPIRE](#)].
- [86] R.K. Sheth and G. Tormen, *Large scale bias and the peak background split*, *Mon. Not. Roy. Astron. Soc.* **308** (1999) 119 [[astro-ph/9901122](#)] [[INSPIRE](#)].
- [87] R.K. Sheth and G. Tormen, *An excursion set model of hierarchical clustering: ellipsoidal collapse and the moving barrier*, *Mon. Not. Roy. Astron. Soc.* **329** (2002) 61 [[astro-ph/0105113](#)] [[INSPIRE](#)].
- [88] J.S. Bullock et al., *Profiles of dark haloes. Evolution, scatter, and environment*, *Mon. Not. Roy. Astron. Soc.* **321** (2001) 559 [[astro-ph/9908159](#)] [[INSPIRE](#)].
- [89] B. Bose et al., *On the road to per cent accuracy IV: ReACT — computing the non-linear power spectrum beyond  $\Lambda$ CDM*, *Mon. Not. Roy. Astron. Soc.* **498** (2020) 4650 [[arXiv:2005.12184](#)] [[INSPIRE](#)].
- [90] VIRGO CONSORTIUM collaboration, *Stable clustering, the halo model and nonlinear cosmological power spectra*, *Mon. Not. Roy. Astron. Soc.* **341** (2003) 1311 [[astro-ph/0207664](#)] [[INSPIRE](#)].
- [91] R. Takahashi et al., *Revising the halofit model for the nonlinear matter power spectrum*, *Astrophys. J.* **761** (2012) 152 [[arXiv:1208.2701](#)] [[INSPIRE](#)].
- [92] K. Heitmann et al., *The Coyote universe II: cosmological models and precision emulation of the nonlinear matter power spectrum*, *Astrophys. J.* **705** (2009) 156 [[arXiv:0902.0429](#)] [[INSPIRE](#)].
- [93] T. Nishimichi et al., *Dark quest. I. Fast and accurate emulation of halo clustering statistics and its application to galaxy clustering*, *Astrophys. J.* **884** (2019) 29 [[arXiv:1811.09504](#)] [[INSPIRE](#)].
- [94] S.K. Giri and A. Schneider, *Emulation of baryonic effects on the matter power spectrum and constraints from galaxy cluster data*, *JCAP* **12** (2021) 046 [[arXiv:2108.08863](#)] [[INSPIRE](#)].
- [95] G. Aricò et al., *The BACCO simulation project: a baryonification emulator with neural networks*, *Mon. Not. Roy. Astron. Soc.* **506** (2021) 4070 [[arXiv:2011.15018](#)] [[INSPIRE](#)].
- [96] K. Heitmann et al., *The Mira-Titan universe: precision predictions for dark energy surveys*, *Astrophys. J.* **820** (2016) 108 [[arXiv:1508.02654](#)] [[INSPIRE](#)].
- [97] S. Habib et al., *HACC: simulating sky surveys on state-of-the-art supercomputing architectures*, *New Astron.* **42** (2016) 49 [[arXiv:1410.2805](#)] [[INSPIRE](#)].
- [98] PLANCK collaboration, *Planck 2015 results. XIII. Cosmological parameters*, *Astron. Astrophys.* **594** (2016) A13 [[arXiv:1502.01589](#)] [[INSPIRE](#)].
- [99] R.E. Angulo and S.D.M. White, *One simulation to fit them all — changing the background parameters of a cosmological  $N$ -body simulation*, *Mon. Not. Roy. Astron. Soc.* **405** (2010) 143 [[arXiv:0912.4277](#)] [[INSPIRE](#)].
- [100] M. Archidiacono, S. Hannestad and J. Lesgourgues, *What will it take to measure individual neutrino mass states using cosmology?*, *JCAP* **09** (2020) 021 [[arXiv:2003.03354](#)] [[INSPIRE](#)].
- [101] D. Blas, J. Lesgourgues and T. Tram, *The Cosmic Linear Anisotropy Solving System (CLASS) II: approximation schemes*, *JCAP* **07** (2011) 034 [[arXiv:1104.2933](#)] [[INSPIRE](#)].
- [102] M. Zennaro et al., *Initial conditions for accurate  $N$ -body simulations of massive neutrino cosmologies*, *Mon. Not. Roy. Astron. Soc.* **466** (2017) 3244 [[arXiv:1605.05283](#)] [[INSPIRE](#)].
- [103] R.E. Angulo and A. Pontzen, *Cosmological  $N$ -body simulations with suppressed variance*, *Mon. Not. Roy. Astron. Soc.* **462** (2016) L1 [[arXiv:1603.05253](#)] [[INSPIRE](#)].
- [104] Y.B. Zeldovich, *Gravitational instability: an approximate theory for large density perturbations*, *Astron. Astrophys.* **5** (1970) 84 [[INSPIRE](#)].

- [105] M. Davis, F.J. Summers and D. Schlegel, *Large scale structure in a universe with mixed hot and cold dark matter*, *Nature* **359** (1992) 393 [INSPIRE].
- [106] A. Klypin, J. Holtzman, J. Primack and E. Regos, *Structure formation with cold plus hot dark matter*, *Astrophys. J.* **416** (1993) 1 [astro-ph/9305011] [INSPIRE].
- [107] E. Sefusatti, M. Crocce, R. Scoccimarro and H. Couchman, *Accurate estimators of correlation functions in Fourier space*, *Mon. Not. Roy. Astron. Soc.* **460** (2016) 3624 [arXiv:1512.07295] [INSPIRE].
- [108] G. Tormen, *The assembly of matter in galaxy clusters*, *Mon. Not. Roy. Astron. Soc.* **297** (1998) 648 [astro-ph/9802290] [INSPIRE].
- [109] G. Tormen and L. Moscardini, *Properties of cluster satellites in hydrodynamical simulations*, *Mon. Not. Roy. Astron. Soc.* **350** (2004) 1397 [astro-ph/0304375] [INSPIRE].
- [110] C. Giocoli, G. Tormen and F.C. Bosch, *The population of dark matter subhaloes: mass functions and average mass loss rates*, *Mon. Not. Roy. Astron. Soc.* **386** (2008) 2135 [arXiv:0712.1563] [INSPIRE].
- [111] G. Despali et al., *The universality of the virial halo mass function and models for non-universality of other halo definitions*, *Mon. Not. Roy. Astron. Soc.* **456** (2016) 2486 [arXiv:1507.05627] [INSPIRE].
- [112] W.A. Watson et al., *The halo mass function through the cosmic ages*, *Mon. Not. Roy. Astron. Soc.* **433** (2013) 1230 [arXiv:1212.0095] [INSPIRE].
- [113] J.L. Tinker et al., *The large scale bias of dark matter halos: numerical calibration and model tests*, *Astrophys. J.* **724** (2010) 878 [arXiv:1001.3162] [INSPIRE].
- [114] E. Massara, F. Villaescusa-Navarro and M. Viel, *The halo model in a massive neutrino cosmology*, *JCAP* **12** (2014) 053 [arXiv:1410.6813] [INSPIRE].
- [115] A. Schneider et al., *Matter power spectrum and the challenge of percent accuracy*, *JCAP* **04** (2016) 047 [arXiv:1503.05920] [INSPIRE].
- [116] G. Parimbelli et al., *DEMNUi: comparing nonlinear power spectra prescriptions in the presence of massive neutrinos and dynamical dark energy*, *JCAP* **11** (2022) 041 [arXiv:2207.13677] [INSPIRE].
- [117] S. Saito, M. Takada and A. Taruya, *Impact of massive neutrinos on nonlinear matter power spectrum*, *Phys. Rev. Lett.* **100** (2008) 191301 [arXiv:0801.0607] [INSPIRE].
- [118] Y.Y.Y. Wong, *Higher order corrections to the large scale matter power spectrum in the presence of massive neutrinos*, *JCAP* **10** (2008) 035 [arXiv:0809.0693] [INSPIRE].
- [119] B. Audren et al., *Neutrino masses and cosmological parameters from a Euclid-like survey: Markov chain Monte Carlo forecasts including theoretical errors*, *JCAP* **01** (2013) 026 [arXiv:1210.2194] [INSPIRE].
- [120] R. de Belsunce and L. Senatore, *Tree-level bispectrum in the effective field theory of large-scale structure extended to massive neutrinos*, *JCAP* **02** (2019) 038 [arXiv:1804.06849] [INSPIRE].
- [121] R. Ruggeri, E. Castorina, C. Carbone and E. Sefusatti, *DEMNUi: massive neutrinos and the bispectrum of large scale structures*, *JCAP* **03** (2018) 003 [arXiv:1712.02334] [INSPIRE].
- [122] M. Costanzi et al., *Cosmology with massive neutrinos III: the halo mass function and an application to galaxy clusters*, *JCAP* **12** (2013) 012 [arXiv:1311.1514] [INSPIRE].
- [123] F. Hassani, J. Adamek, R. Durrer and M. Kunz, *Biased tracers as a probe of beyond- $\Lambda$ CDM cosmologies*, *Astron. Astrophys.* **668** (2022) A56 [arXiv:2206.14179] [INSPIRE].
- [124] M. Martinelli et al., *Euclid: impact of non-linear and baryonic feedback prescriptions on cosmological parameter estimation from weak lensing cosmic shear*, *Astron. Astrophys.* **649** (2021) A100 [arXiv:2010.12382] [INSPIRE].

Paper II

# The void-galaxy cross-correlation function with massive neutrinos and modified gravity

**Renate Mauland, Øystein Elgarøy, David F. Mota, and Hans A. Winther**

Published in *Astronomy & Astrophysics*, A&A 674 A185 (2023).  
DOI: 10.1051/0004-6361/202346287.







# The void-galaxy cross-correlation function with massive neutrinos and modified gravity

R. Mauland<sup>✉</sup>, Ø. Elgarøy, D. F. Mota, and H. A. Winther

Institute of Theoretical Astrophysics, University of Oslo, PO Box 1029 Blindern, 0315 Oslo, Norway  
e-mail: renate.mauland-hus@astro.uio.no

Received 1 March 2023 / Accepted 3 May 2023

## ABSTRACT

Massive neutrinos and  $f(R)$ -modified gravity have degenerate observational signatures that can impact the interpretation of results in galaxy survey experiments, such as cosmological parameter estimations and gravity model tests. Because of this, it is important to investigate astrophysical observables that can break these degeneracies. Cosmic voids are sensitive to both massive neutrinos and modifications of gravity and provide a promising ground for disentangling the above-mentioned degeneracies. In order to analyse cosmic voids in the context of non- $\Lambda$ CDM cosmologies, we must first understand how well the current theoretical framework operates in these settings. We performed a suite of simulations with the RAMSES-based  $N$ -body code ANUBISIS, including massive neutrinos and  $f(R)$ -modified gravity both individually and simultaneously. The data from the simulations were compared to models of the void velocity profile and the void-halo cross-correlation function (CCF). This was done both with the real space simulation data as model input and by applying a reconstruction method to the redshift space data. In addition, we ran Markov chain Monte Carlo (MCMC) fits on the data sets to assess the capability of the models to reproduce the fiducial simulation values of  $f\sigma_8(z)$  and the Alcock-Paczynski parameter,  $\epsilon$ . The void modelling applied performs similarly for all simulated cosmologies, indicating that more accurate models and higher resolution simulations are needed in order to directly observe the effects of massive neutrinos and  $f(R)$ -modified gravity through studies of the void-galaxy CCF. The MCMC fits show that the choice for the void definition plays an important role in the recovery of the correct cosmological parameters, but otherwise, there is no clear distinction between the ability to reproduce  $f\sigma_8$  and  $\epsilon$  for the various simulations.

**Key words.** neutrinos – gravitation – large-scale structure of Universe – cosmological parameters – methods: data analysis

## 1. Introduction

Cosmic voids are underdense regions in the large-scale structure (LSS) which together with halos, walls, and filaments make up the cosmic web. They have recently become a popular independent probe for cosmological parameters as they provide information about the parameter combination  $f\sigma_8(z)$  through the study of redshift space distortions (RSDs) from the imprint left on the quadrupole of the void-galaxy cross-correlation function (CCF; Cai et al. 2016; Nadathur & Percival 2019; Nadathur et al. 2019b). Further on, careful modelling of the RSDs around voids originating from the peculiar velocities of galaxies also opens up for the applied fiducial cosmology to be tested through the Alcock-Paczynski effect (Alcock & Paczyński 1979; Sutter et al. 2012; Hamaus et al. 2022). In addition to this, the empty nature of cosmic voids makes them sensitive to diffuse components of our Universe, such as massive neutrinos, and effects of modified gravities which scale inversely with density (Zivick et al. 2015; Cai et al. 2015; Massara et al. 2015; Falck et al. 2018; Kreisch et al. 2019; Fiorini et al. 2022).

The presence of massive neutrinos suppresses structure formation on scales smaller than the neutrino free-streaming length (Lesgourgues & Pastor 2006), while  $f(R)$ -modified gravity enhances it on scales smaller than the Compton wavelength of the scalaron (e.g., Cataneo et al. 2015). This results in observational degeneracies which have previously been studied in simulations (Baldi et al. 2014; Giocoli et al. 2018; Contarini et al. 2021).

Both massive neutrinos and modified gravity are independently large research fields. Determining the absolute mass scale of neutrinos is not only an important quest within particle physics but also essential in order to understand LSS formation within cosmology. The massive neutrinos make up a fraction of the matter content of the Universe ranging from 0.5–2% based on the lower and upper limits of the sum of the neutrino masses,  $0.06 \text{ eV} \leq \sum m_\nu \leq 2.4 \text{ eV}$ , provided by particle physics experiments (Particle Data Group 2022; Aker et al. 2022). This range can be further constrained through cosmological observations. Effects of massive neutrinos on LSS and signatures left in the cosmic microwave background (CMB; Archidiacono et al. 2017) can be used to estimate the sum of the neutrino masses. New space missions, such as *Euclid* (Laureijs et al. 2011), are now sensitive enough to accurately pick up on the effects of massive neutrinos on the matter power spectrum. *Euclid* aims to measure the sum of the neutrino masses to a precision better than 0.03 eV. This will be achieved through a combined analysis of galaxy clustering and weak gravitational lensing. For small neutrino masses,  $\sum m_\nu < 0.1 \text{ eV}$ , this is precise enough to determine the neutrino mass hierarchy.

Although constraints from cosmology are typically tighter than the ones obtained from particle physics experiments, they do depend on an assumed cosmological model. Because of this, disentangling degeneracies between massive neutrinos and various cosmologies is important in order to fully determine the neutrino mass scale. Accounting for massive neutrinos when studying alternatives to  $\Lambda$ CDM (Lambda cold dark matter) is

therefore also necessary to make sure that constraints on the model in question are properly estimated. For  $f(R)$ -modified gravity, the constraints on the model parameters might be slightly alleviated when massive neutrinos are included in the estimates, due to their degeneracy.

The theory of general relativity (GR) has been thoroughly investigated in high density regions, for instance through local solar system tests (Will 2014). To adhere to the resulting measurements, modified gravity theories typically need to be screened as a function of density. This contributes to the constraints on the parameters of these models and also makes deviations from  $\Lambda$ CDM hard to observe in highly screened environments. Cosmic voids are underdense regions sensitive to both massive neutrinos and  $f(R)$ -modified gravity. Because of this, voids have been proposed as a means to separate their known degenerate effects. The void size function at high redshifts for large voids is found by Contarini et al. (2021) to be a promising candidate for the task.

Before further exploring voids in the context of massive neutrinos and  $f(R)$ -modified gravity, we must first take a look at the theory behind the models developed to extract cosmological information from them. In our case, we investigate the void-galaxy CCF in redshift space, the void velocity profile, and a reconstruction method for putting galaxy positions observed from redshift space back into real space. These are all based on linear theory and, to a degree, a standard  $\Lambda$ CDM universe. In this paper, we explore the need for change in these models in order to use them to describe voids in a universe with massive neutrinos and  $f(R)$ -modified gravity. To do so, we compared them to  $N$ -body simulations containing massive neutrinos and  $f(R)$ -modified gravity, both independently and combined. We studied how well the model for the void velocity profile and the void-halo CCF in redshift space fit the simulation data in each case. The latter was done both by using all the real space information from the simulations directly as model input and also by treating the simulation data as observational data, using redshift space halo positions and a reconstruction method to gain an estimate of the corresponding real space positions of the halos. In addition, we performed Markov chain Monte Carlo (MCMC) fits for  $f\sigma_8(z)$  and the Alcock-Paczynski parameter,  $\epsilon$ , in order to test how well we are able to recover the fiducial cosmology.

This paper is structured as follows: We start by presenting background theory for cosmic voids, massive neutrinos, and  $f(R)$ -modified gravity in Sect. 2 and then explain our simulation set-up in Sect. 3. In Sect. 4 we detail the methodical approach of the paper before reporting our results in Sect. 5. Finally, we conclude in Sect. 6.

## 2. Theory

### 2.1. Cosmic voids

In the following subsections, we recap some models developed to extract information from cosmic voids. This includes the modelling of the void-galaxy CCF in redshift space, the velocity profile, and a reconstruction process. In addition, we briefly explain how voids can be used to test cosmology through the Alcock-Paczynski effect. The numerical definition of voids in this work is addressed in Sect. 4.2.

#### 2.1.1. Cross-correlation function

The void-galaxy CCF gives us information about how galaxies are distributed around voids as a function of the void-centre galaxy separation (Cai et al. 2016; Nadathur & Percival 2019;

Woodfinden et al. 2022). In real space, we denote this separation vector by  $\mathbf{r}$ , and in redshift space by  $\mathbf{s}$ . As we observe in redshift space, deconstructing the separation vectors into components perpendicular and parallel to the line-of-sight (LOS) is advantageous, and gives the following relations

$$s_{\perp} = r_{\perp}, \quad (1)$$

$$s_{\parallel} = r_{\parallel} + \frac{v_{\parallel}}{aH}. \quad (2)$$

Here,  $H$  is the Hubble rate,  $a$  the scale factor, and  $v_{\parallel}$  the component of the galaxy peculiar velocity parallel to the LOS. The LOS can be defined as from the observer to the void centre, the galaxy or the midpoint between them. We use the observer to void-centre definition in this paper.

The void-galaxy CCF in redshift space,  $\xi^s(\mathbf{s})$ , can be related to the void-galaxy CCF in real space,  $\xi^r(\mathbf{r})$ , by the streaming model (Peebles 1980; Fisher 1995; Paillas et al. 2021):

$$1 + \xi^s(\mathbf{s}) = \int (1 + \xi^r(\mathbf{r}))P(v_{\parallel}, \mathbf{r})d\mathbf{v}_{\parallel}, \quad (3)$$

where  $P(v_{\parallel}, \mathbf{r})$  is the probability distribution function (PDF) of the galaxies' peculiar velocities parallel to the LOS. This is a mapping from real to redshift space, based on the fact that void-galaxy pairs are conserved when moving between the two<sup>1</sup>. The galaxy velocities can further be separated into two components, one describing the coherent outflow velocity away from the void centre, and the other an additional stochastic motion of the galaxies. The first term can be assumed spherically symmetric around and radially directed out from the void centre when averaging over a large number of voids, due to statistical isotropy in real space. Following this argument, we can write the LOS galaxy velocity component as

$$v_{\parallel}(r, \mu_r) = v_r(r)\mu_r + \tilde{v}_{\parallel}, \quad (4)$$

where  $\tilde{v}_{\parallel}$  is the random velocity component parallel to the LOS,  $\mu_r = \cos \theta$ , and  $\theta$  is the angle between the LOS and  $\mathbf{r}$  so that  $v_r(r)\mu_r$  is the part of the coherent outflow velocity profile projected along the LOS.

By performing a coordinate change from  $v_{\parallel} \rightarrow \tilde{v}_{\parallel}$ , as shown in Woodfinden et al. (2022), Eq. (3) can be written as

$$1 + \xi^s(\mathbf{s}) = \int (1 + \xi^r(\mathbf{r}))P(\tilde{v}_{\parallel}, \mathbf{r})J_{rs}d\tilde{v}_{\parallel}, \quad (5)$$

where  $J_{rs}$  is the Jacobian resulting from the shift from real to redshift space and  $P(\tilde{v}_{\parallel}, \mathbf{r})$  is the PDF of the random velocity component centred around zero. Writing out the Jacobian we get the expression

$$J_{rs} = \left[ 1 + \frac{v_r}{raH} + \frac{(v'_r - v_r/r)}{aH}\mu_r^2 \right]^{-1}, \quad (6)$$

with derivatives with respect to  $r$  denoted by a prime. Simulations show that  $P(\tilde{v}_{\parallel}, \mathbf{r})$  is approximated well by a Gaussian (Nadathur & Percival 2019; Paillas et al. 2021) and we therefore consider

$$P(\tilde{v}_{\parallel}, \mathbf{r}) = \frac{1}{\sqrt{2\pi\sigma_{v_{\parallel}}^2(r)}} \exp\left(-\frac{\tilde{v}_{\parallel}^2}{2\sigma_{v_{\parallel}}^2(r)}\right), \quad (7)$$

with the additional assumption of a spherically symmetric velocity dispersion,  $\sigma_{v_{\parallel}}^2(r)$ .

<sup>1</sup> In order for this to hold, the voids must be consistently identified either in real or redshift space for both  $\xi^r(\mathbf{r})$  and  $\xi^s(\mathbf{s})$ . However, identification in redshift space leads to an orientation-dependent selection bias of the possible voids (Chuang et al. 2017; Nadathur et al. 2019a). To avoid this, we always identify voids in real space in this paper.

### 2.1.2. Velocity modelling

Equation (5) depends on the coherent mean outflow velocity profile around the void,  $\mathbf{v}(r) = v_r(r)\hat{\mathbf{r}}$ . This quantity can be provided to the model through a template, for example, obtained from a simulation, or it can be modelled separately. Typically, using linear perturbation theory and the continuity equation (Peebles 1980, 1993), the expression

$$v_r^{\text{lin}}(r) = -\frac{1}{3}f a H \Delta(r)r \quad (8)$$

is used for the radial outflow velocity profile. Here,  $f = d \ln D / d \ln a$  is the linear growth rate, with  $D$  as the growth factor, and  $\Delta(r)$  is the integrated density,

$$\Delta(r) = \frac{3}{r^3} \int_0^r \delta(x)x^2 dx, \quad (9)$$

with  $\delta(r)$  the dark matter overdensity profile around the void. Nadathur et al. (2019b) show that  $\Delta(r) \propto \sigma_8$ , which leads to  $v_r(r)$  depending on the combination of the parameters  $f\sigma_8$ , where  $\sigma_8$  is the amplitude of the linear matter power spectrum at a scale of  $8 h^{-1} \text{Mpc}$ . It is also worth noting that in the process of deriving Eq. (8), the growth rate is assumed constant, which does not hold for cosmologies with massive neutrinos or modified gravity, where the growth rate is scale-dependent (e.g., Hernández 2017; Mirzatuny & Pierpaoli 2019).

Although Eq. (8) is commonly used to model the coherent outflow velocity, the expression in Eq. (5) should hold for any spherically symmetric velocity profile. One other example of this is the more general velocity profile from Paillas et al. (2021), which introduces an extra degree of freedom,

$$v_r^{\text{gen}}(r) = -\frac{1}{3} \frac{f a H \Delta(r)r}{1 + A_v \xi_0(r)}. \quad (10)$$

Here,  $\xi_0(r)$  is the void-galaxy CCF monopole and  $A_v$  is a free parameter. This expression is able to better fit the void velocity profile by adjusting  $A_v$ . However, the value of  $A_v$  must be estimated from, for example, simulations if we want to use Eq. (10) for void-galaxy CCF modelling.

### 2.1.3. Reconstruction

When working with observational data, we only have access to galaxy positions in redshift space. However, the model of the void-galaxy CCF in redshift space depends on the real space void-galaxy CCF. One way to obtain this quantity is by using a reconstruction method to estimate the positions of galaxies in real space.

In the context of voids, Nadathur et al. (2019a) propose one such method, based on Nusser & Davis (1994). It involves solving the Zel'dovich equation (Zel'dovich 1970),

$$\nabla \cdot \Psi + \frac{f}{b} \nabla \cdot (\Psi \cdot \hat{\mathbf{r}}) \hat{\mathbf{r}} = -\frac{\delta_g}{b}, \quad (11)$$

for the displacement field,  $\Psi$ . Here,  $f$  is the growth rate and  $b$  is the linear bias relating the galaxy overdensity field,  $\delta_g$ , to the matter overdensity field,  $\delta$ , in redshift space. The displacement field,  $\Psi$ , relates the Eulerian and Lagrangian positions of the galaxies. A part of this displacement, given by

$$\Psi_{\text{RSD}} = -f(\Psi \cdot \hat{\mathbf{r}})\hat{\mathbf{r}}, \quad (12)$$

is due to the linear RSDs resulting from the galaxies' peculiar velocities. By shifting the galaxy positions in redshift space by

$-\Psi_{\text{RSD}}$ , we can approximately obtain their real space positions. As seen above, this procedure depends on an input value of the growth rate,  $f$ , and the linear galaxy bias,  $b$ , which combined make the reconstruction parameter  $\beta = f/b$ . Consequentially, the reconstruction method depends on a fiducial cosmological model through the growth rate.

### 2.1.4. The Alcock-Paczyński effect

One way to inspect a chosen cosmology is through the Alcock-Paczyński (AP) effect (Alcock & Paczyński 1979). This test only involves the geometry of the Universe and is performed by studying the ratio of the observed angular and redshift size of an object with a known shape. An example is cosmic voids, which on average should have a spherical configuration. A correctly chosen fiducial cosmology should, when converting from observed redshifts to physical distances, reproduce the spherical shape of the average void. Deviations from this show up as anisotropies in the void-galaxy CCF in addition to the contribution from peculiar velocities. If we can model the RSDs from velocities accurately enough, the AP effect can be used on voids as a test of the fiducial cosmology.

We parameterise the AP effect through the parameters

$$\alpha_{\parallel} = \frac{D_H(z)}{D_H^{\text{fid}}(z)}, \quad \alpha_{\perp} = \frac{D_A(z)}{D_A^{\text{fid}}(z)}, \quad (13)$$

which are distance ratios parallel and perpendicular to the LOS between the true cosmology and the fiducial cosmological model<sup>2</sup>. Here,  $D_H(z) = c/H(z)$ , which is the Hubble distance at redshift  $z$ , and  $D_A(z)$  is the comoving angular diameter distance.

Taking into account the difference between the true cosmology and the fiducial model, the void-galaxy CCF in redshift space scales like

$$\xi^s(s_{\parallel}, s_{\perp}) = \xi^{s, \text{fid}}(\alpha_{\parallel} s_{\parallel}^{\text{fid}}, \alpha_{\perp} s_{\perp}^{\text{fid}}) \quad (14)$$

due to the void-galaxy pair separation,  $s^{\text{fid}}$ , dependency of the calculation. The two AP parameters can be rewritten into

$$\alpha = \alpha_{\perp}^{2/3} \alpha_{\parallel}^{1/3}, \quad (15)$$

$$\epsilon = \frac{\alpha_{\perp}}{\alpha_{\parallel}}, \quad (16)$$

where  $\alpha$  characterises the volume dilation and  $\epsilon$  quantifies anisotropic distortions, which largely affect the quadrupole of the CCF, as Nadathur et al. (2019b) demonstrate. When performing the calculation of the CCF model, the input parameters  $\xi^s(r)$ ,  $\Delta(r)$ , and  $\sigma_{\eta}$  are scaled by  $\alpha$  in order to not use the absolute void size as a standard ruler (Nadathur et al. 2019a). This leaves only a dependence on  $\epsilon$ . The underlying assumption behind the AP modelling in Eq. (14) is that the positions of voids in a fiducial cosmology where the AP parameters are not unity, is (in a statistical sense) just an AP stretching of the void positions in the true cosmology. This is not always the case, and the implications of this assumption for extracting constraints from the void-galaxy CCF in future surveys is the topic of an upcoming paper.

<sup>2</sup> In our case, we already know that the fiducial cosmology should match the true cosmology as we are performing this test on simulated data. Still, this gives us an opportunity to test how well we reproduce the fiducial cosmology and could also be used to estimate the constraining power of an observed data set of similar resolution.

## 2.2. Massive neutrinos

From neutrino flavour oscillation experiments, we know that at least two of the three neutrino mass states have a non-zero mass (Fukuda et al. 1998; Ahmad et al. 2002; Araki et al. 2005). Currently, the flavour oscillation experiments of solar and atmospheric neutrinos put constraints on the differences between the neutrino mass states given by (Particle Data Group 2022)

$$\Delta m_{21}^2 = (7.53 \pm 0.18) \times 10^{-5} \text{ eV}^2, \quad (17)$$

$$\Delta m_{32}^2 = (-2.536 \pm 0.034) \times 10^{-3} \text{ eV}^2 \text{ (IH)}, \quad (18)$$

$$\Delta m_{32}^2 = (2.453 \pm 0.033) \times 10^{-3} \text{ eV}^2 \text{ (NH)}. \quad (19)$$

These experiments are not yet sensitive enough to distinguish between the ordering of the mass states, and we, therefore, have two possibilities: the normal hierarchy (NH), where  $m_1 < m_2 \ll m_3$ , and the inverted hierarchy (IH), where  $m_3 \ll m_1 < m_2$ . Put together, these measurements provide a lower bound on the sum of the neutrino masses at  $\sum m_\nu \gtrsim 0.06 \text{ eV}$  and  $\sum m_\nu \gtrsim 0.1 \text{ eV}$  for the NH and IH respectively. An upper bound on the sum of the neutrino masses is also provided by particle physics and the most recent constraint, at  $\sum m_\nu \lesssim 2.4 \text{ eV}$ , comes from the KATRIN experiment, which investigates the single  $\beta$ -decay of molecular tritium (Aker et al. 2022).

Massive neutrinos make up a fraction of the matter content of the Universe,  $\Omega_\nu$ , described through the relation (Lesgourgues & Pastor 2006)

$$\Omega_\nu h^2 \approx \frac{\sum m_\nu}{93.14 \text{ eV}}. \quad (20)$$

Typically, this is taken out of the dark matter budget,  $\Omega_c$ , so that the total matter content,  $\Omega_m = \Omega_c + \Omega_\nu + \Omega_b$ , stays constant. Here,  $\Omega_b$  and  $\Omega_m$  denote the energy density of baryons and the total matter respectively. As the massive neutrinos are relativistic at early times, they free-stream out of local peaks in the density throughout the first stages of structure formation (Lesgourgues & Pastor 2006). This, in addition to massive neutrinos altering the background evolution, leads to a suppression of matter fluctuations on scales smaller than the neutrino free-streaming length. The strength of this scale-dependent suppression depends on the neutrino mass and shows up in the linear matter power spectrum at small scales as

$$\frac{\Delta P_m}{P_m} \approx -8f_\nu. \quad (21)$$

This is a comparison between a cosmology with massless neutrinos and massive neutrinos, where  $P_m$  is the linear matter power spectrum considering the total matter and  $f_\nu = \Omega_\nu/\Omega_m$ . At non-linear scales, this suppression is known to be even stronger, with a maximum around  $k \sim 1 h \text{ Mpc}^{-1}$ , followed by a turn-around which results in a spoon-like shape of the matter power spectrum ratio (Hannestad et al. 2020).

The presence of massive neutrinos results in observable features in the LSS and CMB (Will 2014), which makes it possible to obtain an upper bound on the sum of the neutrino masses through cosmological observations. Recently, Di Valentino et al. (2021) find  $\sum m_\nu \leq 0.09 \text{ eV}$  at a 95% confidence level by analysing a combination of data sets. This puts pressure on the IH, which might further be confirmed by the *Euclid* space mission (Laureijs et al. 2011). It should, however, be noted that although cosmology can provide a tighter upper bound on the sum of the neutrinos masses than current particle physics experiments, the analysis depends on the choice of a cosmological model.

## 2.3. $f(R)$ -modified gravity

In the concordance  $\Lambda$ CDM model, we have the general theory of relativity (GR) with the Einstein-Hilbert action

$$S = \int \frac{R}{16\pi G} \sqrt{-g} d^4x, \quad (22)$$

where  $R$  is the Ricci scalar and  $g$  is the determinant of the metric tensor,  $g_{\mu\nu}$ . To derive the Einstein field equations, we also need to insert the Lagrangian density of matter,  $\mathcal{L}_m$ , which describes the matter in the theory,

$$S = \int \left( \frac{R}{16\pi G} + \mathcal{L}_m \right) \sqrt{-g} d^4x. \quad (23)$$

In  $f(R)$ -modified gravity theories, the Einstein-Hilbert action is modified by adding a function depending on the Ricci scalar,

$$S = \int \left( \frac{R + f(R)}{16\pi G} + \mathcal{L}_m \right) \sqrt{-g} d^4x. \quad (24)$$

For the specific case of Hu-Sawicki  $f(R)$ -modified gravity, we have

$$f(R) = -m^2 \frac{c_1(R/m^2)^n}{c_2(R/m^2)^n + 1}, \quad (25)$$

where  $m^2 = H_0^2 \Omega_m$  and  $c_1, c_2$ , and  $n$  are constant, dimensionless, non-negative parameters that describe the model (Hu & Sawicki 2007). Requiring that the model gives dark energy in the form of a cosmological constant, these three parameters can be reduced to two,  $n$  and  $f_{R0}$ , where

$$f_{R0} = -n \frac{c_1}{c_2} \left( \frac{\Omega_m}{3(\Omega_m + 4\Omega_\Lambda)} \right)^{n+1} \quad (26)$$

and  $c_1/c_2 = 6\Omega_\Lambda/\Omega_m$ . Increasing the value of  $|f_{R0}|$  gives greater deviations from GR, which has an effect on structure formation. This was demonstrated in Hu & Sawicki (2007), where raising the value of  $|f_{R0}|$  showed an enhancement in the matter power spectrum on small scales.

The  $f(R)$  model has become the ‘fiducial’ model used to investigate cosmological signatures of modified gravity. It is well studied in the literature and constraints have already been produced based on various cosmological probes. For example, an analysis by Cataneo et al. (2015) including cluster, CMB, supernova, and baryon acoustic oscillation (BAO) data obtains an upper bound on the Hu-Sawicki  $f(R)$  theory given by  $\log_{10} |f_{R0}| < -4.79$  for  $n = 1$  at 95.4% confidence level. This familiarity is the reason why we chose Hu-Sawicki  $f(R)$  as our modified gravity model for this work. We set the fiducial value to  $|f_{R0}| = 10^{-5}$ , as this is the value that the LSS is currently able to probe (Koyama 2016). In addition, we occasionally include some analysis with  $|f_{R0}| = 10^{-4}$  to enhance the effects of the modified theory, even though this value has been ruled out by some probes (e.g., Cataneo et al. 2015).

## 2.4. Massive neutrinos and $f(R)$ gravity degeneracy

Modifications of gravity are often described as adding a fifth force which, in addition to gravity, works attractively. This fifth force is in  $f(R)$ -modified gravity carried by the scalaron, the scalar degree of freedom, quantified by  $df/dR$ . The Compton wavelength of the scalaron,  $\lambda_c$ , determines the range of the fifth force, which also establishes the scale on which Hu-Sawicki

$f(R)$ -modified gravity enhances structure formation (e.g., Linares et al. 2014; Cataneo et al. 2015),

$$\lambda_c^0 = 3 \sqrt{\frac{(n+1)}{\Omega_m + 4\Omega_\Lambda}} \sqrt{\frac{|f_{R0}|}{10^{-6}}} h^{-1} \text{Mpc}. \quad (27)$$

For  $|f_{R0}| = 10^{-5}$  and  $n = 1$ , this corresponds to scales  $k \geq 0.1 h \text{Mpc}^{-1}$  at redshift zero.

Massive neutrinos change the time of matter-radiation equality, leading to changes in the LSS. In addition, they suppress structure formation on scales smaller than the neutrino free-streaming length (Lesgourgues & Pastor 2006),

$$\lambda_{\text{FS}} = 7.7 \frac{1+z}{\sqrt{\Omega_\Lambda + \Omega_m(1+z)^3}} \left( \frac{1 \text{ eV}}{\sum m_\nu} \right) h^{-1} \text{Mpc}, \quad (28)$$

due to their inability to cluster as relativistic particles. This corresponds to scales of  $k \geq 0.02 h \text{Mpc}^{-1}$  for  $\sum m_\nu = 0.15 \text{ eV}$  at redshift zero.

The scales where structure formation is enhanced by  $f(R)$  gravity coincide with the neutrino free-streaming length. The suppression effect of the massive neutrinos can therefore, depending on neutrino mass and the value of  $f_{R0}$ , counteract the structure enhancement of  $f(R)$ -modified gravity. This degeneracy has been shown to affect observables such as the matter power spectrum, the halo mass function (HMF) and the halo bias (Baldi et al. 2014).

### 3. Simulations

A variety of simulations incorporating massive neutrinos and modified gravity in different ways already exist (e.g., Adamek et al. 2022; Winther et al. 2015), although fewer take both into account simultaneously (e.g., Baldi et al. 2014; Giocoli et al. 2018). We approach this in our own way, by developing a RAMSES-based code, ANUBISIS, which offers the option of both massive neutrinos and several different modified gravity theories. This code is a merger between ANUBIS<sup>3</sup> and ISIS, as explained in further detail below.

#### 3.1. ANUBIS

For massive neutrino simulations, we have implemented neutrino particles in the  $N$ -body and hydrodynamical code RAMSES (Teyssier 2002). RAMSES implements the particle mesh (PM) method with adaptive mesh refinement (AMR), which enables higher resolution in denser regions of the simulation box. As RAMSES is a Newtonian  $N$ -body code, the most straightforward way to add neutrinos is to implement them as their own particle family and alter the equations of motion (EOM) to handle arbitrarily high momenta. Originally, the gravitational potential is calculated by solving the Poisson equation, but we instead solved the geodesic equation written in terms of canonical momentum, as commonly done for  $N$ -body codes including relativistic particles (Ma & Bertschinger 1994; Adamek et al. 2017, 2022). As a first approach, we ignored frame-dragging, scattering of particles on gravitational waves, and anisotropic stress, leaving us with the EOMs

$$\frac{\partial q_i}{\partial \tau} = - \frac{2q^2 + m^2 a^2}{\sqrt{q^2 + m^2 a^2}} \frac{\partial \phi_i}{\partial x^i}, \quad (29)$$

$$\frac{\partial x_i}{\partial \tau} = \frac{q_i}{\sqrt{q^2 + m^2 a^2}}, \quad (30)$$

<sup>3</sup> <https://github.com/renmau/anubis>

where  $q$  is the canonical momentum,  $a$  is the scale factor,  $m$  is the cold dark matter (CDM) particle mass,  $\partial \phi / \partial x^i$  is the gravitational force (which for modified gravity models includes additional fifth-forces),  $\tau$  is conformal time, and  $x_i$  is the coordinate three-position vector.

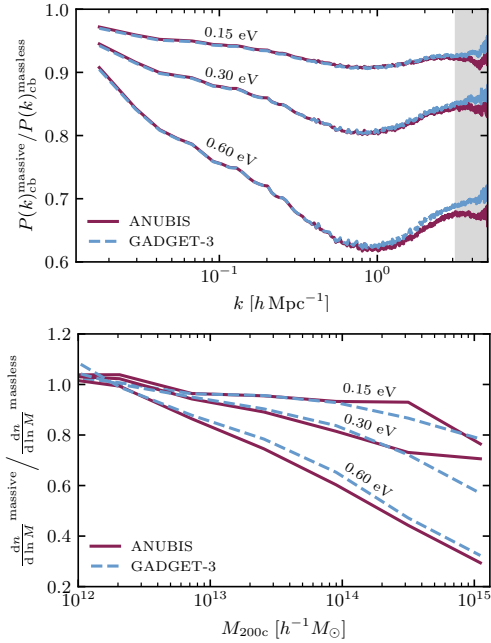
In addition to including the massive neutrinos as a new particle family, we also incorporated radiation into the background evolution through the Hubble function, with an additional option to read the Hubble function,  $H(z)$ , from file. As of now, we have made no changes to how the time-stepping scheme already incorporated in RAMSES operates, which makes for quite slow calculations for the lighter neutrino masses. This could be implemented at a later stage by, for example, detaching the neutrino particles from the grid and allowing them to travel further, letting the CDM particles solely determine the size of the time steps, or by requiring that the neutrino runs use the same refinements and level structure as an equivalent massless neutrino simulation. The latter alternative would allow a more direct comparison between  $\Lambda$ CDM and massive neutrino simulations, especially when studying various ratio properties.

The performance of the ANUBIS code is tested against other codes incorporating massive neutrinos in the massive neutrino code comparison project (MNCCP) within *Euclid* (Adamek et al. 2022), although with a somewhat lower resolution than what is expected for convergence within 1% between the RAMSES and GADGET-3 codes (Schneider et al. 2016). The upper panel of Fig. 1 displays the neutrino suppression on the CDM + baryon (cb) matter power spectrum for different values of the sum of the neutrino masses at  $z = 0$  for both ANUBIS and GADGET-3. The plot shows good agreement between the two codes, especially for lower neutrino masses. At higher masses, the codes start to deviate at smaller scales. This is most likely due to internal differences in resolution for RAMSES, between the  $\Lambda$ CDM and massive neutrino simulations. As the neutrino mass increases, structure formation is more suppressed, leading to fewer refinements created by the RAMSES AMR-scheme. This results in a slightly lower resolution for the neutrino simulations, compared to the  $\Lambda$ CDM one, which shows up in the ratio. This can be resolved by a higher particle density. The lower panel of Fig. 1 displays the neutrino suppression on the HMF for the same neutrino masses as for the matter power spectrum ratios in the upper panel. The magnitude of the suppression is in agreement for both GADGET-3 and ANUBIS, and increases with the halo mass, corresponding to the findings of Brandbyge et al. (2010).

#### 3.2. ISIS

ISIS is a cosmological  $N$ -body code incorporating scalar-tensor gravitational theories including screening mechanisms into RAMSES (Linares et al. 2014). This is done by implementing a non-linear implicit solver for a generic scalar field, which can treat various scalar-tensor-modified gravity theories. This also includes  $f(R)$  theories, which can be rewritten into the scalar-tensor format. In particular, ISIS contains Hu-Sawicki  $f(R)$ -modified gravity, as described in Sect. 2.3.

The upper panel of Fig. 2 shows the ratio of the cb matter power spectrum for a  $\Lambda$ CDM (`1cdm_small`) and  $f(R)$  (`fofr_small`) simulation run with ISIS, with the parameter  $|f_{R0}| = 10^{-4}$ . Here, we can clearly see the enhancement of structure at small scales, with a peak at similar scales to the trough in the neutrino suppression in Fig. 1. For the HMF in the bottom panel of Fig. 2, the amount of large mass halos is increased, compared to  $\Lambda$ CDM, as opposed to the ANUBIS simulations with massive neutrinos that show a decrease. This enhancement is due



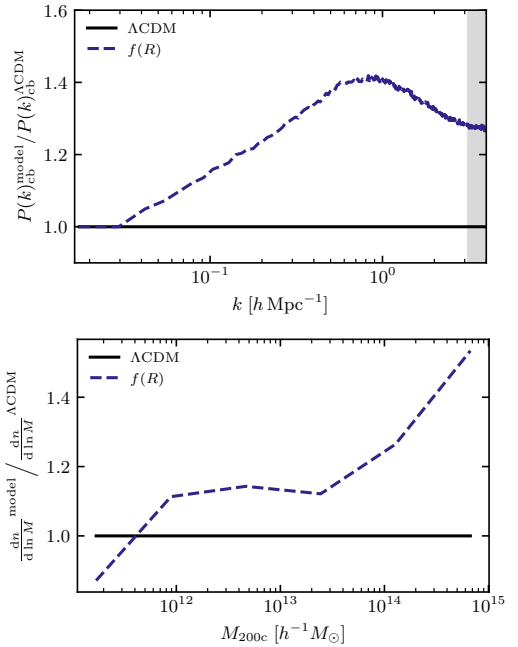
**Fig. 1.** Comparison of the neutrino suppression on the cb power spectrum and HMF for ANUBIS and GADGET-3 at  $z = 0$  for various values of the sum of the neutrino masses. *Top*: the neutrino suppression on the cb power spectrum. The greyed-out area indicates the parts of the ratios lying outside of the Nyquist frequency of the simulations. *Bottom*: the neutrino suppression on the HMF. Only halos with  $N_{\text{part}} \geq 11$  are included.

to a boost of gravity resulting from the fifth force present in  $f(R)$ -modified gravity. Summed up, these figures show the opposite behaviour of what is observed in Sect. 3.1, as expected.

The two simulations introduced here, dubbed `1cdm_small` and `fofr_small`, are occasionally used as additions to the simulations performed for this work. This is further explained in the following section, along with the simulation details.

### 3.3. ANUBIS + ISIS = ANUBISIS

To obtain a RAMSES-based code which includes both the effects of massive neutrinos and  $f(R)$  gravity, we have merged the ANUBIS and ISIS codes into one code, ANUBISIS. This provides us with the opportunity to run simulations with massive neutrinos and modified gravity both independently and simultaneously. For this paper, we have performed a suite of such simulations with properties as presented in Table 1. Summarised, we have six simulations, one with  $\Lambda$ CDM cosmology, one with Hu-Sawicki  $f(R)$ -modified gravity, two with  $\Lambda$ CDM and massive neutrinos, and two with massive neutrinos and Hu-Sawicki  $f(R)$  gravity combined. In addition to these six simulations run with the ANUBISIS code, we also have two simulations, one  $\Lambda$ CDM and one  $f(R)$ , which was previously run with the ISIS code, as presented in Sect. 3.2. These are included as the  $f(R)$  simulation was run with  $|f_{R0}| = 10^{-4}$ , and therefore better demonstrates the effects of modified gravity in specific cases where we are interested in studying this further.



**Fig. 2.** CDM + baryon (cb) matter power spectrum and HMF of the `fofr_small` simulation, compared to `1cdm_small`. The power spectrum and HMF ratios are displayed in the top and bottom panels respectively. For the power spectrum ratio, the different  $\sigma_8$ -values of the simulations are taken into account through scaling, and the greyed-out area indicates the parts of the ratios lying outside of the Nyquist frequency of the simulations.

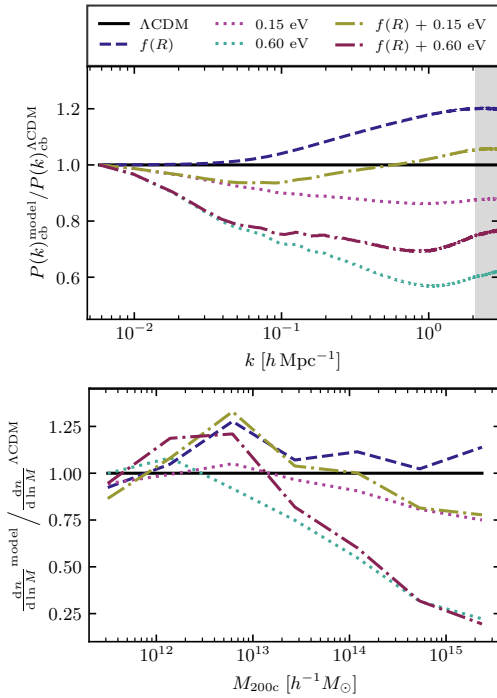
In this section, we present some general properties of the ANUBISIS simulations. To better help distinguish the results, we introduce a general linestyle guide where pure  $\Lambda$ CDM is always shown as a full line,  $f(R)$  as a dashed line, massive neutrino runs as a dotted line, and the combination of  $f(R)$ -modified gravity and massive neutrinos as a dash-dotted line. The upper panel of Fig. 3 shows the ratio of the CDM+baryon (cb) matter power spectrum between the various ANUBISIS simulations and the  $\Lambda$ CDM case. At large scales, there is originally a slight excess in the power spectrum for the massive neutrino and  $f(R)$  + massive neutrino runs. This appears as a result of the grid settings used in the simulations, which is further explained in Appendix A. Essentially, it amounts to a  $\sigma_8$ -scaling (2–3% difference), which is accounted for in the figure. On smaller scales, we observe the expected suppression of structure for the massive neutrino simulations and an enhancement of structure for the  $f(R)$  simulation. The  $f(R) + 0.15$  eV simulation is slightly suppressed, compared to the pure  $f(R)$  run, but it is still dominated by the modified gravity effects due to the low neutrino mass. The  $f(R) + 0.6$  eV simulation, on the other hand, is mostly dominated by the massive neutrinos due to the high neutrino mass, but it is still slightly enhanced, compared to the pure 0.6 eV run.

In the bottom panel of Fig. 3, the HMF of the various simulations, compared to  $\Lambda$ CDM, is shown. In general, we again see that the massive neutrinos suppress the formation of the most massive halos. This is mostly due to the massive neutrinos

**Table 1.** Simulation overview showing the type of simulation and the corresponding properties.

Simulation	Type	$L_{\text{box}} [h^{-1} \text{Mpc}]$	$N_{\text{cdm}}$	$N_{\nu}$	$ f_{R0} $	Mass resolution [ $h^{-1} M_{\odot}$ ]
lcdm	$\Lambda\text{CDM}$	1536	$1024^3$	0	0	$2.99 \times 10^{11}$
fofr	$f(R)$	1536	$1024^3$	0	$10^{-5}$	$2.99 \times 10^{11}$
015ev	0.15 eV	1536	$1024^3$	$2 \times 1024^3$	0	$2.95 \times 10^{11}$
06ev	0.60 eV	1536	$1024^3$	$2 \times 1024^3$	0	$2.85 \times 10^{11}$
fofr_015ev	$f(R) + 0.15 \text{ eV}$	1536	$1024^3$	$2 \times 1024^3$	$10^{-5}$	$2.95 \times 10^{11}$
fofr_06ev	$f(R) + 0.60 \text{ eV}$	1536	$1024^3$	$2 \times 1024^3$	$10^{-5}$	$2.85 \times 10^{11}$
lcdm_small	$\Lambda\text{CDM}$	512	$512^3$	0	0	$8.85 \times 10^{10}$
fofr_small	$f(R)$	512	$512^3$	0	$10^{-4}$	$8.85 \times 10^{10}$

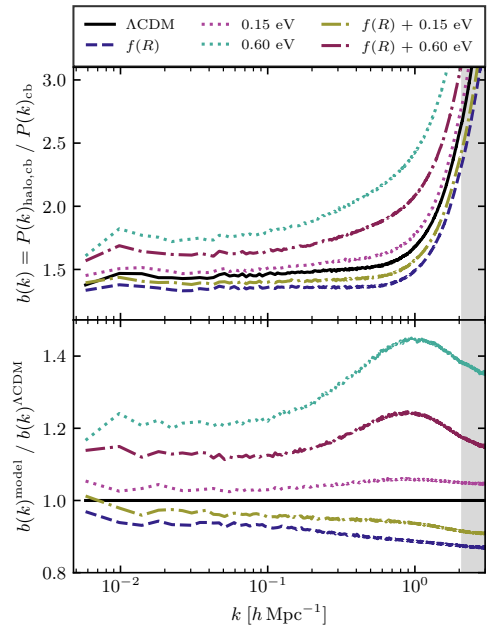
**Notes.** The top six entries show the simulations run with the ANUBISIS code, and the bottom two show simulations previously run with the ISIS code. For the simulations involving Hu-Sawicki  $f(R)$  gravity, we always set  $n = 1$  in Eq. (26).



**Fig. 3.** CDM + baryon (cb) matter power spectrum and HMF of the different ANUBISIS simulations, compared to  $\Lambda\text{CDM}$ . The power spectrum and HMF ratios are displayed in the *top* and *bottom* panels respectively. For the power spectrum, the greyed-out area indicates the parts of the ratios lying outside of the Nyquist frequency of the simulations.

reducing the maximum cluster mass on a linear level (Brandbyge et al. 2010). Because of the fifth force contribution to gravity, we again expect the opposite effect for the  $f(R)$  simulation. This is, however, not very clear for the  $|f_{R0}| = 10^{-5}$  simulation. If we instead look back at the smaller box simulations from ISIS in Fig. 2 with  $|f_{R0}| = 10^{-4}$ , this effect is much more prominent.

Another interesting property is the scale-dependent halo bias. Here, we define it as the ratio between the cross-power

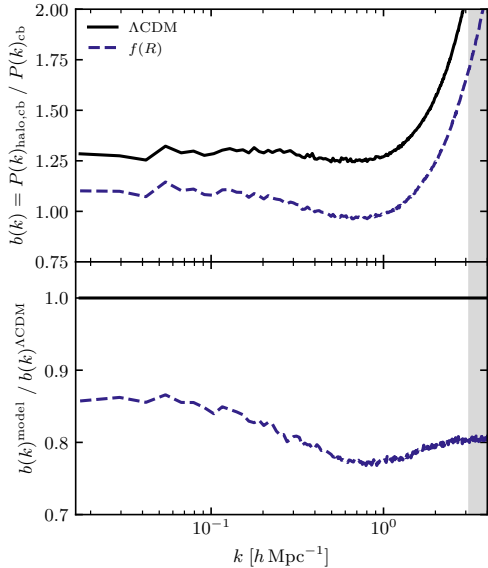


**Fig. 4.** Scale-dependent halo bias for the various ANUBISIS simulations. The *upper* panel shows the value of the bias for each simulation, while the *lower* panel shows the ratio with  $\Lambda\text{CDM}$  for each model. The greyed-out area indicates the parts lying outside of the Nyquist frequency of the simulations.

spectrum of halos and CDM+baryons and the auto matter power spectrum of CDM+baryons,

$$b(k) = \frac{P(k)_{\text{halo,cb}}}{P(k)_{\text{cb}}}. \quad (31)$$

This is defined by the cold species instead of the total matter, as it yields a more universal and scale-independent result in the presence of massive neutrinos (Castorina et al. 2014). In Fig. 4, we see the halo bias for the ANUBISIS simulations at the top, and the ratio of the biases, compared to  $\Lambda\text{CDM}$ , at the bottom. The ratios show a bump at the same scales where we see a trough for the massive neutrino power spectrum ratios. In our



**Fig. 5.** Scale-dependent halo bias for the fofr\_small and lcdm\_small simulations. The upper panel shows the value of the bias for each simulation, while the lower panel shows the ratio with  $\Lambda$ CDM. The greyed-out area indicates the parts lying outside of the Nyquist frequency of the simulations.

case, this shows that our halo power spectrum is less sensitive to the neutrino mass than the cb power spectrum, as discussed by Hassani et al. (2022). In Fig. 5 we also show the scale-dependent bias for the pure ISIS simulations. In general, we see that the halo bias increases with neutrino mass and decreases with the  $f_{\text{RO}}$  parameter, compared to  $\Lambda$ CDM, in line with previous findings in the literature (e.g., Arnold et al. 2019; Chiang et al. 2019).

Looking at the bias values on linear scales, we can calculate an estimate of the linear halo bias. This is presented in Table 2, together with  $\beta$  and  $\sigma_8$ . The two latter are simulation parameters,  $\beta$  being the reconstruction parameter of Sect. 2.1.3 and  $\sigma_8$  the amplitude of the linear matter power spectrum at a scale of  $8 h^{-1} \text{Mpc}$ . For the  $\Lambda$ CDM and massive neutrino simulations,  $\sigma_8$  is a known parameter obtained from the linear power spectrum calculated by CLASS<sup>4</sup> as a part of the initial condition set-up (see Sect. 3.4). For the simulations including modified gravity, an estimation of the linear  $\sigma_8$ -value was found by observing that  $\sigma_{8,\text{CLASS}}^{\nu} / \sigma_{8,\text{CLASS}}^{\Lambda\text{CDM}} \approx \sigma_{8,\text{ANUBISIS}}^{\nu} / \sigma_{8,\text{ANUBISIS}}^{\Lambda\text{CDM}}$  for the linear values calculated from CLASS and the non-linear values calculated from ANUBISIS. We then assumed that this relation also holds in the modified gravity context.

### 3.4. Initial conditions

The initial conditions used for the ANUBISIS simulations were generated by following the same procedure as outlined in Adamek et al. (2022). In short, the linear matter power spectra and transfer functions were generated by CLASS (Lesgourgues 2011; Blas et al. 2011), and rescaled to  $z = 127$  through the

<sup>4</sup> [https://github.com/lesgourg/class\\_public](https://github.com/lesgourg/class_public)

**Table 2.** Linear bias, reconstruction parameter, and  $\sigma_8$  for the various simulations.

Simulation	$b$	$\beta$	$\sigma_8$
lcdm	1.436	0.3715	0.85
fofr	1.349	0.3954	0.89
015ev	1.484	0.3595	0.82
06ev	1.739	0.3067	0.73
fofr_015ev	1.397	0.3818	0.86
fofr_06ev	1.624	0.3285	0.76
lcdm_small	1.271	0.4146	0.80
fofr_small	1.091	0.4830	0.91

**Notes.** The linear halo bias,  $b$ , is found by taking the average of the scale-dependent bias for  $k < 0.05 h^{-1} \text{Mpc}$ . Values of  $\beta = f/b$  are estimated using the  $\Lambda$ CDM growth rate value,  $f = \Omega_m^{0.55}$ . The  $\sigma_8$ -values are known for the  $\Lambda$ CDM and neutrino simulations and otherwise estimated as explained in the main text.

REPS<sup>5</sup> code (Zennaro et al. 2017), which takes the effects of massive neutrinos into account through a two-fluid description and by including radiation in the background evolution and implementing a scale-dependent growth rate. Positions and velocities for the CDM and neutrino particles were then generated by a version of the N-GenIC code<sup>6</sup> that also has been modified to include the scale-dependence of the growth rate and growth factor in the presence of massive neutrinos.

For the initial conditions, we used  $\Omega_b = 0.049$  and  $\Omega_c \approx 0.27$ . We kept the total matter density fixed at  $\Omega_m \approx 0.319$  by adjusting the ratio of  $\Omega_c$  and the neutrino density parameter,  $\Omega_\nu = \sum m_\nu / (93.14 h^2 \text{eV})$ . Besides this, we used the Hubble constant,  $h = 0.67$ , the scalar spectral index,  $n_s = 0.9619$ , the CMB temperature,  $T_{\text{CMB}} = 2.7255 \text{K}$ , and the amplitude of the primordial power spectrum,  $A_s = 2.215 \times 10^{-9}$ , at the pivot scale  $k_p = 0.05 \text{Mpc}^{-1}$ . This is the same cosmology as applied by Adamek et al. (2022).

We used the method outlined above to generate initial conditions for our  $\Lambda$ CDM and massive neutrino simulations. For the simulations including  $f(R)$ -modified gravity, we used the outputs from the other simulations at  $z = 4$  as initial conditions. The deviations from GR are small at this stage, and only become more important at later times, as demonstrated for  $z = 3$  and  $|f_{\text{RO}}| = 10^{-5}$  by Zhao et al. (2011). For the two independent ISIS runs, the initial conditions were generated by Grafic2 (Bertschinger 2001), with the parameters  $\Omega_c = 0.267$ ,  $\Omega_b = 0.045$ ,  $h = 0.719$ , and  $n_s = 1.0$ .

## 4. Method

In this section, we detail the various codes and packages used to study our simulation data. We also provide an overview of the full analysis process.

### 4.1. Halo finder

To identify halos in our simulations, we used the ROCKSTAR<sup>7</sup> halo finder (Behroozi et al. 2012). ROCKSTAR locates halos in phase space by applying the 3D friends-of-friends (FOF) method

<sup>5</sup> <https://github.com/matteozennaro/reps>

<sup>6</sup> [https://github.com/franciscovillaescusa/N-GenIC\\_growth](https://github.com/franciscovillaescusa/N-GenIC_growth)

<sup>7</sup> <https://bitbucket.org/gfcstanford/rockstar/src/main/>



to pinpoint overdense regions. For each of the groups created in the FOF procedure, the linking length (the characteristic length scale grouping the particles together) is reduced progressively, so that subgroups emerge in a hierarchical structure. Seeds are then placed in the lowest substructures and particles are assigned to the halo seed within the shortest phase-space distance. From this, the relationship between host and subhalos is computed and unbound particles are removed. Finally, halo properties are calculated.

When applying ROCKSTAR to our simulations, we read the gadget files directly to obtain the CDM particle properties and the cosmological parameters. The force resolution was set to be approximately the smallest distance resolved by the simulation, and the linking length was set to  $l = 0.28 h^{-1} \text{Mpc}$ , which is 0.2 of the mean inter-particle separation. In the end, we removed the subhalos and were left with a host halo catalogue. As shown in Adamek et al. (2022), ANUBIS underestimates the number of halos, especially at low mass. This can be improved upon by increasing the particle density but was not done for the simulations presented in this paper. Because of this, we made no further mass cuts to the halo catalogue.

#### 4.2. Void finder

When identifying voids within the halo catalogue of a simulation, we must first define a void numerically. In this paper, we apply two different void definitions, spherical voids and voxel voids.

For the spherical void detection, we used the void finder module implemented in Pylians<sup>8</sup>, which is based on the method detailed in Banerjee & Dalal (2016). Here, the algorithm is provided with a range of radii corresponding to spherical regions of various sizes to be investigated, along with an overdensity threshold given by  $\Delta = \rho/\bar{\rho} - 1$ . Starting with the largest radius, the simulation box is divided into a grid and the density profile is calculated in each voxel and smoothed on a scale corresponding to the given radius. Voxels with densities below the threshold are identified and sorted. Starting with the lowest density voxel, all the voxels around it within the given radius are considered and added as a part of the void. This is then repeated for the next to lowest density voxel and so on. If any of the voxels within the corresponding radius are already assigned to another void, the new void is rejected. Once this is done for all the voxels below the density threshold, the algorithm moves on to the next to largest radius provided, smooths the density field at that scale, and once again proceeds as explained above. This is repeated for all the radii given initially, and the resulting voids identified are spherical regions of these specific sizes, with the centre at the lowest density voxel. In our case, we set  $\Delta = -0.75$  and provided the algorithm with 47 void radii between  $16\text{--}82 h^{-1} \text{Mpc}$ .

For detecting voids by using the voxel void definition, we employed the Revolver<sup>9</sup> void finder (Nadathur et al. 2019c). Here, the voxel voids are defined by using a watershed method. The simulation box is divided into a grid and local minima of the density field are located. Around each of these minima, surrounding voxels with increasing overdensity are added to the pool up until a voxel with a lower overdensity than the one previously added is discovered. Using this definition, the identified voids may have any shape, as opposed to the spherical void definition. The centre of the void again lies within the voxel with the lowest density. The Revolver void finder can also perform

reconstruction when provided with a halo catalogue given in redshift space. This is based on linear theory, as described in Sect. 2.1.3, and requires the halo bias,  $b$ , and growth rate,  $f$ , as input parameters. For a more detailed description of the spherical and voxel void definitions, along with other void-identifying algorithms, see Massara et al. (2022).

#### 4.3. Covariance matrix

Each of our simulation boxes only has one realisation. To obtain an estimate of the uncertainty in the redshift space void-halo CCF calculated from the simulation data, we attained the covariance matrix through a Jackknife method. We applied the Jackknife estimator as implemented in Pycorr<sup>10</sup>, following Mohammad & Percival (2022).

The ANUBISIS simulation boxes were equally divided into  $n = 512$  sub-boxes<sup>11</sup>. Individual Jackknife realisations were then made by calculating the correlation function for the full volume with one of the sub-boxes removed at a time. This lead to  $n$  Jackknife realisations, each with a volume fraction  $(n-1)/n$  of the original volume. Based on this, each element in the covariance matrix,  $C_{ij}$ , is given by

$$C_{ij} = \frac{n-1}{n} \sum_{k=1}^n [\xi_i^k - \bar{\xi}_i][\xi_j^k - \bar{\xi}_j], \quad (32)$$

where

$$\bar{\xi}_i = \frac{1}{n} \sum_{k=1}^n \xi_i^k \quad (33)$$

is the mean estimate from all the  $n$  Jackknife realisations.

It is important to note that since we only have one simulation of each individual case, and we used the data from the simulations to calculate  $\xi^r$ ,  $v_r(r)$ , and  $\sigma_{\eta}$ , the model and data  $\xi^s$  are correlated. Ideally, the input parameters should be calculated from the average of many mock simulations, as is done in for example Woodfinden et al. (2022) and Nadathur et al. (2019b), to avoid this problem, along with the issue of the uncertainty associated with only having one measurement of  $\xi^r$ . One way to deal with the correlated errors is to calculate the covariance matrix for the CCF of the difference between the model and the data,  $\xi_{\text{diff}}^s = \xi_{\text{model}}^s - \xi_{\text{data}}^s$ . A more detailed explanation and demonstration of the effects of this approach can be found in Appendix A of Radinović et al. (2023). We did not include this step in our analysis as we focus more on the comparison between the simulations as opposed to reducing the statistical error for a single simulation.

#### 4.4. Analysis pipeline

For the ANUBISIS simulation data, the CDM and neutrino particles were given separate identifiers. It is the CDM particle information that goes into the procedure detailed below unless otherwise stated.

First, the particle data were given to the ROCKSTAR halo finder, which identified halos in the simulation boxes as detailed in Sect. 4.1. This provided both the positions and velocities of the halos, enabling us to put the halos into redshift space if needed. The halo catalogues were then given to the Revolver

<sup>8</sup> <https://github.com/franciscovillaescusa/Pylians3>

<sup>9</sup> <https://github.com/seshnadathur/Revolver>

<sup>10</sup> <https://github.com/cosmodesi/pycorr>

<sup>11</sup> We ran tests using both less (216) and more (2744) Jackknife samples and found similar estimates for the covariance matrix.

void finder, which identified voxel voids in between the halos, as explained in Sect. 4.2. In order to test how well reconstruction (Sect. 2.1.3) performs in the case of massive neutrinos and modified gravity, this step was not only performed directly on the real space halo catalogue but also with the redshift space halo catalogue as input. We performed the reconstruction step by applying `RevoLver`, which solves Eq. (11) through an iterative fast Fourier transform algorithm (Burden et al. 2014, 2015). This is the same algorithm used for BAO reconstruction (e.g., Gil-Mafin et al. 2020; Bautista et al. 2021). We then had two void catalogues, one directly identified in real space, and one in reconstructed real space, both found by the voxel void definition. We then performed the same void finding with the spherical void definition, as detailed in Sect. 4.2, both with the real space and reconstructed real space halo positions. After obtaining void catalogues in real and reconstructed real space, for the voxel and spherical void definitions, we performed a radius cut at  $21 h^{-1} \text{Mpc}$  for all catalogues, to eliminate void discoveries that coincide with the average spacing between halos. For each catalogue, the remaining voids with their coinciding halos were then stacked on top of each other to obtain an ‘average’ void with more statistically robust properties and spherical symmetry. From the halo distribution in and around these voids, we calculated the density profile, mean velocity profile, and LOS velocity dispersion. The latter was computed as detailed by Radinović et al. (2023). These are all ingredients needed to calculate the void-halo CCF in redshift space as shown in Eq. (5).

We want to compare the modelled void-halo CCF in redshift space with the void-halo CCF calculated directly from the simulation data. In order to obtain the latter we used the correlation function estimation wrapper, `Pycorr`, which currently utilises the `Corrfunc`<sup>12</sup> CCF engine (Sinha & Garrison 2019, 2020). Provided the redshift space halo catalogue, real space void catalogue, and randomly distributed reference catalogues, `Pycorr` calculates the void-halo CCF of the simulation data as we would observe it. This is done using the Landy-Szalay estimator (Landy & Szalay 1993),

$$\xi(r, \mu) = \frac{D_1 D_2(r, \mu) - D_1 R_2(r, \mu) - D_2 R_1(r, \mu) + R_1 R_2(r, \mu)}{R_1 R_2(r, \mu)}, \quad (34)$$

where  $D$  is the simulated data catalogues,  $R$  is the random catalogues, and 1 and 2 are the halos and voids. We used 50 bins between  $0-150 h^{-1} \text{Mpc}$  for  $r$ , the spatial distance between the pairs, and 200 bins from  $-1$  to  $1$  for  $\mu$ , the angular separation. For the random catalogues, we used 50 times as many halos and voids as the simulations. `Pycorr` also has an inbuilt Jackknife estimator, which allowed us to calculate the covariance matrix of the CCF, as described in Sect. 4.3. We calculated the void-halo CCF using both the voids identified in real space and in reconstructed real space.

Having the simulated CCF, we used `Victor`<sup>13</sup> to calculate the theoretical model and compare it to the data, both in the real and reconstructed case. To do so, `Victor` requires  $\xi^s$  from the simulations, a covariance matrix, and  $\xi^r$ ,  $v_r(r)$ ,  $\Delta_{\text{DM}}$ , and  $\sigma_{v_{\parallel}}$  as input to the model. `Victor` also assesses the goodness of fit between the data and the model, and provides a  $\chi^2$  value upon request.

Through an interface with `Cobaya` (code for bayesian analysis<sup>14</sup>, Torrado & Lewis 2019, 2021), we can also use `Victor`

<sup>12</sup> <https://github.com/manodeep/Corrfunc>

<sup>13</sup> <https://github.com/seshnadathur/victor>

<sup>14</sup> <https://github.com/CobayaSampler/cobaya>

to perform MCMC fits of the parameters in the void-halo CCF model. We assumed a Gaussian form of the likelihood

$$\log \mathcal{L} = -\frac{1}{2} (\xi_{\text{model}}^s - \xi_{\text{data}}^s) \mathbf{C}^{-1} (\xi_{\text{model}}^s - \xi_{\text{data}}^s)^{\text{T}}, \quad (35)$$

along with flat priors for the parameters  $f\sigma_8$ ,  $\sigma_{v_{\parallel}}$ ,  $\beta$ , and  $\epsilon$ , encompassing the fiducial values. In the case where we used the actual real space data from the simulations,  $\beta$  was not included. In the case of reconstruction,  $\beta$  was allowed to vary. When comparing CCF data to theory, reconstruction was only performed for the fiducial  $\beta$ -value of each simulation. However, to allow for  $\beta$  to vary for the MCMC fits, we performed reconstruction, void finding, and the CCF calculation repeatedly for 11 different  $\beta$ -values, which were provided to `Victor` to perform the fit. Ideally, covariance matrices should also be computed in each reconstruction case, as it depends on  $\beta$ . This is a time-consuming task, and as a first approach, we instead assumed a fixed  $\beta = \beta^{\text{fiducial}}$  for all the covariance matrices. We also kept the input  $\xi^r$  equal to the one calculated for  $\beta^{\text{fiducial}}$  in all cases, meaning that the  $\beta$ -dependence only shows up in  $\xi^s$ . This is the same approach taken by Radinović et al. (2023).

## 5. Results

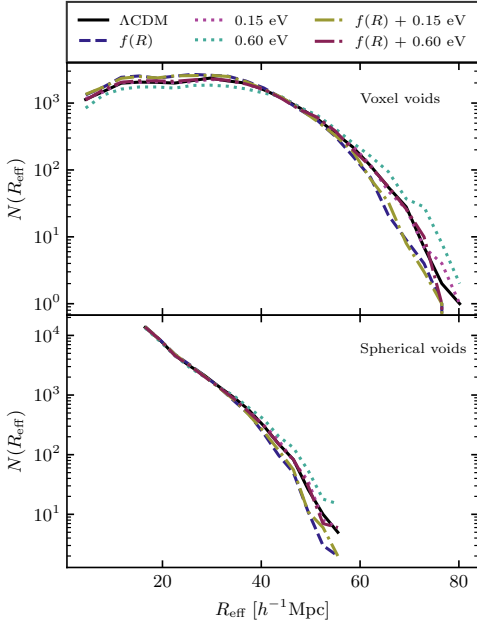
In this section, we present the results of our analysis. In addition, we discuss the implications of our results.

### 5.1. Void abundance

First, we take a look at the general void population identified in all the ANUBISIS simulations. In Fig. 6 we show the abundance of voids depending on the effective void radius. At the top, the voxel void definition has been used to find the voids, and at the bottom, the spherical void definition. For the voxel voids, the difference in the number of voids is clearly apparent in the approximate range  $10-40 h^{-1} \text{Mpc}$ . For the spherical voids, however, this is not the case. If we zoom in, the same ordering is present, but this is not apparent at first glance due to the high number of voids identified in the given range. The spherical void finding algorithm, as detailed in Sect. 4.2, identifies voids by smoothing the field for a given top-hat radius and declaring spheres with density below a certain threshold as voids. For small radii, this results in a large amount of voids, some of which might be the result of shot noise, for all simulations.

For the  $f(R)$  and  $f(R)$  dominated  $f(R) + 0.15 \text{eV}$  simulations, we see an increase in the number of voids within the  $10-40 h^{-1} \text{Mpc}$  effective radius range, compared to  $\Lambda\text{CDM}$ . This is due to the fifth force enhancing gravity in these regions, resulting in a more effective ‘evacuation’ of the areas. Li et al. (2012) also report a higher number of the large voids in their  $f(R)$  simulations, although it should be noted that their maximum void size is around  $15 h^{-1} \text{Mpc}$  due to their smaller, but higher resolution, simulation boxes.

The most massive neutrino simulation,  $0.60 \text{eV}$ , shows the opposite behaviour. Here, the amount of voids in the given size range is suppressed, compared to  $\Lambda\text{CDM}$ . This is a result of the neutrinos slowing down the clustering and thereby the evolution of the voids towards lower densities. Massara et al. (2015) also report fewer large voids in their massive neutrino simulations, compared to  $\Lambda\text{CDM}$ , where large in their case is in the range  $20-40 h^{-1} \text{Mpc}$ . For very large voids,  $R_{\text{eff}} \geq 45 h^{-1} \text{Mpc}$ , we see a turn-around of the ordering for both void definitions. Cai et al. (2015) also found a higher amount of very large radii ( $\geq 25 h^{-1} \text{Mpc}$ ) voids in their regular GR simulations, compared



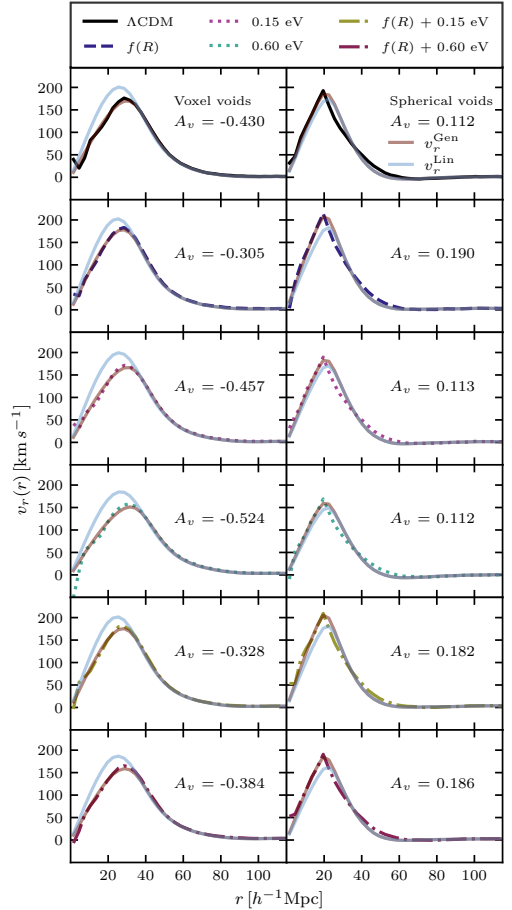
**Fig. 6.** Histogram of effective void size for the various ANUBISIS simulations. The voxel voids display a notable difference in the number of voids in the  $\sim 10\text{--}40 h^{-1}$  Mpc range. Both void definitions also show a slight opposite abundance difference amongst the largest voids in the simulation catalogues.

to  $f(R)$ . Based on investigation they suggest that this is a result of the largest voids being less empty in the  $f(R)$  case, as the enhanced gravity inside makes it easier for halos to form, compared to  $\Lambda$ CDM. When looking at a big region in  $\Lambda$ CDM versus a big region in the  $f(R)$  simulation, the number density of halos would be lower for  $\Lambda$ CDM, making it easier to pass the void identification criteria. The opposite could then be argued for the massive neutrino simulations. It should be noted that the differences observed for very large voids in Fig. 6 are enhanced due to the logarithmic scale, and could also be affected by the small sample size.

For the  $\Lambda$ CDM simulation, we find in total  $N_{\text{halo}} \approx 1.3 \times 10^6$ . From this, we chose a radius cut for the voids as  $R_{\text{eff}}^{\text{cut}} = 1.5(N_{\text{halo}}/V_{\text{box}})^{-1/3} \approx 21 h^{-1}\text{Mpc}$ . This was applied to the void catalogues to make sure that we exclude what are simply empty regions in between halos in the simulations, and not actual voids.

## 5.2. Velocity profile

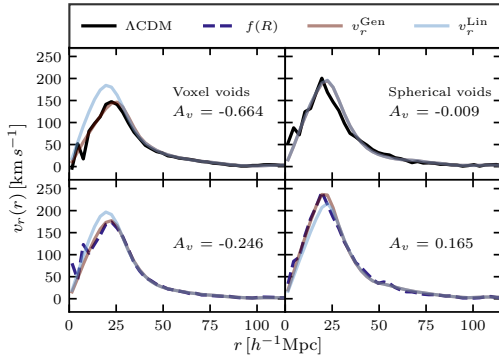
When using galaxy surveys to identify voids, the velocity profile needed for the CCF model is typically modelled by the linear velocity profile or estimated from simulations. Because of this, we want to study how the simulated velocity profiles for various cosmologies compare to the linear model. In Fig. 7, the mean radial outflow void velocity profile for each ANUBISIS simulation is shown for both the voxel and spherical void definitions. The individual profiles are compared to the theoretical linear velocity profile, as shown in Eq. (8), and the more gen-



**Fig. 7.** Radial void velocity profiles for all ANUBISIS simulations together with the linear velocity profile and a fit to the more general velocity profile, presented in Sect. 2.1.2. The voxel and spherical void definitions are shown in the left and right columns respectively. The  $A_v$ -parameter in each panel shows the best-fit value of the general profile.

eral velocity profile, as shown in Eq. (10). For the linear velocity profile, the growth rate,  $f = \Omega_m^{0.55}$ , corresponding to the expected  $\Lambda$ CDM value, was applied for all simulations. In doing so, we ignore the scale dependence of the growth rate in the  $f(R)$  and massive neutrino cosmologies and investigate whether or not this leads to biased results. For the general profile, the best-fit values of the  $A_v$ -parameter are given in each panel of Fig. 7. These were obtained through the least squares method.

The general velocity profile is, with the best fit  $A_v$ -parameter values, by construction, a good match to the velocity profiles found in the simulation data. For the voxel voids, the best-fit parameter value is consistently higher for  $f(R)$  and decreases with increasing neutrino mass, compared to  $\Lambda$ CDM. This is expected as a result of higher velocities in the  $f(R)$  case, and lower in the massive neutrino case. The mixed simulations lie

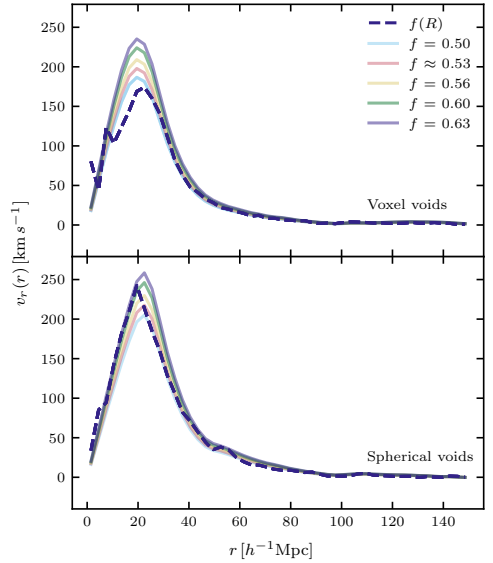


**Fig. 8.** Radial void velocity profiles for the `fofr_small` and `lcdm_small` simulations together with the linear velocity profile and a fit to the more general velocity profile. The voxel and spherical void definitions are shown in the *left* and *right* columns respectively. The  $A_v$ -parameter shows the best-fit value for the general profile.

somewhere in between. For the spherical voids, we do not see the same pattern for the neutrino masses and the value of  $A_v$ . However, for the spherical voids, the general velocity profile does not fit as well as for the voxel voids at higher radii. When estimating  $A_v$ , this must be taken into account, in addition to the peak of the velocity profile. If we could observe the velocity profile directly over a large void sample, the best-fit  $A_v$ -value could be an interesting parameter to explore as a cosmological probe. Observing the velocity profile directly is not possible in traditional galaxy surveys, which is why it is currently modelled or estimated from simulations.

From visual inspection, it is clear that the theoretical linear velocity profile is not a good fit for the data close to the void centre. This is due to a sparse tracer sample in this region and also depends on the void centre definition (Massara et al. 2022). It affects the voxel void definition more than the spherical one. In the voxel void case, the linear model overestimates the clustering. We can see that this is somewhat compensated for in the  $f(R)$  simulations, due to higher velocities. This is even more visible for the pure ISIS simulations, as shown in the lower left panel of Fig. 8. For the spherical voids, this is less of an issue, although the linear model slightly underestimates the clustering. In the latter case, this could be compensated by adopting a different value of the growth rate,  $f$ , in the linear theory model, as demonstrated in Fig. 9. For the voxel voids, increasing the value of  $f$  in line with expectations (e.g., Mirzatuny & Pierpaoli 2019) only increases the discrepancies.

Altogether, it is evident that the linear velocity profile is not a drastically worse fit for the  $f(R)$  or massive neutrino simulations. Before we can address any differences due to cosmology, however, we must make sure that a sparse tracer sample does not affect our model-data comparison. As it stands now, applying the linear velocity profile to the CCF modelling results in modifications similar to changes in  $f\sigma_8$ , due to the offset induced by the number of tracers (Massara et al. 2022). In addition, we should point out that even if the velocity modelling was improved to forgo this issue, the modifications expected from the  $|f_{R0}| = 10^{-5}$   $f(R)$  simulation and the most massive neutrino simulation are mostly on scales smaller than the average void size.



**Fig. 9.** Linear velocity profile, compared to the `fofr_small` simulation, for various values of the growth rate,  $f$ . The regular linestyle and colour show the velocity profile for the simulation. For  $\Lambda$ CDM we have  $f = \Omega_m^{0.55} \approx 0.53$ .

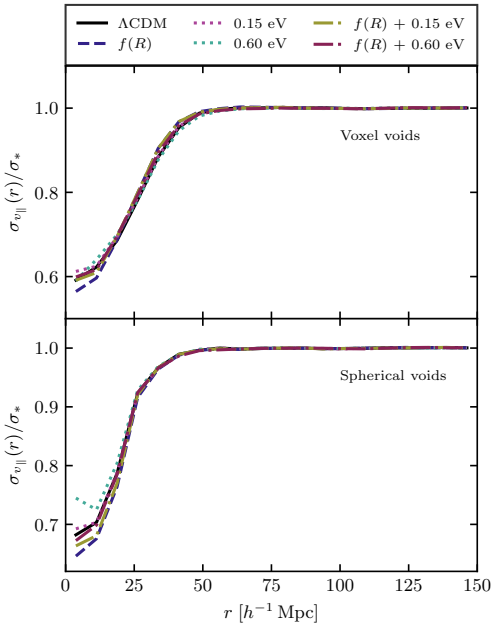
### 5.3. Velocity dispersion

The CCF theory presented in Sect. 2.1.1 depends on the velocity dispersion of the void velocity profile. For all the ANUBISIS simulations, Fig. 10 shows this quantity for both the voxel and spherical void definitions, scaled by the average amplitude beyond  $75 h^{-1} \text{Mpc}$ ,  $\sigma_*$ . The velocity dispersion profile has the same shape for all the various cosmologies, but a different amplitude,  $\sigma_*$ , as presented in Table 3. The relative values of the amplitudes coincide with expectations. The halos in and around the void in the  $f(R)$  simulation feel a stronger gravitational pull towards the edge, compared to the  $\Lambda$ CDM case. In general, there is also more clustering which leads to higher velocities. The relative values of the amplitudes in the  $f(R)$  and  $\Lambda$ CDM cases coincide well with the findings of Fiorini et al. (2022). The opposite behaviour is seen for the massive neutrino simulations, where less clustering results in lower velocities. However, although these differences can be calculated from the simulated data, they can not readily be observed.

### 5.4. Void-halo CCF: data versus model

We are interested in the void-halo CCF of the various simulated cosmologies and how well the theory presented in Sect. 2.1.1 reproduces the simulation data. Figure 11 shows the monopole, quadrupole, and hexadecapole of the void-halo CCF for the ANUBISIS simulations. The left and right columns display the results for the voxel and spherical void definitions respectively. The voids were identified from the real space halo catalogue, and the redshift space halo positions were calculated directly from the real space positions and corresponding LOS velocities.

For the monopole, the differences between the simulations are clearer for the voxel void definition, as was also the case earlier when looking at the void abundance. The shape of the



**Fig. 10.** LOS velocity dispersion scaled by  $\sigma_*$  as given in Table 3. The voxel and spherical void definitions are shown in the *upper* and *lower* panels respectively. All the simulated cosmologies result in similar profile shapes. The largest differences are located towards the void centres, which are dominated by shot noise.

monopole is closely related to the shape of the density profile around the void, as both in essence describe how halos are distributed around the void centre as a function of radius. The  $f(R)$  and  $f(R)+0.15$  eV simulations show the narrowest profiles (most evolved) and the 0.6 eV simulation the broadest (least evolved), while the others fall somewhere in between. From the void abundance histogram in Fig. 6, we saw that the  $f(R)$  case has more voids in the  $10\text{--}40 h^{-1}$  Mpc effective radius range and the 0.6 eV has less, compared to  $\Lambda$ CDM. This further explains what we see here in terms of the shapes of the profiles, as the monopole is based on the overall averaged void from each simulation box. For the voxel void definition, the central value goes towards  $-1.0$ , while for the spherical void definition, we see a very flat core stabilising at around  $-0.88$ . This is again a result of the void-finding algorithm, where a sphere of a given radius with a smoothed density below  $-0.75$  is classified as a void. As mentioned before, this leads to the detection of a large amount of small voids, and in addition, most of the detected voids have central densities that are larger than  $-1.0$ .

The quadrupole is most easily studied for the voxel void definition. Here, we see, in all cases, the expected smooth shape resulting from RSDs as a consequence of halos inside the void moving towards the small overdensity at the edge, but also halos outside the void moving back towards the void edge. For the spherical voids, we instead see a sharp feature preceding the edge of the void. The difference between the quadrupoles of the two void definitions is due to the shapes of the void density profiles and the presence of a velocity dispersion. This is further

**Table 3.** Average value of the LOS velocity dispersion,  $\sigma_*$ , for  $r \geq 75 h^{-1}$  Mpc in the case of voxel voids (VV) and spherical voids (SV).

Simulation	$\sim\sigma_*^{VV}$ [km s $^{-1}$ ]	$\sim\sigma_*^{SV}$ [km s $^{-1}$ ]
lcdm	334.4	334.3
fofr	356.7	356.9
015ev	329.2	328.8
06ev	300.8	300.6
fofr_015ev	351.0	351.0
fofr_06ev	320.8	320.3
lcdm_small	319.4	319.6
fofr_small	388.1	387.9

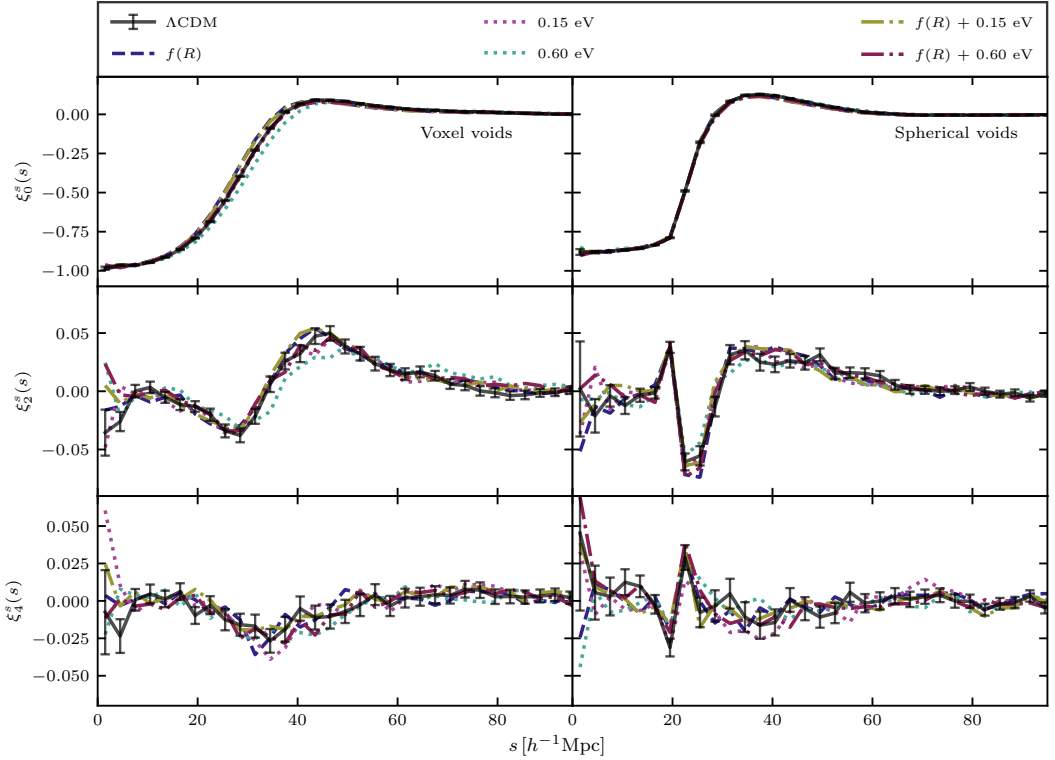
explained through the use of a toy model in Appendix B. Within the error bars, the quadrupole for each simulation is not easily distinguishable. The most massive neutrino simulation shows signs of lower peaks due to overall lower velocities for the voxel void definition, but higher resolution simulations should be performed in order to confirm this.

The hexadecapole is, from the theoretical model, expected to be small (Cai et al. 2016). This is the case for all simulations and both void definitions, except for a little dip in the voxel void  $\xi_4^s$  around  $s \sim 35 h^{-1}$  Mpc. This small signal in the hexadecapole shows why it can still be important to include this multipole when fitting the model to the data to obtain cosmological parameters, instead of assuming it to be zero.

Figures 12–14 respectively display the monopole, quadrupole, and hexadecapole of the void-halo CCF in redshift space as calculated directly from the ANUBISIS simulation data, compared to its theoretical value calculated by *VICTOR* as outlined in Sect. 2.1.1. The simulation data follow the regular colour and linestyle pattern, while the theory is presented with full brown and blue lines. The brown line is the relevant theoretical multipole as calculated by *VICTOR*, with the velocity profile from the simulation data given to the model as a velocity template, and the blue line is the same, only with the linear velocity profile as displayed in Eq. (8) given as input. For each simulation, void definition, and multipole, only the  $\Lambda$ CDM simulation data line has error bars. This is to illustrate their magnitude but otherwise reduce cluttering.

The monopole data-theory comparison in Fig. 12 is presented through the difference between the redshift space and real space monopole. This is done to better display the discrepancies between the data and the two models. For all simulations and both void definitions, we see good agreement. There is a preference towards inputting the velocity profile from the simulations in the model, compared to using the linear velocity profile. This is expected simply because we are providing the model with the actual data that we want to reproduce. We already saw, in Sect. 5.2, that the linear velocity profile does not reproduce the velocity profile directly calculated from the halos in the simulations very well. However, if this study was performed on observational data, we would not have had access to the exact mean outflow velocity profile. We could then either use the linear approximation or make estimates through simulations.

The quadrupole data-theory comparison in Fig. 13 is the most interesting to study, as it is the RSDs observed here that, through modelling, can give us an estimate of the  $f\sigma_8$ -value. It is again evident from visual inspection that the model reproduces the data well for all simulations. For the voxel void definition, applying the linear velocity profile as an approximation gives results within the error bars for all simulations.



**Fig. 11.** Void-halo CCF for the ANUBISIS simulation data. The voxel and spherical void definitions are shown in the *left* and *right* columns respectively. The error bars are estimated using a Jackknife technique and are only shown for the  $\Lambda\text{CDM}$  case for a tidier visual representation of the data.

For the spherical void definition, the consequence of applying the linear velocity profile is more significant, even though the difference between the data and linear theory velocity profiles in Fig. 7 is larger for the voxel void definition. This could be partly because even though the linear and simulation velocity profiles deviate more towards the void centre for the voxel voids, compared to the spherical voids, they actually coincide better for  $r \gtrsim 30 h^{-1}\text{Mpc}$ . This is also where we see some of the larger discrepancies between the spherical void simulation quadrupole and the modelled quadrupole with the linear velocity as input. Even though we see a difference in the model fit for the two void definitions, there is no significant difference in the performance of the model between the various simulated cosmologies. Ideally, we need higher resolution simulations along with more accurate velocity modelling in order to quantify this.

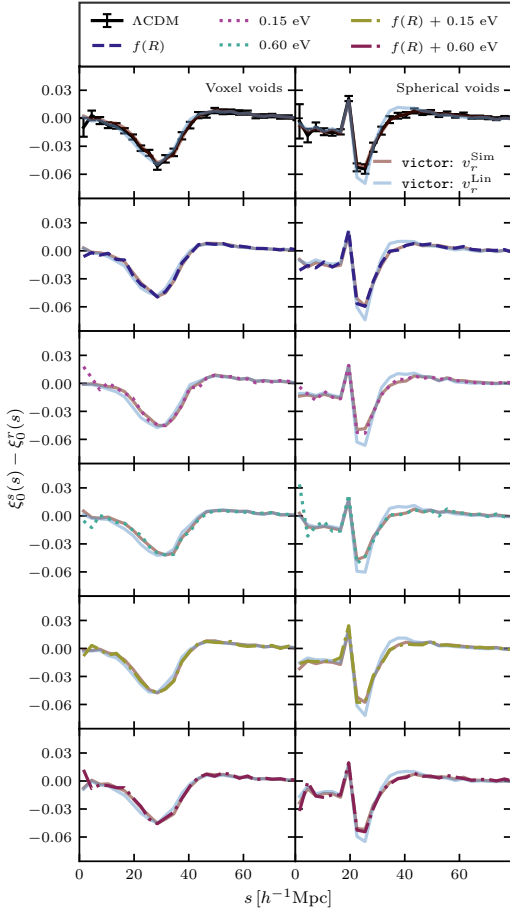
Figure 14 shows that also the hexadecapole is well described by the model for both void definitions. This further encourages including it in analysis when it is available.

### 5.5. Reconstructed void-halo CCF: data versus model

The reconstruction process, detailed in Sect. 2.1.3, assumes linearity and a constant growth rate which might affect its performance when modified gravity or massive neutrinos are intro-

duced. Figure 15 shows how reconstruction performs for each individual ANUBISIS simulation. The lines, following the regular colour and style pattern, show a histogram of the difference between the LOS coordinate (defined as the  $z$ -direction in our simulation boxes) in real space and reconstructed real space. The fainter line, in the same colour, shows a histogram of the difference in the LOS coordinate in real space and redshift space, before any reconstruction is performed. The reconstruction process illustrated in this figure is executed with the fiducial  $\beta$ -values presented in Table 2.

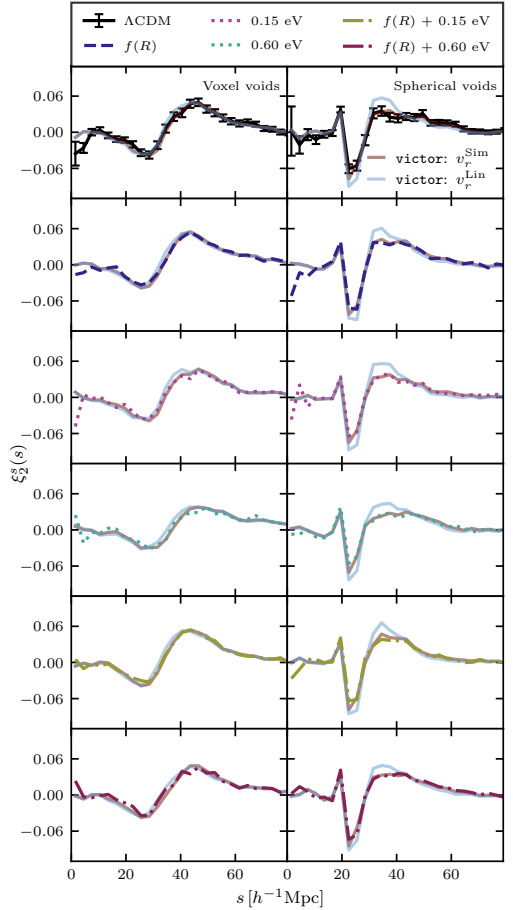
For each simulation, the histogram of the difference between real and redshift space is always broader than that for the difference between real and reconstructed real space. This tells us that performing reconstruction has indeed led us closer to the actual real space values. The method is tested on  $\Lambda\text{CDM}$  simulations by, for example, Nadathur et al. (2019a), Woodfinden et al. (2022) and Radinović et al. (2023), and we achieve similar results in our case. The non- $\Lambda\text{CDM}$  simulations again obtain comparable results to the  $\Lambda\text{CDM}$  reference. Although the  $f(R)$  dominated ones ( $f(R)$  and  $f(R) + 0.15\text{ eV}$ ) seem to perform slightly worse, and the heaviest neutrino mass,  $0.6\text{ eV}$ , slightly better. The reconstruction method is based on linear theory, and one possible explanation for this could therefore be that the massive neutrino simulations, with their suppressed clustering and lower



**Fig. 12.** Difference between the redshift and real space monopole of the void-halo CCF from the ANUBISIS simulations vs. theory calculated by VICTOR. The results are obtained by using the voxel and spherical void definitions in the left and right columns respectively. Two theory results from VICTOR are included, one where the velocity profile is given by linear theory and one where it is given by a template. The template used in this case is the velocity profile calculated from the simulation data.

velocities, are closer to the linear approximation on the scales where the reconstruction is performed. For the  $f(R)$  dominated simulations, the opposite would then be the case. This is further highlighted for the pure ISIS simulations, as shown in Fig. 16, where the deviations from GR are larger. As a test, we also ran the reconstruction process for this simulation when varying the growth rate,  $f$ , by 10–20% (as for Fig. 9). This did not lead to a significant difference in the histogram, but it did show up in the quadrupole as expected, and explained, by Nadathur et al. (2019a).

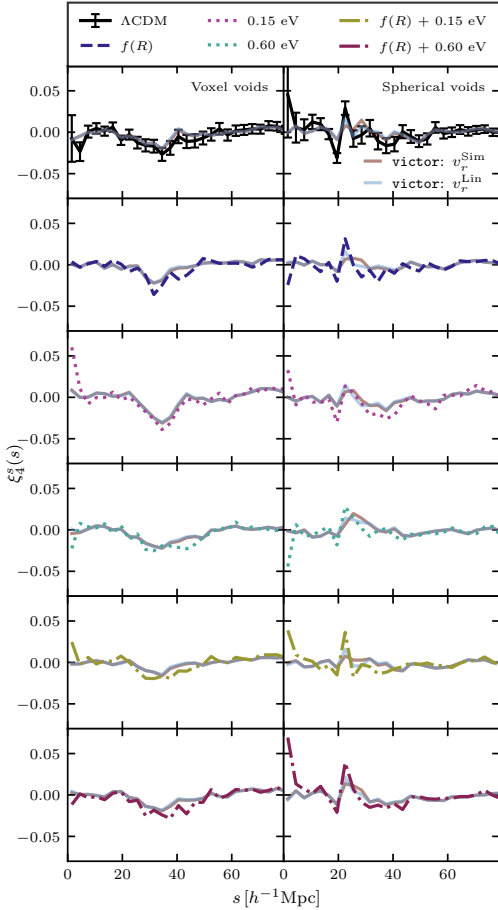
Figure 17 displays the quadrupole of the void-halo CCF for both the simulation data and the theory when the reconstruction step has been performed. In practice, this means that we per-



**Fig. 13.** Quadrupole of the void-halo CCF from the simulations vs. theory calculated by VICTOR. Layout and input as explained for Fig. 12.

formed the analysis as before, but instead of using the actual real space positions to calculate  $\xi^r$ , we instead used the reconstructed real space information. This mimics a possible procedure for performing the quadrupole analysis when using observational data. The model does, however, also require the density profile of the CDM, the mean outflow velocity profile, and the velocity dispersion. For this, we used the same as before, which was calculated from the actual real space data. This works as an approximation, as these quantities are only templates given to the model. For the velocity dispersion, it was also necessary to use the real space simulation data, as we did not have velocity information for the halos in reconstructed real space.

Comparing Figs. 13 and 17, it is clear that the model better fits the data when the reconstruction step is not involved. This is expected, as reconstruction only approximates the real space halo positions, and can not fully recreate the real space CCF. The deviation between the model and data does, however, appear to be comparable for the different ANUBISIS simulations.

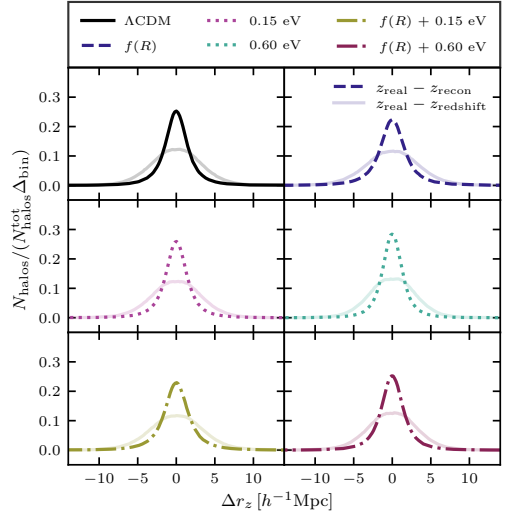


**Fig. 14.** Hexadecapole of the halo-void CCF from the simulations vs. theory calculated by ViCTOR. Layout and input as explained for Fig. 12.

### 5.6. MCMC fits

A way to test the CCF theory for the different simulated cosmologies is to check if they all reproduce the original parameter values of the simulations in a similar manner. Figure 18 displays the posterior distributions of the  $f\sigma_8$  and  $\epsilon$  parameters based on the void-halo CCF simulation data and model calculations for all ANUBISIS simulations. Each triangle plot shows the result for one simulation and both void definitions and follows the regular colour and linestyle pattern. The contours display the 68% and 95% confidence intervals and the grey dashed lines show the fiducial values, although with an assumed value of  $f \approx \Omega_m^{0.55}$  for all simulations. We only display the  $f\sigma_8$  and  $\epsilon$  parameters, as the LOS velocity dispersion,  $\sigma_{v_l}$ , is not an observable. The corresponding parameter values are listed in Table 4.

It is evident from Fig. 18 that the voxel voids more closely reproduce the fiducial parameter values overall. This could possibly be because the voxel void definition results in a smoother



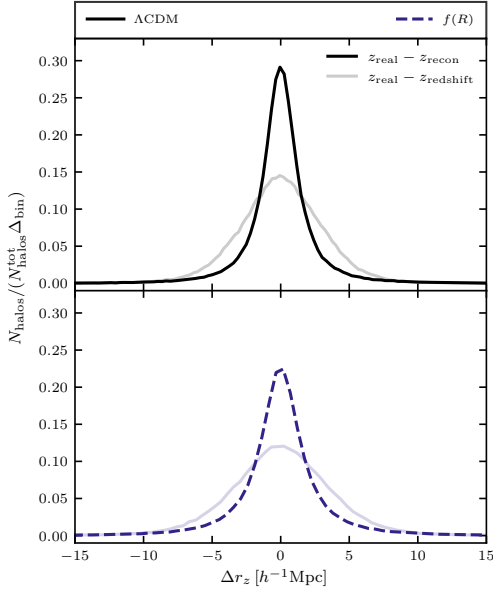
**Fig. 15.** Difference in the LOS coordinate between real space and reconstructed real space for the ANUBISIS simulations shown in the regular linestyle and colour. The weaker full line of the same colour shows the difference between the LOS coordinate in real and redshift space.

CCF that is easier to fit than the very sharply varying spherical void CCF. We do, however, see that the model prediction is able to follow the sharp features (e.g., Fig. 13). The spherical void catalogue also contains a larger amount of voids with effective radii at the lower end of the included radius range, compared to the voxel void catalogue (Fig. 6). It should be further explored whether or not performing the fits in different radius bins would alleviate the discrepancies between the spherical and voxel voids' abilities to reproduce the fiducial parameter values. This investigation is saved for future work.

In general, we find that the spherical voids lead to higher  $f\sigma_8$ -values, compared to the voxel voids. This might be due to a large number of small voids with deep density profiles identified by the spherical void finder. This gives, on average, a higher velocity peak, as can be observed in Figs. 7 and 8, and could lead to larger inferred values of  $f\sigma_8$ . The  $\epsilon$ -values, on the other hand, seem to be quite consistent between the two definitions for all simulations. The fact that the voxel and spherical voids coincide the best in their prediction for the  $f(R) + 0.15$  eV simulation is most likely a coincidence, which illustrates how the different model components and void definitions can vary. In general, even though there is a difference between the void definitions, there does not seem to be a clear distinction for how well the fiducial values are reproduced for the various simulated cosmologies.

In Fig. 19, we see the results of the MCMC fits when the reconstruction step is included and  $\beta$  is allowed to vary. The numerical values are given in Table 4. Again, the voxel void definition better reproduces the fiducial values of the ANUBISIS simulations. In fact, the differences between the voxel and spherical void definitions have increased. We still see quite consistent  $\epsilon$ -values between both void definitions, with a slightly lower value for the spherical voids except for the 0.15 eV and 0.6 eV cases. The  $f\sigma_8$ -values, however, are now consistently lower for





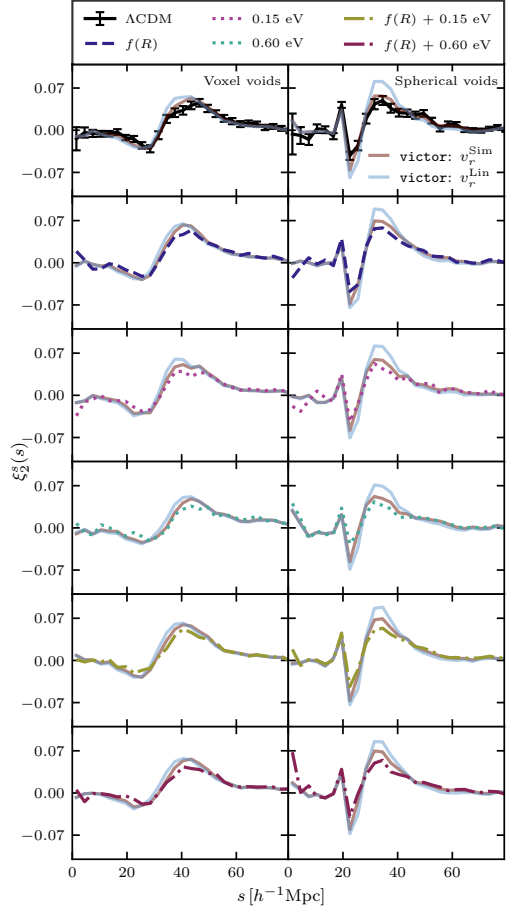
**Fig. 16.** Difference in the LOS coordinate between real and reconstructed real space and real and redshift space for the `fofr_small` and `lcdm_small` simulations.

the spherical voids, compared to the voxel voids, opposite of before. This might lie in the ability of the reconstruction method to correctly predict the high velocities found in the smaller spherical voids. Yet again, there is no clear difference between the simulated cosmologies and how accurately the fiducial parameter values are recovered. This underlines that the reconstruction method should be further studied for various void definitions.

It should be noted that for the fits that include reconstruction and a free  $\beta$ -value, we encounter the issue of a multimodal likelihood surface for  $\beta$ . This issue is more prominent for the voxel void definition than for the spherical one. It does, however, seem to be an artefact of the reconstruction model and, as a first approach, we dealt with it by constraining the range of the flat prior. The new range was chosen to include the most likely values resulting from the parameter fit performed with the original prior.

## 6. Conclusions

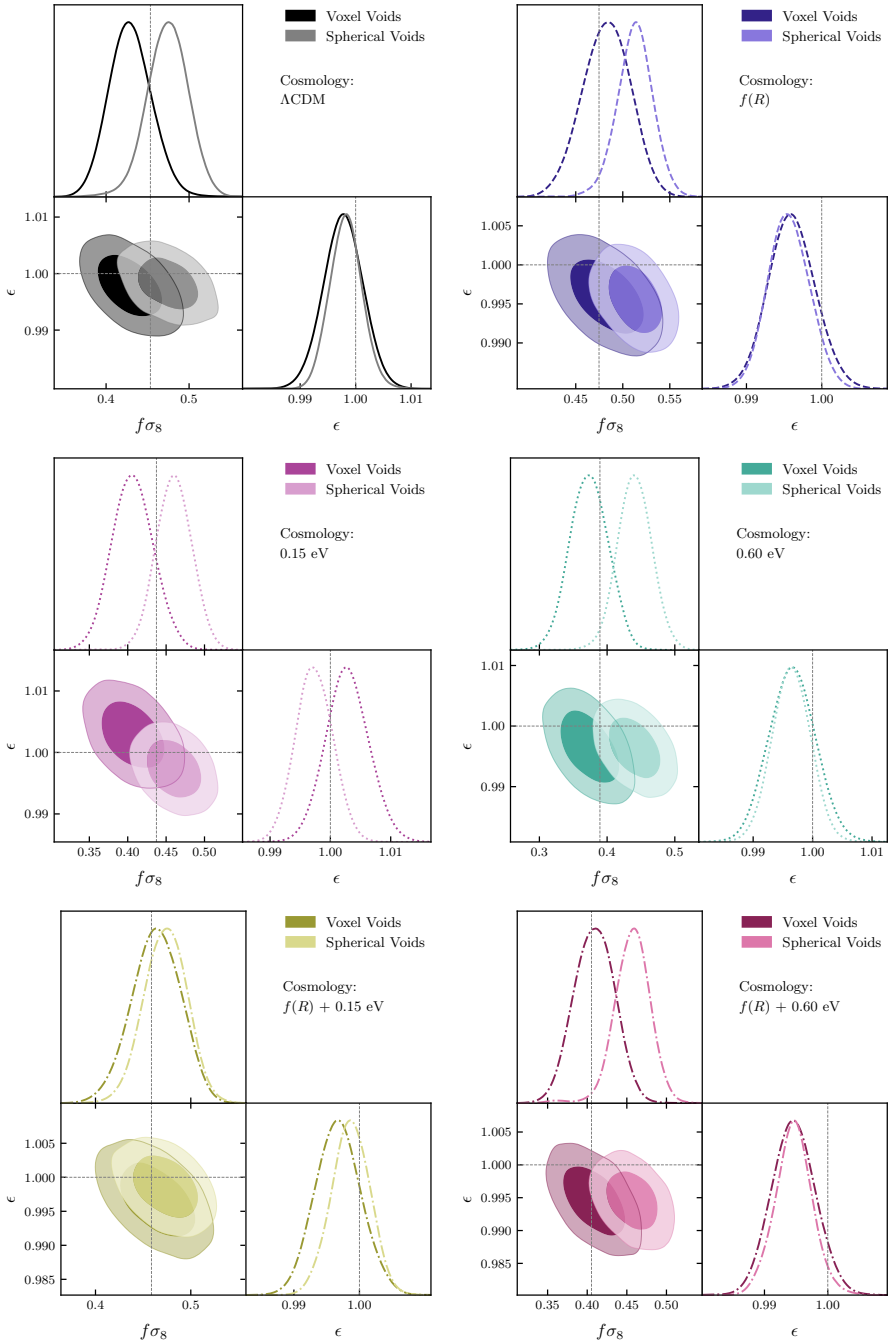
Cosmic voids are promising and independent probes of gravity and cosmology expected to provide stringent constraints on  $f\sigma_8$  and the ratio between the Hubble distance and transverse comoving distance in upcoming space missions such as *Euclid* (Hamaus et al. 2022; Radinović et al. 2023). Voids are also proposed as grounds for studying the effects of massive neutrinos and modified gravity, both separately and simultaneously, and as a way to break known degeneracies (Li et al. 2012; Massara et al. 2015; Voivodic et al. 2017; Kreisch et al. 2019; Perico et al. 2019; Contarini et al. 2021). In this paper, we investigate the performance of models describing the void-halo CCF, the radial mean void velocity profile, and a reconstruction method using ANUBISIS simulations with both massive



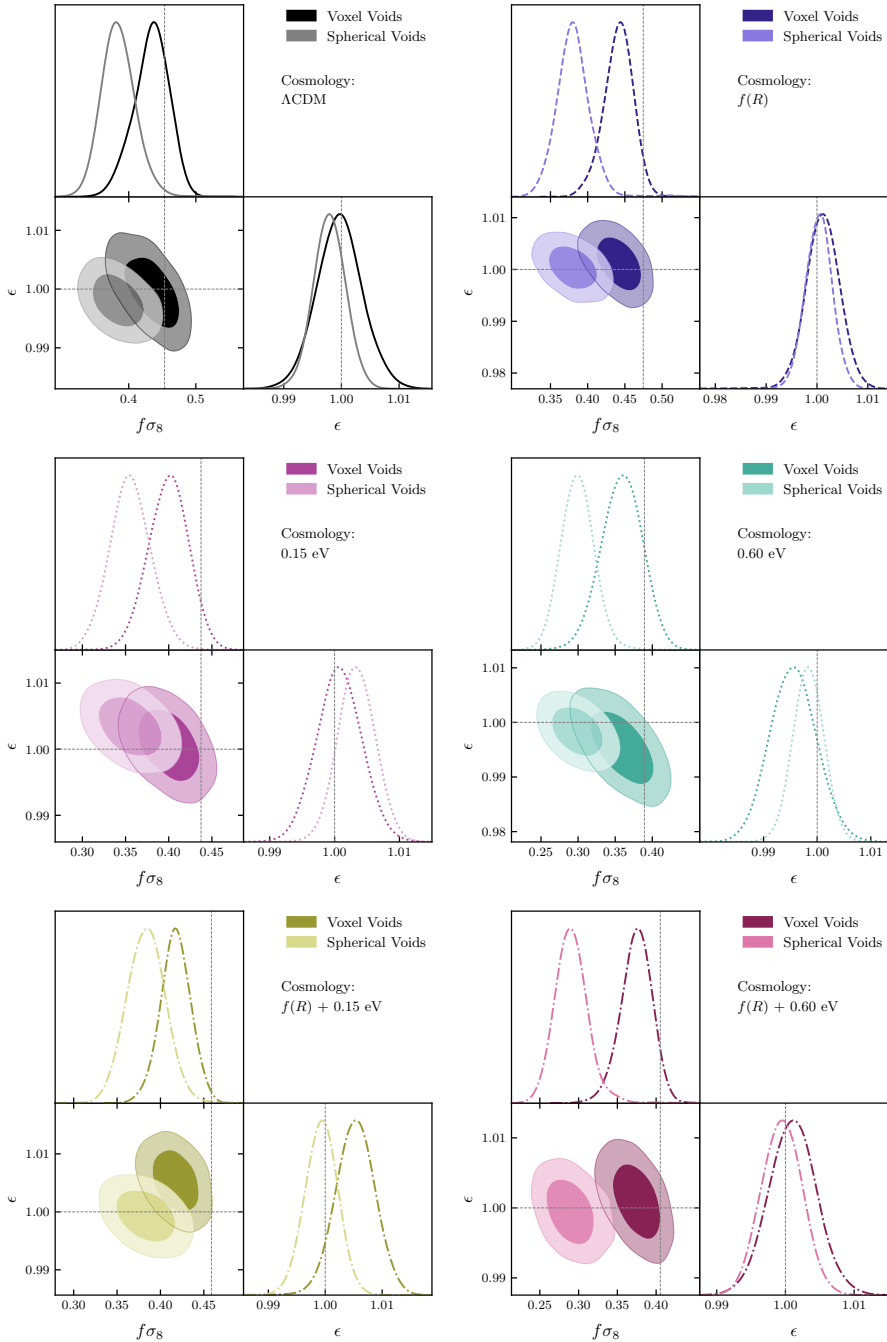
**Fig. 17.** Quadrupole of the reconstructed void-halo CCF from the simulations vs. theory calculated by `VICTOR`. The real space CCF used as theory input is calculated from the reconstructed real space halo catalogue and the voids identified in it. The layout follows Fig. 12.

neutrinos and Hu-Sawicki  $f(R)$  gravity. Our simulation suite consists of six simulations, one reference  $\Lambda$ CDM cosmology, one with Hu-Sawicki  $f(R)$ -modified gravity ( $|f_{R0}| = 10^{-5}$ ), two with massive neutrinos ( $\sum m_\nu = 0.15$  eV, 0.6 eV), and two with both massive neutrinos and modified gravity ( $|f_{R0}| = 10^{-5} + \sum m_\nu = 0.15$  eV, 0.6 eV). Occasionally, we supplement with a  $\Lambda$ CDM and  $f(R)$  simulation ( $|f_{R0}| = 10^{-4}$ ) run with `ISIS`, when we want to investigate the effects of modified gravity further.

We find that the linear void velocity model (Eq. (8)) fits the velocity profiles calculated directly from the data similarly for all ANUBISIS simulations. This is the case both when using the voxel void and spherical void definitions to locate voids in the halo catalogues. In fact, the increased velocities in the  $f(R)$  dominated simulations happen to partially compensate for the bias between the velocity profile calculated from the data and the one calculated from linear theory, arising from a sparse tracer sample



**Fig. 18.** MCMC fits for the ANUBISIS simulations. Each triangle plot shows the  $f\sigma_8$  and  $\epsilon$  estimates of one simulation for both the voxel and spherical void definitions. The grey dashed lines show the fiducial values and the contours display the 68% and 95% confidence intervals.



**Fig. 19.** MCMC fits for the ANUBISIS simulations with reconstruction. Each triangle plot shows the  $f\sigma_8$  and  $\epsilon$  estimates of one simulation for both the voxel and spherical void definitions. The grey dashed lines show the fiducial values and the contours display the 68% and 95% confidence intervals.

**Table 4.** Best fit value for  $f\sigma_8$  and  $\epsilon$  for all ANUBISIS simulations for both the voxel (VV) and spherical (SV) void definition, with and without reconstruction.

Simulation	$f\sigma_{8,VV}$	$f\sigma_{8,SV}$	$\epsilon_{VV}$	$\epsilon_{SV}$	$f\sigma_{8,VV}^{recon}$	$f\sigma_{8,SV}^{recon}$	$\epsilon_{VV}^{recon}$	$\epsilon_{SV}^{recon}$
1cdm	$0.43^{+0.03}_{-0.03}$	$0.47^{+0.03}_{-0.03}$	$0.998 \pm 0.004$	$0.998 \pm 0.004$	$0.43^{+0.03}_{-0.03}$	$0.39^{+0.03}_{-0.03}$	$1.000 \pm 0.005$	$0.999 \pm 0.003$
fofr	$0.48^{+0.03}_{-0.03}$	$0.51^{+0.02}_{-0.02}$	$0.996 \pm 0.004$	$0.996 \pm 0.003$	$0.44^{+0.03}_{-0.02}$	$0.38^{+0.02}_{-0.03}$	$1.001 \pm 0.004$	$1.000 \pm 0.003$
015ev	$0.41^{+0.03}_{-0.03}$	$0.46^{+0.03}_{-0.03}$	$1.003 \pm 0.004$	$0.997 \pm 0.004$	$0.40^{+0.03}_{-0.03}$	$0.36^{+0.03}_{-0.03}$	$1.001 \pm 0.004$	$1.003 \pm 0.003$
06ev	$0.37^{+0.03}_{-0.03}$	$0.44^{+0.03}_{-0.03}$	$0.997 \pm 0.004$	$0.996 \pm 0.004$	$0.36^{+0.03}_{-0.03}$	$0.30^{+0.03}_{-0.03}$	$0.996 \pm 0.005$	$0.998 \pm 0.003$
fofr_015ev	$0.46^{+0.03}_{-0.03}$	$0.47^{+0.03}_{-0.03}$	$0.997 \pm 0.004$	$0.999 \pm 0.003$	$0.42^{+0.02}_{-0.02}$	$0.38^{+0.03}_{-0.03}$	$1.005 \pm 0.004$	$0.999 \pm 0.004$
fofr_06ev	$0.41^{+0.03}_{-0.03}$	$0.46^{+0.03}_{-0.02}$	$0.995 \pm 0.004$	$0.995 \pm 0.004$	$0.37^{+0.03}_{-0.02}$	$0.29^{+0.02}_{-0.03}$	$1.001 \pm 0.004$	$1.000 \pm 0.003$

**Notes.** The limits are given at 68% and the flat prior ranges are  $f\sigma_8 \in [0.08, 1.3]$  and  $\epsilon \in [0.8, 1.2]$ .

(Massara et al. 2022). This shows that the linear velocity model needs to be improved further before differences due to massive neutrinos or modified gravity can be seen clearly. We also fit the velocity profile from the simulation data to a more general velocity model (Eq. (10)), with one free parameter. This model fits the data well and has a different best-fit parameter value for the various simulations. If the radial velocity profile could be observed directly with good precision from galaxy surveys, the value of this free parameter would be an interesting observable. The value is, however, degenerate for massive neutrinos and  $f(R)$ -modified gravity. Similarly, we find that the LOS velocity dispersion profiles have the same shape for all the simulated cosmologies, but different amplitudes. This amplitude is an interesting parameter, but it has the same issue of degeneracy, in addition to not being readily observable.

We compare the monopole, quadrupole, and hexadecapole in redshift space calculated from the simulation data with two theoretical model outcomes calculated by `Victor`. The only difference in the two models is the velocity profile input, which in one case is the radial linear velocity profile and in the other case, the velocity profile calculated from the simulation data. For all the multipoles, we see that the model fits the data with similar accuracy for all the different simulations. As expected, there is a preference towards the model that has the velocity profile from the data given as input, both for the voxel and spherical void definitions. As it stands, we need more accurate modelling and high-resolution surveys if we hope to use the void-galaxy CCF to put constraints on  $f(R)$ -modified gravity or massive neutrinos. However, our simulations show that modified gravity and massive neutrinos affect the monopole and quadrupole in opposite ways, making the void-galaxy CCF yet another degenerate observable.

When calculating the model prediction of the void-halo CCF in redshift space, we have in the above case used the real space CCF information from the simulation boxes as model input. For data obtained from a galaxy survey, this information is unknown and can be approximated through a reconstruction process where the redshift space positions are put back into real space by solving for the displacement field (Nadathur et al. 2019a). When performing reconstruction for all simulations, we find that the process performs similarly for all simulated cosmologies, although slightly better for the most massive neutrino case and slightly worse for the modified gravity case, compared to  $\Lambda$ CDM. This could be due to the reduced clustering and lower velocities in the massive neutrino simulations better adhering to the linear approximations of the reconstruction model, and the opposite for the modified gravity simulation. When fitting the CCF model to the data when the reconstruction step is included, the model

provides a slightly worse fit to the data. This is expected as we are now providing the model with information that only approximates the actual real space CCF that is needed as model input. The model-data fit is, however, comparable for all the ANUBISIS simulations also in this scenario.

During our analysis, we kept the growth rate,  $f$ , constant in all cases, effectively ignoring the scale dependence for modified gravity and massive neutrino cosmologies. We used the expected  $\Lambda$ CDM value,  $f = \Omega_m^{0.55}$ , for all simulations to keep the study consistent, and instead investigated if this choice gives visible biases in our model fits. As recapped above, all model-data fits perform similarly for the different simulations. The linear velocity profile does, however, show a slight improvement for the  $f(R)$  simulations, especially visible for the pure  $\Lambda$ CDM run. We, therefore, tried varying the value of  $f$  in this model to see if this could further improve the fit. For the voxel void definition, which already overestimates the clustering, increasing  $f$  to values more in line with expectations for  $f(R)$ -modified gravity, only contributes to further mismatch between the model and the simulation data. For the spherical void definition, which suffers less from the effect of a sparse tracer sample, increasing  $f$  can give a better fit. This only shows that the choice of void finding algorithm and the current sparse tracer sample issue in the void velocity modelling is important and must be consistently handled before possible effects of a different growth rate in the various simulated cosmologies can be resolved.

For all the ANUBISIS simulations, we performed MCMC fits for  $f\sigma_8$  and the Alcock-Paczyński parameter,  $\epsilon$ . We did this both with and without reconstruction. In both cases, we find that the voxel void definition better recovers the fiducial values of the  $f\sigma_8$ -parameter for the various simulations. The  $\epsilon$ -values are more consistently recovered between the two void definitions. The discrepancies are most prominent when reconstruction is included, where the  $f\sigma_8$ -values recovered for the spherical voids are consequently underestimated for all simulated cosmologies, as opposed to slightly overestimated without the reconstruction step. Still, for both void definitions, the ability to recover the fiducial parameter values is similar for the different simulations. There is no indication that the parameter estimations are more accurate for a  $\Lambda$ CDM cosmology, compared to  $f(R)$ -modified gravity or massive neutrinos.

Our investigations suggest that the current limitations of the void theories must be dealt with in order for the models to be accurate enough to clearly showcase differences between the various simulated cosmologies. This is particularly clear for the velocity profile modelling and the reconstruction method. In addition, higher resolution simulations are necessary to lower the uncertainties in the data. Once this is in place, cosmic voids

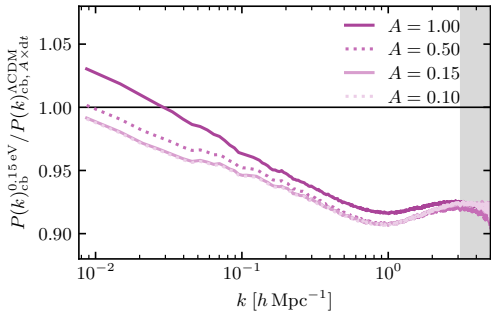
are a promising ground for studying cosmologies with massive neutrinos and  $f(R)$ -modified gravity.

**Acknowledgements.** We thank the Research Council of Norway for their support. Parts of our computations were performed on resources provided by UNINETT Sigma2 – the National Infrastructure for High Performance Computing and Data Storage in Norway. We also wish to thank Slađana Radinović for her contributions in the form of valuable input, discussions and instructions regarding the void component of this paper.

## References

- Adamek, J., Durrer, R., & Kunz, M. 2017, *JCAP*, 2017, 004
- Adamek, J., Angulo, R. E., Arnold, C., et al. 2022, *J. Castander*, 54, 66
- Ahmad, Q. R., Allen, R. C., Andersen, T. C., et al. 2002, *Phys. Rev. Lett.*, 89, 011301
- Aker, M., Beglarian, A., Behrens, J., et al. 2022, *Nat. Phys.*, 18, 160
- Alcock, C., & Paczyński, B. 1979, *Nature*, 281, 358
- Araki, T., Eguchi, K., Enomoto, S., et al. 2005, *Phys. Rev. Lett.*, 94, 081801
- Archidiacono, M., Brinckmann, T., Lesgourgues, J., & Poulin, V. 2017, *JCAP*, 2017, 052
- Arnold, C., Fosalba, P., Springel, V., Puchwein, E., & Blot, L. 2019, *MNRAS*, 483, 790
- Baldi, M., Villaescusa-Navarro, F., Viel, M., et al. 2014, *MNRAS*, 440, 75
- Banerjee, A., & Dalal, N. 2016, *JCAP*, 2016, 015
- Bautista, J. E., Paviot, R., Vargas Magaña, M., et al. 2021, *MNRAS*, 500, 736
- Behroozi, P. S., Wechsler, R. H., & Wu, H. Y. 2012, *ApJ*, 762, 109
- Bertschinger, E. 2001, *ApJS*, 137, 1
- Blas, D., Lesgourgues, J., & Tram, T. 2011, *JCAP*, 2011, 034
- Brandbyge, J., Hannestad, S., Haugbølle, T., & Wong, Y. Y. 2010, *JCAP*, 2010, 014
- Burden, A., Percival, W. J., Manera, M., et al. 2014, *MNRAS*, 445, 3152
- Burden, A., Percival, W. J., & Howlett, C. 2015, *MNRAS*, 453, 456
- Cai, Y. C., Padilla, N., & Li, B. 2015, *MNRAS*, 451, 1036
- Cai, Y. C., Taylor, A., Peacock, J. A., & Padilla, N. 2016, *MNRAS*, 462, 2465
- Castorina, E., Sefusatti, E., Sheth, R. K., Villaescusa-Navarro, F., & Viel, M. 2014, *JCAP*, 2014, 049
- Cataneo, M., Rapetti, D., Schmidt, F., et al. 2015, *Phys. Rev. D - Part. Fields Gravitation Cosmol.*, 92, 044009
- Chiang, C. T., Loverde, M., & Villaescusa-Navarro, F. 2019, *Phys. Rev. Lett.*, 122, 041302
- Chuang, C. H., Kitaura, F. S., Liang, Y., et al. 2017, *Phys. Rev. D*, 95, 063528
- Contarini, S., Marulli, F., Moscardini, L., et al. 2021, *MNRAS*, 504, 5021
- Di Valentino, E., Gariazzo, S., & Mena, O. 2021, *Phys. Rev. D*, 104, 083504
- Falek, B., Koyama, K., Zhao, G. B., & Cautun, M. 2018, *MNRAS*, 475, 3262
- Fiorini, B., Koyama, K., & Izard, A. 2022, *JCAP*, 2022, 028
- Fisher, K. B. 1995, *ApJ*, 448, 494
- Fukuda, Y., Hayakawa, T., Ichihara, E., et al. 1998, *Phys. Rev. Lett.*, 81, 1562
- Gil-Mafin, H., Bautista, J. E., Paviot, R., et al. 2020, *MNRAS*, 498, 2492
- Giocoli, C., Baldi, M., & Moscardini, L. 2018, *MNRAS*, 481, 2813
- Hamaus, N., Aubert, M., Pisani, A., et al. 2022, *A&A*, 658, A20
- Hannestad, S., Upadhye, A., & Wong, Y. Y. 2020, *JCAP*, 2020, 062
- Hassani, F., Adamek, J., Durrer, R., & Kunz, M. 2022, *A&A*, 668, A56
- Hernández, O. F. 2017, *JCAP*, 2017, 018
- Hu, W., & Sawicki, I. 2007, *Phys. Rev. D - Part. Fields Gravitation Cosmol.*, 76, 064004
- Koyama, K. 2016, *Reports on Progress in Physics*, 79, 046902
- Kreisch, C. D., Pisani, A., Carbone, C., et al. 2019, *MNRAS*, 488, 4413
- Landy, S. D., & Szalay, A. S. 1993, *ApJ*, 412, 64
- Laureijs, R., Amiaux, J., Arduini, S., et al. 2011, ArXiv e-prints [arXiv:1110.3193]
- Lesgourgues, J. 2011, ArXiv e-prints [arXiv:1104.2932]
- Lesgourgues, J., & Pastor, S. 2006, *Phys. Rep.*, 429, 307
- Li, B., Zhao, G. B., & Koyama, K. 2012, *MNRAS*, 421, 3481
- Llinares, C., Mota, D. F., & Winther, H. A. 2014, *A&A*, 562, A78
- Ma, C.-P., & Bertschinger, E. 1994, *ApJ*, 429, 22
- Massara, E., Villaescusa-Navarro, F., Viel, M., & Sutter, P. M. 2015, *JCAP*, 2015, 018
- Massara, E., Percival, W. J., Dalal, N., et al. 2022, *MNRAS*, 517, 4458
- Mirzatuyn, N., & Pierpaoli, E. 2019, *JCAP*, 2019, 066
- Mohammad, F. G., & Percival, W. J. 2022, *MNRAS*, 514, 1289
- Nadathur, S., & Percival, W. J. 2019, *MNRAS*, 483, 3472
- Nadathur, S., Carter, P. M., Percival, W. J., Winther, H. A., & Bautista, J. E. 2019a, *Phys. Rev. D*, 100, 023504
- Nadathur, S., Carter, P., & Percival, W. J. 2019b, *MNRAS*, 482, 2459
- Nadathur, S., Carter, P. M., Percival, W. J., Winther, H. A., & Bautista, J. E. 2019c, Astrophysics Source Code Library [record ascl:1907.023]
- Nusser, A., & Davis, M. 1994, *ApJ*, 421, L1
- Paillas, E., Cai, Y. C., Padilla, N., & Sánchez, A. G. 2021, *MNRAS*, 505, 5731
- Particle Data Group (Workman, R. L., et al.) 2022, *PTEP*, 2022, 083C01
- Peebles, E. P. J. 1980, *The Large-scale Structure of the Universe* (Princeton University Press)
- Peebles, E. P. J. 1993, *Principles of Physical Cosmology* (Princeton: Princeton University Press)
- Perico, E. L., Voivodic, R., Lima, M., & Mota, D. F. 2019, *A&A*, 632, A52
- Radinović, S., Nadathur, S., Winther, H. A., et al. 2023, A&A submitted, [ArXiv:2302.05302]
- Schneider, A., Teyssier, R., Potter, D., et al. 2016, *JCAP*, 2016, 047
- Sinha, M., & Garrison, L. 2019, *Commun. Comput. Inf. Sci.*, 964, 3
- Sinha, M., & Garrison, L. H. 2020, *MNRAS*, 491, 3022
- Sutter, P. M., Lavaux, G., Wandelt, B. D., & Weinberg, D. H. 2012, *ApJ*, 761, 187
- Teyssier, R. 2002, *A&A*, 385, 337
- Torrado, J., & Lewis, A. 2019, Astrophysics Source Code Library [record ascl:1910.019]
- Torrado, J., & Lewis, A. 2021, *JCAP*, 2021, 057
- Voivodic, R., Lima, M., Llinares, C., & Mota, D. F. 2017, *Phys. Rev. D*, 95, 024018
- Will, C. M. 2014, *Liv. Rev. Rel.*, 17, 1
- Winther, H. A., Schmidt, F., Barreira, A., et al. 2015, *MNRAS*, 454, 4208
- Woodfinden, A., Nadathur, S., Percival, W. J., et al. 2022, *MNRAS*, 516, 4307
- Zel'dovich, Y. B. 1970, *A&A*, 5, 84
- Zennaro, M., Bel, J., Villaescusa-Navarro, F., et al. 2017, *MNRAS*, 466, 3244
- Zhao, G. B., Li, B., & Koyama, K. 2011, *Phys. Rev. D - Part. Fields Gravitation Cosmol.*, 83, 044007
- Zivick, P., Sutter, P. M., Wandelt, B. D., Li, B., & Lam, T. Y. 2015, *MNRAS*, 451, 4215

## Appendix A: ANUBISIS resolution



**Fig. A.1.** Matter power spectrum ratio between a 0.15 eV massive neutrino simulation and a  $\Lambda$ CDM simulation with varying timestep, performed by ANUBISIS. The simulation box has  $L_{\text{box}} = 1024 h^{-1} \text{Mpc}$ ,  $N_{\text{dm}} = N_r = 1024^3$ , and a fixed coarse base grid of  $512^3$ . The time step is calculated by the RAMSES algorithm for both runs, but for the  $\Lambda$ CDM case it is multiplied by a reduction factor,  $A$ . We see here that one way to compensate for the coarse base grid, especially at large scales, is to shorten the time step. This requires a longer run time for the  $\Lambda$ CDM simulation, but not more memory as would be the result of adopting a finer grid.

In the upper panel of Fig. 3, we present the matter power spectrum ratio for the non- $\Lambda$ CDM simulations, compared to the reference  $\Lambda$ CDM run. We mention that at larger scales there is originally an excess in the power spectrum for the massive neutrino and  $f(R)$  + massive neutrino runs. This is attributed to the coarse base grid settings used in the simulations. With the resources available to us at the time of running ANUBISIS, we made appropriate adjustments in order to constrain our memory and time usage. To accomplish this, we chose a base grid of  $512^3$  for all the simulations, which results in a lower resolution at early times and at large scales where there is less clustering. This is due to the nature of the RAMSES AMR-scheme, which creates more refinements as structure grows. In a ratio comparison, such an internal consequence of the algorithm should cancel out, but as the massive neutrinos contribute when calculating the time steps, the simulations containing these particles automatically operate with smaller time steps. This leads to a more detailed time development of the CDM particles in the massive neutrino and  $f(R)$  + massive neutrino simulations, compared to the  $\Lambda$ CDM and pure  $f(R)$  runs. Effectively, we resolve the simulations containing massive neutrinos better at large scales, resulting in the refinement of more clustering in these cases. This evens out as time passes and more refinements are made, but for large neutrino masses, this also happens for small scales, where the suppressed structure formation leads to fewer refinements within the code, compared to the  $\Lambda$ CDM case. To help even out the issues at large scales, we ran the  $\Lambda$ CDM and pure  $f(R)$  simulations with one-fourth of the time step originally calculated by the code. The effect of adjusting the time step is illustrated in Fig. A.1. Ideally, the simulations should be run with a coarser base grid and with a higher particle density, which would also contribute to better resolution overall. This is not done in our case, due to computational costs.

In the end, this issue is practically equivalent to having a slightly different  $\sigma_8$ -value (2 – 3% lower) at large scales. We

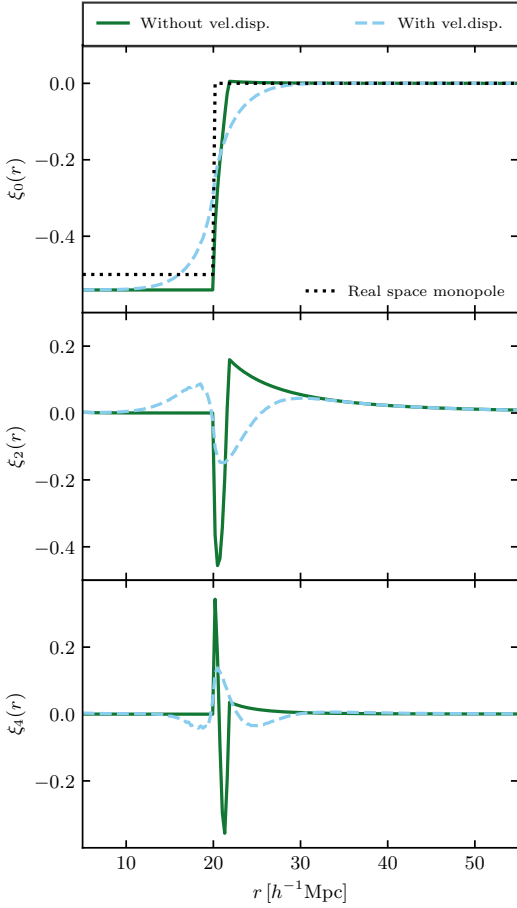
have not accounted for this in our analysis, as the resulting changes are small. For our MCMC fits, the true  $\sigma_8$ -value is still encompassed in the flat prior interval, and the only difference in Figs. 18 and 19 would be a slight adjustment of the fiducial  $f\sigma_8$ -line towards lower values for  $\Lambda$ CDM and  $f(R)$ . Simulations with the same issue still showed good agreement with other codes in the MNCCP (Adamek et al. 2022).

## Appendix B: Quadrupole shape

If the redshift space void-halo CCF model (Eq. 3) did not include a velocity dispersion for the mean outflow velocity profile, the shape of the quadrupole in redshift space would be qualitatively similar for all void definitions. This would mean a trough inside the void due to outflow towards the overdensity at the edge, and a peak outside due to infall towards the same overdensity, akin to the shape we see for the voxel voids in Fig. 11. Adding a velocity dispersion to the model effectively corresponds to ‘smoothing’ the RSD quadrupole.

If we take the real space radial coordinate,  $r$ , to be equal to the redshift space coordinate,  $s$ , in the theory model, then from Eq. (5) it can be shown that for  $v_r/(raH) \ll 1$  we roughly have  $\xi_2^s \propto \frac{d}{dr}(v_r/raH)$ . This means that it is deviations from linearity of the void velocity profile (equivalent to deviations from a flat density profile) that lead to a quadrupole inside the void. To better understand the shape of the quadrupole for different void definitions, it is useful to consider a simple toy model. We define a density profile that is perfectly flat inside the void, and equal to zero outside:  $\delta = \delta_0$  for  $r < R_{\text{void}}$  and  $\delta = 0$  for  $r > R_{\text{void}}$ . This then gives a velocity profile  $v_r \propto r$  inside the void, and  $v_r \propto R_{\text{void}}^3/r^2$  outside, if we apply Eq. (8). This again gives  $\xi_2^s = 0$  inside the void, and  $\xi_2^s \propto R_{\text{void}}^3/r^4$  outside. At the void edge, we have a sharp feature. For real voids, the density profile is never perfectly flat on the inside, and the deviations break the linearity of the outflow velocity, resulting in a trough in the quadrupole inside the void. The flatter the density profile is inside the void, the sharper the peak of the velocity profile is, leading to sharper features in the quadrupole. The monopole, quadrupole, and hexadecapole, in the absence of a velocity dispersion, are illustrated by the green line in Fig. B.1. The sharp features at  $R_{\text{void}}$  are visible both for the quadrupole and hexadecapole.

The above scenario is the case when there is no velocity dispersion. If we add this to the model, the imposed smoothing effect simply reduces the amplitude of the no-dispersion quadrupole for the voxel void definition. This means that the smoothing length given by the size of the velocity dispersion is smaller than the features seen in the no-dispersion quadrupole. On the other hand, for spherical voids, where the density profile is very flat in the void centre and the quadrupole has sharp features as a consequence, this smoothing results in a sharp peak followed by a sharp trough close to the void edge (as seen in Fig. 11). This shows up at the point where the density profile stops being flat, which is also the point where the velocity profile has a sharp peak. The blue dashed line in Fig. B.1 shows this effect clearly for the quadrupole. The smaller the average void is, the larger this first peak is, as the smoothing effect is more dramatic. This shape is also similar to what previous studies have found for Zovov voids (Nadathur et al. 2019a,b; Nadathur & Percival 2019; Massara et al. 2022; Woodfinden et al. 2022), which is not surprising, as these voids also have a fairly flat density profile,  $\delta \sim -1.0$ , at the void centre.



**Fig. B.1.** Monopole, quadrupole, and hexadecapole for the toy model of the void density profile both with (blue dashed line) and without (green line) velocity dispersion. The flat density profile inside the void results in a sharp feature in the quadrupole at the void radius, which smooths out and gives a peak right before the trough inside the void.





Paper III

# **Sesame: A power spectrum emulator pipeline for beyond- $\Lambda$ CDM models**

**Renate Mauland, Hans A. Winther, and Cheng-Zong Ruan**

Submitted to *Astronomy & Astrophysics* (2023).





# Sesame: A power spectrum emulator pipeline for beyond- $\Lambda$ CDM models

Renate Mauland<sup>1</sup>, Hans A. Winther<sup>1</sup>, and Cheng-Zong Ruan<sup>1</sup>

Institute of Theoretical Astrophysics, University of Oslo, P.O.Box 1029 Blindern, N-0315 Oslo, Norway  
 e-mail: renate.mauland-hus@astro.uio.no

Received —; accepted —

## ABSTRACT

The mysterious nature of the dark sector of the  $\Lambda$ -cold-dark-matter ( $\Lambda$ CDM) model is one of the main motivators behind the study of alternative cosmological models. A central quantity of interest for these models is the matter power spectrum, which quantifies structure formation on various scales and can be cross-validated through theory, simulations, and observations. Here, we present a tool that can be used to create emulators for the non-linear matter power spectrum, and similar global clustering statistics, for models beyond  $\Lambda$ CDM with very little computation effort and without the need for supercomputers. We use fast approximate  $N$ -body simulations to emulate the boost,  $B(k, z) = P_{\text{beyond-}\Lambda\text{CDM}}(k, z)/P_{\Lambda\text{CDM}}(k, z)$ , and then rely on existing high-quality emulators made for  $\Lambda$ CDM to isolate  $P_{\text{beyond-}\Lambda\text{CDM}}(k, z)$ . Since both the  $\Lambda$ CDM and beyond- $\Lambda$ CDM models are simulated in our approach, some of the lack of power on small scales due to the low force-resolution in the simulations is factored out, allowing us to extend the emulator to  $k \sim 3 - 5 h \text{Mpc}^{-1}$  and still maintain good accuracy. In addition, errors from the simulation and emulation process can easily be estimated and factored into the covariance when using the emulator on data. As an example of using the pipeline, we create an emulator for the well-studied  $f(R)$  model with massive neutrinos, using approximately 3000 CPU hours of computation time, as opposed to millions of CPU hours for many existing  $\Lambda$ CDM emulators. Provided with the paper is a fully functioning pipeline that generates parameter samples, runs a Boltzmann solver to produce initial conditions, runs the simulations, and then gathers all the data and runs it through a machine learning module to develop the emulator. This tool, named *Sesame*, can be used by anyone to generate a power spectrum emulator for the cosmological model of their choice.

**Key words.** neutrinos – gravitation – cosmology: large-scale structure of Universe – methods: numerical – statistical

## 1. Introduction

The  $\Lambda$ -cold-dark-matter ( $\Lambda$ CDM) model describes our Universe well, yet two of its main components remain elusive. The true natures of dark matter and dark energy are still unknown, but their impact on the Universe has been, and continues to be, widely studied across multiple research fields. In an attempt to forego the dark energy component of the  $\Lambda$ CDM model, alternative theories of gravity have become a popular avenue to explore. These beyond- $\Lambda$ CDM models (see e.g. Clifton et al. 2012; Koyama 2016) have an effect on structure formation, leaving an imprint on the matter power spectrum. This can be further studied through the use of cosmological simulations, which typically require a large amount of computing resources for high-resolution simulations capable of accurately distinguishing between models down to small scales. In addition, a simulation is only performed for a specified set of cosmological parameters, requiring a rerun for any parameter changes. To forgo both of these issues, emulators can be created for desired statistical observables, like the matter power spectrum - a key observable whose theoretical prediction is needed to constrain beyond- $\Lambda$ CDM models in current and near-future weak-lensing surveys (J-PAS Collaboration et al. 2014; LSST Collaboration et al. 2019; DES Collaboration et al. 2021; Euclid Collaboration et al. 2022). The emulators (Heitmann et al. 2013; Kwan et al. 2015; Giblin et al. 2019; Nishimichi et al. 2019; Angulo et al. 2021; Euclid Collaboration et al. 2021; Moran et al. 2023) are typically constructed by performing a high number of  $N$ -body simulations within some

parameter space, and then interpolating to access any desired parameter value. This can be done, for example, through the use of machine learning, training a neural network on highly accurate simulation data. As mentioned above, this typically requires a lot of computing resources, but once the simulations are performed and the training is done, the emulators are simple to use and have both minimal time and memory requirements.

Although highly accurate, a limit of this approach is the ability to easily extend the resulting emulator to new cosmological models. In this paper, we present a full pipeline using fast approximate  $N$ -body simulations and neural network training to create an emulator for the matter power spectrum boost,  $B(k, z) = P_{\text{beyond-}\Lambda\text{CDM}}(k, z)/P_{\Lambda\text{CDM}}(k, z)$ , without the need for a large amount of computing resources. The approximate simulations employ the comoving Lagrangian acceleration (COLA) method (Tassev et al. 2013) to simulate both the  $\Lambda$ CDM and beyond- $\Lambda$ CDM models (Valogiannis & Bean 2017; Winther et al. 2017; Wright et al. 2017; Brando et al. 2022; Fiorini et al. 2022; Brando et al. 2023; Wright et al. 2023), allowing us to extract the boost up to scales of  $k \sim 3 - 5 h \text{Mpc}^{-1}$  to a few percent accuracy. The pipeline is named *Sesame* - from simulations to emulators using approximate methods. As a demonstration of *Sesame*, we create an emulator for the boost between the Hu-Sawicki  $f(R)$  model (Hu & Sawicki 2007) and a dynamical dark energy model,  $w_0 w_c$ CDM. In  $f(R)$ -modified gravity, an additional function of the Ricci scalar,  $R$ , is added to the general relativity (GR) framework (Buchdahl 1970). This function can be designed to recreate a similar expansion history as  $\Lambda$ CDM,

without the need for dark energy. Still, as the nature of gravity is modified, resulting observational signals are expected (see e.g. [de Felice & Tsujikawa 2010](#), for a detailed review). One such signal is the enhancement of structure formation on scales smaller than the Compton wavelength of the scalaron - the scalar degree of freedom of the  $f(R)$  theory,  $df/dR$  (e.g. [Hu & Sawicki 2007](#); [Pogosian & Silvestri 2008](#); [Cataneo et al. 2015](#)). This will show up in the matter power spectrum.

In addition to exploring universe models besides  $\Lambda$ CDM, calculations and simulations within the  $\Lambda$ CDM framework are continuously expanded to reach higher levels of accuracy. One such extension is the inclusion of massive neutrinos. These lightweight particles have often been excluded from cosmological simulations due to their low impact compared to cold dark matter (cdm), which makes up about 84% ([Planck Collaboration et al. 2020](#)) of the matter content of the Universe. However, improvements in telescopes and satellites now give us an observational accuracy high enough to measure the impact of neutrinos on structure formation - suppression on scales smaller than the neutrino free-streaming length ([Lesgourgues & Pastor 2006](#)). The newly launched *Euclid* satellite is expected to measure the effect of massive neutrinos directly on the matter power spectrum, thereby putting tighter constraints on the neutrino mass scale ([Laureijs et al. 2011](#)). Because of this, we include modified gravity, massive neutrinos, and dark energy in the form of the well-known  $w_0w_a$  Chevallier-Polarski-Linder (CPL) parametrisation ([Chevallier & Polarski 2001](#); [Linder 2003](#)) when creating our emulator. The inclusion of massive neutrinos in the  $f(R)$  simulations is also particularly important, due to the degeneracy between the effects of neutrinos and  $f(R)$ -modified gravity on structure formation on non-linear scales (e.g. [Baldi et al. 2014](#)).

Simulations including massive neutrinos ([Potter et al. 2016](#); [Adamek et al. 2017](#); [Liu et al. 2018](#); [Dakin et al. 2019](#); [Partmann et al. 2020](#); [Weinberger et al. 2020](#); [Springel et al. 2021](#); [Euclid Consortium et al. 2023](#)), modified gravity ([Li et al. 2012](#); [Puchwein et al. 2013](#); [Llinares et al. 2014](#); [Winther et al. 2015](#); [Hassani & Lombriser 2020](#); [Ruan et al. 2022](#)), and both ([Baldi et al. 2014](#); [Wright et al. 2017](#); [Giocoli et al. 2018](#); [Mauland et al. 2023](#)) already exist with various methods of implementation, along with models, fits, and emulators to extract the boost or the matter power spectrum directly for these cosmological models (e.g. [Zhao 2014](#); [Winther et al. 2019](#); [Hannestad et al. 2020](#); [Bose et al. 2020, 2021](#); [Ramachandra et al. 2021](#); [Euclid Collaboration et al. 2021](#); [Arnold et al. 2022](#); [Bose et al. 2023](#)). The main takeaway from this paper is therefore not the  $f(R)$ -modified gravity emulator (although it will be provided), but the full pipeline, *Sesame*, which includes the drawing of parameter samples, running the simulations, training the neural network, and creating the emulator for the boost,  $B(k, z)$ . This tool can be used to produce an emulator for a desired cosmological model by implementing said model into the simulations and using a suitable Boltzmann solver to extract the initial conditions. The resulting accuracy of both the simulations and the emulator can be tuned by the choice of simulation settings and neural network architecture.

This paper is structured as follows: In Sect. 2, we present some background theory for the matter power spectrum,  $f(R)$ -modified gravity, and massive neutrinos. This is followed by an outline of the methods applied in Sect. 3, including a description of the full pipeline. In Sect. 4 we go through some simulation details, and then present our results in Sect. 5. Finally, we conclude in Sect. 6.

## 2. Theory

In this section, we present some background information for the key components of this work. We first outline the necessary details on the matter power spectrum, followed by  $f(R)$ -modified gravity and massive neutrinos.

### 2.1. Matter power spectrum

The matter power spectrum,  $P(k)$ , is defined as (e.g. [Dodelson & Schmidt 2020](#)):

$$(2\pi)^3 P(k) \delta_D(\mathbf{k} - \mathbf{k}') = \langle \tilde{\delta}(\mathbf{k}) \tilde{\delta}(\mathbf{k}')^* \rangle, \quad (1)$$

where  $k$  is the wavenumber,  $\delta_D$  is the Dirac-delta function, and  $\tilde{\delta}(\mathbf{k})$  is the Fourier transform of the overdensity field,  $\delta(\mathbf{x})$ . The power spectrum is the Fourier transform of the two-point correlation function,  $\xi(r)$ , which describes the excess probability, over random, of finding two objects separated by a distance  $r$ . Analysing the matter power spectrum gives great insight into the clustering of matter at different times and scales, in addition to how variations in cosmological parameters affect structure formation.

When studying alternative models to the concordance  $\Lambda$ CDM model of our Universe, the ratio between the power spectrum in the alternative model and that of  $\Lambda$ CDM holds valuable information about the deviations between them. Different components of a cosmological model, like massive neutrinos or modified gravity, have theoretically predicted impacts on the power spectrum (e.g. [Lesgourgues & Pastor 2006](#); [Song et al. 2007](#); [Koyama et al. 2009](#)). As the matter power spectrum can be observed from various surveys ([Chabanier et al. 2019](#); [LSST Collaboration et al. 2019](#); [Euclid Collaboration et al. 2022](#)), its shape is well known, and it can therefore be used to constrain these cosmological models. As an example in this paper, we are interested in the differences in the power spectrum between a  $w_0w_a$ CDM universe with GR as the gravity model and one with  $f(R)$ -modified gravity as the gravity model, both with the inclusion of massive neutrinos,

$$B(k, z) = \frac{P_{f(R)}(k, z \mid \Omega_\Lambda, \Omega_{\text{cdm}}, \Omega_b, n_s, \sigma_8^{f(R)}, w_0, w_a, h, M_\nu, f_{R0})}{P_{\text{GR}}(k, z \mid \Omega_\Lambda, \Omega_{\text{cdm}}, \Omega_b, n_s, \sigma_8, w_0, w_a, h, M_\nu)}. \quad (2)$$

Here,  $\Omega_\Lambda$ ,  $\Omega_{\text{CDM}}$ , and  $\Omega_b$  are the energy densities of dark energy, dark matter, and baryons respectively;  $n_s$  is the scalar spectral index;  $h$  is the *Hubble* constant today;  $\sigma_8$  and  $\sigma_8^{f(R)}$  denote the normalisation of the linear matter power-spectra at  $z = 0$ ;  $f_{R0}$  is the Hu-Sawicki  $f(R)$ -modified gravity parameter (see Sect. 2.2.1);  $M_\nu$  denotes the sum of the neutrino masses, and  $w_0$  and  $w_a$  are dynamical dark energy parameters for the CPL parametrisation of the dark energy equation of state ([Chevallier & Polarski 2001](#); [Linder 2003](#)),

$$w = w_0 + w_a \frac{z}{1+z}, \quad (3)$$

where  $w_0 = -1$  and  $w_a = 0$  correspond to a cosmological constant.

### 2.2. Beyond- $\Lambda$ CDM models

Beyond- $\Lambda$ CDM is a broad term encompassing everything that is not the  $\Lambda$ CDM model. There are too many beyond- $\Lambda$ CDM models proposed in the literature to be covered here, but a review can be found in [Bull et al. \(2016\)](#).

The simplest models are dark energy models that mainly only modify the background evolution through the *Hubble* function,  $H(a)$ . These are the so-called quintessence models (Wetterich 1988) and parametrised models for the dark energy equation of state,  $w(a)$ , like CPL. Next in the level of complexity, we have models where the quintessence field is coupled to matter (often only dark matter), dubbed coupled-quintessence models (Amendola 2000). Then we have modified gravity models, where an extra degree of freedom is introduced, giving rise to a fifth force for the full matter sector. To be able to evade local gravity constraints, these models often need a screening mechanism to hide the modifications in high-density environments where such gravity tests have been performed (see e.g. Khoury & Weltman 2004b; Clifton et al. 2012; Koyama 2016). In addition to the models mentioned so far, we also have models of dark matter beyond cold dark matter (e.g. axions Marsh 2016), non-standard inflationary models (Martin et al. 2014), and many more. The model we will use here for demonstrating how an emulator can be created using *Sesame* is a  $f(R)$  modified gravity model. This is chosen as it is well known and because it is already implemented in the applied code base.

### 2.2.1. $f(R)$ -modified gravity

In  $f(R)$ -modified gravity theory (Sotiriou & Faraoni 2010), the Einstein-Hilbert action of GR is extended by a function,  $f(R)$ ,

$$S = \left( \int \frac{R + f(R)}{16\pi G} + \mathcal{L}_m \right) \sqrt{-g} d^4x. \quad (4)$$

Here,  $R$  is the Ricci scalar,  $G$  is the Newtonian gravitational constant,  $\mathcal{L}_m$  is the matter Lagrangian density, and  $g$  is the determinant of the metric tensor,  $g_{\mu\nu}$ . The  $f(R)$  function can take many forms, one of which is given by

$$f(R) = -m^2 \frac{c_1(R/m^2)^n}{c_2(R/m^2)^n + 1}, \quad (5)$$

proposed by Hu & Sawicki (2007). Here  $c_1, c_2$ , and  $n$  are dimensionless, constant, and non-negative parameters of the model and  $m^2 = H_0^2 \Omega_{\text{cdm}}$ , with  $H_0$  the value of the *Hubble* parameter today. This  $f(R)$  function was designed so that cosmological tests at high redshifts yield the same results as for GR. In addition, in the limit where  $c_2(R/m^2)^n \gg 1$ , Eq. (5) can be written as  $f(R) = -m^2 c_1/c_2 + O((m^2/R)^n)$ , showing that a cosmological constant, and thereby a similar background evolution to that of  $\Lambda$ CDM, can be obtained by equating  $-m^2 c_1/c_2$  with  $-2\Lambda$ . This corresponds to a relation given by  $c_1/c_2 = 6\Omega_\Lambda/\Omega_{\text{cdm}}$  between the two parameters  $c_1$  and  $c_2$ . The equation of motion of the scalar degree of freedom,  $f_R$ , of the  $f(R)$ -model is then given by

$$f_R \equiv \frac{df(R)}{dR} \approx -n \frac{c_1}{c_2} \left( \frac{m^2}{R} \right)^{n+1}. \quad (6)$$

By fixing the value of  $f_{R0}$ , the present-day background value of the scalar degree of freedom, an independent connection can be found for  $c_1$  and  $c_2$ . This enables the model to be fully specified by the parameters  $f_{R0}$  and  $n$ . We will apply  $n = 1$  in this paper.

From theory and simulations, the impact of this form of  $f(R)$ -modified gravity on structure formation, and thereby the matter power spectrum, can be predicted for various values of  $f_{R0}$ . In general, this modification to gravity enhances structure formation on small scales (Hu & Sawicki 2007; Pogosian & Silvestri 2008; Cataneo et al. 2015), as a result of an attractive force,

dubbed the fifth force, which appears in addition to Newtonian gravity. The effects of this, in order for the theory to be compatible with observations (Will 2014), are suppressed in high-density regions due to a chameleon screening effect (Khoury & Weltman 2004a; Brax et al. 2008). The value of  $f_{R0}$  controls the threshold at which the screening kicks in and recovers GR. Values above  $f_{R0} \sim -10^{-5}$  are in general ruled out from cosmological observations (Cataneo et al. 2015; Koyama 2016), although massive neutrinos, which have the opposite effect on structure formation, have not always been taken into account in these analyses (Baldi et al. 2014).

### 2.3. Massive neutrinos

From particle physics, we know that there are three neutrino mass states,  $\nu_i$  with  $i = 1, 2, 3$  (e.g. Thomson 2013). The absolute mass scale,  $m_{\nu_i}$  (often shortened to  $m_i$ ), of each state is unknown, but neutrino oscillation experiments give us constraints on the mass difference between the states (Particle Data Group et al. 2022)

$$\begin{aligned} \Delta m_{21}^2 &= (7.53 \pm 0.18) \times 10^{-5} \text{ eV}^2, \\ \Delta m_{32}^2 &= (-2.519 \pm 0.033) \times 10^{-3} \text{ eV}^2 \text{ (IH)}, \\ \Delta m_{32}^2 &= (2.437 \pm 0.033) \times 10^{-3} \text{ eV}^2 \text{ (NH)}, \end{aligned} \quad (7)$$

where IH denotes the inverted hierarchy ( $m_3 \ll m_1 < m_2$ ) and NH the normal hierarchy ( $m_1 < m_2 \ll m_3$ ). This gives a lower bound of  $\sum m_\nu \gtrsim 0.1 \text{ eV}$  and  $\sum m_\nu \gtrsim 0.06 \text{ eV}$  for the sum of the neutrino masses for the inverted and normal hierarchies respectively. An upper bound is given by  $\sum m_\nu \lesssim 2.4 \text{ eV}$ , based on the KATRIN single  $\beta$ -decay experiment (KATRIN Collaboration et al. 2022).

In addition to particle physics experiments, the sum of the neutrino masses can be constrained through cosmological observations. As neutrinos make up a fraction of the energy content of the Universe, given by (Lesgourgues & Pastor 2006)

$$\Omega_\nu \approx \frac{\sum m_\nu}{93.14 \text{ eV } h^2}, \quad (8)$$

they affect the formation of structure. At early times, the massive neutrinos are relativistic, and free-stream out of overdense regions. This, in addition to alterations of the background evolution, like the time of matter-radiation equality, leads to a suppression of the matter power spectrum on scales smaller than the neutrino free-streaming length (Lesgourgues & Pastor 2006),

$$\lambda_{\text{FS}} = 7.7 \frac{1+z}{\sqrt{\Omega_\Lambda + \Omega_m(1+z)^3}} \left( \frac{1 \text{ eV}}{\sum m_\nu} \right) h^{-1} \text{ Mpc}. \quad (9)$$

Here,  $\Omega_m = \Omega_{\text{cdm}} + \Omega_b + \Omega_\nu$  is the total energy density of matter and the other parameters are as explained before. The suppression of structure formation is observable and can help constrain the sum of the neutrino masses. A recent combination of various probes finds  $\sum m_\nu \lesssim 0.09 \text{ eV}$  at 95% confidence (Di Valentino et al. 2021) and one of the science goals of the *Euclid* mission is to measure  $\sum m_\nu$  to more than 0.03 eV precision through the use of weak gravitational lensing and galaxy clustering (Laureijs et al. 2011).

Although cosmological observations can be used to obtain tighter upper bounds on the sum of the neutrino masses, it is important to take into account the dependence on the choice of a cosmological model. Hu-sawicki  $f(R)$ -modified gravity, as mentioned above, has the opposite effect of massive neutrinos

on structure formation, and thus results in degenerate observables like the matter power spectrum, halo mass function (HMF), halo bias, and void-galaxy cross-correlation function (Baldi et al. 2014; Mauland et al. 2023).

### 3. Method

In this section, we introduce the methods behind the simulations and machine learning codes used to create the emulator. We also detail the steps that need to be taken before applying the pipeline and the steps taken within the pipeline itself.

#### 3.1. Simulations

The simulations in this paper were performed with the COLASolver implemented in the FML library<sup>1</sup>. This is a fast and approximate particle-mesh (PM)  $N$ -body code which employs the COLA method introduced by Tassev et al. (2013). The COLASolver succeeds the MG-PICOLA<sup>2</sup> code (Winther et al. 2017) and has various options for cosmologies and gravity models, including dynamical dark energy and  $f(R)$ -modified gravity. It also contains massive neutrinos, using a grid-based method as proposed in Brandbyge & Hannestad (2009), which was implemented and tested by Wright et al. (2017).

##### 3.1.1. The COLA method

The COLA method (Tassev et al. 2013) is based on the fact that structure formation on large scales is well described by Lagrangian perturbation theory (LPT). We can use this to our advantage and solve for the displacement,  $\delta\mathbf{x}$ , between a particle's LPT trajectory,  $\mathbf{x}_{\text{LPT}}$ , and its full trajectory,  $\mathbf{x}$ . The geodesic equation for the particles is given by

$$\frac{d\mathbf{x}}{d\tau} = \mathbf{v}, \quad (10)$$

$$\frac{d\mathbf{v}}{d\tau} = -\nabla\Phi, \quad (11)$$

which, when setting  $\mathbf{x} = \delta\mathbf{x} + \mathbf{x}_{\text{LPT}}$ , becomes

$$\frac{d\delta\mathbf{x}}{d\tau} = \delta\mathbf{v}, \quad (12)$$

$$\frac{d\delta\mathbf{v}}{d\tau} = -\nabla\Phi - \frac{d^2\mathbf{x}_{\text{LPT}}}{d\tau^2}. \quad (13)$$

The additional COLA force is easily computed from the displacement fields that are already calculated when creating the initial conditions. In this COLA frame (the frame co-moving with the LPT trajectories), the initial velocity of the particles is simply  $\delta\mathbf{v} = 0$ , and stays small on large scales during the evolution. This allows us to take much larger time steps than in usual  $N$ -body simulations, while still maintaining high accuracy on the largest scales, reducing the simulation time substantially. When increasing the number of timesteps, the method converges towards a full PM  $N$ -body code. The COLA method has become an increasingly popular method for cheaply generating simulations and mock galaxy catalogues (Tassev et al. 2015; Feng et al. 2016; Izard et al. 2016; Koda et al. 2016; Leclercq et al. 2020; Brando et al. 2023; Wright et al. 2023).

<sup>1</sup> <https://github.com/HAWinther/FML/tree/master/FML/COLASolver>

<sup>2</sup> <https://github.com/HAWinther/MG-PICOLA-PUBLIC>

#### 3.1.2. Screened modified gravity

The COLASolver we use already contains implementations of a wide range of modified gravity models, like  $f(R)$  gravity, the symmetron, DGP, and Jordan-Brans-Dicke (de Felice & Tsujikawa 2010; Hinterbichler et al. 2011; Dvali et al. 2000; Joudaki et al. 2022). A typical modified gravity model has a Poisson equation which in linear perturbation theory, and in Fourier space, reads (see e.g. Winther et al. 2017)

$$\Phi(k, z) = -\frac{3}{2k^2}\Omega_m a \delta_m(k, z) \frac{G_{\text{eff}}(k, z)}{G}. \quad (14)$$

Here,  $G_{\text{eff}}(k, z)/G$  represents an effective Newtons constant, which might depend on both time and scale. For example, for the  $f(R)$  model, we have

$$\frac{G_{\text{eff}}(k, z)}{G} = 1 + \frac{1}{3} \frac{k^2}{k^2 + a^2 m_{f(R)}^2}, \quad (15)$$

where  $m_{f(R)}^{-1}$  is the range of the fifth-force. This is exact on linear scales, but it does not include the important screening effect seen in many modified gravity models. To accurately take this into account, one must solve the non-linear partial differential equation (PDE) for the extra degree of freedom of the theory (e.g. the scalar field,  $f_R$ , for the case of  $f(R)$  gravity). The COLASolver includes the possibility of doing exactly this, but it is quite time-consuming. Instead, we therefore rely on the method of Winther & Ferreira (2015). Here, the Poisson equation is taken to be

$$\Phi(k, z) = \Phi_N(k, z) - \frac{3}{2k^2}\Omega_m a \delta_m^{\text{eff}}(k, z) \left( \frac{G_{\text{eff}}(k, z)}{G} - 1 \right), \quad (16)$$

where the first term is standard Newtonian gravity and the second term is the contribution from the fifth force. The effective density,  $\delta_m^{\text{eff}}$ , (in real space) is given by

$$\delta_m^{\text{eff}}(\mathbf{x}, z) = \delta_m(\mathbf{x}, z) F(\Phi_N, \nabla\Phi_N, \nabla^2\Phi_N, \dots), \quad (17)$$

where the function  $F$  estimates the screening. In this way,  $F = 1$  corresponds to no screening. For different models, we can use spherical symmetry to compute the  $F$  function. For example, for  $f(R)$ , we have

$$F = \min \left[ 1, \frac{3|f_{R0}|}{2|\Phi_N|} \left( \frac{\Omega_m + 4\Omega_\Lambda}{\Omega_m a^{-3} + 4\Omega_\Lambda} \right)^{n+1} \right], \quad (18)$$

which only depends on the local value of the standard Newtonian potential. This is easily (and cheaply) computed in the code using Fourier transforms, making the cost an order of magnitude lower than solving the full equation of motion.

In the COLASolver, different screening methods have been implemented for a wide range of models. The above approximation is accurate, but it is not perfect (depending on the model). Because of this, one should always compare the results to full  $N$ -body simulations, to assess the accuracy. If higher accuracy is needed, there is a possibility of improving it. One simple fix is to modify the screening method by introducing a fudge factor (or function),  $\gamma(a)$ , to scale  $F$  with. Then,  $\gamma(a)$  can be adjusted by comparing to exact simulations. This has been done for  $f(R)$  by Winther & Ferreira (2015), by fitting a constant factor to match a particular redshift. As the main purpose of this paper is to set up a general pipeline, and because emulators for the particular example model used here already exist (e.g. Ramachandra et al. 2021; Arnold et al. 2022; Sáez-Casares et al. 2023), we choose to not adjust  $\gamma(a)$  and our screened simulations thus have  $\gamma = 1$ .

### 3.1.3. Massive neutrinos

Massive neutrinos were for a long time considered beyond  $\Lambda$ CDM, at least from the perspective of  $N$ -body simulations. This has changed over the last decade, and most simulations these days do include the effect of massive neutrinos.

In the COLASolver, massive neutrinos are treated as a field evolving according to linear theory, as proposed by Brandbyge & Hannestad (2009). After creating the CDM+baryon particles, we compute and store the initial density field,  $\delta_{\text{cb}}(k, z_{\text{ini}})$ , and evaluate

$$\delta_{\nu}(k, z) = \frac{T_{\nu}(k, z)}{T_{\nu}(k, z_{\text{ini}})} \frac{T_{\nu}(k, z_{\text{ini}})}{T_{\text{cb}}(k, z_{\text{ini}})} \delta_{\text{cb}}(k, z_{\text{ini}}), \quad (19)$$

where  $T_{\text{cb}}$  and  $T_{\nu}$  are the CDM+baryon and neutrino transfer functions respectively. This is then added as a source to the Poisson equation (here for GR)

$$\Phi = -\frac{3}{2k^2} \Omega_m a [(1 - f_{\nu})\delta_{\text{cdm}} + f_{\nu}\delta_{\nu}], \quad (20)$$

where  $f_{\nu} = \Omega_{\nu}/\Omega_m$ . For more information about the neutrino implementation, see Wright et al. (2017). The implementation of massive neutrinos used here was previously included in a massive neutrino code comparison project (Euclid Consortium et al. 2023), and showed percent level agreement in the power spectrum compared to more exact methods of including massive neutrinos.

### 3.2. Machine learning

To create an emulator for the power spectrum boost,  $B(k, z)$ , we utilise PyTorch-Lightening<sup>3</sup>, a lightweight wrapper for the Python PyTorch package<sup>4</sup>. PyTorch is a machine-learning framework focusing on deep learning, and it provides the tools necessary to train neural networks with multiple layers. It requires our data as input, separated into three different categories: training, testing, and validation. The training data is used to train the neural network. This is the data that the neural network learns from. During the learning process, the neural network occasionally sees the validation data, as a means to help tune the model, but does not learn from it. Once the neural network is fully trained and the emulator is created, it can be evaluated against the test data to assess its performance. The architecture of the neural network training can be designed by the user by deciding the number of hidden dimensions, number of neurons, the batch size, and more<sup>5</sup>. The number of hidden dimensions governs how many layers there are between the input and output layers. Each of these layers has a given number of neurons, which perform computations on the training data before passing it to the next layer. The data is also commonly divided into smaller subsets, containing a set number of samples in each batch. This allows for a more efficient training process.

For our neural network training, we assigned data to the training, validation, and test sets by drawing Latin hypercube samples (McKay et al. 1979; Heitmann et al. 2006) for each data set, corresponding to a 80 – 10 – 10 percent distribution. This ensured that each set had an even distribution of parameters in the available parameter set. We also tested both two and three hidden layers, in addition to varying the number of neurons in each

layer, ranging from 8 – 512 in different combinations. Finally, we tested the batch size, varying from 16 – 256. From our example case of  $f(R)$ -modified gravity, we created three different emulators, two including unscreened  $f(R)$  gravity, one for the linear power spectrum boost and one for the non-linear, and one for the non-linear screened  $f(R)$  gravity power spectrum boost. They all have a batch size of 64 and two hidden layers, but the two unscreened  $f(R)$  emulators use 16 neurons in the first hidden layer and 8 in the second, while the screened  $f(R)$  emulator has 128 and 64 neurons due to a more complicated shape for some of the curves. This can be further optimised and changed by the user based on the desired accuracy of the training process and will depend on the simulations and the parameters that are varied.

### 3.3. Pipeline

The full pipeline used for this work is made available at [https://github.com/renmau/Sesame\\_pipeline](https://github.com/renmau/Sesame_pipeline), including instructions on how to use it. It can be applied as is for cosmologies with  $f(R)$  modified gravity and massive neutrinos, or extended to different cosmologies as wished. Here follows an outline of the steps necessary both to use the pipeline, and taken inside the pipeline itself:

First of all, the desired cosmological model, if not already included in the COLASolver, must be implemented. Likewise, the model must be implemented in a Boltzmann solver in order to obtain the initial conditions, or an already existing solver with the necessary cosmology can be used. Once this is done, the simulation setup must be tested for the model in question to obtain the number of time steps, box size, grid resolution, and so on, that gives the desired convergence within the code itself. With the optimal setup obtained, the boosts dependence on cosmological parameters must be tested in order to determine which parameters should be included when creating the emulator. When this is decided, the priors on the parameters must be chosen, along with a fiducial cosmology and the number of desired samples to simulate for the neural network to work on. These are the steps that need to be taken outside of the pipeline. Once this is in order, Latin hypercube sampling is employed to sample the parameter space evenly. The way the pipeline is set up now, individual parameter samples are drawn for the training, testing, and validation sets so that they make up a 80 – 10 – 10 percentile distribution of the total amount of samples. Alternatively, one can draw all the samples at once and then distribute the samples into data sets later. The desired amount of samples for the various cosmological parameters is written to file, together with the desired simulation settings of the COLASolver. The information in this file is then used to generate a bash script where new parameter files for the COLASolver are created. This script is then activated and the simulations are run for both the beyond- $\Lambda$ CDM and  $\Lambda$ CDM model for all the samples. This creates multiple outputs of the matter power spectrum at various redshifts in each case. The boost,  $B(k, z) = P_{\text{beyond-}\Lambda\text{CDM}}(k, z)/P_{\Lambda\text{CDM}}(k, z)$ , is then calculated for each parameter combination and redshift, and smoothed with a Savitzky-Golay filter (Savitzky & Golay 1964). The smoothing is performed to reduce small fluctuations and thereby make the curves easier to estimate for the neural network. The parameter values, redshifts,  $\log_{10} k$ , and  $B(k, z)$  are written into three separate files that go into the neural network learning. 80% of the sample data goes into a training file, 10% into a validation file, and the remaining 10% into a test file, as mentioned above. These are then fed to the neural network, and the power spectrum ratio emulator is created. In this step, the architecture of the neural network must also be decided. This

<sup>3</sup> <https://www.pytorchlightning.ai/index.html>

<sup>4</sup> <https://github.com/pytorch/pytorch>,  
<https://pytorch.org/>

<sup>5</sup> See the PyTorch-Lightening documentation for detailed instructions.

might take some trial and error, in order to obtain the desired accuracy.

At this point, the boost emulator for the desired cosmology has been created. To extract  $P_{\text{beyond-}\Lambda\text{CDM}}(k, z)$ , we can now depend on already existing high-quality emulators for  $\Lambda\text{CDM}$  (e.g. Angulo et al. 2021; Euclid Collaboration et al. 2021; Moran et al. 2023). Ideally, the final step should be to run a high resolution  $N$ -body simulation to determine the accuracy of the boost within the COLASolver. This would likely be the most expensive part to perform out of everything detailed above, but gives us an estimate of the simulation errors. Alternatively, if high-resolution simulations already exist for the cosmological model of interest, these can be used instead. In addition to this, we can get an estimate of the emulator errors by comparing the emulator performance to the test set. Both of these error estimates can then be baked into the covariance when using the emulator to fit to data, to ensure that all errors are included.

#### 4. Simulations

For the example case of the  $f(R)$  model, we performed two main sets of simulations with the COLASolver (Sect. 3.1) to obtain the power spectrum boost. One setup had unscreened  $f(R)$  gravity, while the other included screening mechanisms. For these runs, we picked 550 samples of five cosmological parameters, varied within the intervals

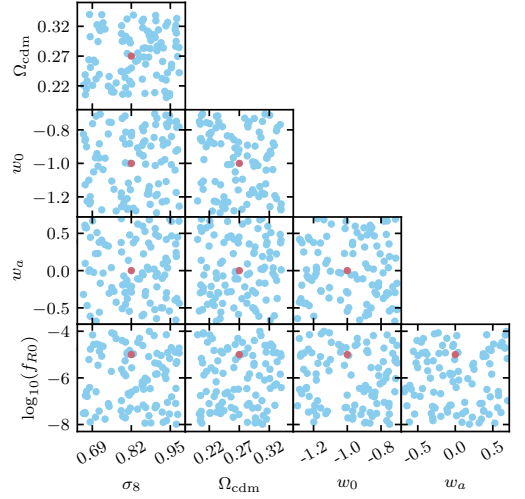
$$\begin{aligned} \sigma_8 &\in [0.66, 0.98], \\ \Omega_{\text{cdm}} &\in [0.20, 0.34], \\ w_0 &\in [-1.3, -0.7], \\ w_a &\in [-0.7, 0.7], \end{aligned} \quad (21)$$

$$\log_{10} f_{R0} \in [-8.0, -4.0].$$

These intervals, with the exception of  $\log_{10} f_{R0}$ , are based on the EuclidEmulator2, and are either the same ( $w_0, w_a$ ) or slightly larger ( $\Omega_{\text{cdm}}, \sigma_8$ ) than the intervals used by Euclid Collaboration et al. (2021)<sup>6</sup>. A sample selection of 100 parameter samples can be seen in Fig. 1.

The simulation setup and the fiducial cosmology are given in Table 1. In each case, we had  $L_{\text{box}} = 350 h^{-1} \text{Mpc}$ ,  $N_{\text{grid}} = 768$ , and  $N_{\text{part}} = 640$ . The simulations were started at  $z_{\text{ini}} = 30.0$  and used 30 timesteps up until  $z = 0.0$ . Regarding the simulation setup we used, note that COLA simulations in general often use a large force-grid with  $N_{\text{grid}} = (2 - 3)N_{\text{part}}$  (see e.g. Izard et al. 2016). This is in order to have enough force-resolution to be able to create and resolve small halos - a crucial property if one is to create mock galaxy catalogues. The dark matter power-spectrum, on the other hand, is less sensitive to this, and we can therefore get away with using a smaller grid. When it comes to choosing the final simulation setup, it is important to always perform convergence tests of how the boost,  $B$ , changes with respect to the box size, the number of particles, the force resolution (the grid size), the number of time-steps, and other accuracy parameters like the initial redshift. This is essential to ensure that the result within COLA is converged. This has been done for the setup used here, as seen in Fig. 2. Once this is done, the true accuracy can be assessed by comparing the COLA result to high-resolution  $N$ -body simulations. The power spectrum boost for the 100 parameter samples mentioned above can be seen in Fig. 3 for three different scenarios; linear boost with unscreened

<sup>6</sup> A convenience of using the COLASolver to perform the simulations is that it is fast, and therefore, extending the parameter intervals is computationally cheap compared to more accurate full  $N$ -body simulations.



**Fig. 1.** Sample distribution for 100 of the total 550 samples. The burgundy dot shows the fiducial cosmology parameter values, as given in Table 1.

**Table 1.** Fiducial values for the main simulations and for parameter variation tests run with a slightly different setup. If a parameter does not vary, this is its default value. The  $M_\nu$  parameter refers to the sum of the neutrino masses and is given in eV. The main simulations have  $L_{\text{box}} = 350 h^{-1} \text{Mpc}$ ,  $N_{\text{grid}} = 768$ , and  $N_{\text{part}} = 640$ . The parameter test runs have  $L_{\text{box}} = 350 h^{-1} \text{Mpc}$  and  $N_{\text{grid}} = N_{\text{part}} = 640$ .

Parameter	Fiducial value	Test value
$A_s$	$2.1 \times 10^{-9}$	$2.1 \times 10^{-9}$
$\sigma_8$	0.82	0.83
$n_s$	0.96	0.96
$h$	0.67	0.67
$M_\nu$	0.058	0.0
$\Omega_{\text{cdm}}$	0.27	0.27
$\Omega_b$	0.049	0.05
$w_0$	-1.0	-1.0
$w_a$	0.0	0.0
$\log_{10} f_{R0}$	-5.0	-5.0

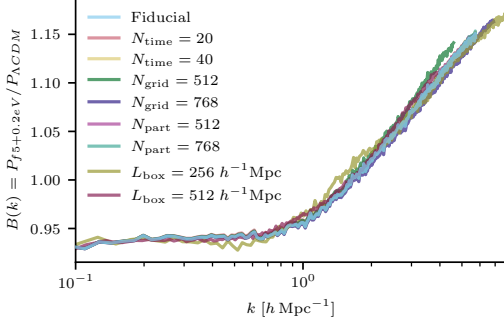
$f(R)$  gravity, non-linear boost with unscreened  $f(R)$  gravity, and non-linear boost with screened  $f(R)$  gravity.

For every sample, COLASolver was run twice, once with  $f(R)$ -modified gravity and the selected value of  $f_{R0}$ , and once with regular GR. We ran our simulations for GR and  $f(R)$  using the same initial conditions (i.e. we use the same value of  $A_s$ ), which translates into

$$\left(\sigma_8^{f(R)}\right)^2 = \int \frac{k^3}{2\pi^2} P_{\text{GR}}(k, z=0) \left(\frac{D_{f(R)}(k, z)}{D_{\text{GR}}(z)}\right)^2 \frac{dk}{k}, \quad (22)$$

where the growth factors,  $D$ , are normalised to unity in the early Universe. This ensures that the boost,  $B$ , is unity at early times, while today  $\sigma_8^{f(R)}$  is slightly higher for our  $f(R)$  simulations than our GR simulations. We used amplitude-fixed initial conditions (Angulo & Pontzen 2016; Villaescusa-Navarro et al. 2018;





**Fig. 2.** Convergence test for the COLASolver simulation setup for the screened boost between a  $f(R)$  gravity simulation with  $|f_{R0}| = 10^{-5}$  and  $M_\nu = 0.2 \text{ eV}$ , and a  $\Lambda$ CDM simulation with massless neutrinos, at  $z = 0.0$ . The fiducial setup is the same as the test setup in Table. 1, namely  $N_{\text{time}} = 30$ ,  $N_{\text{grid}} = N_{\text{part}} = 640$ , and  $L_{\text{box}} = 350 h^{-1} \text{ Mpc}$ . Here,  $N_{\text{time}}$  denotes the number of time steps. The only parameter changed from the test setup to the final setup is  $N_{\text{grid}}$ , which was increased to  $N_{\text{grid}} = 786$  due to the resolution on non-linear scales.

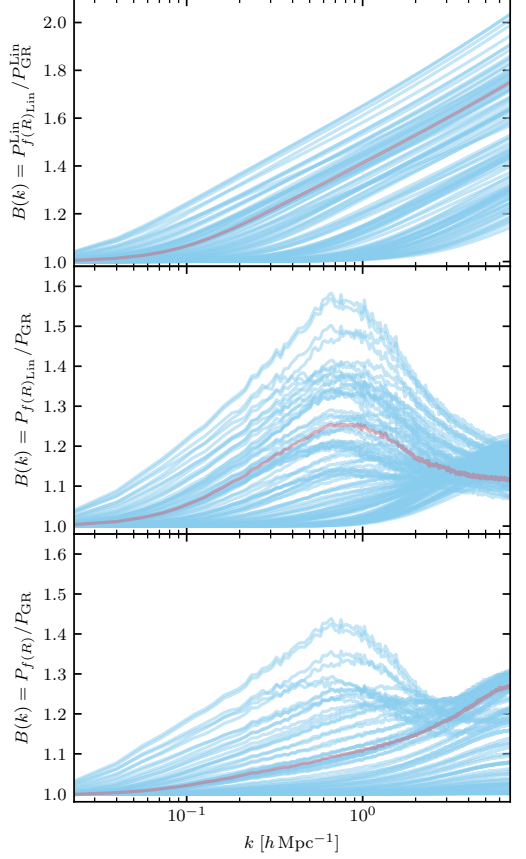
Klypin et al. 2020) for our simulations to suppress the effects of cosmic variance.

In order to know which cosmological parameter to include as variables in the emulator training, we performed some test simulations. Figure 4 displays the non-linear boost for the unscreened  $f(R)$  case, with  $|f_{R0}| = 10^{-5}$ , when different parameters are allowed to vary. From this, it is clear that  $\sigma_8$ ,  $\Omega_{\text{cdm}}$ ,  $w_0$ , and possibly  $w_a$  are the most influential parameters on the power spectrum ratio. Because of this,  $\sigma_8$ ,  $\Omega_{\text{cdm}}$ ,  $w_0$ ,  $w_a$ , and  $\log_{10} f_{R0}$ , in addition to  $z$  and  $k$ , were chosen as the parameters to vary when producing the data used to train the neural network when creating the boost emulator. Tests performed where  $\sigma_8$  is not kept fixed for the  $f(R)$  and GR initial conditions show a larger variation for all the parameters in general. However, fixing  $\sigma_8$  shows that some of this effect is due to the difference in clustering. We also performed tests with screened  $f(R)$  gravity and a different value for  $f_{R0}$ . These tests also pointed toward the same parameter choices.

## 5. Results

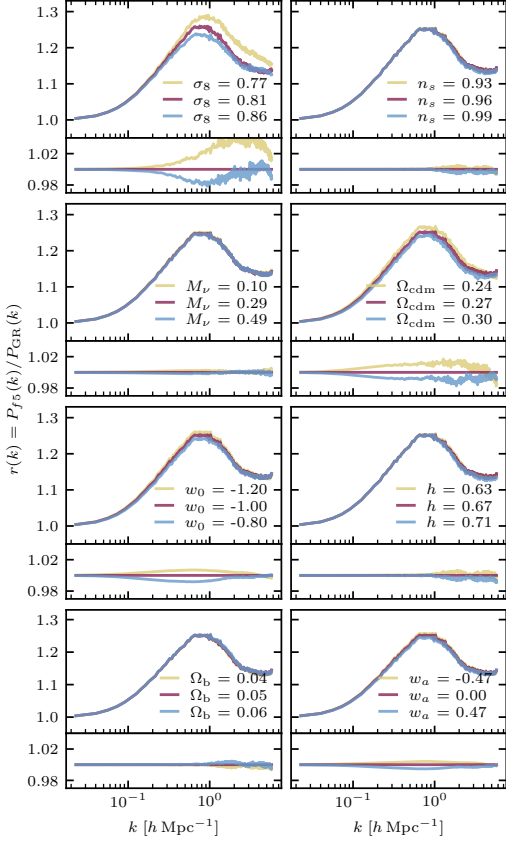
In this section, we present the results for our example boost emulator with  $f(R)$ -modified gravity for three different cases: the linear power spectrum boost with unscreened  $f(R)$  gravity, the non-linear power spectrum boost with unscreened  $f(R)$  gravity, and the non-linear power spectrum boost with screened  $f(R)$  gravity. The emulator results compared to the test data sets can be seen in Figs. 5, 6, and 7 respectively, for three different redshifts.

In general, we see that the fully linear case has better agreement between the emulator and test data for all redshifts, compared to the non-linear cases. This is most likely due to the simplicity of the boost curve, making it easier for the neural network to predict. The same effect is also seen for higher redshifts in all three cases, where the curves flatten out and become easier for the learning processes to capture accurately. Overall, the fully linear boost emulator agrees with the COLASolver simulations to below one percent accuracy on all scales and all redshifts (Fig. 5). For the non-linear unscreened  $f(R)$  case (Fig. 6), we have agreement to below 1% up to  $k \sim 1 h \text{ Mpc}^{-1}$  for red-



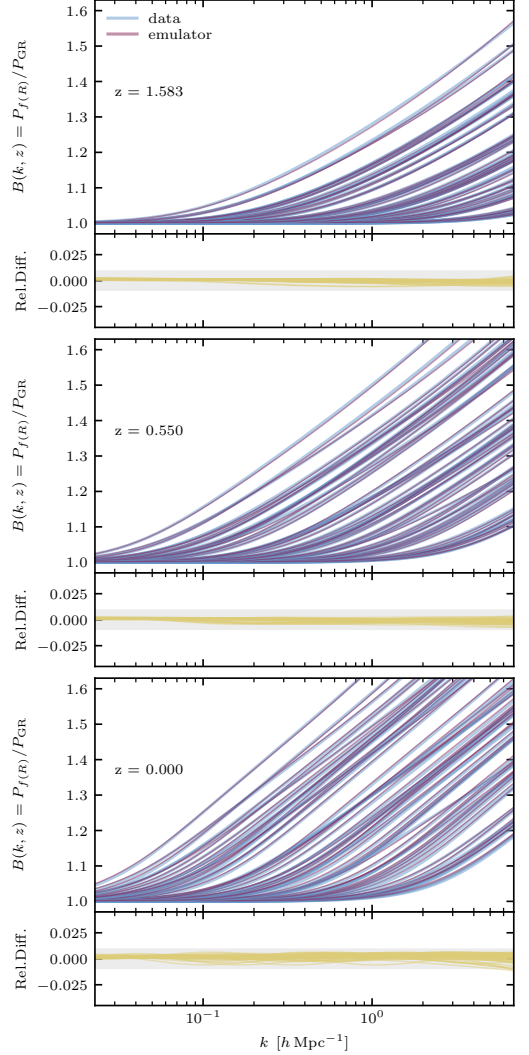
**Fig. 3.** Matter power spectrum (CDM + baryons) boost for modified gravity and GR for the 100 samples shown in Fig. 1 at  $z = 0.0$ . The upper and middle panel shows the linear and non-linear boost for unscreened  $f(R)$  gravity. The lower panel shows the non-linear boost for screened  $f(R)$  gravity. The burgundy line displays the boost for the fiducial cosmology, as listed in Table 1.

shifts  $z = 1.58$  and  $z = 0.55$ , and otherwise agreement to around 2% at smaller scales. For  $z = 0.00$ , we have close to 1% agreement up to  $k \sim 0.3 h \text{ Mpc}^{-1}$ , and between 2 – 3% agreement otherwise. For the non-linear boost in the screened  $f(R)$  gravity case (Fig. 7), we have below one percent accuracy up to  $k \sim 1 h \text{ Mpc}^{-1}$  for  $z = 1.58$ , and below 2% up until the very smallest scales. For  $z = 0.55$ , we deviate from below 1% at  $k \sim 0.2 h \text{ Mpc}^{-1}$ , but again stay within 2% until  $k \sim 5 h \text{ Mpc}^{-1}$ . When we reach redshift zero there are some larger outliers, resulting in some differences around 3 – 4%, although the bulk of the set stays below 2%. Still, for the non-linear boost emulator, both in the case of screened and unscreened  $f(R)$  gravity, it is clear, when compared to Fig. 3, that the curves with the largest discrepancy between predictions and simulations can differ quite a lot from the fiducial expectation. This is not unexpected, as the training set for the neural network will contain



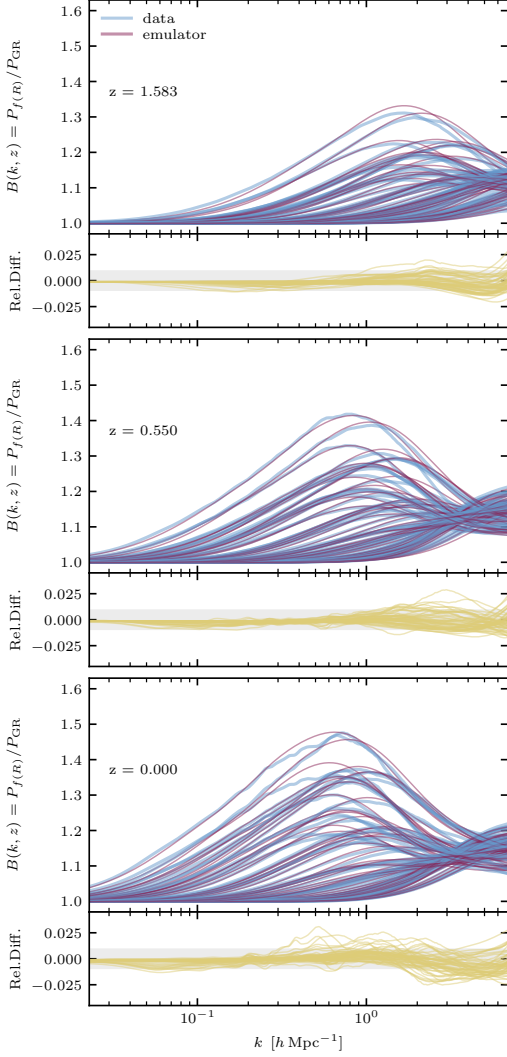
**Fig. 4.** Boost for modified gravity with  $f_{R0} = -10^{-5}$  and GR for different parameter variations. The ratios are shown in the larger panels for three different parameter values, while the narrower panels connected to each large panel show the corresponding ratios of ratios for the three different parameter values, with the middle value as the baseline. The parameters are varied while holding the rest constant, and the fiducial test cosmology is given in Table 1. When varying  $\Omega_{cdm}$ ,  $\Omega_b$  is kept constant, meaning that  $\Omega_m$  varies accordingly. When  $\Omega_b$  is varied,  $\Omega_{cdm}$  also varies so that  $\Omega_m$  is kept constant at a value of 0.32. There is no screening invoked for the  $f(R)$  simulations. The  $M_\nu$  parameter refers to the sum of the neutrino masses and is given in eV.

fewer samples with parameter values that lie close to the edges of the allowed intervals, therefore making the predictions less robust for periphery samples. An example of this is shown in Fig. 8, where an outlier is highlighted. The corresponding parameter sample, compared to the fiducial values, is given in Table 2. The error can be further approved by adjusting the neural network architecture, but will depend on the features in the curve and the parameters included in the training process, and must therefore be adjusted individually for anyone interested in applying the pipeline. It should also be mentioned that for the screened  $f(R)$  gravity emulator (Fig. 7), there could be some overfitting for the simplest curves, due to the relatively complex architecture containing 128 and 64 neurons in the two hidden



**Fig. 5.** Emulator performance compared to the test data sets for various redshifts for the linear boost with unscreened  $f(R)$  gravity. The emulator results, along with the simulations, are given in the larger panels, while the narrower panels display the corresponding relative difference, given by  $B_{emulator}/B_{simulation} - 1$ . The grayed-out area in the same panel shows  $\pm 1\%$ , and the Nyquist frequency of the simulations is  $k \approx 5.7 h \text{ Mpc}^{-1}$ .

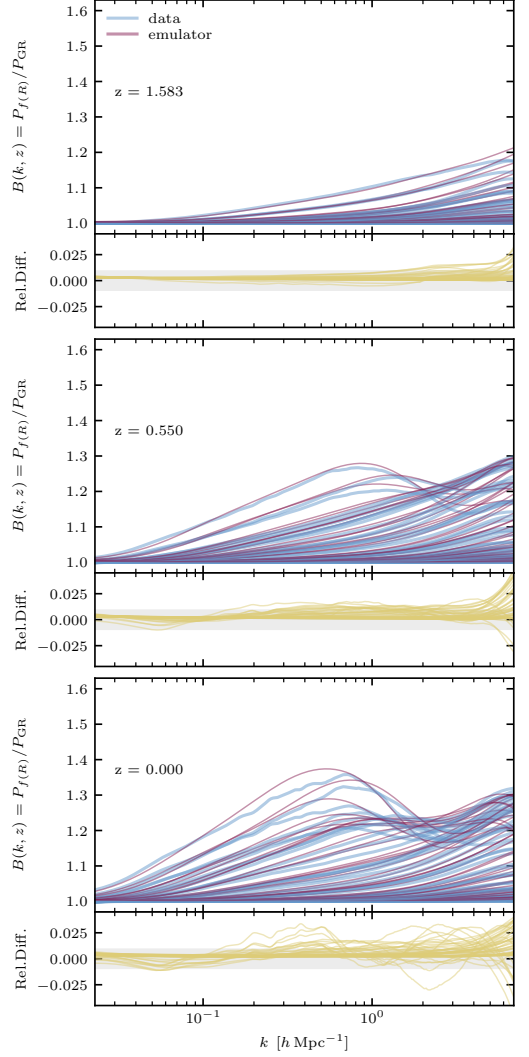
layers. We found that this was necessary in order to catch the shape of the more complex curves, like the one highlighted in Fig. 8. This could possibly be remedied by supplying the neural network with smoother data curves.



**Fig. 6.** Emulator performance compared to the test data sets for various redshifts for the non-linear boost with unscreened  $f(R)$  gravity. Figure setup as explained for Fig. 5.

## 6. Conclusions

Emulators for various global clustering statistics are memory and time-saving. However, creating them often requires a lot of resources through the use of large  $N$ -body simulation suites. Because of this, the construction of accurate emulators usually depends on the use of supercomputers. In this paper, we have presented a full pipeline, *Sesame*, for creating emulators for the matter power spectrum boost,  $B(k, z) = P_{\text{beyond-}\Lambda\text{CDM}}(k, z)/P_{\Lambda\text{CDM}}(k, z)$ , for beyond- $\Lambda$ CDM models, without the need for large computing resources. The

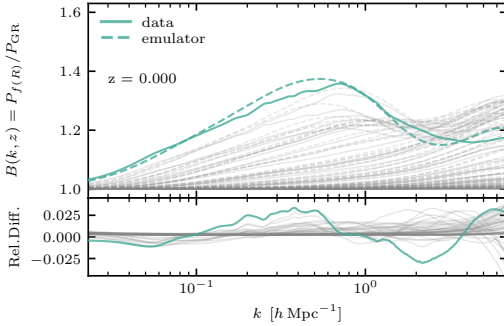


**Fig. 7.** Emulator performance compared to the test data sets for various redshifts for the non-linear boost with screened  $f(R)$  gravity. Figure setup as explained for Fig. 5.

pipeline employs the fast and approximate COLA method (Tassev et al. 2013; Wright et al. 2017; Winther et al. 2017) to perform the simulations, simulating both the beyond- $\Lambda$ CDM and  $\Lambda$ CDM model. This allows us to extract the boost up to higher  $k$ -values, due to some of the internal code artifacts canceling, as demonstrated in e.g. Euclid Consortium et al. (2023). The simulation data is then used to train a neural network, through the PyTorch Lightning deep learning module, resulting in a boost emulator. At this point, we rely on existing  $\Lambda$ CDM emulators to extract  $P_{\text{beyond-}\Lambda\text{CDM}}(k, z)$ .

**Table 2.** Parameters for one of the samples with the largest discrepancy between simulated and emulated boost for the screened  $f(R)$  gravity case, compared to the fiducial values. The parameters  $\Omega_{\text{cdm}}$ ,  $w_0$ , and  $\log_{10} f_{R0}$  all have values close to the interval boundaries of the emulator training data.

Parameter	Fiducial sample	Outlier sample
$\sigma_8$	0.82	0.87
$\Omega_{\text{cdm}}$	0.27	0.21
$w_0$	-1.0	-1.1
$w_a$	0.00	-0.46
$\log_{10} f_{R0}$	-5.00	-4.04



**Fig. 8.** Lower panel of Fig. 7 with one of the largest outliers highlighted in green. The rest of the results are as before, but muted with a gray colour. The parameter sample values of the outlier can be found in Table 2.

Using the pipeline will consist of the following steps:

- Implement the model or parametrisation you want to emulate in the COLASolver. This most commonly consists of implementing the *Hubble* function and how to compute the gravitational potential. Here, already implemented models can be used as examples. For most models, this will be a minor task.
- Pick the simulation setup and do a convergence test to ensure that the setup is converged within the code itself.
- Pick which cosmological parameters you are interested in varying. For this, it is useful to study how the boost,  $B$ , changes when varying individual cosmological parameters, and select the ones that have a significant impact. From our experience, looking at different modified gravity models that deviate from  $\Lambda$ CDM only close to today, as long as the power ( $\sigma_8$ ) is kept the same (depending on the model), either in the initial conditions or at  $z = 0$ , it is often  $\sigma_8$  (or  $A_s$ ) and  $\Omega_m$  that are the most relevant.
- Pick the priors of the parameters you want to vary and the number of samples you want to include, and use this to generate the Latin hypercube samples (script provided in the pipeline).
- Generate all the input for COLASolver, meaning the input files and the necessary power spectra, by running a Boltzmann solver (script provided in the pipeline for CLASS (Lesgourgues 2011; Blas et al. 2011)).
- Run the simulations to produce all the data files containing the power spectra needed to compute the boosts (script provided in the pipeline).

- Gather all the data and make the files needed for the emulator (script provided in the pipeline).
- Determine the neural network architecture (often trial and error) and run the training to produce the emulator (script provided in the pipeline).
- Check the accuracy of the emulator and redo the previous step if needed until you have something acceptable (script to compare the emulator with data provided in the pipeline).
- Estimate the errors. The emulation error can be obtained from the training set and the error of the simulations themselves can be estimated by running a set of high-resolution  $N$ -body simulations or by using already existing simulations.

As an example of using this pipeline, we created three emulators for  $f(R)$ -modified gravity, including massive neutrinos. The three emulators estimate the boost in the cases of linear and non-linear boost for unscreened  $f(R)$  gravity, and the non-linear boost for screened  $f(R)$  gravity. The first two of these have not been made before, while for the last case there already exists several emulators (e.g. Ramachandra et al. 2021; Arnold et al. 2022; Sáez-Casares et al. 2023). The fully linear emulator has below-percent accuracy compared to the simulations, while the non-linear boost emulators have around 2% accuracy. When using emulators to fit data, this error between the emulator and simulations should be taken into account. In addition, the approximate simulation method, COLA, has an error compared to full  $N$ -body simulations, which must also be folded into the error budget.

With the paper, we provide the full pipeline at [https://github.com/remau/Sesame\\_pipeline](https://github.com/remau/Sesame_pipeline). *Sesame* can then be used by anyone to create emulators for their desired beyond- $\Lambda$ CDM model, either by employing one of the models already incorporated in COLASolver code, or by implementing the desired model and then applying the pipeline.

*Acknowledgements.* We would like to thank the Research Council of Norway for their support.

## References

- Adamek, J., Durrer, R., & Kunz, M. 2017, *Journal of Cosmology and Astroparticle Physics*, 2017, 004
- Amendola, L. 2000, *Physical Review D*, 62, 043511
- Angulo, R. E. & Pontzen, A. 2016, *Monthly Notices of the Royal Astronomical Society: Letters*, 462, L1
- Angulo, R. E., Zennaro, M., Contreras, S., et al. 2021, *Monthly Notices of the Royal Astronomical Society*, 507, 5869
- Arnold, C., Li, B., Giblin, B., Harnois-Déraps, J., & Cai, Y. C. 2022, *Monthly Notices of the Royal Astronomical Society*, 515, 4161
- Baldi, M., Villaescusa-Navarro, F., Viel, M., et al. 2014, *Monthly Notices of the Royal Astronomical Society*, 440, 75
- Blas, D., Lesgourgues, J., & Tram, T. 2011, *Journal of Cosmology and Astroparticle Physics*, 2011, 034
- Bose, B., Cataneo, M., Tröster, T., et al. 2020, *Monthly Notices of the Royal Astronomical Society*, 498, 4650
- Bose, B., Tsedrik, M., Kennedy, J., et al. 2023, *Monthly Notices of the Royal Astronomical Society*, 519, 4780
- Bose, B., Wright, B. S., Cataneo, M., et al. 2021, *Monthly Notices of the Royal Astronomical Society*, 508, 2479
- Brandbyge, J. & Hannestad, S. 2009, *Journal of Cosmology and Astroparticle Physics*, 2009, 002
- Brando, G., Fiorini, B., Koyama, K., & Winther, H. A. 2022, *Journal of Cosmology and Astroparticle Physics*, 2022, 051
- Brando, G., Koyama, K., & Winther, H. A. 2023, *Journal of Cosmology and Astroparticle Physics*, 2023, 045
- Brax, P., Van De Bruck, C., Davis, A. C., & Shaw, D. J. 2008, *Physical Review D - Particles, Fields, Gravitation and Cosmology*, 78, 104021
- Buchdahl, H. A. 1970, *Monthly Notices of the Royal Astronomical Society*, 150, 1

- Bull, P., Akrami, Y., Adamek, J., et al. 2016, *Physics of the Dark Universe*, 12, 56
- Cataneo, M., Rapetti, D., Schmidt, F., et al. 2015, *Physical Review D - Particles, Fields, Gravitation and Cosmology*, 92, 044009
- Chabanier, S., Millea, M., & Palanque-DeLabrouille, N. 2019, *Monthly Notices of the Royal Astronomical Society*, 489, 2247
- Chevallier, M. & Polarski, D. 2001, *International Journal of Modern Physics D*, 10, 213
- Clifton, T., Ferreira, P. G., Padilla, A., & Skordis, C. 2012, *Physics Reports*, 513, 1
- Dakin, J., Brandbyge, J., Hannestad, S., Haugbølle, T., & Tram, T. 2019, *Journal of Cosmology and Astroparticle Physics*, 2019, 052
- de Felice, A., & Tsujikawa, S. 2010, *Living Reviews in Relativity*, 13, 1
- DES Collaboration, Abbott, T. M. C., Adamów, M., et al. 2021, *The Astrophysical Journal Supplement Series*, 255, 20
- Di Valentino, E., Gariazzo, S., & Mena, O. 2021, *Physical Review D*, 104, 083504
- Dodelson, S. & Schmidt, F. 2020, Academic Press, Elsevier, 1
- Dvali, G., Gabadadze, G., & Porrati, M. 2000, *Physics Letters B*, 485, 208
- Euclid Collaboration, Knabenhans, M., Stadel, J., et al. 2021, *Monthly Notices of the Royal Astronomical Society*, 505, 2840
- Euclid Collaboration, Scaramella, R., Amiaux, J., et al. 2022, *Astronomy & Astrophysics*, 662, A112
- Euclid Consortium, Adamek, J., Angulo, R. E., et al. 2023, *Journal of Cosmology and Astroparticle Physics*, 2023, 035
- Feng, Y., Chu, M. Y., Seljak, U., & McDonald, P. 2016, *Monthly Notices of the Royal Astronomical Society*, 463, 2273
- Fiorini, B., Koyama, K., & Izard, A. 2022, *Journal of Cosmology and Astroparticle Physics*, 2022, 028
- Giblin, B., Cataneo, M., Moews, B., & Heymans, C. 2019, *Monthly Notices of the Royal Astronomical Society*, 490, 4826
- Giocoli, C., Baldi, M., & Moscardini, L. 2018, *Monthly Notices of the Royal Astronomical Society*, 481, 2813
- Hannestad, S., Wong, Y. Y., Thibault, V., et al. 2020, *Journal of Cosmology and Astroparticle Physics*, 2020, 028
- Hassani, F. & Lombriser, L. 2020, *Monthly Notices of the Royal Astronomical Society*, 497, 1885
- Heitmann, K., Higdon, D., Nakhleh, C., & Habib, S. 2006, *The Astrophysical Journal*, 646, L1
- Heitmann, K., Lawrence, E., Kwan, J., Habib, S., & Higdon, D. 2013, *The Astrophysical Journal*, 780, 111
- Hinterbichler, K., Khoury, J., Levy, A., & Matas, A. 2011, *Physical Review D - Particles, Fields, Gravitation and Cosmology*, 84, 103521
- Hu, W. & Sawicki, I. 2007, *Physical Review D - Particles, Fields, Gravitation and Cosmology*, 76, 064004
- Izard, A., Crocce, M., & Fosalba, P. 2016, *Monthly Notices of the Royal Astronomical Society*, 459, 2327
- J-PAS Collaboration, Benitez, N., Dupke, R., et al. 2014, arXiv:1403.5237
- Joudaki, S., Ferreira, P. G., Lima, N. A., & Winther, H. A. 2022, *Physical Review D*, 105, 043522
- KATRIN Collaboration, Aker, M., Beglarian, A., et al. 2022, *Nature Physics* 2022 18:2, 18, 160
- Khoury, J. & Weltman, A. 2004a, *Physical Review D*, 69, 044026
- Khoury, J. & Weltman, A. 2004b, *Physical Review Letters*, 93, 171104
- Klypin, A., Prada, F., & Byun, J. 2020, *Monthly Notices of the Royal Astronomical Society*, 496, 3862
- Koda, J., Blake, C., Beutler, F., Kazin, E., & Marin, F. 2016, *Monthly Notices of the Royal Astronomical Society*, 459, 2118
- Koyama, K. 2016, *Reports on Progress in Physics*, 79, 046902
- Koyama, K., Taruya, A., & Hirata, T. 2009, *Physical Review D - Particles, Fields, Gravitation and Cosmology*, 79, 123512
- Kwan, J., Heitmann, K., Habib, S., et al. 2015, *The Astrophysical Journal*, 810, 35
- Laureijs, R., Amiaux, J., Arduini, S., et al. 2011, arXiv:1110.3193
- Leclercq, F., Faure, B., Lavaux, G., et al. 2020, *Astronomy & Astrophysics*, 639, A91
- Lesgourgues, J. 2011, arXiv:1104.2932
- Lesgourgues, J. & Pastor, S. 2006, *Physics Reports*, 429, 307
- Li, B., Zhao, G. B., Teyssier, R., & Koyama, K. 2012, *Journal of Cosmology and Astroparticle Physics*, 2012, 051
- Linder, E. V. 2003, *Physical Review Letters*, 90, 4
- Liu, J., Bird, S., Matilla, J. M. Z., et al. 2018, *Journal of Cosmology and Astroparticle Physics*, 2018, 049
- Linares, C., Mota, D. F., & Winther, H. A. 2014, *Astronomy & Astrophysics*, 562, A78
- LSST Collaboration, Ivezić, Z., Kahn, S. M., et al. 2019, *The Astrophysical Journal*, 873, 111
- Marsh, D. J. 2016, *Physics Reports*, 643, 1
- Martin, J., Ringeval, C., & Vennin, V. 2014, *Physics of the Dark Universe*, 5, 75
- Mauland, R., Elgarøy, Ø., Mota, D. F., & Winther, H. A. 2023, *Astronomy & Astrophysics*, 674, A185
- McKay, M. D., Beckman, R. J., & Conover, W. J. 1979, *Technometrics*, 21, 239
- Moran, K. R., Heitmann, K., Lawrence, E., et al. 2023, *Monthly Notices of the Royal Astronomical Society*, 520, 3443
- Nishimichi, T., Takada, M., Takahashi, R., et al. 2019, *The Astrophysical Journal*, 884, 29
- Particle Data Group, Workman, R. L., & Others. 2022, *PTEP*, 2022, 083C01
- Partmann, C., Fidler, C., Rampf, C., & Hahn, O. 2020, *Journal of Cosmology and Astroparticle Physics*, 2020, 018
- Planck Collaboration, Aghanim, N., Akrami, Y., et al. 2020, *Astronomy & Astrophysics*, 641, A6
- Pogosian, L. & Silvestri, A. 2008, *Physical Review D - Particles, Fields, Gravitation and Cosmology*, 77, 023503
- Potter, D., Stadel, J., & Teyssier, R. 2016, arXiv:1609.08621
- Puchwein, E., Baldi, M., & Springel, V. 2013, *Monthly Notices of the Royal Astronomical Society*, 436, 348
- Ramachandra, N., Valogiannis, G., Ishak, M., & Heitmann, K. 2021, *Physical Review D*, 103, 123525
- Ruan, C. Z., Hernández-Aguayo, C., Li, B., et al. 2022, *Journal of Cosmology and Astroparticle Physics*, 2022, 018
- Sáez-Casares, I., Rasera, Y., & Li, B. 2023, arXiv:2303.08899
- Savitzky, A. & Golay, M. J. 1964, *Analytical Chemistry*, 36, 1627
- Song, Y. S., Hu, W., & Sawicki, I. 2007, *Physical Review D - Particles, Fields, Gravitation and Cosmology*, 75, 044004
- Sotiriou, T. P. & Faraoni, V. 2010, *Reviews of Modern Physics*, 82, 451
- Springel, V., Pakmor, R., Zier, O., & Reinecke, M. 2021, *Monthly Notices of the Royal Astronomical Society*, 506, 2871
- Tassev, S., Eisenstein, D. J., Wandelt, B. D., & Zaldarriaga, M. 2015, arXiv:1502.07751
- Tassev, S., Zaldarriaga, M., & Eisenstein, D. J. 2013, *Journal of Cosmology and Astroparticle Physics*, 2013, 036
- Thomson, M. 2013, Cambridge University press
- Valogiannis, G. & Bean, R. 2017, *Physical Review D*, 95, 103515
- Villaescusa-Navarro, F., Naess, S., Genel, S., et al. 2018, *The Astrophysical Journal*, 867, 137
- Weinberger, R., Springel, V., & Pakmor, R. 2020, *The Astrophysical Journal Supplement Series*, 248, 32
- Wetterich, C. 1988, *Nuclear Physics B*, 302, 668
- Will, C. M. 2014, *Living Reviews in Relativity* 2014 17:1, 17, 1
- Winther, H. A., Casas, S., Baldi, M., et al. 2019, *Physical Review D*, 100, 123540
- Winther, H. A. & Ferreira, P. G. 2015, *Physical Review D - Particles, Fields, Gravitation and Cosmology*, 91, 123507
- Winther, H. A., Koyama, K., Manera, M., Wright, B. S., & Zhao, G. B. 2017, *Journal of Cosmology and Astroparticle Physics*, 2017, 006
- Winther, H. A., Schmidt, F., Barreira, A., et al. 2015, *Monthly Notices of the Royal Astronomical Society*, 454, 4208
- Wright, B. S., Sen Gupta, A., Baker, T., Valogiannis, G., & Fiorini, B. 2023, *Journal of Cosmology and Astroparticle Physics*, 2023, 040
- Wright, B. S., Winther, H. A., & Koyama, K. 2017, *Journal of Cosmology and Astroparticle Physics*, 2017, 054
- Zhao, G. B. 2014, *The Astrophysical Journal Supplement Series*, 211, 23



# Bibliography

- Adamek, J. et al. (July 2016). “gevolution: a cosmological N-body code based on General Relativity”. In: *Journal of Cosmology and Astroparticle Physics* vol. 2016, no. 07, p. 053.
- Alcock, C. and Paczyński, B. (Oct. 1979). “An evolution free test for non-zero cosmological constant”. In: *Nature 1979 281:5730* vol. 281, no. 5730, pp. 358–359.
- Alexander, S., Bernardo, H., and Toomey, M. W. (July 2022). “Addressing the Hubble and  $H_0$  Tensions with a Kinetically Mixed Dark Sector”. In: *Journal of Cosmology and Astroparticle Physics* vol. 2023, no. 3.
- Arnold, C. et al. (Feb. 2019). “The modified gravity light-cone simulation project – I. Statistics of matter and halo distributions”. In: *Monthly Notices of the Royal Astronomical Society* vol. 483, no. 1, pp. 790–805.
- Bagla, J. S. (Nov. 2005). “Cosmological N-Body simulation: Techniques, Scope and Status”. In: *Current Science* vol. 88, pp. 1088–1100. arXiv: 0411043 [astro-ph].
- Baldi, M. et al. (May 2014). “Cosmic degeneracies – I. Joint N-body simulations of modified gravity and massive neutrinos”. In: *Monthly Notices of the Royal Astronomical Society* vol. 440, no. 1, pp. 75–88.
- Baumann, D. (June 2022). “Cosmology”. In: *Cambridge University Press*.
- Behroozi, P. S., Wechsler, R. H., and Wu, H. Y. (Dec. 2012). “The ROCKSTAR Phase-Space Temporal Halo Finder and the Velocity Offsets of Cluster Cores”. In: *Astrophysical Journal* vol. 762, no. 2, p. 109.
- Bekenstein, J. D. (Oct. 2004). “Relativistic gravitation theory for the modified Newtonian dynamics paradigm”. In: *Physical Review D* vol. 70, no. 8, p. 083509.
- Benson, A. J. et al. (Feb. 2000). “The nature of galaxy bias and clustering”. In: *Monthly Notices of the Royal Astronomical Society* vol. 311, no. 4, pp. 793–808.
- Brandbyge, J. and Hannestad, S. (May 2009). “Grid based linear neutrino perturbations in cosmological N-body simulations”. In: *Journal of Cosmology and Astroparticle Physics* vol. 2009, no. 05, p. 002.
- Brandt, T. D. (June 2016). “Constraints on MACHO Dark Matter from Compact Stellar Systems in Ultra-Faint Dwarf Galaxies”. In: *The Astrophysical Journal Letters* vol. 824, no. 2.
- Brax, P. et al. (Nov. 2008). “f(R) gravity and chameleon theories”. In: *Physical Review D - Particles, Fields, Gravitation and Cosmology* vol. 78, no. 10, p. 104021.
- Carroll, B. W. and Ostlie, D. A. (2014). “An introduction to modern astrophysics.” In: *Pearson*, p. 1470.

- Castorina, E. et al. (Feb. 2014). “Cosmology with massive neutrinos II: on the universality of the halo mass function and bias”. In: *Journal of Cosmology and Astroparticle Physics* vol. 2014, no. 02, p. 049.
- Castro, T., Marra, V., and Quartin, M. (Dec. 2016). “Constraining the halo mass function with observations”. In: *Monthly Notices of the Royal Astronomical Society* vol. 463, no. 2, pp. 1666–1677.
- Cataneo, M. et al. (Aug. 2015). “New constraints on  $f(R)$  gravity from clusters of galaxies”. In: *Physical Review D - Particles, Fields, Gravitation and Cosmology* vol. 92, no. 4, p. 044009.
- Chiang, C. T., Loverde, M., and Villaescusa-Navarro, F. (Feb. 2019). “First Detection of Scale-Dependent Linear Halo Bias in N-Body Simulations with Massive Neutrinos”. In: *Physical Review Letters* vol. 122, no. 4, p. 041302.
- Contarini, S. et al. (June 2021). “Cosmic voids in modified gravity models with massive neutrinos”. In: *Monthly Notices of the Royal Astronomical Society* vol. 504, no. 4, pp. 5021–5038.
- Dakin, J., Hannestad, S., and Tram, T. (Apr. 2022). “The cosmological simulation code CONCEPT 1.0”. In: *Monthly Notices of the Royal Astronomical Society* vol. 513, no. 1, pp. 991–1014.
- De Blok, W. J. (2010). “The core-cusp problem”. In: *Advances in Astronomy* vol. 2010.
- Del Popolo, A. and Pace, F. (Apr. 2016). “The Cusp/Core problem: supernovae feedback versus the baryonic clumps and dynamical friction model”. In: *Astrophysics and Space Science 2016 361:5* vol. 361, no. 5, pp. 1–20.
- Desjacques, V., Jeong, D., and Schmidt, F. (Nov. 2018). “Large-Scale Galaxy Bias”. In: *Physics Reports* vol. 733, pp. 1–193.
- Despali, G. et al. (Mar. 2016). “The universality of the virial halo mass function and models for non-universality of other halo definitions”. In: *Monthly Notices of the Royal Astronomical Society* vol. 456, no. 3, pp. 2486–2504.
- Di Valentino, E., Gariazzo, S., and Mena, O. (Oct. 2021). “Most constraining cosmological neutrino mass bounds”. In: *Physical Review D* vol. 104, no. 8, p. 083504.
- Dodelson, S. and Schmidt, F. (Jan. 2020). “Modern Cosmology”. In: *Academic Press, Elsevier*, no. Second Edition, pp. 1–494.
- Duffy, L. D. and Van Bibber, K. (Oct. 2009). “Axions as dark matter particles”. In: *New Journal of Physics* vol. 11, no. 10, p. 105008.
- Efstathiou, G. et al. (Feb. 1985). “Numerical techniques for large cosmological N-body simulations”. In: *Astrophysical Journal Supplement Series* vol. 57, pp. 241–260.
- Euclid Collaboration et al. (June 2023). “Euclid: Constraints on  $f(R)$  cosmologies from the spectroscopic and photometric primary probes”. In: *arXiv:2306.11053*.
- Euclid Consortium et al. (June 2023). “Euclid: modelling massive neutrinos in cosmology - a code comparison”. In: *Journal of Cosmology and Astroparticle Physics* vol. 2023, no. 6, p. 035.



- Fisher, K. B. (Aug. 1995). “On the validity of the streaming model for the redshift space correlation function in the linear regime”. In: *Astrophysical Journal* vol. 448, pp. 494–499.
- Fukuda, Y. et al. (Aug. 1998). “Evidence for Oscillation of Atmospheric Neutrinos”. In: *Physical Review Letters* vol. 81, no. 8, p. 1562.
- Giocoli, C., Baldi, M., and Moscardini, L. (Dec. 2018). “Weak lensing light-cones in modified gravity simulations with and without massive neutrinos”. In: *Monthly Notices of the Royal Astronomical Society* vol. 481, no. 2, pp. 2813–2828.
- Gunn, J. E. and Gott J. Richard, I. (Aug. 1972). “On the Infall of Matter Into Clusters of Galaxies and Some Effects on Their Evolution”. In: *The Astrophysical Journal* vol. 176, pp. 1–19.
- Hagstotz, S. et al. (July 2019). “Joint halo-mass function for modified gravity and massive neutrinos – I. Simulations and cosmological forecasts”. In: *Monthly Notices of the Royal Astronomical Society* vol. 486, no. 3, pp. 3927–3941.
- Hannestad, S., Upadhye, A., and Wong, Y. Y. (Nov. 2020). “Spoon or slide? The non-linear matter power spectrum in the presence of massive neutrinos”. In: *Journal of Cosmology and Astroparticle Physics* vol. 2020, no. 11, p. 062.
- Hastie, T., Tibshirani, R., and Friedman, J. (2009). “The Elements of Statistical Learning - Data Mining, Inference, and Prediction”. In: *Springer, Second Edition*. Springer Series in Statistics, pp. 1–737.
- Hernández, O. F. (June 2017). “Neutrino masses, scale-dependent growth, and redshift-space distortions”. In: *Journal of Cosmology and Astroparticle Physics* vol. 2017, no. 06, p. 018.
- Hu, W. and Sawicki, I. (Sept. 2007). “Models of  $f(R)$  cosmic acceleration that evade solar system tests”. In: *Physical Review D - Particles, Fields, Gravitation and Cosmology* vol. 76, no. 6, p. 064004.
- Ishak, M. (Dec. 2018). “Testing general relativity in cosmology”. In: *Living Reviews in Relativity 2018 22:1* vol. 22, no. 1, pp. 1–204.
- Joyce, A., Lombriser, L., and Schmidt, F. (Oct. 2016). “Dark Energy Versus Modified Gravity”. In: *Annual Review of Nuclear and Particle Science* vol. 66, pp. 95–122.
- Kamionkowski, M. and Kovetz, E. D. (Sept. 2016). “The Quest for B Modes from Inflationary Gravitational Waves”. In: *Annual Review of Astronomy and Astrophysics* vol. 54, pp. 227–269.
- KamLAND Collaboration et al. (Mar. 2005). “Measurement of neutrino oscillation with KamLAND: Evidence of spectral distortion”. In: *Physical Review Letters* vol. 94, no. 8, p. 081801.
- KATRIN Collaboration et al. (Feb. 2022). “Direct neutrino-mass measurement with sub-electronvolt sensitivity”. In: *Nature Physics 2022 18:2* vol. 18, no. 2, pp. 160–166.
- Khoury, J. and Weltman, A. (Feb. 2004). “Chameleon cosmology”. In: *Physical Review D* vol. 69, no. 4, p. 044026.
- Koyama, K. (Mar. 2016). “Cosmological tests of modified gravity”. In: *Reports on Progress in Physics* vol. 79, no. 4, p. 046902.

- Laureijs, R. et al. (Oct. 2011). “Euclid Definition Study Report”. In: *arXiv:1110.3193*.
- Lesgourgues, J. and Pastor, S. (July 2006). “Massive neutrinos and cosmology”. In: *Physics Reports* vol. 429, no. 6, pp. 307–379.
- LiteBIRD Collaboration et al. (Apr. 2023). “Probing cosmic inflation with the LiteBIRD cosmic microwave background polarization survey”. In: *Progress of Theoretical and Experimental Physics* vol. 2023, no. 4.
- Llinares, C., Mota, D. F., and Winther, H. A. (Feb. 2014). “ISIS: a new N-body cosmological code with scalar fields based on RAMSES - Code presentation and application to the shapes of clusters”. In: *Astronomy & Astrophysics* vol. 562, A78.
- Marsland, S. (Jan. 2014). “Machine learning: An algorithmic perspective”. In: *Chapman & Hall/CRC, Second Edition*, pp. 1–452.
- Martin, J. (July 2012). “Everything you always wanted to know about the cosmological constant problem (but were afraid to ask)”. In: *Comptes Rendus Physique* vol. 13, no. 6-7, pp. 566–665.
- Massey, R., Kitching, T., and Richard, J. (July 2010). “The dark matter of gravitational lensing”. In: *Reports on Progress in Physics* vol. 73, no. 8.
- Mauland, R. et al. (June 2023). “The void-galaxy cross-correlation function with massive neutrinos and modified gravity”. In: *Astronomy & Astrophysics* vol. 674, A185.
- Meszaros, P. (1974). “The behaviour of point masses in an expanding cosmological substratum”. In: *Astronomy and Astrophysics* vol. 37, no. 2, pp. 225–228.
- Mirzatuny, N. and Pierpaoli, E. (Sept. 2019). “An accurate fitting function for scale-dependent growth rate in Hu-Sawicki  $f(R)$  gravity”. In: *Journal of Cosmology and Astroparticle Physics* vol. 2019, no. 09, p. 066.
- Nadathur, S., Carter, P., and Percival, W. J. (Jan. 2019). “A Zeldovich reconstruction method for measuring redshift space distortions using cosmic voids”. In: *Monthly Notices of the Royal Astronomical Society* vol. 482, no. 2, pp. 2459–2470.
- Nadathur, S. et al. (Apr. 2019). “Beyond BAO: improving cosmological constraints from BOSS with measurement of the void-galaxy cross-correlation”. In: *Physical Review D* vol. 100, no. 2.
- Navarro, J. F., Frenk, C. S., and White, S. D. M. (May 1996). “The Structure of Cold Dark Matter Halos”. In: *The Astrophysical Journal* vol. 462, p. 563.
- Nguyen, Q. L. et al. (Dec. 2021). “3-3-1 Self interacting dark matter and the galaxy core-cusp problem”. In: *Modern Physics Letters A* vol. 36, no. 3.
- Oh, S. H. et al. (May 2015). “High-Resolution Mass Models of Dwarf Galaxies from LITTLE THINGS”. In: *The Astronomical Journal* vol. 149, no. 6, p. 180.
- Paillas, E. et al. (July 2021). “Redshift-space distortions with split densities”. In: *Monthly Notices of the Royal Astronomical Society* vol. 505, no. 4, pp. 5731–5752.
- Particle Data Group, Workman, R. L., et al. (2022). “Review of Particle Physics”. In: *PTEP* vol. 2022, p. 083C01.

- Peacock, J. A. and Heavens, A. F. (Oct. 1990). “Alternatives to the Press–Schechter cosmological mass function”. In: *Monthly Notices of the Royal Astronomical Society* vol. 243, no. 1, pp. 133–143.
- Peebles, E. P. J. (1980). “The large-scale structure of the universe”. In: *Princeton University Press*.
- (Dec. 1993). “Principles of Physical Cosmology”. In: *Princeton University Press*.
- Planck Collaboration et al. (Sept. 2020a). “Planck 2018 results - I. Overview and the cosmological legacy of Planck”. In: *Astronomy & Astrophysics* vol. 641, A1.
- Planck Collaboration et al. (Sept. 2020b). “Planck 2018 results - VI. Cosmological parameters”. In: *Astronomy & Astrophysics* vol. 641, A6.
- Poulin, V. et al. (June 2023). “Sigma-8 tension is a drag”. In: *Physical Review D* vol. 107, no. 12, p. 123538.
- Press, W. H. et al. (Feb. 1974). “Formation of Galaxies and Clusters of Galaxies by Self-Similar Gravitational Condensation”. In: *Astrophysical Journal* vol. 187, pp. 425–438.
- Quinn, T. et al. (Oct. 1997). “Time stepping N-body simulations”. In: *arXiv:astro-ph/9710043*.
- Riess, A. G. et al. (Sept. 1998). “Observational Evidence from Supernovae for an Accelerating Universe and a Cosmological Constant”. In: *The Astronomical Journal* vol. 116, no. 3, pp. 1009–1038.
- Riess, A. G. et al. (July 2022). “A Comprehensive Measurement of the Local Value of the Hubble Constant with 1 km s<sup>-1</sup> Mpc<sup>-1</sup> Uncertainty from the Hubble Space Telescope and the SH0ES Team”. In: *The Astrophysical Journal Letters* vol. 934, no. 1, p. L7.
- Rubin, V. C., Ford, W. K., and Thonnard, N. (1980). “Rotational Properties of 21 Sc Galaxies with a Large Range of Luminosities and Radii, from NGC 4605 (R = 4 kpc) to UGC 2885 (R = 122 kpc)”. In: *The Astrophysical Journal* vol. 238, pp. 471–487.
- Sakharov, D. (May 1991). “Violation of cp in variance, C asymmetry, and baryon asymmetry of the universe”. In: *Soviet Physics - Uspekhi* vol. 34, no. 5, pp. 392–393.
- Schneider, A. et al. (Apr. 2016). “Matter power spectrum and the challenge of percent accuracy”. In: *Journal of Cosmology and Astroparticle Physics* vol. 2016, no. 04, p. 047.
- Schumann, M. (Aug. 2019). “Direct detection of WIMP dark matter: concepts and status”. In: *Journal of Physics G: Nuclear and Particle Physics* vol. 46, no. 10.
- Sirko, E. (Dec. 2005). “Initial Conditions to Cosmological N -Body Simulations, or, How to Run an Ensemble of Simulations ”. In: *The Astrophysical Journal* vol. 634, no. 2, pp. 728–743.
- SNO Collaboration et al. (June 2002). “Direct Evidence for Neutrino Flavor Transformation from Neutral-Current Interactions in the Sudbury Neutrino Observatory”. In: *Physical Review Letters* vol. 89, no. 1, p. 011301.

- Sotiriou, T. P. and Faraoni, V. (Mar. 2010). “f(R) theories of gravity”. In: *Reviews of Modern Physics* vol. 82, no. 1, pp. 451–497.
- Springel, V. et al. (July 2021). “Simulating cosmic structure formation with the gadget-4 code”. In: *Monthly Notices of the Royal Astronomical Society* vol. 506, no. 2, pp. 2871–2949.
- Tanimura, H. et al. (June 2023). “Testing decaying dark matter models as a solution to the S8 tension with the thermal Sunyaev-Zel’dovich effect”. In: *Astronomy & Astrophysics* vol. 674, A222.
- Tassev, S., Zaldarriaga, M., and Eisenstein, D. J. (June 2013). “Solving large scale structure in ten easy steps with COLA”. In: *Journal of Cosmology and Astroparticle Physics* vol. 2013, no. 06, p. 036.
- Teyssier, R. (Apr. 2002). “Cosmological hydrodynamics with adaptive mesh refinement - A new high resolution code called RAMSES”. In: *Astronomy & Astrophysics* vol. 385, no. 1, pp. 337–364.
- Thomson, M. (Sept. 2013). “Modern Particle Physics”. In: *Cambridge University press*.
- Totsuji, H. and Kihara, T. (1969). “The Correlation Function for the Distribution of Galaxies”. In: *Publications of the Astronomical Society of Japan* vol. 21, p. 221.
- Watson, D. F., Berlind, A. A., and Zentner, A. R. (Aug. 2011). “A Cosmic Coincidence: The Power-Law Galaxy Correlation Function”. In: *The Astrophysical Journal* vol. 738, no. 1, p. 22.
- Will, C. M. (Dec. 2014). “The Confrontation between General Relativity and Experiment”. In: *Living Reviews in Relativity 2014 17:1* vol. 17, no. 1, pp. 1–117.
- Winther, H. A. et al. (Aug. 2017). “COLA with scale-dependent growth: applications to screened modified gravity models”. In: *Journal of Cosmology and Astroparticle Physics* vol. 2017, no. 08, p. 006.
- Woodfinden, A. et al. (Sept. 2022). “Measurements of cosmic expansion and growth rate of structure from voids in the Sloan Digital Sky Survey between redshift 0.07 and 1.0”. In: *Monthly Notices of the Royal Astronomical Society*.
- Wright, B. S., Winther, H. A., and Koyama, K. (Oct. 2017). “COLA with massive neutrinos”. In: *Journal of Cosmology and Astroparticle Physics* vol. 2017, no. 10, p. 054.
- Wright, B. S. et al. (June 2019). “Investigating the degeneracy between modified gravity and massive neutrinos with redshift-space distortions”. In: *Journal of Cosmology and Astroparticle Physics* vol. 2019, no. 06, p. 040.
- Xu, G. (May 1995). “A New Parallel N-Body Gravity Solver: TPM”. In: *The Astrophysical Journal Supplement Series* vol. 98, p. 355.
- Zel’dovich, Y. B. (1970). “Gravitational instability: An approximate theory for large density perturbations.” In: *Astronomy & Astrophysics* vol. 5, pp. 84–89.
- Zhao, G. B., Li, B., and Koyama, K. (Feb. 2011). “N-body simulations for f(R) gravity using a self-adaptive particle-mesh code”. In: *Physical Review D - Particles, Fields, Gravitation and Cosmology* vol. 83, no. 4, p. 044007.
- Zwicky, F. (Jan. 2009). “Republication of: The redshift of extragalactic nebulae”. In: *General Relativity and Gravitation* vol. 41, no. 1, pp. 207–224.